DISSERTATION

submitted to the

Combined Faculty of Natural Sciences and Mathematics
of Heidelberg University, Germany
for the degree of
Doctor of Natural Sciences

and to the

Doctoral College of Physics and Chemistry-Physics (ED 182)
of the University of Strasbourg, France
for the degree of
Docteur de l'univeristé de Strasbourg

put forward by
Tobias Martin Wintermantel

born in Tübingen, Germany
Oral examination: January 13, 2021

Complex systems dynamics in laser excited ensembles of Rydberg atoms

Supervisors:

Prof. Dr. Matthias Weidemüller	Ruprecht-Karls-Universität Heidelberg
Prof. Dr. Shannon Whitlock	Université de Strasbourg

Referees:

Prof. Dr. Selim Jochim	Ruprecht-Karls-Universität Heidelberg
Prof. Dr. Matthias Weidemüller	Ruprecht-Karls-Universität Heidelberg
Prof. Dr. Shannon Whitlock	Université de Strasbourg

Additional committee members:

Prof. Dr. Tilman Enss	Ruprecht-Karls-Universität Heidelberg
Prof. Dr. Ulrich Schwarz	Ruprecht-Karls-Universität Heidelberg

Abstract

In this thesis I present experimental and theoretical results showing that an ultracold gas under laser excitation to Rydberg states offers a controllable platform for studying the interesting complex dynamics that can emerge in driven-dissipative systems. The findings can be summarized according to the following three main insights: (i) The discovery of self-organized criticality (SOC) in our Rydberg system under facilitated excitation via three signatures: self-organization of the density to a stationary state; scale invariant behavior; and a critical response in terms of power-law distributed excitation avalanches. Additionally, we explore a mechanism inherent to our system which stabilizes the SOC state. We further investigate this stabilization via a controlled, variable driving of the system. These analyses can help answer the question of why scale invariant behavior is so prevalent in nature. (ii) A striking connection between the power-law growth of the Rydberg excitation number and epidemic spreading is found. Based on this, an epidemic network model is devised which efficiently describes the collective excitation dynamics. The importance of heterogeneity in the emergent Rydberg network and associated Griffiths effects provide a way to explain the observation of non-universal power laws. (iii) A novel quantum cellular automata implementation is proposed using atomic arrays together with multifrequency laser fields. This provides a natural framework to study the relation between microscopic processes and global dynamics, where special rules are found to generate entangled states with applications in quantum metrology and computing.

Zusammenfassung

In dieser Arbeit stelle ich experimentelle und theoretische Ergebnisse vor, die zeigen, dass ein ultrakaltes Gas unter Laseranregung in Rydberg-Zustände eine kontrollierbare Plattform für die Untersuchung der interessanten, komplexen Dynamik bietet, die in getriebenen dissipativen Systemen entstehen kann. Die Ergebnisse lassen sich in die folgenden drei Bereiche gliedern: (i) Die Entdeckung der selbstorganisierten Kritikalität (SOC) in unserem Rydberg-System unter fazilitierter Anregung durch drei Signaturen: Selbstorganisation der Dichte zu einem stationären Zustand, skaleninvariantes Verhalten sowie eine kritische Reaktion in Form von potenzgesetzlich verteilten

Anregungslawinen. Zudem finden wir einen inhärenten und einen kontrollierten Mechanismus, der den SOC-Zustand stabilisiert. Dies kann bei der Beantwortung der Frage helfen, warum skaleninvariantes Verhalten in der Natur so weit verbreitet ist. (ii) Es besteht ein auffälliger Zusammenhang zwischen dem potenzgesetzlichen Wachstum der Rydberg-Anregungszahl und der epidemischen Ausbreitung. Darauf aufbauend wird ein epidemisches Netzwerkmodell entwickelt, das die kollektive Anregungsdynamik effizient beschreibt. Die Bedeutung der Heterogenität im entstehenden Rydberg-Netzwerk und die damit verbundenen Griffiths-Effekte eröffnen die Möglichkeit, die Beobachtung von nicht-universellen Potenzgesetzen zu erklären. (iii) Es wird eine neuartige Implementierung von Quanten-Zellularautomaten vorgeschlagen, welche auf atomaren Anordnungen zusammen mit Multifrequenz-Laserfeldern basiert. Dies bietet einen natürlichen Rahmen, um die Beziehung zwischen mikroskopischen Prozessen und globaler Dynamik zu untersuchen, wobei spezielle Regeln gefunden werden, um verschränkte Zustände für Anwendungen in der Quantenmetrologie und -informatik zu erzeugen.

Résumé

Dans cette thèse, je présente des résultats expérimentaux et théoriques montrant qu'un gaz ultra-froid sous excitation laser aux états de Rydberg offre une plateforme contrôlable pour l'étude d'une intéressante dynamique complexe qui peut émerger dans les systèmes drivés-dissipatifs. Les conclusions peuvent être résumées selon les trois idées principales suivantes : (i) La découverte de la criticité auto-organisée dans notre système de Rydberg sous excitation facilitée peut aider à répondre à la question suivante : Pourquoi le comportement invariant d'échelle est si répandu dans la nature ? (ii) Un lien frappant est établi entre la croissance de la loi de puissance du nombre d'excitation de Rydberg et la propagation des épidémies. L'importance de l'hétérogénéité dans le réseau Rydberg émergeant et les effets Griffith associés permettent d'expliquer l'observation de lois de puissance non universelles. (iii) Une nouvelle mise en œuvre d'automates cellulaires quantiques est proposée en utilisant des réseaux atomiques associés à des champs laser multifréquences. Cela fournit un cadre naturel pour étudier la relation entre les processus microscopiques et la dynamique globale, où des règles spéciales sont trouvées pour générer des états enchevêtrés pour des applications en métrologie et en informatique quantique.

List of publications

The results presented in this thesis have led to the following manuscripts and peer-reviewed publications, which have been written and published during the course of my doctoral studies:

- **Epidemic growth and Griffiths effects on an emergent network of excited atoms**
  T. M. Wintermantel, M. Buchhold, S. Shevate, M. Morgado, Y. Wang, G. Lochead, S. Diehl, and S. Whitlock
  arXiv:2007.07697 (2020), accepted in Nature Communications

- **Unitary and Nonunitary Quantum Cellular Automata with Rydberg Arrays**
  T. M. Wintermantel, Y. Wang, G. Lochead, S. Shevate, G. K. Brennen, and S. Whitlock
  Physical Review Letters 124, 070503 (2020)

- **Signatures of self-organized criticality in an ultracold atomic gas**
  S. Helmrich, A. Arias, G. Lochead, T. M. Wintermantel, M. Buchhold, S. Diehl, and S. Whitlock
  Nature 577, 481-486 (2020)

- **Hydrodynamic stabilization of self-organized criticality in a driven Rydberg gas**
  K. Klocke, T. W. Wintermantel, G. Lochead, S. Whitlock, and M. Buchhold
  arXiv:2009.11908 (2020), under review in Physical Review Letters

- **Preparation of hundreds of microscopic atomic ensembles in optical tweezer arrays**
  Y. Wang, S. Shevate, T. M. Wintermantel, M. Morgado, G. Lochead, and S. Whitlock
  npj Quantum Information 6, 54 (2020)

- **Realization of a Rydberg-Dressed Ramsey interferometer and electrometer**
  A. Arias, G. Lochead, T. M. Wintermantel, S. Helmrich, and S. Whitlock
  Physical Review Letters 122, 053601 (2019)

The author furthermore contributed to the following publication:

- **A quantum simulation algorithm for continuous optimization**
  A. O. Leonteva, U. Abdulkarimova, T. M. Wintermantel, A. Jeannin-Girardon, P. Parrend, and P. Collet
  Proceedings of the 2020 Genetic and Evolutionary Computation Conference Companion, 199-200 (2020)

Contents

1

From complex systems to Rydberg gases

At the root of physics, and ultimately underlying all sciences, lies the endeavor to build models which can describe the observations and in turn to draw conclusions to better understand nature. Finding this mapping between the microscopic and macroscopic scale is challenged by the often encountered complex systems, where it is hard to predict the global dynamics from the underlying processes (see Sec. 1.1). Interestingly, in nature one often observes very similar complex dynamics and structures emerging in apparently very different systems with associated universal features, scale invariance, power-law behavior or self-organization (see Sec. 1.2). In this thesis, I will present ultracold atoms laser excited to Rydberg states as a viable approach to introduce and study complex non-equilibrium dynamics in a controlled system (see Sec. 1.3).

1.1 Introduction to complex systems

Systems theory [1, 2] provides a systematic approach to investigate and model such complex systems in nature, science and society [3, 4]. A complex system is defined by its individuals, their relationships and the boundary, which separates the system from its environment. The relations and correlations between the individuals are formed by microscopic processes or interactions. Driven-dissipative, open systems additionally interact with the environment, for example via input and output of energy or particles. Detection methods allow to observe the intriguing appearance of global features which are quite distinct from the properties of the individuals, for example self-organization, pattern formation or turbulence. Such complexity, i.e. the difficulty in finding suitable mappings and models between the global features and the underlying processes, can arise due to a quickly growing relevant parameter space (computationally challenging), due to nonlinearities and extreme sensitivity to initial conditions (chaotic), or due to collective behavior which is hard to predict (emergence).

Now we will elaborate on a mapping between open complex systems, as defined above, and our physical system, an ultracold gas under Rydberg laser excitation. In the preparation of the ultracold gas, we benefit from the elaborate techniques that have been developed in recent years concerning the cooling, trapping, manipulation and detection

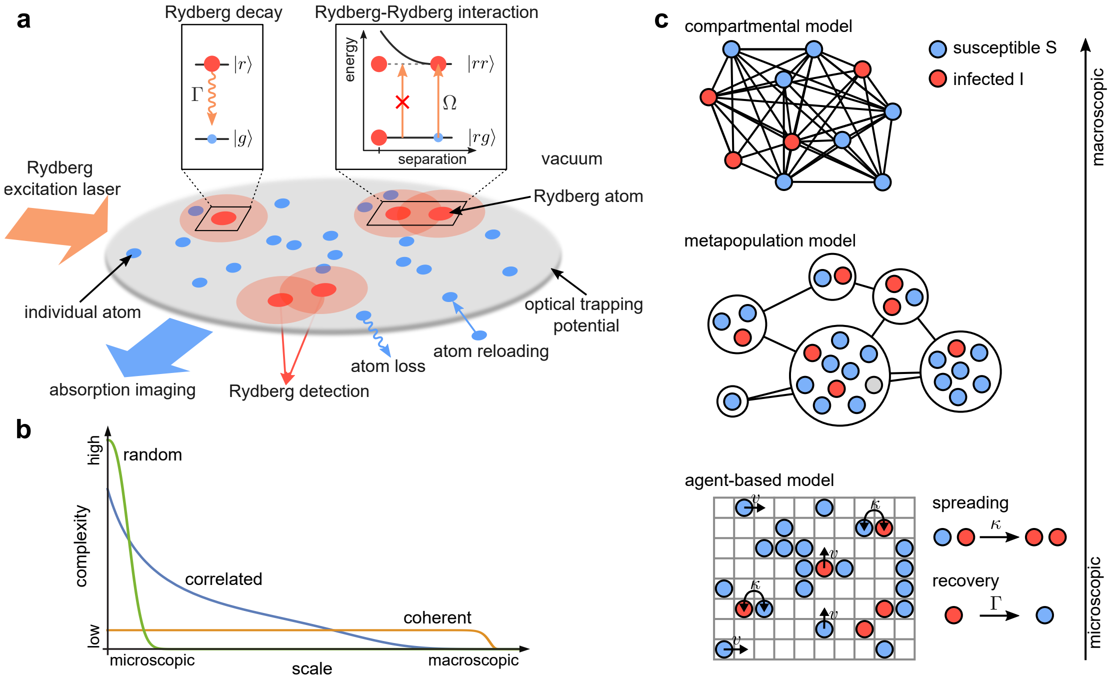

Fig. 1.1: Complexity in systems and corresponding model approaches. a Schematic of an open complex system with ultracold Rydberg atoms. The ultracold gas (system) consists of typically $\sim 10^5$ potassium-39 atoms (individuals) at a temperature of $10\,\mu$K. They can move within the corresponding optical trapping potential, which defines the boundary to the surrounding ultra-high vacuum. Kinetic constraints (relations) between atoms can be formed by laser coupling Ω in combination with the Rydberg-Rydberg interaction. This excitation also deposits energy from the environment into the system carried by the laser photons (energy input). Atom reloading can be implemented via atom reservoirs or tuning of the excitation laser (particle input). Rydberg excitations decay with rate Γ, emitting photons into the vacuum (energy output). In this process, atoms can get lost out of the system (particle output). To probe the system, we can measure the ground state atoms via absorption imaging or the Rydberg states via electric field ionization (detection). **b** To characterize the complexity in a system, it has to be put into relation to the corresponding scale. Random microscopic processes produce a high amount of complexity on the small scale, however the randomness averages out on higher scales, where the complexity is largely reduced. On the other hand, fully coherent systems show about the same amount of complexity over a wide range of scale. Correlated systems are in between these two extremes. Reproduced from [3], licensed under the Creative Commons Attribution License. **c** Approaches to model complex systems dynamics, exemplified for epidemiology, where each individual can be either susceptible S or infected I. An infected individual can infect a susceptible neighbor (disease spreading κ), or it can recover from the disease (recovery Γ). At the lowest level, an agent-based model incorporates these processes on a microscopic scale. In a metapopulation model, each subpopulation can be model by a SIS model with interconnections between subpopulations given by the network structure. The macroscopic compartmental model corresponds to a homogeneous, fully connected network, allowing for few and simple equations to model the dynamics.

of ultracold atoms [5]. These are combined with the exaggerated properties of Rydberg atoms to incorporate the necessary features of an open complex system into our driven-dissipative ultracold gas, as schematically drawn in Fig. 1.1a:

- **Individuals:** Single atoms will emulate the role of individuals in complex systems. Typical conditions are $N \sim 10^5$ individual potassium atoms at temperatures of $\sim 10\,\mu\mathrm{K}$. Each atom is either in the ground state $|g\rangle$ or in the Rydberg excited state $|r\rangle$.
- **Relations between individuals:** Laser excitation can be used in combination with the Rydberg-Rydberg interaction to introduce correlations (kinetic constraints) and nonlinear behavior into the excitation dynamics (cf. Sec. 2.2 and 2.3).
- **Boundary:** The boundary of the system will be defined by the trapping potential which restricts the volume within the atoms (individuals) can move. Elaborate techniques have been developed to structure these optical potentials spatially (see Sec. 3.3) [6–10].
- **Environment:** The trapped atom cloud is surrounded by ultra-high vacuum (see Sec. 3.1), which isolates the system to a high degree from detrimental environmental noise and temperature.
- **Input from the environment:** Energy input is introduced by laser driving from the ground state $|g\rangle$ to the Rydberg state $|r\rangle$ (cf. Sec. 3.4). Particle input can be provided by reloading from atom reservoirs (see Sec. 4.4) or by a controlled ramping of the excitation laser power (cf. Sec. 4.5).
- **Output into the environment:** The Rydberg excitations decay after a characteristic lifetime and dissipate energy into the vacuum (cf. Sec. 2.1). Furthermore, atoms loss out of the trap can occur during the decay process.
- **Detection:** Ground state atoms can be detected via absorption imaging (cf. Sec. 3.1) and Rydberg states via electric field ionization (cf. Sec. 3.5).

To get a better intuition of what complexity means in different systems [3, 11], we will consider three different cases of how the relations between the individuals are formed, with corresponding complexity profiles sketched in Fig. 1.1b:

- **Random:** If we assume a random process (green curve), this creates a high complexity on the microscopic scale, as each individual has its own degrees of freedom. But when going to higher scales, this randomness averages out successively such that there are no remaining spatial structures or correlations on the global scale. This means that while the random microscopic state has a high degree of complexity, the complexity required for describing the macroscopic scale is low. A physically motivated example would be a thermal gas, where describing in full detail the microscopic flight trajectories and scattering events of the atoms is complicated. However, macroscopic observables like pressure, volume or temperature follow a simple relation (ideal gas law).

- **Coherent:** If the microscopic process is fully coherent[1] between all individuals (orange curve), a single individual shares the same degrees of freedom as the global system. Hence, the degree of complexity is similar over a wide range of scales. As an example we take a crystalline atomic structure. Now knowing the flight trajectory of a single atom (microscopic scale) defines the position of all other atoms and hence describes the flight trajectory of the macroscopic crystal as a whole.
- **Correlated:** A correlated process (blue curve) lies within these two extremes, where the degrees of freedom of the individuals are correlated over a certain neighborhood. Then structures can persist on higher scales. While these microscopic correlations decrease the low-scale complexity degree, the complexity towards the macroscopic scale is increased, leading to an intermediate complexity curve. For example, amorphous solids like glasses would represent an intermediate regime with some short- to mid-range correlations at the absence of long-range order.

Consequently, it is important to relate complexity to the corresponding scale when characterizing the degree of complexity in a system. Based on this insight, systems with correlated processes between their individuals (blue complexity curve) represent the most interesting target for future investigations within this thesis.

In the next step, we will introduce different approaches to model complex systems, which will be illustrated using an example from the complex systems subfield of epidemiological modeling. Here, we assume two states, susceptible S (blue) and infected I (red), where susceptible individuals can be infected by neighboring infectious individuals with a rate κ, and infected individuals can become susceptible again with a rate Γ, as illustrated in Fig. 1.1c:

- An agent-based approach models the system on the microscopic scale, including details like the motion v of the individuals [12]. Cellular automata [13] is a closely related framework to study the emergence of complex phenomena from simple interactions between the constituent. See chapter 6 for a proposal on quantum cellular automata.
- If one can divide the system up into subpopulations with similar properties, then a metapopulation approach is feasible [14]. Here, a susceptible-infected-susceptible

---

[1] Note that this does not refer to the quantum mechanical meaning of coherence.

(SIS) model can be applied to each subpopulation with a network describing the interactions between the metapopulations. In Sec. 5.3 a similar SIS network approach will be used to model the experimentally observed Rydberg excitation dynamics.

- For a high separation of scales, many microscopic details average out in a mean-field like manner, yielding a homogeneous, fully connected network between the individuals. This corresponds to the well-known compartmental SIS model [15, 16], described by simple differential equations. See Sec. 4.1 where such a simple model will be used to gain intuition of the self-organization dynamics in our driven-dissipative gas of potassium atoms.

As conceptualized by systems theory, these concepts are not just applicable to a specific system, but to variety of different systems. In section 2.4, similar approaches will be presented for modeling a many-body Rydberg gas. And in chapters 4 and 5 we will see that the epidemic processes presented above bear close similarity to processes that we observe in the Rydberg excitation dynamics.

1.2 Complex systems in physics and beyond

Now we will present exemplary observations of universal and power-law behavior to illustrate the richness of systems in which such complex phenomena can emerge.

An iconic example of universality in dynamical systems is the relation between the temperature and the density around the critical point, shown in Fig. 1.2a for several substances [17]. Despite the differences, e.g., in their mass, size or molecular structure, the data of all substances follows quite well a common single curve. In section 4.2, we will be able to observe a similar rescaling behavior in the experimental data.

Another behavior which emerges in many different systems in nature are power-law distributions. This has been conjectured to be a result of self-organized criticality [21, 22], where a system self-tunes to a critical point (see chapter 4 where we discover this phenomenon in our experimental system). Fig. 1.2b presents the frequency-area distribution of forest fires in southern Australia [18], where the cumulative frequency versus the forest fire area A apparently follows a power-law over a wide region, evidenced by a straight line in this double-logarithmic scale. A quite similar looking distribution, but from the field of astrophysics instead of earth science, is seen in Fig. 1.2c. There, power-law distributions have been observed in solar flares [19, 23], for example in the shown probability $P(\tau_{\mathrm{L}})$ for the time between two solar flare bursts τ_{L}. Other examples of universality and scale-invariance include the distribution of earthquakes

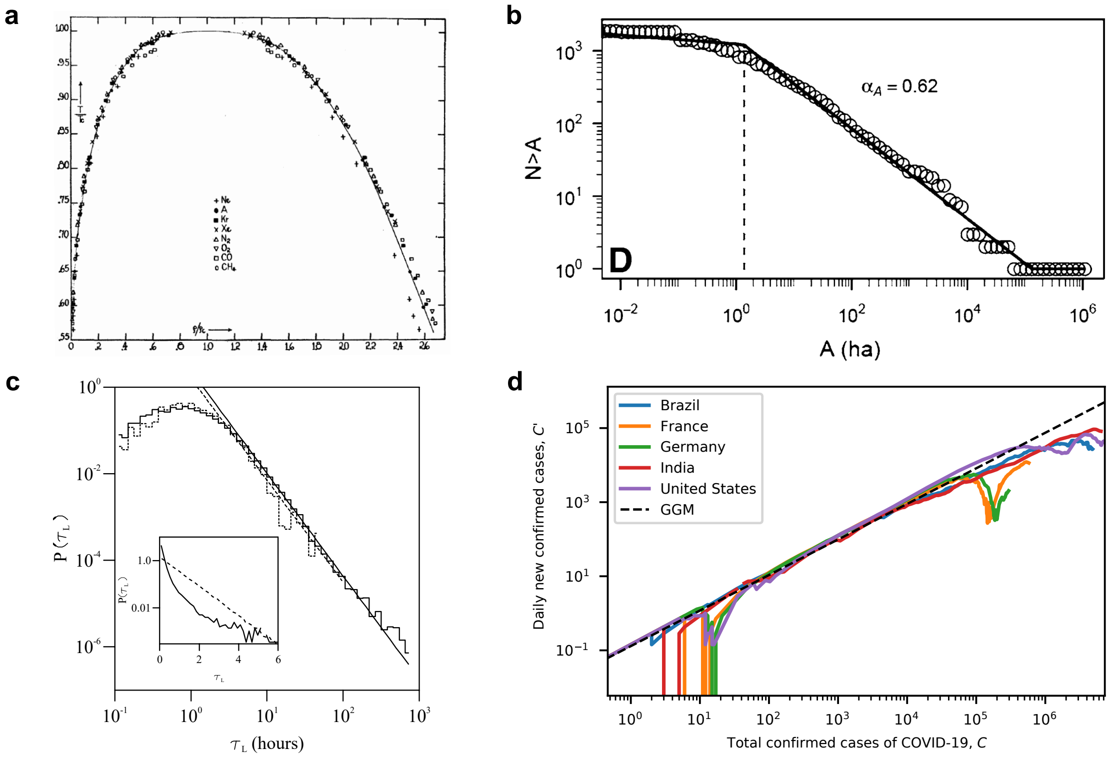

Fig. 1.2: **Exemplary observations of universal behavior and power-law distributions in nature.** **a** Observation of universal behavior in the liquid gas transition. The temperature over the critical temperature T/T_c is shown as a function of the density over the critical density ρ/ρ_c for Ne, Ar, Kr, Xe, N_2, O_2, CO and CH_4. Reproduced from [17], with the permission of AIP Publishing. **b** Probability distribution of the size A of southern Australian forest fires, which follows a power law over several orders of magnitude, evidenced by a straight line in this double-logarithmic representation. Reprinted by permission from Springer Nature [18] Copyright (2020). **c** Probability distribution of the time τ_L between solar flares, showing a wide power-law region. Reprinted with permission from [19]. Copyright (2020) by the American Physical Society. **d** Spreading of the COVID-19 epidemics for selected countries (Brazil, France, Germany, India and the United States). Here, the number of daily new cases C' is plotted against the cumulative number of cases C. The spreading closely follows a linear slope in double-logarithmic space, which can be described by the generalized growth model (GGM, dashed black line). Data from [20].

(cf. Gutenberg–Richter law [24]), craters on the Moon [25] and on Pluto [26], word frequencies [27], citations per publication [28], income [29], wealth [30], firm sizes [31], power-grids, the world-wide-web [32], and many more [33–36].

Apart from such probability distributions, power-law scaling can also emerge in the temporal dynamics of complex systems, for example in the spreading of diseases [37–39]. Subexponential, power-law growth has been observed in the spreading of Measles, Ebola or HIV/AIDS [38]. Another, currently relevant example where power-law growth could be observed is the COVID-19 epidemics. It has been observed in the early growth phase in China [40, 41], South Korea [42], Brazil [43], and Singapore [44]. Fig. 1.2d displays a common representation of the spreading of diseases, where we plot the daily new confirmed cases (incidence rate C') against the total confirmed cases (cumulative cases C) of COVID-19 for the exemplary countries Brazil, France, Germany, India and the United States from January to October 2020 [20]. It follows closely[2] the description by the generalized growth model (GGM) [38]

$$C'(t) = rC^p(t), \tag{1.1}$$

which is a heuristic model to characterize the disease spreading (for more details see Sec. 5.2 where we apply this model to the excitation dynamics in our ultracold Rydberg gas). It is interesting to note the similarity in the growth behavior between the countries despite the different geographies, climates, societies etc.

To summarize, observations of emergent complex behavior are prevalent in nature, science and society. While self-organized criticality could provide an explanation for this, controlled experimental systems with tunable microscopic properties to explore these phenomena have remained scarce. In the course of this thesis, will work to establish a controllable platform for studying complex systems such that we will be able to investigate very similar phenomena in an ultracold gas under Rydberg excitation.

1.3 A complex systems approach to ultracold Rydberg gases

In the course of this thesis, we set to investigate the driven-dissipative dynamics in an ultracold Rydberg system as relatively little is known about the non-equilibrium properties and phase structure compared to the equilibrium case. This will built on the connection to open complex systems (cf. Sec. 1.1), which will turn out to be quite close

---

[2] The shown dashed black line corresponds to a generalized growth model with parameter values of $r = 0.13$ and $p = 0.96$.

as we will observe key phenomena of complex systems, including self-organization to the critical state, avalanches, scale invariance, power-law and nonlinear behavior. As a fact, self-organized criticality [21, 22] is a central concept to describe how complexity occurs in nature. At the same time, the physical system will cover different scales, from the disordered many-body regime in a large volume optical trap down to microscopic structures via optical tweezer traps. These microscopic arrays will be used in a proposal for a quantum version of cellular automata [13], which has been conceptualized as a way to study and understand how simple local interactions can give rise to emergent and complex global behavior. Likewise, theoretical concepts from complex systems will turn out to be useful in describing the experimental observations, for example an epidemic network model similar as in Fig. 1.1c. The following outline of the thesis will describe these connections in more detail.

Thesis outline

The subsequent two chapters will substantiate the presented mapping between an ultracold gas under Rydberg excitation and open complex systems (see Sec. 1.1) to establish a framework for studying complex systems dynamics. In chapter 2 the Rydberg properties and Rydberg-Rydberg interactions of potassium will be introduced, which can be used to add dissipation and correlated, nonlinear driving into the system. Furthermore, different theoretical models to simulate many-body Rydberg systems will be compared. Chapter 3 will focus on the experimental implementation of the framework, giving an overview over the experimental apparatus with the ultra-high vacuum setup, the laser cooling system, the versatile optical trapping capabilities, the Rydberg excitation scheme and the detection setups.

The following three chapters will present the main scientific findings that were enabled with this framework. In Chapter 4, the atomic gas will be coupled to Rydberg excited states via a nonlinear two-body facilitated excitation process. To gain intuition on self-organization, a common form of emergent behavior, the evolution of the atomic density will be modeled in a simple compartmental model approach. Self-organized criticality (SOC) will be experimentally confirmed by monitoring the atomic density as well as the Rydberg excitation density (active density), showing self-organization, scale-invariant behavior and power-law distributed excitation avalanches. We will furthermore investigate an inherent and a controlled atom reloading mechanism in the system.

In Chapter 5, the growth dynamics under facilitated Rydberg excitation will be investigated, yielding a fast power-law growth of the excitation number, which is well-described by the generalized growth model (Eq. 1.1). To better understand the experimental observations, an epidemic network model will be developed to describe the subexponential growth behavior as well as rare-region effects.

Motivated by the newly implemented capability to structure the atomic gas via optical tweezers, we will theoretically investigate in Chapter 6 a quantum cellular automata proposal based on an array of Rydberg excited atoms, where the rules are defined on a local three-site neighborhood. This will allow to directly map microscopic manipulations to macroscopic observations and will open up a new avenue to investigate the quantum version of classical complex dynamics as well as promising new approaches to quantum information processing.

Finally, Chapter 7 will conclude this thesis with the results and an exploration of possible future research opportunities.

Dissipation and correlated excitation dynamics with Rydberg states

2

In this chapter, we will theoretically explore how Rydberg states in potassium-39 can be used to study complex systems dynamics in our ultracold atomic gas. First, the properties of the excitation to single Rydberg states are described, which naturally introduces drive and dissipation. Next, the interactions between two Rydberg atoms are investigated and how this can introduce correlations in the excitation dynamics, via the blockade of excitations or enhanced, off-resonant excitation (facilitation). As the full quantum mechanical modeling of a many-body system becomes quickly unfeasible, different approximations to simulate the Rydberg excitation dynamics are presented.

2.1 Rydberg properties of potassium-39

Rydberg atoms are atoms with a bound electron in a state with high principal quantum number n, with typical values between $10 - 100$ [45–47]. The corresponding energy levels below the ionization threshold E_i are given by

$$E = E_\mathrm{i} - \frac{Ry}{(n - \delta_{n,l,j})^2}, \tag{2.1}$$

with the Rydberg constant corrected for the reduced mass $Ry = m_e/(m + m_e)Ry_\infty$ and the quantum defect of the Rydberg electron $\delta_{n,l,j}$ [45, 48–50], which accounts for deviations from a hydrogen atom. The principal quantum number and the quantum defect can be combined in the effective principal quantum number

$$n^* = n - \delta_{n,l,j}, \tag{2.2}$$

while the quantum defect can be parameterized by the Ritz expansion

$$\delta_{n,l,j} = \delta_0 + \frac{\delta_2}{(n - \delta_0)^2} + \frac{\delta_4}{(n - \delta_0)^4} + \dots, \tag{2.3}$$

with the Rydberg-Ritz coefficients $\delta_0, \delta_2, \delta_4, \dots$ [50, 51]. The quantum defect varies slowly with n and is close to zero for states with high orbital angular momentum $l > 3$, so-called hydrogen-like states. For potassium-39 in the limit of high n, the relevant quantum defect values are $\delta(s_{1/2}) = 2.18$, $\delta(p_{1/2}) = 1.71$, $\delta(d_{1/2}) = 0.28$ and $\delta(f_{1/2}) = 0.01$ for these $l = 0, 1, 2, 3$ orbital angular momentum states, respectively [50, 52].

Fig. 2.1a presents the calculated[1] energy level structure[2] for the $s\,(l = 0)$, $p\,(l = 1)$, $d\,(l = 2)$ and $f\,(l = 3)$ orbital angular momentum states of potassium-39, where the ionization energy is set to zero, $E_{\mathrm{i}} = 0$. The electron binding energy scales with $n^{*\,-2}$ whereas the energy difference between adjacent n states scales as $n^{*\,-3}$. In Fig. 2.1b, the corresponding wavelength λ from the ground state $|g\rangle = |4s_{1/2}\rangle$ to the $|r\rangle = |np_{1/2}\rangle$ Rydberg state is plotted. Note that the required wavelength for single-photon Rydberg excitation from the ground state lies in the ultraviolet (UV) range, where it is more challenging to obtain high-power and narrow-linewidth laser sources. As an alternative, the excitation process can be split up into two transitions (two-photon Rydberg excitation).

Another effect of higher principal quantum numbers n is that the orbital radius of the electronic wave function increases proportional to $n^{*\,2}$, leading to a higher probability density away from the nucleus. This is visible in Fig. 2.1c in the normalized radial wave function $|rR(r)|^2$ of the Radial Schrödinger equation for four exemplary principal quantum numbers of $n = 10$, $n = 30$, $n = 50$ and $n = 70$. Note the large spatial extent of the electronic wave function of the Rydberg state compared to ground state atoms. The large spatial extent also affects the dipole moment, which also increases with $n^{*\,2}$.

The smaller wave function overlap of Rydberg orbitals with the low n orbitals results in a lower spontaneous decay rate and an increased radiative lifetime τ^0_{nl} of the Rydberg states, which scales with $n^{*\,3}$. However, there is an additional relevant decay channel for low angular momentum Rydberg states which is induced by black body radiation (BBR) [45], such that the lifetime is reduced according to

$$\frac{1}{\tau_{nl}} = \frac{1}{\tau^0_{nl}} + \frac{1}{\tau^{\mathrm{BBR}}_{nl}}. \tag{2.4}$$

In the limit of high n, the black-body radiation contribution τ^{BBR}_{nl} can be approximated as [45]

$$\frac{1}{\tau^{\mathrm{BBR}}_{nl}} = \frac{4\alpha^3 k_B T}{3\hbar n^2}, \tag{2.5}$$

with the fine structure constant α, the Boltzmann constant k_B and temperature T. Fig. 2.1d presents calculations of the $np_{1/2}$ Rydberg state lifetime limited by spontaneous emission at zero temperature (blue, $T = 0\,\mathrm{K}$) and including transitions induced by

---

[1] The Rydberg property calculations here were conducted with the Python package ARC-Alkali-Rydberg-Calculator [53] presented in Ref. [50].

[2] Note that the (hyper-)fine structure is not accounted for here.

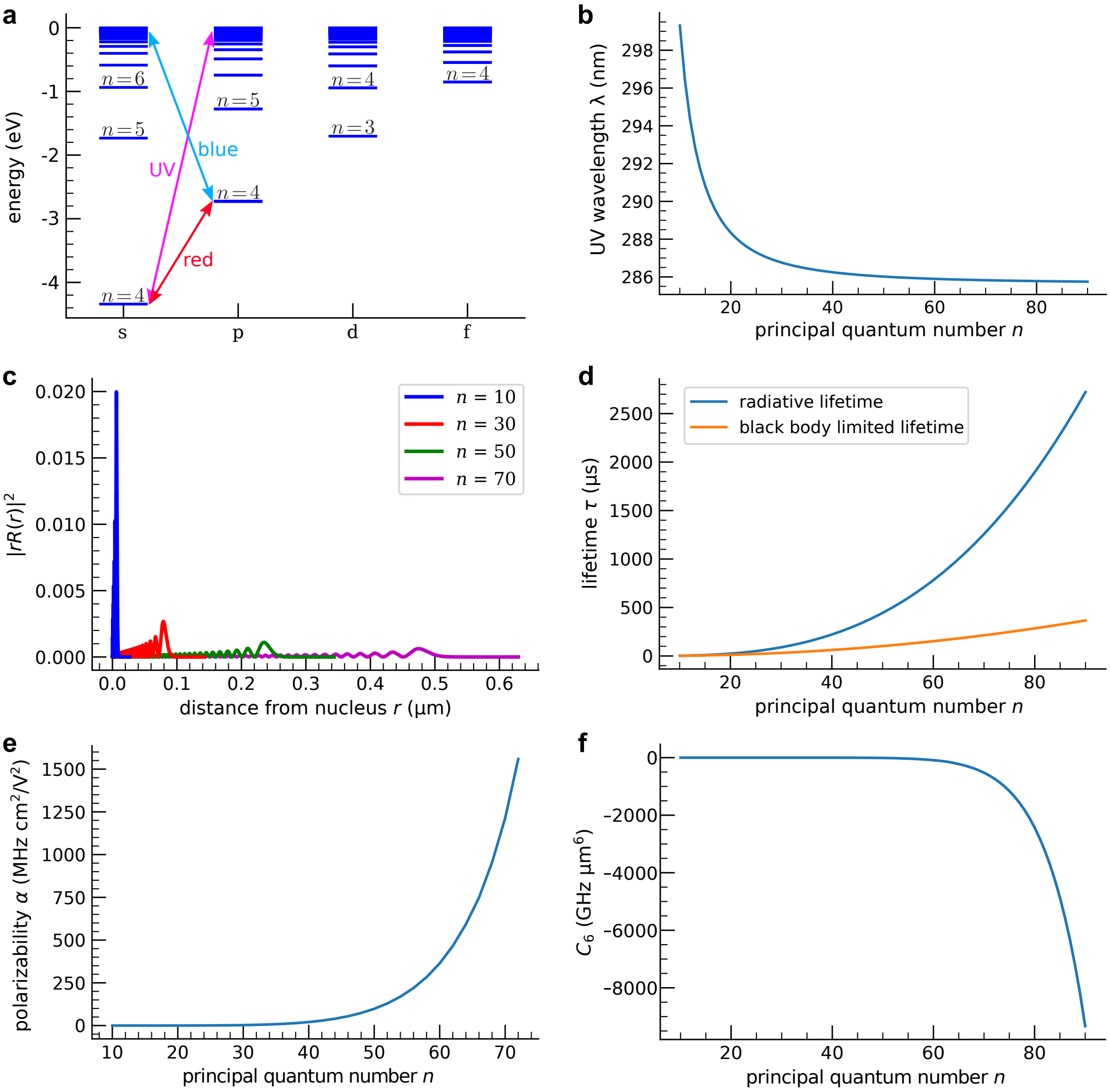

Fig. 2.1: **Rydberg properties of potassium-39.** **a** Energy level spectrum for ns, np, nd and nf orbital angular momentum states. The colored arrows indicate the two coupling schemes from the ground state $|g\rangle = 4s_{1/2}$ to the Rydberg manifold available in our experimental apparatus: single-photon Rydberg excitation in the ultra-violet (UV) wavelength range or two-photon Rydberg excitation involving a red and a blue laser. The electron binding energy scales with $n^{*\,-2}$ while the energy difference between adjacent n states scales with $n^{*\,-3}$. **b** Single-photon Rydberg excitation wavelength λ from the ground state $|g\rangle = 4s_{1/2}$ to the $|r\rangle = np_{1/2}$ Rydberg state. **c** Corresponding radial electronic wave function $|rR(r)|^2$ for four exemplary Rydberg states $n = 10$, $n = 30$, $n = 50$ and $n = 70$. The electron orbital radius scales with $n^{*\,2}$. **d** Lifetime τ of the $np_{1/2}$ Rydberg state limited by spontaneous decay back to the ground state (blue, at $T = 0\,\mathrm{K}$) and by additionally including black body radiation (BBR) at room temperature (orange, at $T = 300\,\mathrm{K}$). The radiative lifetime scales with $n^{*\,3}$. **e** Polarizability α of the $|np_{1/2}, m_j = 1/2\rangle$ Rydberg state series in potassium-39. The polarizability scales with $n^{*\,7}$. **f** Van der Waals coefficient C_6 between two Rydberg states in $|np_{1/2}, m_j = 1/2\rangle$ with relative orientation angles $\theta = \phi = 0$. The van der Waals interaction coefficient C_6 scales with $n^{*\,11}$. These plots were produced with the Python package ARC-Alkali-Rydberg-Calculator [53].

black-body radiation at room temperature (orange, $T = 300\,\mathrm{K}$) as a function of the principal quantum number n. Note the relatively long lifetimes of typical Rydberg states of $\gtrsim 10\,\mu\mathrm{s}$, especially when compared to the lifetime of $26\,\mathrm{ns}$ on the $D2$ transition. For Rydberg experiments in room temperature environments, black-body radiation is the limiting factor. To overcome this, experiments could be performed under cryostatic temperatures of the vacuum system.

Furthermore, the increase in orbital radius also affects the polarizability α to electric fields, which strongly scales with ${n^*}^7$, as visible in Fig. 2.1e calculated for the $np_{1/2}$ Rydberg series of potassium-39. As for practical experimental purposes, this requires careful consideration to minimize non-conducting surfaces due to the possible accumulation of space charges as well as precise control on the electric fields (see Sec. 3.5).

In the next section, we will look at the implications of these exaggerated Rydberg properties on the interactions between Rydberg atoms.

2.2 Rydberg-Rydberg interactions

Let us assume two atoms at positions $\vec{r_1}$ and $\vec{r_2}$ with a relative vector between the atoms $\vec{R}$ of magnitude R. The Hamiltonian of the two interacting atoms can be written as

$$\hat{H} = \hat{H}_1^{\mathrm{a}} + \hat{H}_2^{\mathrm{a}} + \hat{H}_{12}^{\mathrm{int}}(\vec{R}), \tag{2.6}$$

where $\hat{H}_{1,2}^{\mathrm{a}}$ are the atomic Hamiltonians and $\hat{H}_{12}^{\mathrm{int}}(\vec{R})$ describes the interaction between the two atoms. If the interaction is strong, as typical for short interatomic distances, the full Hamiltonian has to be diagonalized, which can result in a more complex energy level structure. For larger distances with smaller interaction strength, $\hat{H}_{12}^{\mathrm{int}}(\vec{R})$ can be treated perturbatively.

We assume separations R beyond the LeRoy radius, where the wave function overlap of the two atoms is small and the interaction is dominated by the electrostatic interaction between the two valence electrons. In this regime, the multipole expansion can be applied to the pairwise atom interaction [54, 55]. Assuming neutral atoms, the leading non-zero term in this multipole expansion is the dipole-dipole interaction

$$\hat{V}_{\mathrm{dd}} = \frac{\vec{\mu_1} \cdot \vec{\mu_2}}{R^3} - \frac{3(\vec{R} \cdot \vec{\mu_1})(\vec{R} \cdot \vec{\mu_2})}{R^5}. \tag{2.7}$$

As neutral atoms in low angular momentum states and in zero external field do not possess a permanent dipole moment, this interaction arises from transition dipoles between states with different symmetry. If the two atoms are in the same state, the dipole interaction can arise from a second-order process, where a dipole produced by a quantum fluctuation induces a dipole in the other atom, resulting in an interaction between the two dipoles. To describe this effect, we assume a two-level description of our system with the initial Rydberg pair state $|ns, ns\rangle$, and the closest adjacent pair state $|n'p, n''p\rangle$. The dipole-dipole operator $\hat{V}_{\mathrm{dd}}$ couples the two transitions $|ns\rangle \leftrightarrow |n'p\rangle$ and $|ns\rangle \leftrightarrow |n''p\rangle$ with dipole moments $\vec{\mu_1}$ and $\vec{\mu_2}$, respectively [56]. Then we can write the interaction Hamiltonian as

$$H^{\mathrm{int}} = \begin{pmatrix} 0 & V_{\mathrm{dd}} \\ V_{\mathrm{dd}} & \Delta_{\mathrm{F}} \end{pmatrix}, \tag{2.8}$$

with the dipole-dipole interaction strength V_{dd} and the energy mismatch between the two pair states, the so-called Förster defect $\Delta_{\mathrm{F}} = E_{n'p} + E_{n''p} - 2E_{ns}$. We can diagonalize this Hamiltonian to get the energy eigenvalues

$$E_{\pm} = \frac{\Delta E_{\mathrm{F}}}{2} \pm \sqrt{\left(\frac{\Delta E_{\mathrm{F}}}{2}\right)^2 + V_{\mathrm{dd}}^2}. \tag{2.9}$$

The Förster defect Δ_{F} can be tuned with a DC electric field, where a value of close to zero $\Delta_{\mathrm{F}} \approx 0$ results in the so-called Förster resonance [57]. We define the transition point between two extremal limits $\Delta E_{\mathrm{F}} \ll V_{\mathrm{dd}}$ and $\Delta E_{\mathrm{F}} \gg V_{\mathrm{dd}}$ as the point where the interaction strength equals the Förster defect $V_{\mathrm{dd}} = \Delta_{\mathrm{F}}$, which corresponds to the so-called van der Waals radius

$$R_{\mathrm{vdW}} = \left(\frac{C_6}{|\Delta_{\mathrm{F}}|}\right)^{\frac{1}{6}}. \tag{2.10}$$

In the first limit $R < R_{\mathrm{vdW}}$ with $\Delta E_{\mathrm{F}} \ll V_{\mathrm{dd}}$, there is a strong admixing between the two pair states $|ns, ns\rangle$ and $|n'p, n''p\rangle$, and we obtain a resonant dipolar interaction

$$E_{\pm} = \pm\frac{\mu_1\mu_2}{R^3} = \pm\frac{C_3}{R^3}, \tag{2.11}$$

where the dipole-dipole coefficient $C_3 = R^3 \langle ns, ns| \hat{V}_{\mathrm{dd}} |n'p, n''p\rangle$ scales with n^{*4}. For calculating the pair state energy level structure, the strong admixing requires full diagonalization of the pair state interaction Hamiltonian.

In the opposite limit $R > R_{\mathrm{vdW}}$ with $\Delta E_{\mathrm{F}} \gg V_{\mathrm{dd}}$, the admixing between the states is small, resulting in the van der Waals interactions

$$E_{-} = -\frac{\mu_1^2\mu_2^2}{\Delta_{\mathrm{F}} R^6} = -\frac{C_6}{R^6}, \tag{2.12}$$

where the van der Waals coefficient C_6 scales as ${n^*}^{11}$. It can be perturbatively calculated as the sum over all dipole-coupled pair states $|r', r''\rangle$

$$C_6 = \sum_{n',n''} \frac{|\langle r', r''| \hat{V}_{\mathrm{dd}} |ns, ns,\rangle|^2}{\Delta_{\mathrm{F}}(ns, ns, r', r'')}. \tag{2.13}$$

The sign of Δ_{F} determines if the interactions are of a repulsive or attractive nature. While van der Waals interactions between s states are in general repulsive ($C_6 < 0$) and close to isotropic, the interaction between states involving higher orbital angular momenta are usually anisotropic, where the interaction strengths depends on the relative orientation and where the sign might change between repulsive $C_6 < 0$ and attractive $C_6 > 0$. Fig. 2.1f presents the result of a perturbative calculation of the C_6 coefficient between two Rydberg atoms in the $|rr\rangle = |np_{1/2}, m_j = 1/2;\, np_{1/2}, m_j = 1/2\rangle$ pair state.

2.3 Rydberg blockade and facilitation

Fig. 2.2a presents in the upper panel the calculated pair-state energy level diagram for $|rr\rangle$, where both atoms are in the Rydberg state $66s_{1/2}, m_j = 1/2$, as a function of the internuclear distance R, assuming a relative orientation in the $\theta = \phi = 0$ axis [50]. The color encodes the overlap probability with other pair states. We concentrate our analysis on the prominent red curve as it is by far the strongest interaction effect. This pair-state energy curve bends upwards for shorter internuclear distances as an effect of the repulsive Rydberg-Rydberg interactions. At distances below $3\,\mu\mathrm{m}$ we observe a complicated regime with a plethora of energy curves and level crossings. Below this panel there are the other relevant energy levels of the pair state with one Rydberg atom and one ground-state atom $|rg\rangle$ (degenerate with $|gr\rangle$), and of the pair state with two ground-state atoms $|gg\rangle$. These states do not show interaction shifts on this scale and hence these two levels are flat.

Now I will consider two different Rydberg excitation schemes in this system. In the first case, highlighted by the green shading in Fig. 2.2a, the bare $|g\rangle \rightarrow |r\rangle$ transition is coupled with Rabi frequency Ω_1 on resonance ($\Delta_1 = 0$). Hence, the first excitation step $|gg\rangle \rightarrow |rg\rangle$ is always resonant, independent of R. In the second excitation $|rg\rangle \rightarrow |rr\rangle$, the upper energy level shifts upwards with decreasing R and at some point it will be shifted outside of the excitation linewidth γ_{B}. Then the excitation becomes off-resonant and the second Rydberg excitation is suppressed for small separations, indicated by the red cross. This is called the Rydberg blockade effect [58–67] with the characteristic

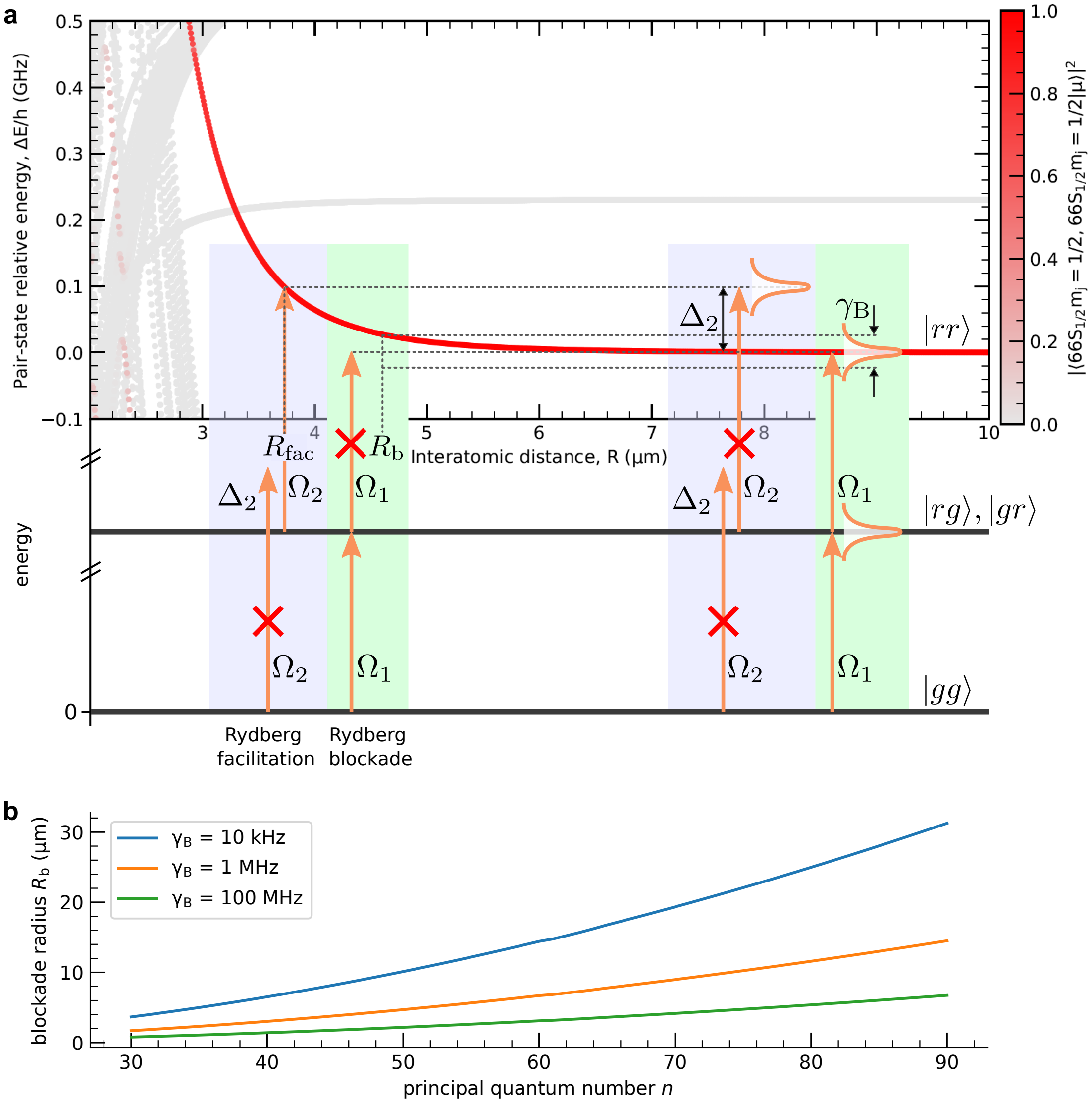

Fig. 2.2: Rydberg-Rydberg interaction leading to blockade and facilitation. **a** Pair-state energy as a function of the internuclear distance R. The top panel shows the calculated energy for the pair state $|rr\rangle$ with both potassium-39 atoms in the Rydberg state $66s_{1/2}, m_j = 1/2$ for a relative orientation of $\theta = \phi = 0$. The color encodes the overlap probability of other pair states with the bare $|rr\rangle$ state. Below this panel, the energy levels of the pair state with one Rydberg and one ground state $|rg\rangle$ and with two ground state atoms $|gg\rangle$ are sketched. The orange arrows indicate two different laser fields: The first field (green shading) couples $|g\rangle$ to $|r\rangle$ in resonance with the bare Rydberg transition (detuning $\Delta_1 = 0$) with Rabi coupling frequency Ω_1. The second laser (purple shading) with coupling Ω_2 is detuned by $\Delta_2 = 0.1\,\mathrm{GHz}$. The characteristic energy width of the transition is characterized by γ_B. While for interatomic distances $R > R_\mathrm{b}$ the laser field Ω_1 is resonant for the transition $|rg\rangle \to |rr\rangle$, it becomes off-resonant for $R < R_\mathrm{b}$ and the Rydberg excitation of the second atom is suppressed (red cross). This is the so-called Rydberg blockade effect with the corresponding blockade radius R_b. As the laser Ω_2 is detuned by Δ_2 from the bare transition, the excitation of the first Rydberg state $|gg\rangle \to |rg\rangle$ is suppressed (red cross). However, if there is one Rydberg atom already, the excitation of the second Rydberg state $|rg\rangle \to |rr\rangle$ becomes resonantly coupled at the facilitation radius R_fac, where the interaction energy shift compensates the detuning (Rydberg facilitation). **b** Calculated blockade radius R_b for two Rydberg $ns_{1/2}$ states as a function of the principal quantum number n for three different excitation linewidths γ_B of $10\,\mathrm{kHz}$ (blue), $1\,\mathrm{MHz}$ (orange) and $100\,\mathrm{MHz}$ (green). These plots were produced with the Python package ARC-Alkali-Rydberg-Calculator [53].

blockade radius R_b, which is defined as the distance where the pair-state energy $|rr\rangle$ shift equals the excitation linewidth γ_B

$$R_\mathrm{b} = \left(\frac{C_6}{\gamma_\mathrm{B}}\right)^{\frac{1}{6}} . \tag{2.14}$$

Here the excitation linewidth γ_B is a placeholder for the dominant broadening mechanism, e.g. the state linewidth Γ, the laser linewidth γ, the Rabi frequency Ω (power broadening), Fourier broadening, differential light shifts, or Doppler broadening by atom motion.

In the second case, highlighted by the purple shading, the laser field with coupling frequency Ω_2 is detuned by $\Delta_2 = 0.1\,\mathrm{GHz}$. For $|\Delta_2| > \gamma_\mathrm{B}$, the first excitation step is off-resonant and hence suppressed, indicated by the red crosses. However, once in the state with one Rydberg excitation (caused by seed excitation or off-resonant excitation), the second excitation step $|rg\rangle \rightarrow |rr\rangle$ becomes resonant at a distance R_fac, where the interaction shift of the pair-state energy compensates the detuning. This effect, where secondary excitations are resonantly excited at the facilitation radius

$$R_\mathrm{fac} = \left(\frac{C_6}{|\Delta|}\right)^{\frac{1}{6}} , \tag{2.15}$$

is called Rydberg anti-blockade or facilitation [68, 69]. It is a nonlinear processes in in the excitation number, as the fast facilitated excitation is dependent on an existing nearby Rydberg state and it introduces correlated laser driving as it only applies certain atoms fulfilling the facilitation constraint. In conclusion, the facilitation radius and the blockade radius have the same expression, just with different denominators. Fig. 2.2b shows plots of the Rydberg blockade (facilitation) radius as a function of principal quantum number n, calculated from the formula 2.14 (2.15) above, for excitation linewidths γ_B (detunings Δ) of $10\,\mathrm{kHz}$ (blue), $1\,\mathrm{MHz}$ (orange), and $100\,\mathrm{MHz}$ (green).

For comparison, Fig. 2.3a presents the energy level diagram for the $|rr\rangle$ pair state with both atoms in the Rydberg state $66p_{1/2}, m_j = 1/2$. We observe a more complicated level structure, with more avoided level crossings and more admixing of the $|66p_{1/2}, m_j = 1/2, 66p_{1/2}, m_j = 1/2\rangle$ state with other pair states. The energy level starting from the bare $|rr\rangle$ state at large separations R starts to bend down creating a potential, such that Rydberg facilitation is also possible for small negative detunings. Fig. 2.3b shows the corresponding energy level diagram for the $|66p_{3/2}, m_j = 3/2, 66p_{3/2}, m_j = 3/2\rangle$ pair state. The level structure is more similar to the case of $66s_{1/2}, m_j = 1/2$ (Fig. 2.2a) with only one repulsive branch and fewer (avoided) level crossings for this relative orientation ($\theta = \phi = 0$). The $|66p_{3/2}\rangle$ and $|66p_{1/2}\rangle$ Rydberg states will be used in the ex-

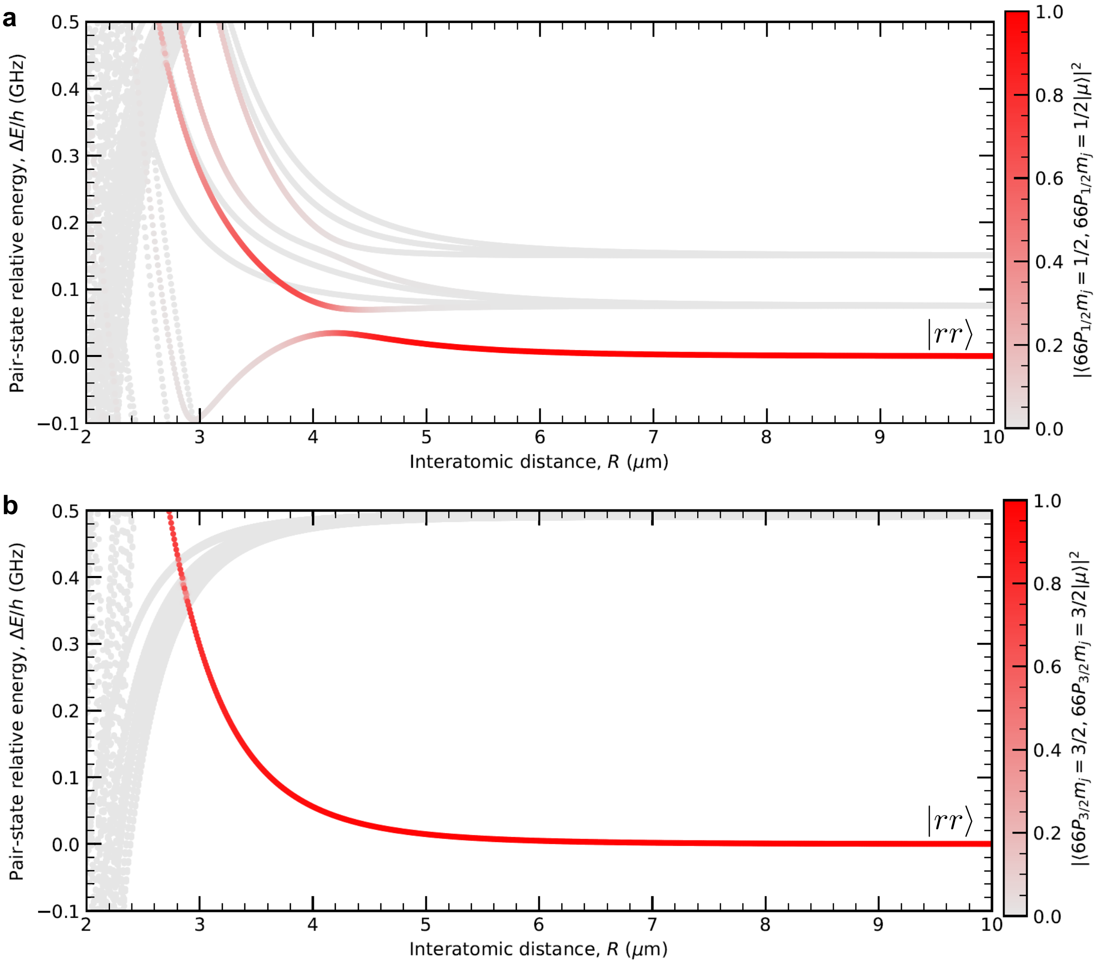

Fig. 2.3: Pair-state energy level diagram for two $66p$ Rydberg states. **a** Energy of the Rydberg pair state $|rr\rangle$ with both atoms in the state $|66p_{1/2}, m_j = 1/2\rangle$ as a function of internuclear distance R for a relative orientation between the Rydberg states of $\theta = \phi = 0$. The color encodes the overlap probability of other pair states with the bare $|66p_{1/2}, m_j = 1/2, 66p_{1/2}, m_j = 1/2\rangle$ state. **b** Corresponding energy level diagram for the $|rr\rangle = |66p_{3/2}, m_j = 3/2, 66p_{3/2}, m_j = 3/2\rangle$ Rydberg pair state for otherwise same parameters as in subfigure a. These plots were produced with the Python package ARC-Alkali-Rydberg-Calculator [53].

perimental studies on self-organized criticality with Rydberg field ionization in chapter 4 and on Rydberg excitation growth in chapter 5, respectively.

2.4 Many-body treatment of the excitation dynamics

So far, we have considered the properties of single Rydberg atoms as well as the interactions between two Rydberg states. In this section, we will assume an open system consisting of individual atoms interacting with the electromagnetic field and interacting with each other mediated via Rydberg states.

This is described by the full Hamiltonian

$$\hat{H}_{\text{sys}} = \sum_k \left(\hat{H}_k^{\text{a}} + \hat{H}_k^{\text{al}} + \sum_{l \neq k} \hat{H}_{kl}^{\text{int}} \right), \tag{2.16}$$

with the individual atomic Hamiltonian $\hat{H}_k^{\text{a}}$, the Hamiltonian describing the atom light interaction $\hat{H}_k^{\text{al}}$ and the interaction $\hat{H}_{kl}^{\text{int}}$ between the Rydberg atoms k and l.

Quantum master equation

A quantum master equation in Lindblad form, which includes dissipation via the Lindblad jump operators, can be used to describe the open system dynamics of the atom-light interaction and the van der Waals interaction between Rydberg atoms by

$$\partial_t \hat{\rho} = \frac{i}{\hbar}[\hat{\rho}, \hat{H}] + \sum_k \mathcal{L}_k(\hat{\rho}) \tag{2.17}$$

with the commutator $[\cdot,\cdot]$ and the many-body density matrix $\hat{\rho}$. The Hamiltonian is given by

$$\hat{H} = \sum_k \left(\left(\sum_{l \neq k} \frac{1}{2} \frac{C_6}{R_{kl}^6} \hat{\sigma}_l^{rr} - \Delta \right) \hat{\sigma}_k^{rr} + \frac{\Omega}{2} \left(\hat{\sigma}_k^{gr} + \hat{\sigma}_k^{rg} \right) \right) \tag{2.18}$$

with the Rabi frequency Ω from the ground state $|g\rangle$ to the Rydberg state $|r\rangle$ and $\sigma_k^{\alpha\beta} = |\alpha\rangle \langle\beta|_k$. The Lindblad superoperator $\mathcal{L}$ is used to incorporate dissipation by spontaneous decay with rate Γ and dephasing with rate γ^{de}

$$\mathcal{L}_k(\hat{\rho}) = \Gamma \hat{\sigma}_k^{gr} \hat{\rho} \hat{\sigma}_k^{rg} + \gamma^{\text{de}} \hat{\sigma}_k^{rr} \hat{\rho} \hat{\sigma}_k^{rr} - \frac{\gamma^{\text{de}} + \Gamma}{2} \left(\hat{\sigma}_k^{rr} \hat{\rho} + \hat{\rho} \hat{\sigma}_k^{rr} \right). \tag{2.19}$$

If we think back to Fig. 1.1c, this full Hamiltonian describing all the details corresponds to the microscopic scale (see Fig. 2.4a). This approach will be used to model the evolution

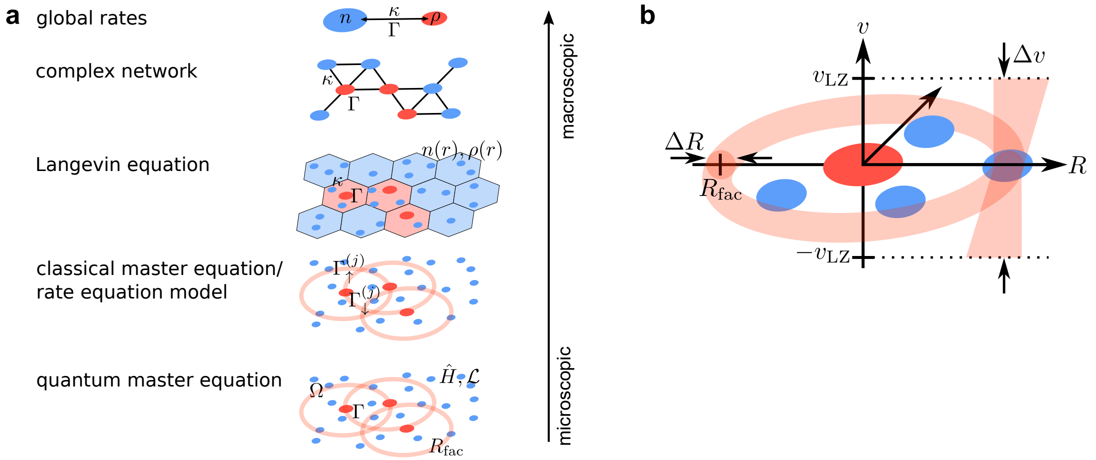

Fig. 2.4: Approaches to model a many-body Rydberg system. a Different approaches to model many-body Rydberg systems. A full quantum master equation can potentially describe all of the microscopic processes of the many-body system. On a lowest scale of approximation, a classical master equation can be applied in the case of strong decoherence to model the excitation dynamics. Further simplifications can be made by introducing coarse graining over the characteristic volume provided by the facilitation radius, leading to effective rates that can be used in the Langevin equation or in complex network approaches. When further averaging over the whole system, assuming sufficient heterogeneity, one ends up with a few, simple global rates. **b** Facilitation condition in phase space with internuclear distance R and relative velocity v for coarse graining. The facilitation volume is given by the radius R_{fac}. In addition to the spatial constraint ΔR around the facilitation radius R_{fac}, we further restrict the relative velocity around Δv, modeled by the Landau-Zener velocity v_{LZ}. This can be used to calculate an effective facilitation rate κ over the coarse grained volume.

in our quantum cellular automata implementation, as presented in chapter 6, where we are interested in the effect of the microscopic quantum processes on the global system evolution. In practice, however, it becomes quickly unfeasible to analytically or numerically solve this full quantum master equation with increasing number of particles.

To theoretically model the experimental results of chapters 4 and 5, reasonable approximations have to be applied, leading to different approaches on the different scales (see Fig. 2.4a).

Classical master equation

The classical master equation or rate equation model [70, 71] is based on the assumption that the coherence is washed out due to strong decoherence processes such as decay and dephasing. Thus the coherences can be adiabatically eliminated, yielding classical rate equations for the populations.

Langevin equation

To further simplify the approach, instead of considering each particle, one might use coarse graining over a characteristic length scale of the system. A Langevin equation with such a coarse graining procedure for the collective excitation dynamics can naturally include the atom motion and can be used to connect to non-equilibrium properties. Such an approach is used in chapter 4 to describe the self-organized criticality dynamics in our system

$$\begin{aligned} \partial_t \rho_t =& \ (D\nabla^2 - \Gamma + \kappa n_t)\rho_t - 2\kappa {\rho_t}^2 + \tau(n_t - 2\rho_t) + \xi_t, \\ n_t =& \ n_0 - b\Gamma \int_0^t \mathrm{d}t' \rho_{t'} + D_T \int_0^t \mathrm{d}t' \nabla^2 n_{t'}, \end{aligned} \tag{2.20}$$

for the active density ρ_t and the total remaining density n_t (see Ref. [72] for more details). Excited state and ground state diffusion are characterized by D and D_T. κ, Γ and τ are the rates for facilitation, decay and spontaneous excitation, respectively. Atom loss out of the population is parameterized by b and autocorrelated multiplicative noise is introduced via ξ_t.

Complex network model

An epidemic model on a heterogeneous network, as applied in section 5.3, again uses a coarse graining approach over the facilitation area, where we describe the probability of an excitation/infection of node i by a stochastic master equation

$$\frac{dE[I_i(t)]}{dt} = E\left[-\Gamma I_i(t) + \kappa N_i \Big(1 - I_i(t)\Big) \sum_j a_{ij} I_j(t)\right], \tag{2.21}$$

where $E[\cdot]$ denotes the expectation value of an infection ($I_i = 1$) on site i (see Sec. 5.3 for more details). The probability of transmission of the infection from node j to i is mainly governed by the node weights N_i and the adjacency matrix a_{ij}. We find this as an efficient method to model the experimentally observed power-law Rydberg excitation growth and the subsequent saturation or power-law relaxation.

Global rate model
In the simplest approximation of a completely homogeneous system in the limit of fast dephasing, a global rate model results in two simple differential equations,

$$\begin{aligned} \dot{n} &= -\kappa n \rho + \Gamma \rho \\ \dot{\rho} &= +\kappa n \rho - \Gamma \rho, \end{aligned} \tag{2.22}$$

similar to the compartmental models in epidemiology (cf. Sec. 1.1). Such an approach will be used in section 4.1 to gain intuition into the self-organization dynamics in our driven-dissipative system and the underlying absorbing state phase transition.

Phase-space facilitation condition
Fig. 2.4b shows a sketch of the phase-space facilitation condition to explain the introduction of a length scale for coarse graining and the resulting effective rates. So far we have established that there is a certain facilitation shell ΔR (depending on the excitation linewidth, see Sec 2.3) around the facilitation radius R_{fac}. If the situation is nonstatic and the atoms are moving, this should factor in as fast atoms spend less time in the facilitation shell. In section 5.3 we characterize this velocity dependence by the relative velocity window Δv given by the Landau-Zener velocity v_{LZ} and find this additional constraint as an essential ingredient for understanding the heterogeneity in the system.

Conclusion

In summing up, the exaggerated properties of Rydberg states make them a versatile asset for our experimental platform, where approximate many-body models exist for our parameter regime to more efficiently simulate the system dynamics. We drive the system with an external laser which addresses two specific states (ground and Rydberg), where spatial correlation and nonlinearities in this excitation can be introduced via the Rydberg-Rydberg interaction (blockade and facilitation). The lifetimes of typical Rydberg states of $\gtrsim 10\,\mu\mathrm{s}$ lie in an experimentally accessible range and are comparable to the facilitation rates, creating interesting competition between driving and decay. Furthermore, the strong scaling of the Rydberg properties with the principal quantum number n allows a wide tuning range and hence flexibility to study quite different parameter regimes.

The next chapter will present a detailed description of the experimental apparatus for studying complex systems dynamics in ultracold Rydberg gases.

3

Apparatus for Rydberg excitation of ultracold potassium atoms

This chapter presents how the framework to study complex systems dynamics with an ultracold potassium gas under Rydberg excitation is experimentally implemented. We start with a short overview of the key elements around the science vacuum chamber in Sec. 3.1, before we go into more detail on the individual parts according the order in a typical experimental sequence. The experimental sequence starts with the laser cooling and trapping stages provided by the laser system on the D1 and D2 line (see Sec. 3.2), producing a cold gas of potassium atoms with a typical atom number $N \sim 10^5$ and temperature $T \sim 10\,\mu\mathrm{K}$. Subsequently, the atoms are loaded into one of the available optical trapping geometries (cf. Sec. 3.3). This optically trapped gas in the vacuum chamber provides a well-isolated system as a starting point for the studies on complex system dynamics described in the following chapters of this thesis. The excitation to highly excited Rydberg states, implemented by a versatile laser system for single-photon and two-photon Rydberg excitation (see Sec. 3.4), allows the introduction of three key features: First, driving by the energy intake from the excitation laser; Second, the finite lifetime of the Rydberg states adds an inherent dissipation mechanism; Third, the strong and long-range Rydberg-Rydberg interactions can create interesting relations and correlations between the individual atoms in the gas. Finally, the system dynamics can be probed via ground state absorption imaging (cf. Sec. 3.1) or via Rydberg field ionization detection (see Sec. 3.5).

I want to especially highlight parts that were upgraded after the move and rebuilt from Heidelberg to Strasbourg, mainly concerning the optical traps (see Sec. 3.3) and Rydberg detection via electric filed ionization (cf. Sec. 3.5).

Further details can be found in a series of theses in our group, see Refs. [73–83].

3.1 Overview of the experimental apparatus

This section gives a short overview of the experimental apparatus based on Fig. 3.1, a sketch[1] centered on the science chamber:

- **Science chamber.** The part of the vacuum chamber where the experiments with potassium atoms excited to Rydberg states are performed. This specific science chamber[2] was selected for extensive optical access and a large volume. We require multiple laser beams to enter the chamber for various tasks like laser cooling, optical trapping, Rydberg excitation and imaging. Six CF63, four CF40 and sixteen CF16 viewports provide the substantial optical access required. The 8 inch diameter of the chamber allows to place several components inside the vacuum, for example the objective lens, a radio-frequency (RF) coil and a Rydberg detector with electric field compensation electrodes (Sec. 3.5). The pressure in the science chamber of $3 \times 10^{-9}\,\mathrm{mbar}$ is sustained using an ion[3] and a titanium-sublimation pump[4]. According to the view of Fig. 3.1, these pumps connect from the right side of the science chamber via additional vacuum parts, but they were omitted in this sketch for clarity.

- **Two-dimensional magneto-optical trap (2D MOT).** The glass cell[5] of the 2D MOT design [85] contains up to three dispensers[6], one of which is heated up by an electrical current of $1.8\,\mathrm{A}$. The potassium atoms emerging from it are cooled and trapped by two orthogonal pairs of four beams in combination with two magnetic coil pairs creating a gradient field. This reduces the velocity components in the two dimensions orthogonal to the symmetry axis of the glass cell and creates an atomic beam, which enters the science chamber through a differential pumping tube. We have an additional, near-resonant laser beam, called the pusher beam (not shown in Fig. 3.1), propagating along this axis, which pushes the cooled atoms towards the science chamber. The glass cell is connected to an additional ion pump dedicated for the 2D MOT setup.

- **Three-dimensional magneto-optical trap (3D MOT).** Three orthogonal pairs of counter-propagating beams together with a gradient magnetic field create the three-dimensional magneto-optical trap [5, 87, 88]. Due to the narrow hyperfine splitting in the $4p_{3/2}$ manifold (cf. Fig. 3.2a), the attainable temperature is limited

---

[1] This computer-generated graphic as well as the following similar graphics were created with the software blender 2.81 [84].

[2] Kimball Physics MCF800-SphSq-G2E4C4A16

[3] Agilent Technologies VacIon Plus 150 Ion Pump StarCell

[4] Agilent Technologies TSP Cartridge Filament Source

[5] Japan Cell, anti-reflection coated on the outer surface.

[6] Currently: Alvatec AS-3-K-100-F with natural isotope composition of potassium, with abundances of the main isotopes ^{39}K, ^{41}K and ^{40}K of 92.3%, 6.7% and 0.01%, respectively [86].

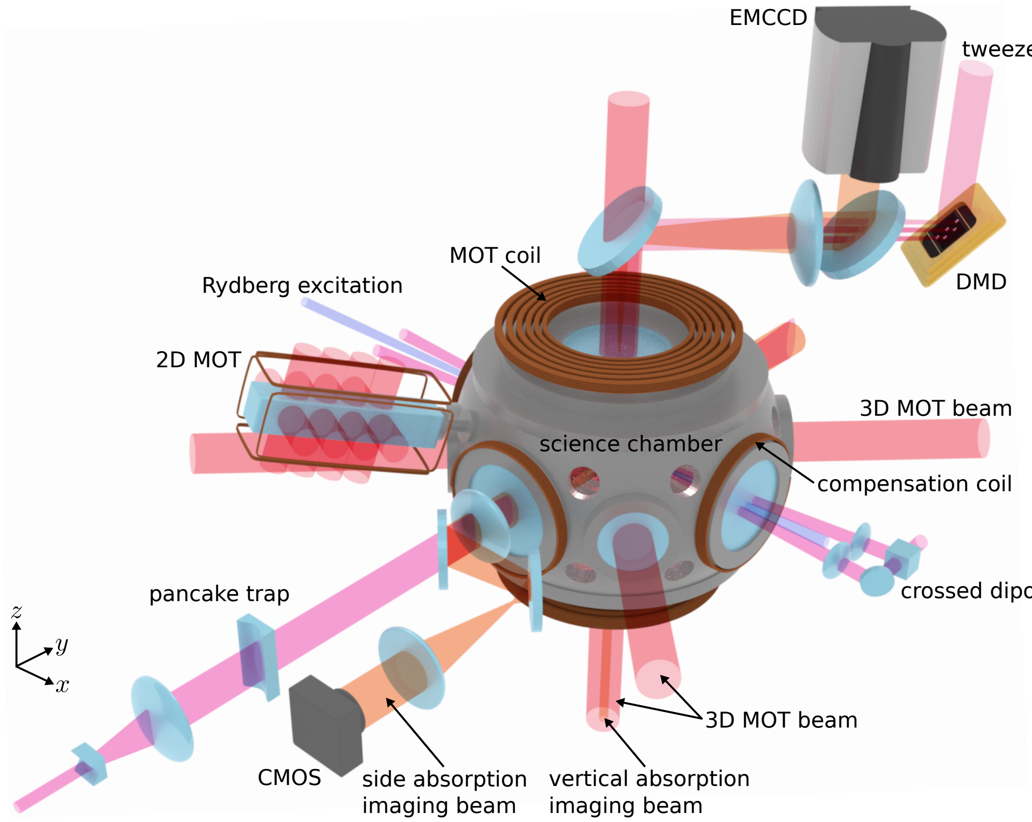

Fig. 3.1: Overview of the apparatus for Rydberg excitation of ultracold potassium atoms. A two-dimensional magneto-optical trap (2D MOT) serves as the atom source by supplying an atomic beam directed towards the center of the three-dimensional magneto-optical trap (3D MOT). The optical access of the science chamber allows for multiple optical traps: a cigar-shaped crossed dimple trap, pancake-shaped trap and arbitrarily placed optical tweezers imaged from a digital micromirror device (DMD). For diagnostics, we can image the atoms from the side (along y) onto a complementary metal–oxide–semiconductor (CMOS) camera as well as from the top (along z) with a high-resolution imaging setup onto an electron-multiplying charge-coupled device camera (EMCCD). The laser beam for Rydberg excitation enters the chamber along x.

to $\sim 500\,\mu\mathrm{K}$. A subsequent lambda-enhanced gray molasses cooling stage on the D1 line [76, 79, 89–93], which uses the same beam path as the 3D MOT beams, lowers the temperature to $\sim 10\,\mu\mathrm{K}$. See Sec. 3.2 for more details on the laser setup for the D1 and D2 transitions.

- **MOT coils.** The two home-built coils[7] are made out of hollow-core wire for water cooling. The current of up to $200\,\mathrm{A}$[8] can be reversed in one coil using a home-built H-bridge [77], which switches between anti-Helmholtz configuration (opposing currents) and Helmholtz configuration (rectified currents). The gradient field in anti-Helmholtz configuration is used in the MOT and compressed MOT (CMOT) phase, with calculated magnetic field gradients in the center of $7\,\mathrm{G/cm}$ and $27\,\mathrm{G/cm}$, respectively[9]. The homogeneous magnetic field, when the coils are in the Helmholtz configuration, can be used for Feshbach resonances up to $400\,\mathrm{G}$[10].
- **Compensation coils.** Six home-built compensation coils are placed in orthogonal pairs to compensate for external magnetic fields. The horizontal compensation coil pairs[11] in x and y direction are placed outside the CF63 viewports. The two vertical z compensation coils[12] are placed directly next to the MOT coils.
- **Optical traps.** The experimental setup was designed to allow for flexibility in the available trap geometries. The experimental measurements presented in this thesis were performed using the crossed dimple trap entering along x and the pancake trap propagating along y (see Sec. 3.3 for more details). Furthermore, optical setups for a large volume reservoir trap and an optical lattice are available.
- **Side imaging.** The atom cloud is imaged via a $4f$ setup[13] with 1-fold magnification from the side along y onto a complementary metal–oxide–semiconductor (CMOS) based camera[14]. We commonly use this setup for absorption imaging of the atom cloud using a resonant beam with the D2 transition, which allows us to extract the optical density, the atom number and the size of the cloud, typically after a short time-of-flight expansion in free space. A dichroic mirror[15] in front of the lens close to the viewport separates the $767\,\mathrm{nm}$ imaging light from the $1064\,\mathrm{nm}$ pancake trap light.

---

[7] One coil consists of two identical pancakes, where each one consists of two layers with 12 windings each. The inner (outer) diameter of the windings is $19\,\mathrm{cm}$ ($29.6\,\mathrm{cm}$).

[8] Delta Elektronika SM6000 SM 30-200 supplying up to $200\,\mathrm{A}$ and $30\,\mathrm{V}$

[9] The calculated conversion factor in the center of the chamber is $0.25\,\mathrm{G/cmA}$.

[10] The calculated conversion factor in the center of the chamber is $2\,\mathrm{G/A}$.

[11] Each coil is made out of 10 layers of 2 windings with an inner diameter of $120\,\mathrm{mm}$. The calculated conversion factor for the center of the chamber is $0.36\,\mathrm{G/A}$.

[12] Each coil is made out of 3 layers of 10 windings with an inner diameter of $192\,\mathrm{mm}$. The calculated conversion factor for the center of the chamber is $0.93\,\mathrm{G/A}$.

[13] Two lenses with $f = 202.8\,\mathrm{mm}$

[14] IDS UI-3240ML-NIR

[15] Thorlabs DMLP950L

- **Vertical high-resolution imaging.** An aspheric objective lens[16] inside the vacuum chamber together with a second, long focal length lens[17] creates a high-resolution imaging system [79] with 47-fold magnification onto an electron-multiplying charge-coupled device (EMCCD) camera[18]. This allows for absorption imaging using a beam propagating upwards along the z axis as well as for fluorescence imaging.
- **Rydberg laser excitation.** The ultra-violet (UV) laser for single-photon Rydberg excitation and the blue laser for two-photon Rydberg excitation are focused to the center of the science chamber along x. See Sec. 3.4 for more details on the Rydberg excitation lasers.

3.2 Laser setup for cooling on the D1 and D2 transitions

The laser system presented in this section is mainly used to achieve cold temperatures and high densities in the atom gas, such that an optical trap can be efficiently loaded as a starting point of the later experiments. The laser cooling scheme consisting of 2D MOT, 3D MOT, compressed MOT and D1 gray molasses allows for temperatures of the atomic sample of $\sim 10\,\mu\mathrm{K}$ at atomic densities of $10^{11}\mathrm{cm}^{-3}$ [79]. Other purposes of the laser system include e.g. diagnostics via absorption imaging or optical pumping. The laser system is designed to work with both bosonic ^{39}K as well as fermionic ^{40}K, requiring only small changes of the optical setup. As the work in this thesis was performed exclusively with ^{39}K, we will focus on the corresponding configuration.

Fig. 3.2a shows the transitions of potassium-39 on the D1 and D2 lines with their corresponding frequencies as well as the hyperfine structure of the three manifolds, where the numbers in parenthesis indicate the energy shift in MHz [86, 94]. We observe, that the hyperfine splitting is quite narrow with respect to the natural linewidth of $6\,\mathrm{MHz}$, especially in the $|4^2p_{3/2}\rangle$ manifold. The resulting increased off-resonant scattering rate requires a higher ratio of repump to cooler during the magneto-optical trap (MOT). To overcome the limitations caused by this, gray molasses (GM) cooler and repump lasers, blue-detuned on the D1 line, realize an additional cooling stage. For laser locking on both lines, we use the cross-over (Xover) transition.

---

[16] Asphericon A45-32 HPX with a numerical aperture of 0.61 and effective focal length of $32\,\mathrm{mm}$. The aspheric lens is coated with indium thin oxide (ITO) on the bottom side to increase electronic conductivity. Otherwise charges could accumulate and lead to the build-up of stray electric fields, affecting the Rydberg states.

[17] CVI Laser Optics PLCX-50.8-772.6-UV-700-900 with $f \approx 1500\,\mathrm{mm}$.

[18] Andor iXon Ultra 897 UCS-EXF

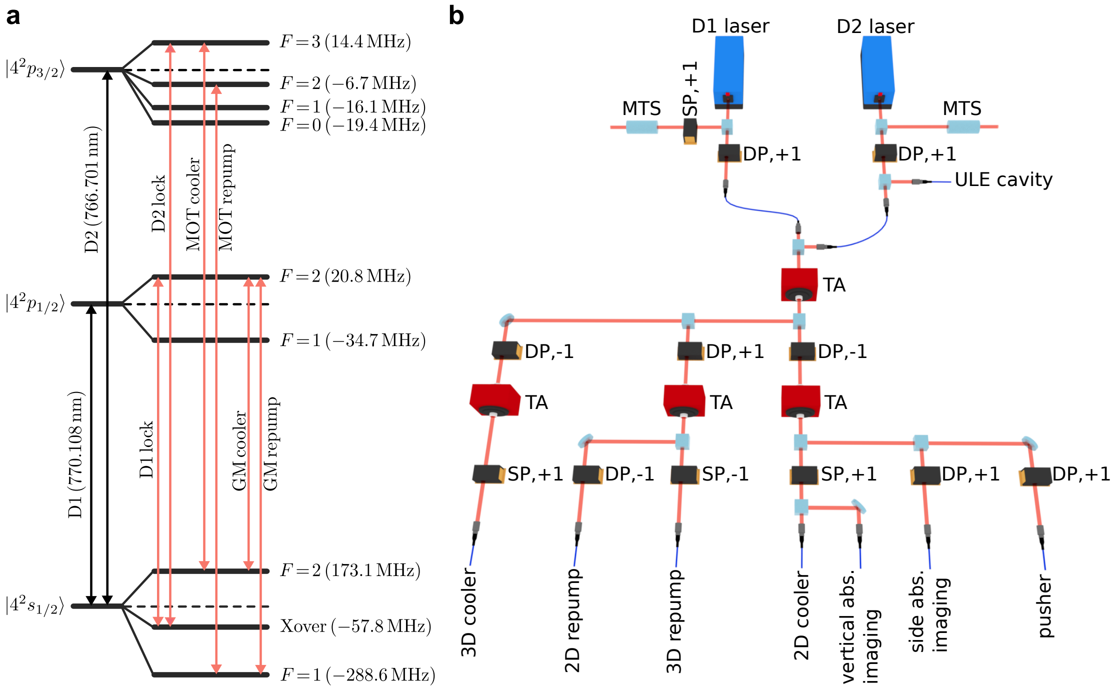

Fig. 3.2: Laser system for addressing the D1 and D2 lines in potassium. **a** Level structure of ^{39}K on the D1 and D2 transition, showing the D1 and D2 lock as well as the magneto-optical trap (MOT) and gray molasses (GM) cooler and repump transitions. The ground state manifold $|4^2s_{1/2}\rangle$ is split up into two hyperfine states $F=1$ and $F=2$, where for locking we use the additional Xover transition. The hyperfine splitting, especially on the D2 line, is quite narrow. **b** Schematic of the laser setup to produce the optical frequencies to address the D1 and D2 transitions. Two diode lasers are locked to the D1 and D2 line (according to subfigure a) via modulation transfer spectroscopy (MTS). Acousto-optic modulators (AOM) are used in single-pass (SP) or double-pass (DP) configuration to shift the laser frequency via the first positive (+1) or first negative (-1) order. Tapered amplifiers (TA) are seeded with light either from the D1 or D2 laser to increase the laser power. Finally, the different frequencies are fiber-coupled to the science chamber.

A schematic of the laser setup to create the corresponding frequencies is presented in Fig. 3.2b. Two diode lasers[19] running at $766.7\,\mathrm{nm}$ (D1) and at $770\,\mathrm{nm}$ (D2) are locked via modulation transfer spectroscopy (MTS) [73]. The D2 laser can alternatively be locked to the ultra-stable ULE reference cavity (see Sec. 3.4 for more details). Acousto-optic modulators (AOM)[20] are used in single-pass (SP) or double-pass (DP) configuration to increase/decrease the laser frequency by the RF driving frequency via the first positive (+1)/ negative (-1) order. The AOMs are furthermore used as on/off switches or to tune laser powers. With the double-pass AOMs in front of the lasers, we switch between either D1 or D2 light, which is coupled into an optical fiber and seeds a first tapered amplifier (TA)[21]. It amplifies $5\,\mathrm{mW}$ up to $2\,\mathrm{W}$, which is split up into three branches. Each branch is in turn amplified by another TA and frequency shifted by AOMs to create the required frequencies for the cooler and repump for the 3D MOT beams (3D cooler & 3D repump) and the 2D MOT beams (2D cooler & 2D repump), the pusher beam in the 2D MOT as well as side and vertical absorption imaging beams. All of these are coupled into optical fibers, transporting the light to the science chamber.

3.3 Optical trapping

This section will focus on the optical trapping [96] geometries at our disposal, into which the atoms are loaded after the laser cooling stages (see Sec. 3.2), including a cigar-shaped dimple, a pancake trap, and arbitrarily placed optical tweezers.

3.3.1 Crossed dimple trap

The dimple is a commonly used, elongated, cigar-shaped trap, which will be used in the non-interfering configuration in the experimental studies presented in chapter 4.

Optical setup

This crossed dimple trap is created by two far red-detuned beams of wavelength $\lambda = 1064\,\mathrm{nm}$, crossing at an angle of 7.5 degree (Fig. 3.3a). The input laser light of typically $5\,\mathrm{W}$ power is derived from a master oscillator power amplifier (MOPA) laser[22] and sent through a photonic crystal fiber[23]. The power can be tuned via a high-power AOM[24]. A thin-film polarizer (TFP) splits the incoming beam up into two beams of

---

[19] Toptica DL Pro with Toptica DigiLock 110 locking electronics

[20] Gooch and Housego 3110-120 and 3200-124

[21] home-built, see Ref. [95] for more details

[22] Coherent Mephisto MOPA 55W

[23] NKT Photonics LMA-PM-15, $12.6\,\mu\mathrm{m}$ mode field diameter

[24] Gooch and Housego 3080

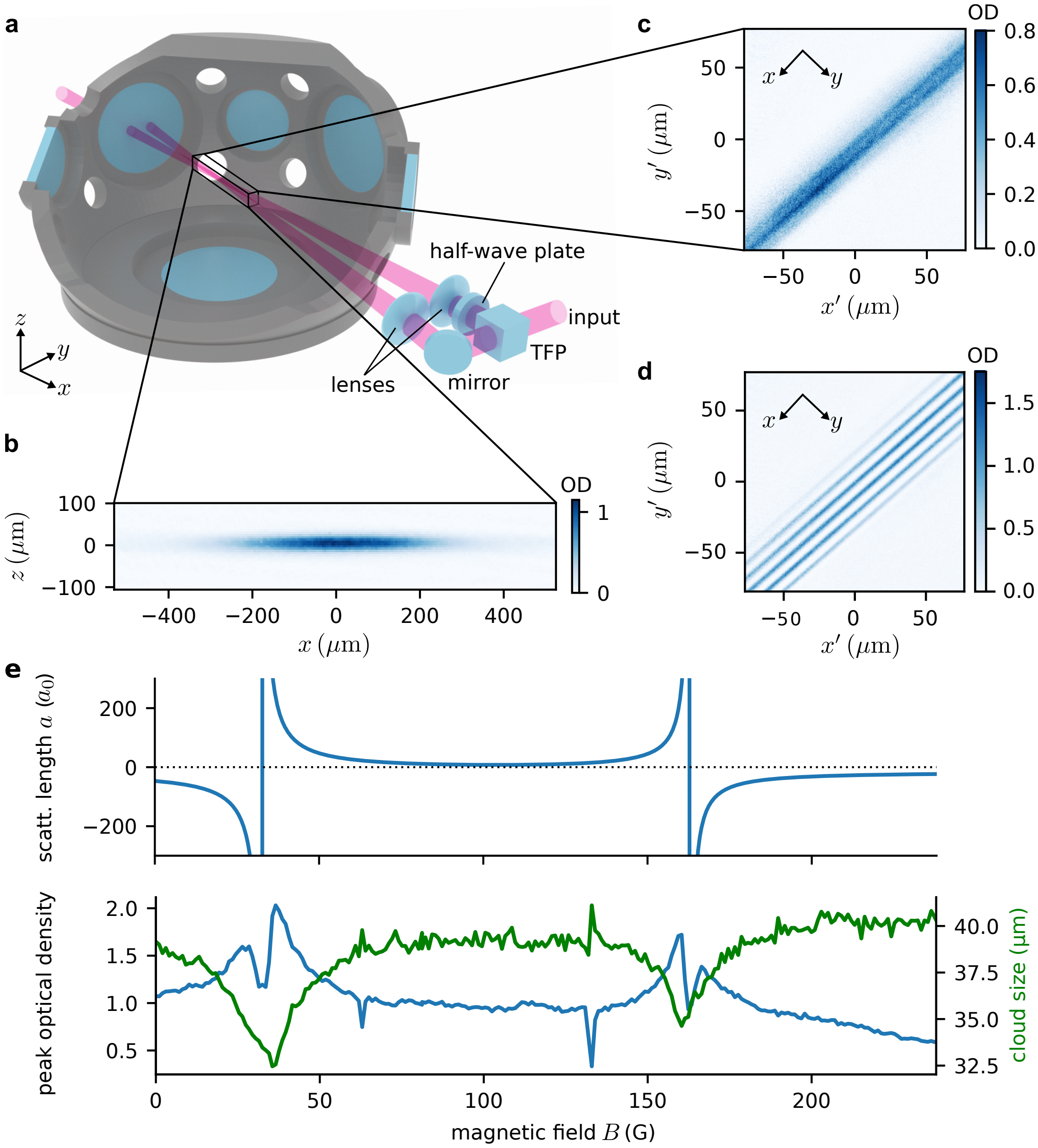

Fig. 3.3: Crossed dimple trap. a A thin-film polarizer (TFP) divides the incoming $1064\,\mathrm{nm}$ light into two beams. Two lenses focus the beams to the center of the science chamber, where the two foci are overlapped. **b** Side absorption image along y of an atomic cloud trapped in the dipole trap. This crossed dimple trap can be operated in two modes, selected by a half-wave plate in one beam path: **c** If both beams are linearly polarized orthogonal to each other, the light does not interfere and the resulting trap geometry at the crossing volume is cigar-shaped, visible in this absorption image along the vertical z axis. **d** On the other hand, polarization along the same axis leads to vertical two-dimensional sheets separated by the interference fringes of $8\,\mu\mathrm{m}$ period in the x-y plane. The color bars indicate the optical density (OD) of the atom cloud. **e** A Feshbach magnetic field scan of potassium-39 in the optical dipole trap. Calculated scattering length a (*top*) together with the measured peak optical density (*bottom, blue*) and cloud size (*bottom, green*) after a hold time in the non-interfering crossed dimple trap as a function of the applied homogeneous magnetic field B.

equal power, which are focused via two $f = 300\,\mathrm{mm}$ lenses into the science chamber, where the two beams overlap and create a beam waist of approx. $30\,\mu\mathrm{m}$. The relative polarization between both beams can be tuned using a half-wave plate in one of the two arms, switching between an interfering or non-interfering configuration at the overlap region.

Fig. 3.3b shows the optical density of the trap, measured with a side absorption image. Via the high-resolution setup along the z axis, we can gain spatial information along the x-y plane. Fig. 3.3c and Fig. 3.3d show vertical absorption images of the non-interfering and the interfering crossed dimple trap, where the polarization of the two laser beams is orthogonal and parallel, respectively. The clearly visible interference fringed has a period of $8\,\mu\mathrm{m}$, as expected from the crossing angle.

Typically, we load the dipole trap with $N \sim 10^5$ potassium-39 atoms. After evaporating down the trap power by about a factor of ten, the temperature is $\sim 10\,\mu\mathrm{K}$, with corresponding trapping frequencies of $\omega_x/2\pi = 60\,\mathrm{Hz}$ and $\omega_{y,z} = 900\,\mathrm{Hz}$ and widths of the Gaussian atom distribution ($e^{-1/2}$) of $\sigma_x = 200\,\mu\mathrm{m}$ and $\sigma_{y,z} = 10\,\mu\mathrm{m}$ for the weak and tight axes, respectively.

Feshbach scan

Fig. 3.3e presents a scan of the homogeneous magnetic field produced by the MOT coils in Helmholtz configuration (see Sec. 3.1). This can be used to tune to the vicinity of available Feshbach resonances. As potassium-39 has a small negative scattering length, these Feshbach resonances are commonly used to enhance the scattering cross section and thus improve the rethermalization time of the atom cloud during evaporative cooling.

The top panel shows the calculated scattering length

$$a(B) = a_{\mathrm{bg}} \left(1 - \frac{\Delta B^1}{B - B_0^1} - \frac{\Delta B^2}{B - B_0^2} \right), \tag{3.1}$$

for ^{39}K in the spin-polarized ground state $|4s_{1/2}, F = 1, m_F = -1\rangle$, where two relatively broad Feshbach resonances are available below $200\,\mathrm{G}$[25], with resonance centers $B_0^1 = 32.6(15)\,\mathrm{G}, B_0^2 = 162.8(9)\,\mathrm{G}$, resonance widths $\Delta B^1 = 55\,\mathrm{G}, \Delta B^2 = -37\,\mathrm{G}$, with a background scattering length of $a_{\mathrm{bg}} = -19a_0$ [97, 98].

The bottom panel shows a corresponding experimental measurement, where we first spin-polarize our sample in the dimple trap to the $|4s_{1/2}, F = 1, m_F = -1\rangle$ state. We achieve this in a two-step process: we first acuumulate the population in the $|F = 2,\, m_F = -2\rangle$ state by optical pumping on the D1 line with σ^- polaized light. Subsequently, we apply a

---

[25] Maximum magnetic field achievable with our setup.

Landau-Zener sweep with an RF field[26] between $|F = 2,\, m_F = -2\rangle$ and $|F = 1,\, m_F = -1\rangle$ and blow-away the remaining atoms in the $|F = 2\rangle$ manifold with the D1 cooler. Then we quickly switch on the homogeneous magnetic field to a given value using the H-bridge [77] and ramp down the trap power from $4.6\,\mathrm{W}$ to $0.6\,\mathrm{W}$ in one second. Finally, we observe the remaining peak optical density (*blue*) and cloud size (*green*) after a short time of flight of $0.5\,\mathrm{ms}$ via absorption imaging. At the two expected Feshbach resonance positions at $B_0 = 32.6\,\mathrm{G}$ and $B_0 = 162.8\,\mathrm{G}$, a loss feature is visible manifested by a reduced peak optical density. Right next to this loss feature however, the peak optical density increases above its baseline of about a and cloud size is reduced, which corresponds to a higher atomic density and lower temperature and is indicative of an evaporative cooling effect. We observe two additional small features at $63\,\mathrm{G}$ and $133\,\mathrm{G}$, which were not given in the literature for $|F = 1, m_F = -1\rangle$. However, the first resonance is close to a resonance between $|F = 1, m_F = 0\rangle$ states and might hint to a small admixture thereof.

3.3.2 Pancake trap

Another available optical trap is the so-called pancake trap. Its name is derived from its geometry - the vertical direction is much narrower compared to the two horizontal axes. This makes it interesting as it is quasi two-dimensional with respect to the Rydberg excitation (facilitation and blockade) for the Rydberg states typically used in this thesis. It will be used for the Rydberg excitation growth studies in chapter 5.

Optical setup

Fig. 3.4a,b illustrates the optical setup to create the pancake trap geometry [79]. An incoming beam of wavelength $\lambda = 1064\,\mathrm{nm}$, derived from a MOPA laser[27] using a high-power AOM[28], is vertically expanded by a concave cylindrical lens[29] $f_z = -22.7\,\mathrm{mm}$. At the first of the two spherical doublet lenses[30] $f_s = 202.8\,\mathrm{mm}$, the beam is recollimated along z. A second concave cylindrical lens[31] $f_x = -25.9\,\mathrm{mm}$, orthogonal to the first, acts along the x axis, such that the beam is highly elongated in the vertical direction. This results in a tight vertical focus after the second spherical lens f_s whereas the waist along x is wider.

A typical side absorption image with the resulting optical density encoded in the color is given in Fig. 3.4d, where we can observe the typical trap shape. The horizontal width

---

[26] Applied with the in-vacuum coil.

[27] The same Coherent Mephisto MOPA 55W laser as for the crossed dimple trap.

[28] Gooch and Housego 3080

[29] CVI Laser Optics SCC-15.0-10.2-UV-1064

[30] CVI Laser Optics LAI-190.0-50.0

[31] Newport Spectra-Physics CSV025AR.33

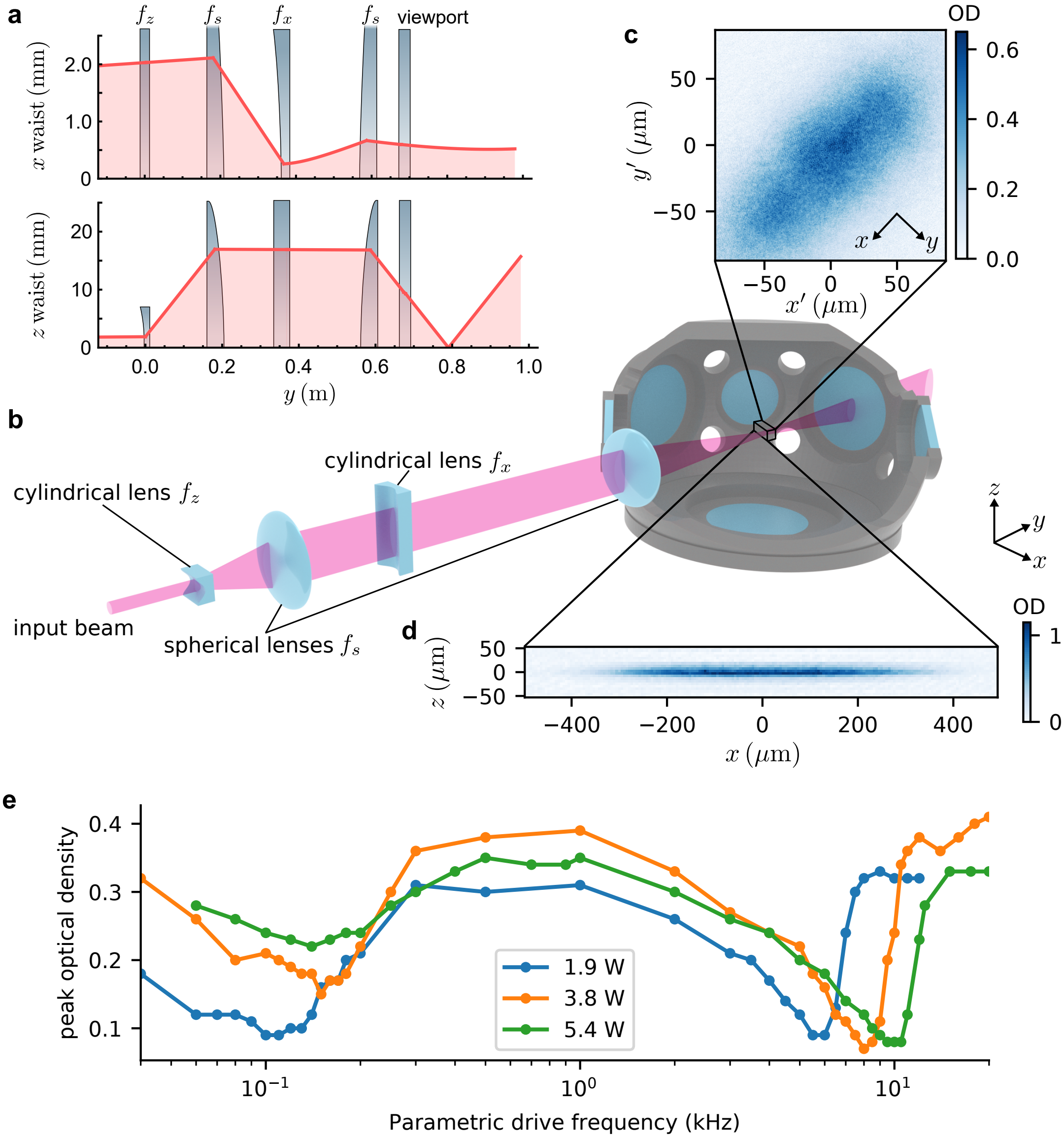

Fig. 3.4: Pancake trap. a Calculated Gaussian weights in x and z direction through the optical setup to create a light-sheet in the x-y plane with a tight trapping potential along z. The spherical input beam is elongated along the vertical axis by a concave cylindrical lens with focal length f_z. The first spherical lens f_s recollimates the beam along z, before the second spherical lens in $4f$ configuration creates a tight vertical focus in the center of the science chamber. The second concave cylindrical lens f_x acts along the x axis, allowing to tune the x focal size of the trap. Adapted from [79]. **b** Corresponding three dimensional rendering of the pancake trap setup. **c** High-resolution absorption image of the atom distribution held in the pancake trap. The image is taken from the top along the z axis. **d** Side absorption image of the atom distribution. The image is taken along the y axis. In this case, the trap power is reduced and the atom cloud is evaporated. The color bar encodes the optical density of the atom cloud. **e** Trap frequency measurement via parametric heating. The peak optical density of the remaining atom cloud after the parametric heating is plotted as a function of the trap depth modulation frequency for three different trap laser powers of $1.9\,\mathrm{W}$, $3.8\,\mathrm{W}$ and $5.4\,\mathrm{W}$.

trap power P	$1.9\,\mathrm{W}$	$3.8\,\mathrm{W}$	$5.4\,\mathrm{W}$
temperature T	$6\,\mu\mathrm{K}$	$9\,\mu\mathrm{K}$	$13\,\mu\mathrm{K}$
ν_{para}	$50\,\mathrm{Hz},\ 3.3\,\mathrm{kHz}$	$75\,\mathrm{Hz},\ 4.5\,\mathrm{kHz}$	$70\,\mathrm{Hz},\ 5.5\,\mathrm{kHz}$
ν^x_{calc}	$54\,\mathrm{Hz}$	$76\,\mathrm{Hz}$	$91\,\mathrm{Hz}$
ν^y_{calc}	$154\,\mathrm{Hz}$	$220\,\mathrm{Hz}$	$261\,\mathrm{Hz}$
ν^z_{calc}	$3.8\,\mathrm{kHz}$	$5.4\,\mathrm{kHz}$	$6.5\,\mathrm{kHz}$
trap depth U	$40\,\mu\mathrm{K}$	$80\,\mu\mathrm{K}$	$112\,\mu\mathrm{K}$

Tab. 3.1: **Results of the parametric heating measurement in the pancake trap.** The incoming trap laser power, the temperature of the atom cloud and the trap frequency extracted from the parametric heating ν_{para} are measured quantities, whereas the ν_{calc} and the trap depth U are calculated from Gaussian beam propagation results.

of the atom distribution is much larger compared to the vertical extent, which is close to or below the resolution of this imaging system, especially when we reduce the trap power for evaporative cooling. The vertical high-resolution absorption image in Fig. 3.4c is performed with a smaller cloud to fit it better on the image. The extracted Gaussian widths of the atom cloud are $\sigma_x = 29\,\mu\mathrm{m}$ and $\sigma_y = 75\,\mu\mathrm{m}$.

Trap frequency measurement

To further characterize the trap properties, we measure the trap frequencies via parametric heating [99]. By periodically modulating the trap depth, quadrupole modes are excited, leading to heading and atom loss out of the trap at a modulation of twice the trap frequency. We start with the atomic cloud in the pancake trap of a given power at a temperature of around $10\,\mu\mathrm{K}$. Subsequently, we modulate the trap depth via the AOM RF power for $850\,\mathrm{ms}$. After a short time of flight, we take an absorption image and extract the peak optical density. The peak optical density is plotted in Fig. 3.4e as a function of the modulation frequency for three different trap laser powers of $1.9\,\mathrm{W}$, $3.8\,\mathrm{W}$ and $5.4\,\mathrm{W}$. We observe two main loss resonances, from which we extract two trap frequencies. The low-frequency loss feature is quite broad and might actually consist of two close-by loss resonances of the horizontal axes. Furthermore, the trap frequency positions shift as expected with the square root of the trap intensity. Tab. 3.1 summarizes these findings. Additionally, it shows the measured temperature of the atom cloud before parametric heating via thermal expansion during time of flight. Via Gaussian beam propagation though the optical system, we calculate the given expected trap frequencies and depth.

3.3.3 Optical tweezer traps

> *This section is based on the following publication:*
> [10] **Preparation of hundreds of microscopic atomic ensembles in optical tweezer arrays**, Y. Wang, S. Shevate, T. M. Wintermantel, M. Morgado, G. Lochead, and S. Whitlock, npj Quantum Information 6, 54 (2020)

Here, a versatile system to create different trap geometries by arbitrarily shaping the trap light is presented. This new experimental capability of structuring the atomic density distribution has motivated the theoretical proposal of quantum cellular automata in an array of Rydberg excited atoms [100], presented in chapter 6.

Fig. 3.5a shows an illustration of the setup that we use to create hundreds of microtraps [83]. The output of a $780\,\mathrm{nm}$ wavelength diode laser[32] is amplified by a TA[33] and coupled into an optical fiber to create a clean Gaussian mode. The chosen wavelength of $780\,\mathrm{nm}$ is a trade off between a lower off-resonant scattering rate versus a higher trap depth at fixed power as well as proximity to the design wavelength of $767\,\mathrm{nm}$ of the optical high-resolution setup. After the fiber, the digital micro-mirror device (DMD)[34] is illuminated with more than $400\,\mathrm{mW}$ of collimated light. Depending on the state of the micromirror, it either reflects the incoming light towards (white pixels) or away from (black pixels) the high-resolution imaging setup. An exemplary DMD pattern is shown in Fig. 3.5b, where a nonlinear change in pattern spot sizes corrects for the Gaussian envelope of the illumination beam to improve the homogeneous filling of the microtraps. The reflected tweezer trap light now propagates in the inverse direction through the high-resolution imaging system consisting of a large focal length lens together with the aspherical objective lens inside the vacuum chamber (see Sec. 3.1). This effectively creates a 47-fold demagnified image of the DMD pattern onto the atoms, which are held in the pancake trap. After $200\,\mathrm{ms}$ overlap time to load the tweezers with atoms from the pancake trap, we turn off the pancake and the atoms remain trapped in the tweezers. Read-out of the tweezer arrays is possible via high-resolution fluorescence or absorption imaging along z, where a dichroic mirror separates the imaging light ($767\,\mathrm{nm}$ or $770\,\mathrm{nm}$) from the tweezer trap light at $780\,\mathrm{nm}$. A total of 484 filled atom arrays with spot sizes of $\sim 0.75\,\mu\mathrm{m}$ ($e^{-1/2}$ radii in the absorption image), a period of $3.5\,\mu\mathrm{m}$ and a mean of 38 atoms per tweezer is visible in the high-resolution absorption image of Fig. 3.5c [10], created from the DMD pattern shown in Fig. 3.5b. Note that one is not restricted to symmetric lattices, but can project an arbitrary pixel pattern onto the DMD. This versatility of achievable trap geometries in the two-dimensional plane

---

[32] Toptica DL pro

[33] home-built, see Ref. [95] for more details

[34] Vialux V-7000 VIS with Texas Instruments DLP7000BFLP 1024×768 micro mirror array, $13.7\,\mu\mathrm{m}$ pitch

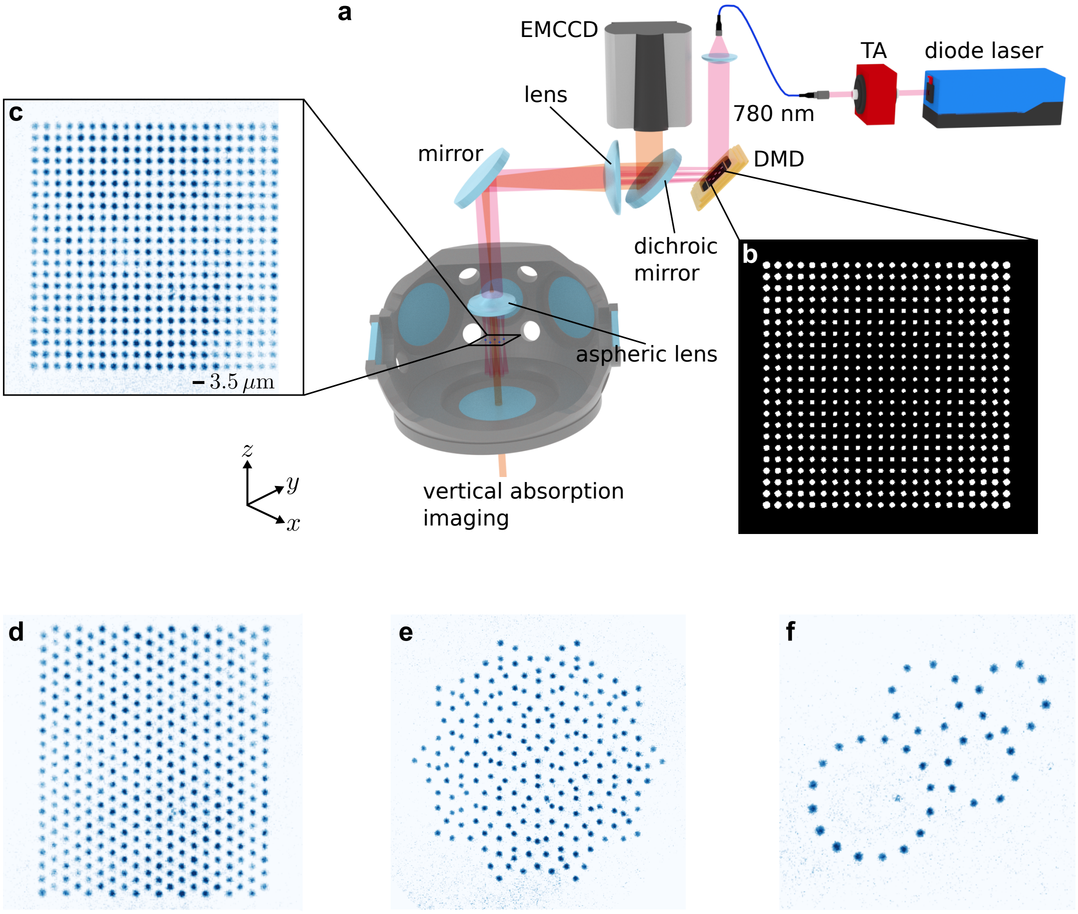

Fig. 3.5: Setup to create optical tweezer traps. **a** Schematic of the optical setup. The $780\,\mathrm{nm}$ light for creation of the microtraps is derived from a diode laser and amplified by a tapered amplifier (TA). This collimated light illuminates the digital micromirror device (DMD), which reflects the light according to the applied pattern. The reflected light pattern is imaged onto the atom plane using a $4f$ setup including an aspheric objective lens inside the vacuum chamber, where the atoms are trapped towards the high intensity regions. A vertical beam is used to create absorption images onto a camera (EMCCD). **b** Binary pattern projected onto the DMD to create a 22×22 square lattice geometry. Each pixel encodes the position of one micromirror, where white (black) micromirrors reflect (do not reflect) the incoming light onto the atoms. A gradient on the spot sizes corrects for the inhomogeneous laser illumination profile. **c** Vertical high-resolution absorption image of 484 filled microtraps with $3.5\,\mu\mathrm{m}$ lattice period, created by the DMD pattern shown in **b**. Each microtrap is filled with approx. 38 atoms. As we can project arbitrary patterns on the DMD, the achievable trap geometries are quite flexible, including for example a **d** triangular lattice, **e** quasi-crystalline Penrose pattern and **f** ring structures. Adapted from [10].

is demonstrated by a triangular lattice (Fig. 3.3.3d), a quasi-crystalline Penrose pattern (Fig. 3.3.3e) and ring structures (Fig. 3.3.3f).

3.4 Single-photon and two-photon Rydberg excitation

The following gives an overview of the laser systems for single and two-photon Rydberg excitation [80, 82, 101]. One photon excitation, compared to two-photon-excitation, has the advantage of requiring no intermediate state which would lead to extra decoherence due to off-resonant scattering events [9]. The challenge, however, is to obtain high Rabi coupling frequencies, as the dipole coupling element is smaller and as it is more difficult to create high power laser light of the required short wavelength in the ultra-violet (UV) range. The presented experimental results in the following thesis (Sec. 4 and 5) were therefore conducted exclusively with single-photon UV Rydberg excitation. In Sec. 6 we theoretically consider a novel quantum cellular automata implementation that could be implemented using two-photon Rydberg excitation.

Single-photon excitation

To excite from the ground state manifold of potassium-39 ($|4s_{1/2}\,F=1\rangle$ or $|4s_{1/2}\,F=2\rangle$) to a Rydberg state requires an energy corresponding to a wavelength of about $286\,\mathrm{nm}$, where the exact wavelength depends on the selected Rydberg state $|np_{1/2}\rangle$ or $|np_{3/2}\rangle$ (cf. Fig. 3.6a). As we use one photon, we couple to p states according to electric dipole selection rules. The laser system creating this UV light is sketched in Fig. 3.6b. A diode-pumped solid-state laser[35] is used to pump the dye ring laser[36]. This creates an output of approximately $4\,\mathrm{W}$ at $572\,\mathrm{nm}$ wavelength, which is frequency doubled[37] to $286\,\mathrm{nm}$ with power of routinely $200\,\mathrm{mW}$ [82].

Two-photon excitation

Instead of using a single photon, the excitation energy can also be provided by two photons, usually far-detuned[38] from an intermediate state to reduce off-resonant scattering which increases the decoherence rate. Here we choose the intermediate state out of the $|4p\rangle$ manifold (see Fig. 3.6c), such that the lower transition has a wavelength of $767\,\mathrm{nm}$ or $770\,\mathrm{nm}$ (red) and the upper photon a wavelength of approximately $457\,\mathrm{nm}$ (blue). As we use two photons, electric dipole selection rules allow coupling to $|ns\rangle$ or $|nd\rangle$ Rydberg states. An interesting alternative would be to choose the intermediate state from the $5p$ manifold, with $404\,\mathrm{nm}$ ($979\,\mathrm{nm}$) as the lower (upper) transition [102]. Here, the lower transition has a narrower linewidth, and the upper transition has a higher electric dipole

---

[35] Spectra-Physics Millenia eV with up to $22\,\mathrm{W}$ output power at a wavelength of $532\,\mathrm{nm}$.

[36] Sirah Matisse DX operated with Rhodamine 6G.

[37] Sirah Wavetrain II

[38] Typically of hundreds of MHz.

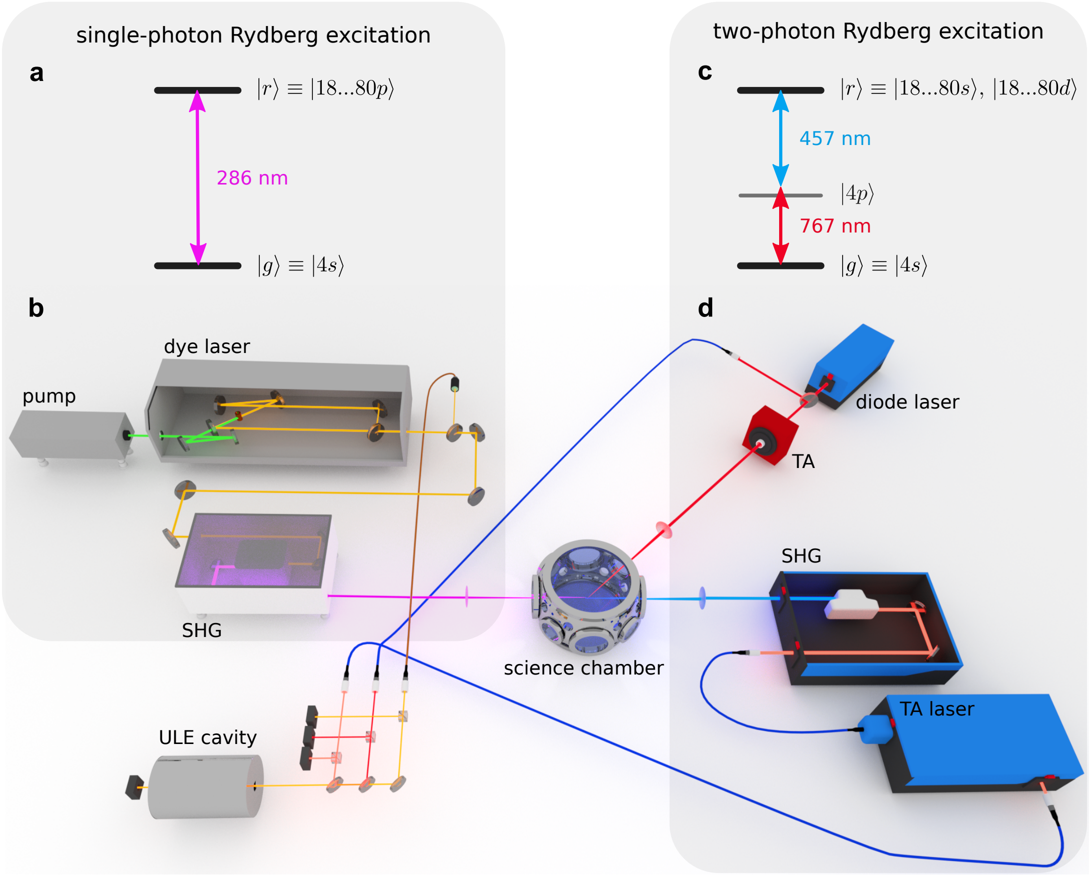

Fig. 3.6: Schematic diagram of the laser system for single-photon and two-photon Rydberg excitation. a Level scheme for one-photon Rydberg excitation. The ground state $|g\rangle$, which is in the $|4s\rangle$ manifold for ^{39}K, is coupled to a Rydberg state $|r\rangle$ with typical principal quantum numbers ranging from $n = 18$ to $n = 80$ by a laser field with a wavelength of about $286\,\mathrm{nm}$ (the exact wavelength depends on the selected Rydberg state). **b** Laser system creating ultra-violet (UV) laser light for single-photon Rydberg excitation. A dye laser, pumped by $532\,\mathrm{nm}$ laser light, creates a wavelength of $572\,\mathrm{nm}$ which is frequency-doubled to the UV range ($286\,\mathrm{nm}$) via nonlinear second harmonic generation (SHG). **c** Level scheme for two-photon Rydberg excitation. The ground state $|g\rangle$ is coupled to the Rydberg state $|r\rangle$ via two laser fields with wavelengths of $767/700\,\mathrm{nm}$ and approximately $457\,\mathrm{nm}$, which are typically far-detuned from the intermediate state $|4p\rangle$ of potassium 39 to reduce off-resonant scattering. Due to the two-photon excitation, Rydberg $|ns\rangle$ and $|nd\rangle$ states are accessible. **d** Laser system creating two laser fields for two-photon Rydberg excitation. The lower transition frequency ($767\,\mathrm{nm}$) is created by a diode laser, which is amplified by a tapered amplifier (TA). This is the same laser system which is also used for the magneto-optical traps etc. The blue light for the upper transition ($457\,\mathrm{nm}$) originates from a $914\,\mathrm{nm}$ TA laser output inserted into a second-harmonic generation (SHG) cavity. Both laser beams are overlapped on the atoms to induce two-photon transitions. All three laser systems can be stabilized to the same stable reference cavity made out of an ultra-low expansion (ULE) glass spacer (*bottom left*). Modified from [80].

element as well as higher readily available laser powers, which contributes to higher effective coherence times.

Fig. 3.6d shows a schematic of the two laser setups creating the red and blue wavelengths. The red light, created by a diode laser[39] amplified by a home-built TA, is derived from the same setup as the laser for addressing the D1 and D2 transitions (Sec. 3.2). To create the blue light, a TA laser[40] running at a wavelength of about $913\,\mathrm{nm}$ is frequency doubled[41] to $457\,\mathrm{nm}$, resulting in $\sim 500\,\mathrm{mW}$ of blue light.

Locking
All three laser systems can be locked via Pound-Drever-Hall (PDH) stabilization [103, 104] of the wavelengths $572\,\mathrm{nm}$[42], $767\,\mathrm{nm}$ and $913\,\mathrm{nm}$ to the same ultra-stable, high-finesse reference cavity[43] made out of an ultra-low expansion (ULE) glass spacer. Fiber-coupled electro-optical modulators (EOM)[44] are used to create the PDH modulation at $20\,\mathrm{MHz}$. For the UV and blue excitation laser, the EOMs also create sidebands of up to $600\,\mathrm{MHz}$, allowing for spectroscopy of the Rydberg series.

3.5 Rydberg detection via electric field ionization

The here introduced detection scheme gives direct access to the number of Rydberg atoms. It was implemented during my PhD thesis, whereas before we could only detect ground state atoms via absorption imaging. This direct measurement of the Rydberg atom number allowed for some major results presented in this thesis, e.g. the detection of excitation avalanches in self-organized criticality (Sec. 4.3) and the observation of epidemic growth of the Rydberg excitation number in chapter 5.

The approach presented here is based on electric field ionization with subsequent detection of the created ions [46, 47, 105]. In an alternative approach Rydberg states are depumped to the ground state and measured with subsequent fluorescence detection [106, 107].

Rydberg detector assembly
Fig. 3.7a presents a sketch of our home-built Rydberg ion detection setup [105, 108]. As Rydberg atoms are sensitive to external electric fields, the setup includes eight electrodes

---

[39] Toptica DL Pro

[40] Toptica TA-pro

[41] Toptica SHG-pro

[42] The dye laser system comes with a reference cell for locking, which is less stable and has a lower finesse compared to the ULE cavity.

[43] Stable Laser Systems ATF 6010-4. Measured finesses of $\mathcal{F}_\lambda = \{21200 \pm 2100, 23200 \pm 700, 13300 \pm 600\}$ for $\lambda = \{767, 913, 572\}$ nm [80].

[44] Jenoptik PM594 ($572\,\mathrm{nm}$), Qubig Q1603-UHD/1 ($767\,\mathrm{nm}$) and Jenoptik PM905 ($913\,\mathrm{nm}$)

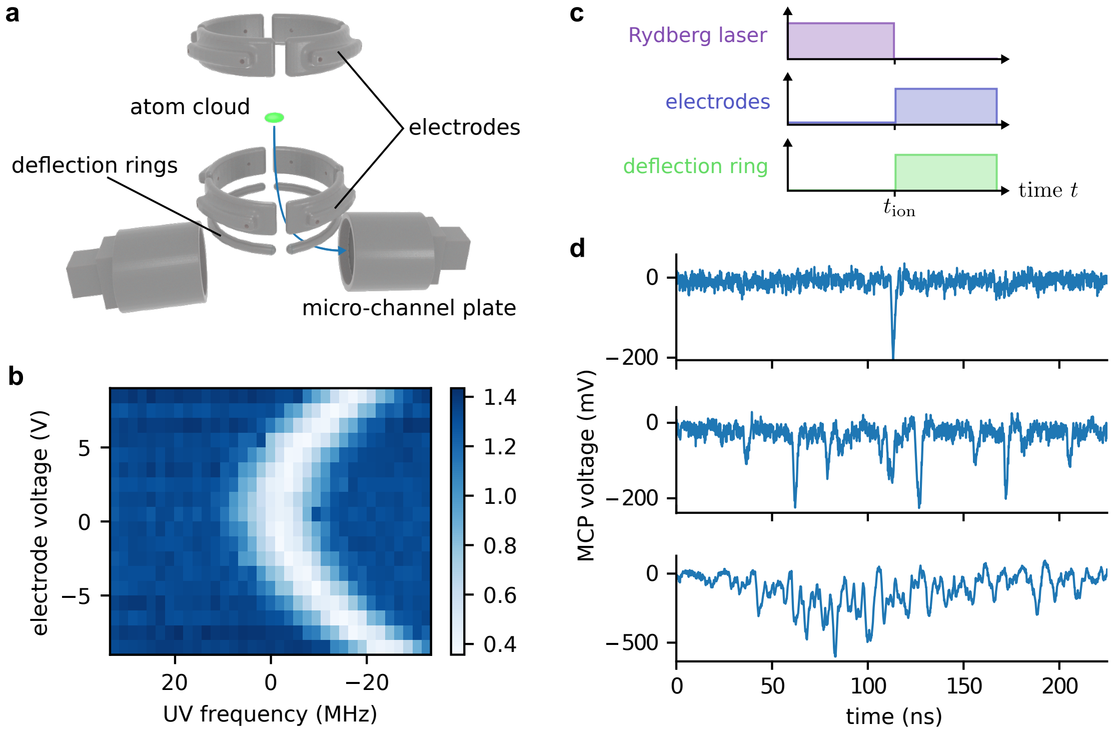

Fig. 3.7: Rydberg ion detection. a Rydberg detector assembly. Two sets of four electrodes each, located above and below the atom cloud, allow the compensation of stray electric fields during Rydberg excitation and also allow the ionization of the Rydberg states by applying large voltages. The ions are guided onto a micro-channel plate (MCP) detector by the corresponding deflection ring (ion flight trajectory visualized by the blue arrow). **b** Stark map of the $39p_{3/2}$ Rydberg state. We take spectra of the Rydberg state for different voltages applied to the compensation electrodes. The color encodes the peak optical density of the remaining atom cloud after a Rydberg excitation pulse as a function of the applied UV Rydberg excitation frequency. If the excitation laser is close to resonance, we observe atom loss out of the optical trap and a reduced peak optical density (bright colors). The required compensation field is extracted as the center position of the resulting loss parabola. **c** Experimental sequence for Rydberg ionization. The laser, coupling the atoms to the Rydberg state, is switched off at the ionization time t_{ion}. At the same time, the high voltages are applied to the electrodes (ionization of the instantaneous Rydberg population) and to the deflection ring (guiding of the ions). **d** Exemplary time traces of the micro-channel plate detector voltage for a single ion (*top*), multiple but time-resolved ions (*center*) and bunched, partially overlapping ions (*bottom - note the change in y-axis scale*).

placed around the atom cloud (green) to cancel stray electric fields. For compensation of horizontal x-y components, we interconnect the lower and upper four electrodes to two pairs each, such that the pairs are rotated by $90°$ around z, and apply a compensation voltage[45] to each pair. For compensation along the vertical axis, we treat all four lower and upper electrodes effectively as a pair of two opposing electrodes. For electric field ionization we rapidly switch the compensation electrodes to high voltages (up to $\pm 2.5\,\mathrm{kV}$) using fast switches[46]. The switching speed being faster than other timescales in our atomic system gives us a measure of the instantaneous Rydberg population. A voltage applied to one of the two deflection rings guides the ions towards the corresponding micro-channel plate (MCP) detector[47], as illustrated by the a blue flight trajectory in Fig. 3.7a.

Electric field nulling

To find the voltages for the electrodes that compensate for external electric fields, we directly use the Stark shift of the DC electric stray field on the $39p_{3/2}$ Rydberg state. Fig. 3.7b shows such a Stark map for one electrode pair, where we take spectra of the Rydberg state for different voltages applied to the compensation electrodes. For this we apply a UV Rydberg excitation pulse onto the trapped atom cloud and determine the peak optical density (color bar) of the remaining atoms via absorption imaging. If the UV frequency matches the transition frequency, atoms are excited to Rydberg states and we observe atom loss and hence low optical densities (bright colors)[48]. By fitting the parabolic loss feature to extract the center position, we can determine the compensation voltage, which is $0.25\,\mathrm{V}$ in this example.

Electric field ionization

Fig. 3.7c illustrates the sequence for Rydberg ion detection. At the end of the Rydberg excitation pulse at time t_{ion}, we switch the electrodes from the small compensation values to the large ionization voltages and also switch on the deflection voltage to one of the rings. After a time of flight of the ions of $3\,\mu\mathrm{s}$[49], the created ions impinge upon the MCP and create voltage spikes, which are recorded on a fast oscilloscope[50]. This allows us to extract the instantaneous Rydberg excitation number in the cloud at time t_{ion}. Fig. 3.7d shows time traces of ion events on the MCP for three different regimes: a single ion (*top panel*), nine, temporally separated ions (*center panel*) and multiple, overlapping ions (*bottom panel*), where it becomes hard to identify individual events. Instead of detecting individual troughs, we usually integrate such traces over a time window around the

---

[45] Omega OM-USB-3103, 8-channel, 16-bit analog voltage, output range $\pm 10\,\mathrm{V}$

[46] Behlke HV switches

[47] Hamamatsu F1551-21S

[48] An alternative way to detect the Rydberg resonance position would be to use the Rydberg field ionization signal.

[49] The exact timings change with the applied ionization and deflection voltages.

[50] TeledyneLeCroy WaveRunner 8254M-MS with up to $4\,\mathrm{GHz}$ bandwidth and $40\,\mathrm{GS/s}$ sampling rate

mean arrival time and use a conversion factor to obtain the corresponding Rydberg atom number.

Conclusion

In this chapter, I presented a versatile setup for studying driven-dissipative systems via Rydberg excitation on a laser-cooled gas of potassium-39 atoms, with fast experimental cycle times of $\sim 2\,\mathrm{s}$, temperatures of $\sim 10\,\mu\mathrm{K}$, abundant optical access and tunable interactions via two versatile Rydberg excitation systems. I especially want to highlight the newly implemented capabilities with respect to the trapping geometries as well as Rydberg detection, which will be an important features in enabling the experimental studies on complex systems dynamics presented in the following chapters. For example, self-organized criticality in chapter 4 will be studied in the dipole trap, whereas the Rydberg excitation growth experiments (cf. chapter 5) will be preformed in the pancake trap, and the new optical tweezer capabilities motivated the studies on a possible quantum cellular automata implementation (chapter 6). Likewise, the Rydberg detection setup allows for the confirmation of self-organized criticality via power-law distributed excitation avalanches (see chapter 4) as well as the observation of power-law excitation growth and Griffith effects (see chapter 5).

4

Self-organization towards a critical state with excitation avalanches

Sec. 4.2 and 4.3 are based on the following publication:
[72] **Signatures of self-organized criticality in an ultracold atomic gas**, S. Helmrich, A. Arias, G. Lochead, T. M. Wintermantel, M. Buchhold, S. Diehl, and S. Whitlock, Nature 577, 481-486 (2020)

Sec. 4.4 is based on the following manuscript:
[109] **Hydrodynamic stabilization of self-organized criticality in a driven Rydberg gas**, K. Klocke, T. W. Wintermantel, G. Lochead, S. Whitlock, and M. Buchhold, arXiv:2009.11908 (2020)

After having realized the experimental apparatus which provides a mapping between open complex systems and our ultracold Rydberg gas, the complex non-equilibrium dynamics resulting from the competition between driving, dissipation and interactions is explored in the following chapters. This chapter here is based on the recent discovery of self-organized criticality (SOC) in our system [72][1]. SOC is seen as a way to explain the abundance of complex structures in combination with scale-invariant behavior throughout nature, ranging from noise in electrical circuits [21, 22], activity in neural network [112, 113], the distribution of avalanches [114], earthquakes [115], forest fire [116, 117], disease infections [118] or popularity in social networks [119]. In equilibrium phase transitions, a critical response and scale invariance requires fine-tuning of parameters to the critical point with a vanishing gap. SOC can be understood by adding an additional slow feedback mechanism, such that the critical point becomes an attractor of the dynamics and the dynamical gap converges to zero [116, 120–124]. Still, quantitative experimental verification of the underlying processes remains challenging [125–130].

This chapter starts in section 4.1 with simple exploratory numerical studies to better understand the mechanisms behind SOC. Subsequently, experimental studies to confirm three key signatures of SOC in our system are conducted (cf. Sec. 4.2, see also Ref. [72, 81, 82]). First, we will recap on the measurements using the remaining atom number as an observable, where we are able to observe two signatures of self-organized criticality

---

[1] Recently, similar effects have also been observed for Rydberg excitation in a room-temperature vapor cell [110] and in cold molecular plasmas [111].

(SOC): (i) self-organization to a stationary state with constant atom density and (ii) scale invariance of spatio-temporal correlation functions, specifically of the stationary state density as a function of the driving intensity. Afterwards, we focus on what is probably the most striking signature of SOC: (iii) a critical response to small perturbations, requiring the direct observation of the active density. This was made possible by the newly implemented Rydberg ion detection scheme (see Sec. 3.5), which we upgraded after moving and rebuilding the experiment from Heidelberg to Strasbourg. The observed avalanches show large fluctuations, which can be well described by a power-law distribution (cf. Sec. 4.3). While further investigating the effects of the inhomogeneous atom distribution in the dipole trap in Sec. 4.4, we unravel a mechanism that stabilizes the system around the critical point. In Sec. 4.5, a controlled effective reloading mechanism is implemented into our experiment and used to probe the avalanche size statistics close to the critical point, slightly below in the subcritical phase and slightly above in the supercritical phase.

4.1 An intuitive rate equation model

In the section, the mechanisms behind self-organization to a threshold value and self-organization to a critical state will be explored by solving a simple global rate equation toy model assuming a homogeneous system (cf. Sec.2.4).

Self-organization

Let us assume particle conservation with $b = 0$, such that the following two processes remain, where each individual can be either in the ground state $|g\rangle$ (blue disks) or excited state $|r\rangle$ (red disks) with corresponding densities n and ρ (see Fig. 4.1a):

1. Facilitated excitation with rate κ: a two-body excitation rate, which is nonlinear in the density and where a particle fulfilling the facilitation condition (cf. Sec. 2.3) can be excited conditional on existing excited states (energy intake)[2]

$$|rg\rangle \xrightarrow{\kappa} |rr\rangle \,. \tag{4.1}$$

2. Decay with rate Γ: a single-body decay rate from the excited state back down to the ground state (energy dissipation)

$$|r\rangle \xrightarrow{\Gamma} |g\rangle \,. \tag{4.2}$$

---

[2] As the states $|rg\rangle$ and $|gr\rangle$ are degenerate, for simplicity we take $|rg\rangle$ as a notation representing both states.

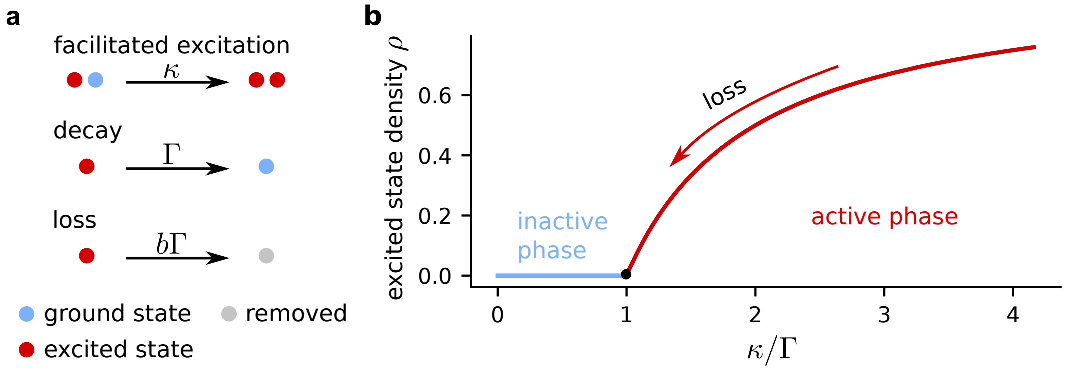

Fig. 4.1: **Absorbing state phase transition underlying self-organization to a critical state.** **a** Three underlying processes: branching or facilitated excitation with rate κ is a two-body processes, where a ground state individuals (blue disk) neighboring an already excited individuals (red disk) is also excited with rate κ. Decay brings excited state back to the ground state with rate Γ. Alternatively, excited individuals are lost out of the system (gray disk) with rate $b\Gamma$. **b** Calculated excited state density ρ as a function of the competition between facilitated excitation and decay κ/Γ. An absorbing state phase diagram emerges from these simple rules, where a critical point (black dot) separates the inactive, absorbing phase with zero excitation density $\rho = 0$ and an active phase with non-zero active density $\rho > 0$. In calculating the steady-state solution of ρ for different ratios of κ/Γ, the loss mechanism was neglected ($b = 0$, i.e. particle conservation). Additional particle dissipation ($b \neq 0$) drives the system from the active phase towards the critical point, due to a reduction of the ground state density n available for facilitated excitation.

To solve for the time dynamics, we rewrite this in terms of two differential equations[3]

$$\begin{aligned}\dot{n} &= -\kappa n\rho + \Gamma\rho \\ \dot{\rho} &= +\kappa n\rho - \Gamma\rho.\end{aligned} \tag{4.3}$$

The solution for a steady state $\dot{n} = \dot{\rho} = 0$ allows for two solutions

1. $\rho = 0$ and $n \geq 0$, which corresponds to the inactive phase, or
2. $n = n_{\mathrm{ss}} = \Gamma/\kappa$ and $\rho > 0$. If we start at $n > n_{\mathrm{ss}}$ ($n < n_{\mathrm{ss}}$), we will observe decay (growth) of n with simulation time t, until the system reaches n_{ss}.

Fig. 4.1b shows the steady-state excited density ρ_{ss} as a function of the ratio between facilitated excitation and decay κ/Γ obtained from numerically solving for the steady state for the differential equations above (Eq. 4.3), starting with a non-zero initial excited density $\rho_0 \neq 0$. We observe an inactive phase with $\rho = 0$ and an active phase with $\rho > 0$, separated by the critical point (black circle). The critical point of the absorbing state phase transition is expected where these two solutions coincide, i.e. $n = n_{\mathrm{ss}} = \Gamma/\kappa$

---

[3] Note that these differential equations are equivalent to the susceptible-infected-susceptible (SIS) model, a compartmental model in epidemiology. The corresponding mappings are $n \rightarrow$ S (susceptible), $\rho \rightarrow$ I (infected), $\kappa \rightarrow \beta$ (spreading) and $\Gamma \rightarrow \gamma$ (recovery).

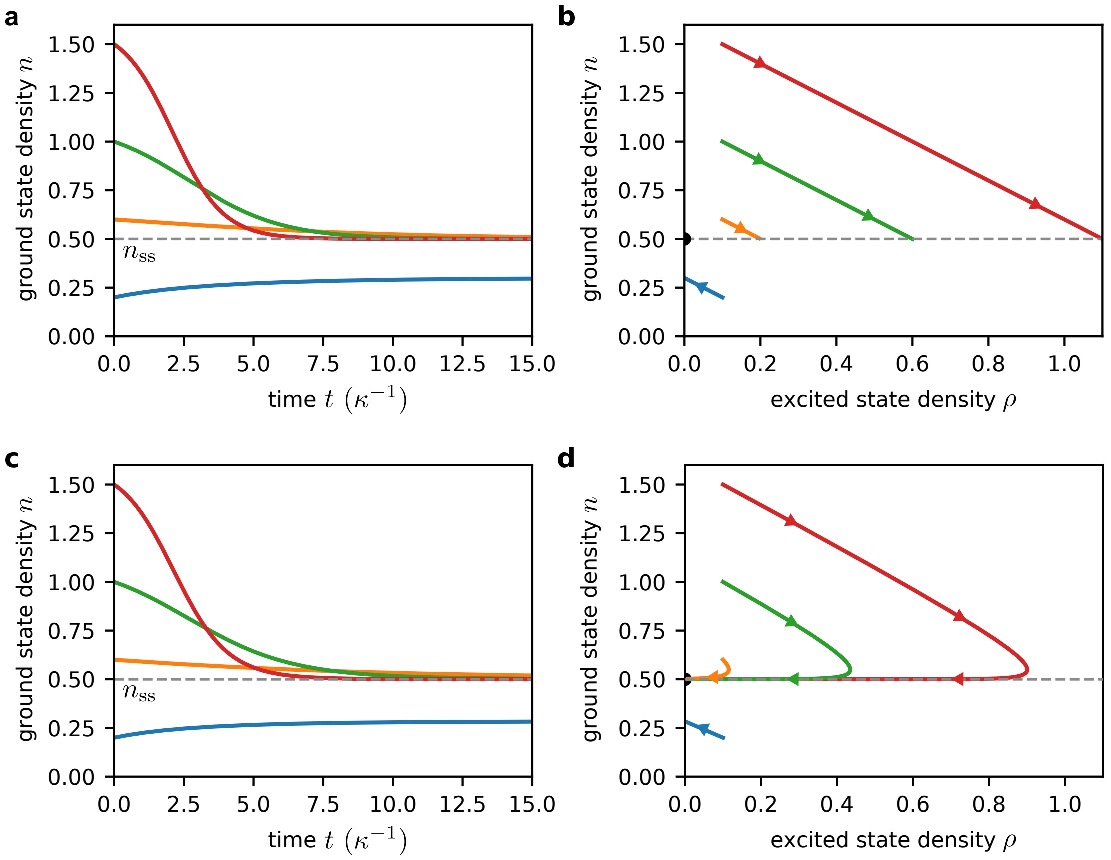

Fig. 4.2: **Self-organization with and without criticality.** **a** Ground state density n as a function of simulation time t for a ratio of facilitation and decay of $\kappa/\Gamma = 2$ and with four different initial ground state densities (color coded in increasing order in blue, orange, green and red, see text for more details). These particle conserving trajectories that initially start above the value for the steady-state solution n_{ss} (dashed gray line) organize towards the threshold value at late times. **b** Same trajectories where the ground state density n is plotted against the corresponding excited state density ρ. We observe a redistribution of population between the states to reach n_{ss}. The color code is consistent with subfigure a and the arrows indicate the flow direction over time. **c** Ground state density n as a function of simulation time t additionally including loss $b\Gamma$. Again, we simulate four different trajectories (color coded in blue, orange, green and red) which vary only in the initial density n. The ones that initially start above the (dashed gray line) organize towards the threshold value n_{ss} at late times. See text for more details. **d** Same trajectories where the ground state density n is plotted against the corresponding excited state density ρ. Due to non-conservation of particles, all curves that initially start above n_{ss} organize towards the critical point (black circle). The color code is consistent with subfigure c and the arrows indicate the flow direction over time.

and $\rho_{\mathrm{ss}} = 0$. Note that as we neglect the loss process ($b = 0$), the particle number is conserved $n + \rho = \mathrm{const.}$ and we can infer n from ρ.[4]

Now we will look at the time dynamics of the ground state density n for four exemplary different initial conditions (Fig. 4.2a). We set $\Gamma = \kappa/2$ and use time units of κ^{-1}. We take a constant $\rho = .1$ and only vary the initial density n to $0.2, 0.6, 1.$ and 1.5 (color coded in blue, orange, green and red, respectively). The curves starting above the steady-state density $n_{\mathrm{ss}} = 0.5$ (dashed gray line) all decay towards n_{ss} as a function of time. Only the one starting below (blue) does not reach n_{ss}. Fig. 4.2b presents the same trajectories with the ground state density n as a function of the excitation density ρ, where we indicate the flow of time with arrows. As the particle number is conserved, we only observe diagonal trajectories in this plot. Although n self-organizes, the system does not self-organize to a critical state, as generally $\rho_{\mathrm{ss}} > 0$. In the next paragraph we will investigate how to self-organize to the critical point instead.

Self-organized criticality

Now we introduce a slow loss mechanism (particle dissipation) into the system with rate $b\Gamma$, where $b \ll 1$. This add the following third rate to the previous two:

3. Particle loss with rate $b\Gamma$: a single-body loss of excited individuals out of the system to a removed state $|l\rangle$ with density λ (particle dissipation)

$$|r\rangle \overset{b\Gamma}{\to} |l\rangle \,. \tag{4.4}$$

To solve for the time dynamics, we rewrite this in terms of differential equations[5]

$$\begin{aligned} \dot{n} &= -\kappa n\rho + \Gamma\rho \\ \dot{\rho} &= +\kappa n\rho - \Gamma\rho - b\Gamma\rho \\ \dot{\lambda} &= b\Gamma\rho. \end{aligned} \tag{4.5}$$

The steady state of the system ($\dot{n} = \dot{\rho} = \dot{\lambda} = 0$) now has a single solution

1. $\rho = 0$ and $n \geq 0$.

We observe very similar behavior in the time evolution of the ground-state density n compared to the previous model with $b = 0$ (Fig. 4.2c). For better comparison, we used the same parameter values of $\Gamma = \kappa/2$, a constant $\rho = 0.1$ and only vary the initial density n as $0.2, 0.6, 1.0$ and 1.5 (same color coding in blue, orange, green and red,

---

[4] In this specific simulation, we normalized the total density to 1, such that we can infer the ground state density as $n_{\mathrm{ss}} = 1 - \rho_{\mathrm{ss}}$.

[5] Note that these differential equations are similar to the susceptible-infected-removed (SIR) model, a compartmental model in epidemiology. The corresponding mappings is $n \to \mathrm{S}$ (susceptible), $\rho \to \mathrm{I}$ (infected) and $\lambda \to \mathrm{R}$ (removed/immune).

respectively), where now $b = 0.1$. However, the active density ρ in Fig. 4.2d, where the arrows indicate the flow direction over time, shows a modified behavior. While it initially follows the diagonal as before, the extra loss mechanism breaking the conservation of $n + \rho$ allows deviation from it and make the trajectories which start above n_{ss} bend towards the critical point, i.e. it shows self-organized criticality.

Note that the used model is a simple rate equation ansatz to gain intuition about the system in terms of the global density evolution, however it does not capture essential parts of the SOC dynamics like the power-law distributed excitation avalanches. It assumes a completely homogeneous system with all to all connections. In our experiments however, we deal with a heterogeneous system, where the exact spatial coordinates in combination with facilitation constraints make it a much more complicated and rich system. In the following sections we will experimentally observe and verify similar self-organization behavior in our ultracold driven-dissipative Rydberg gas.

4.2 Self-organization and scale invariance in bulk observables

The experiments are performed with $\sim 10^5$ ground state potassium-39 atoms trapped in the non-interfering optical dimple trap (see Sec. 3.3.1). The ultra-violet (UV) Rydberg excitation laser uniformly illuminates the atom cloud, which couples the ground state $|g\rangle = |4s_{1/2}, F{=}1\rangle$ (blue spheres) to the Rydberg state $|r\rangle = |39p_{3/2}\rangle$ (red spheres) with a single-atom Rabi frequency $\Omega/2\pi = 190\,\mathrm{kHz}$ and detuning $\Delta/2\pi = 30\,\mathrm{MHz}$ (see Fig. 4.3a). The decay of single Rydberg atoms with rate Γ brings the atoms back to the ground state, or these atoms get lost out of the system in this process, indicated by the auxiliary removed state $|l\rangle$ (gray spheres). We will see that this loss out of the system dominates over the other process in our experiments. Since the Rydberg excitation is off-resonant, this can lead in combination with the Rydberg-Rydberg interaction to a facilitated excitation condition [68, 69], as illustrated for a pair state (cf. Sec. 2.3). If there are no Rydberg excitations, the off-resonant excitation rate is small in the chosen limit of $\Omega \ll \Delta$ [46, 68, 69, 131–140]. However, once there is one Rydberg excitation, neighboring ground state atoms fulfilling the facilitation condition, where the Rydberg-Rydberg interaction energy V compensates the detuning Δ, can get resonantly excited (facilitated excitation). For modeling the system dynamics, we coarse grain the system into regions corresponding to the facilitation volume, where typically ~ 10 atoms fall into these volumes. This leads to effective rates over the coarse graining volume in the effective Langevin equation (cf. Sec.2.4 and Ref. [72] for more details) for the off-resonant excitation rate τ, the facilitated excitation rate κ and the atom loss rate

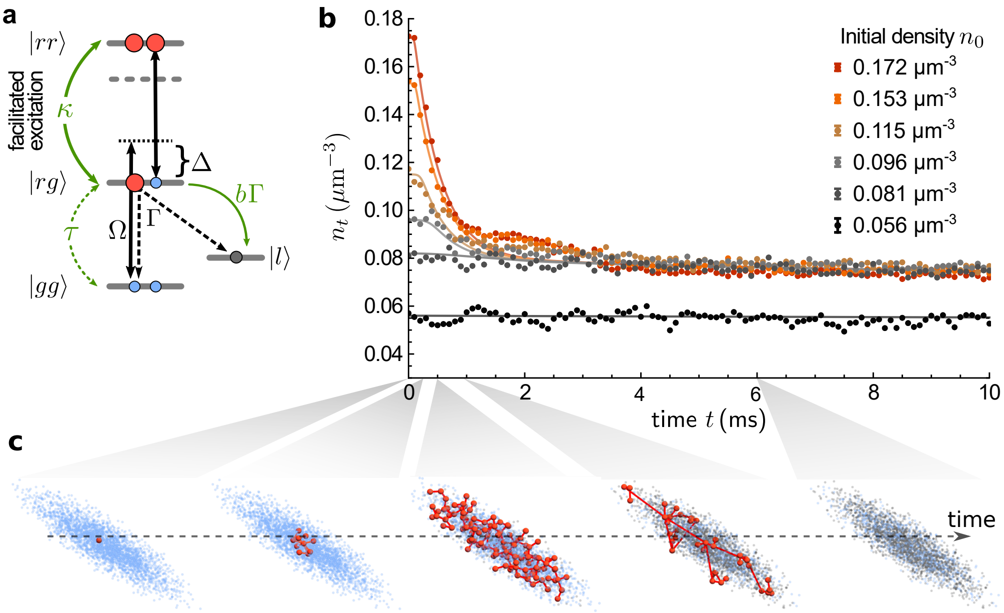

Fig. 4.3: Self-organization of the atom density in an ultracold gas excited to Rydberg states. **a** Relevant atomic level structure. The ground state $|g\rangle$ (blue sphere) is coupled to the Rydberg state $|r\rangle$ (red sphere) with Rabi frequency Ω and detuning Δ. From there, the Rydberg state $|r\rangle$ can either decay with rate Γ or facilitate the resonant excitation of neighboring Rydberg states, when the detuning Δ is compensated by the Rydberg-Rydberg interaction energy. Decay out of the system to removed states $|l\rangle$ provides a feedback mechanism for self-organization to a critical state. **b** Measured density of potassium atoms in the optical dipole trap as a function of the Rydberg excitation time for different initial intensities. After a very short initial plateau, the density falls quickly, reaching the stationary density $n_\mathrm{f} \approx 0.075\,\mu\mathrm{m}^{-3}$ within $\leq 4\,\mathrm{ms}$. Qualitatively similar behavior is observed for all densities which start above n_f. If the initial atom density is already below this value, the density stays constant during the observed Rydberg excitation timescale of up to $10\,\mathrm{ms}$ (black dots). Each data point is the average over three measurements. The solid lines are obtained from mean-field solutions to the effective Langevin equation. **c** Sketch of the self-organization process in a cigar-shaped optical trap. Starting from an initial seed in the Rydberg state (active density, red sphere), the facilitated excitation of ground state atoms leads to a fast growth of the excitations and to the build-up of correlations (red links). At the same time, the decay to removed states reduces the atom density, which in turn lowers the facilitation rate. Once the facilitation rate falls below a critical value, the previously active system enters an inactive phase. Adapted from [72].

$b\Gamma$, as indicated by green arrows. This loss mechanism provides the feedback from the active phase towards the critical point. SOC requires the following hierarchy scale for the individual processes: the facilitation $n_0\kappa$ with initial density n_0 and decay Γ have to be of about the same magnitude, separated from a slower feedback mechanism $b\Gamma$ and an even slower spontaneous excitation rate τ: $n_0\kappa \approx \Gamma \gg b\Gamma \gg \tau$ [72].

Self-organization to a stationary state
Fig. 4.3b displays the remaining atom density n_t in the optical trap, determined via absorption imaging from the side (Sec. 3.1, after applying the UV laser for a time t. Such time traces are measured for different initial densities n_0 at $t = 0$. For the time traces starting at an initial density $> 0.081\,\mu\mathrm{m}^{-3}$, we observe a short initial plateau followed by a fast decay. After a Rydberg excitation time $t \gtrsim 4\,\mathrm{ms}$, the initial fast decay reaches a final density $n_\mathrm{f} = 0.075\,\mu\mathrm{m}^{-3}$, which is stationary on the observed time scale. It is striking, that this final density n_f is independent of the initial density n_0, except where the initial density is already lower than the steady-state density $n_0 < n_\mathrm{f}$. The solid lines are obtained from mean-field solutions to the effective Langevin equation.

Remembering the microscopic processes governing the system, as depicted in Fig. 4.3a, we can qualitatively understand this behavior, as sketched in Fig. 4.3c. Due to the large detuning of the Rydberg excitation laser, the off-resonant seed rate τ is small. Once there is at least one Rydberg atom in the active phase of the system, neighboring atoms can be quickly excited, leading to fast growing excitation clusters. While this growth can reach up to the system size, the decay of Rydberg excitation out of the system (feedback mechanism $b\Gamma$) reduces the atom density and self-tunes the system towards the inactive phase. With reducing density, the number of available ground state atoms is reduced and the facilitation rate is reduced. This reasoning explains the mechanism behind the self-organization to a stationary state with constant atom density, which constitutes the SOC signature (i), as listed in the introduction of this chapter.

Scale-invariance of the stationary density
Signature (ii) concerns the scale invariance of spatio-temporal correlation functions. Here, we will specifically look at the stationary state density as a function of the driving intensity for different initial atom densities n_0 (color coded), presented in Fig. 4.4a. For this we measure the final stationary density n_f after an evolution of $t = 10\,\mathrm{ms}$ for varying UV excitation laser intensity. This time was chosen as here the system has reached the final density n_f. For low driving intensity, the system is in the inactive, absorbing phase, hence the density remains unchanged $n_0 \approx n_\mathrm{f}$. Once the driving intensity is increased, and with it the facilitated excitation rate $\kappa \propto \Omega^2$, the system crosses the critical point into the active phase, where the SOC mechanism drives the system back to a self-organized stationary state with a lower final density n_f. As the total facilitation rate depends on the density of available ground state atoms and the laser driving, the measurements

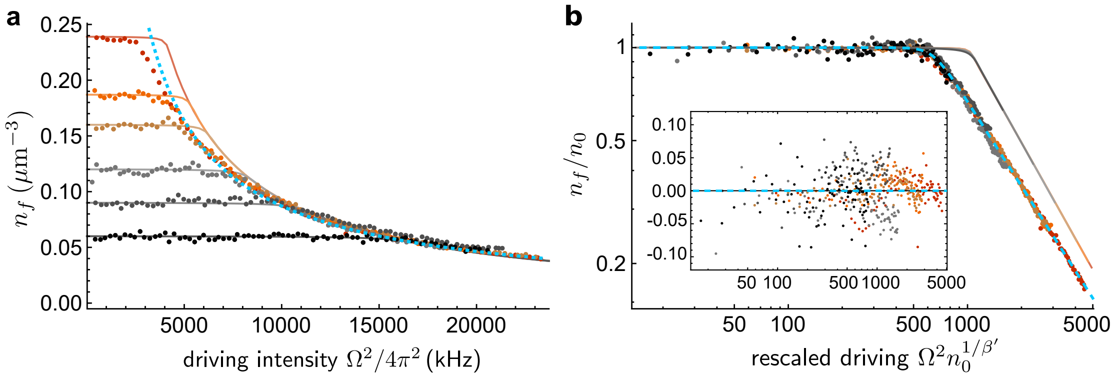

Fig. 4.4: Rescaling of the atom density of the self-organized state as a function of the driving intensity. a Stationary-state density n_f measured after $10\,\mathrm{ms}$ Rydberg excitation as a function of the Rydberg excitation intensity for different initial densities n_0 (see color coding). For large Ω^2 and n_0, all points collapse onto one single power-law curve $n_\mathrm{f} \sim \Omega^{-2\beta}$ (dotted blue line). **b** The same data showing a full data collapse onto a unique scaling function (fit shown as dashed blue line) by rescaling both axis. The inset shows the normalized residuals between rescaled data and fitted scaling function. The solid lines in subfigures a, b are obtained from mean-field solutions of the Langevin equation. Each data point is the mean of five measurements. Adapted from [72].

with higher initial densities cross into the active phase at lower driving intensities. The experimental data with $n_\mathrm{f} < n_0$ falls onto a single curve, which resembles a power law, indicated by the dotted blue line in Fig. 4.4a.

To investigate this scale invariance more quantitatively, we test if we can rescale all of the data onto a universal curve with a clear critical threshold, which would provide strong evidence on the existence of the corresponding scale invariance in our system. For this, we apply the scaling ansatz [124] $n_\mathrm{f} = n_0 f(\Omega^2 n_0^{1/\beta'})$ and replot n_f/n_0 as a function of the rescaled variable $\Omega^2\, n_0^{1/\beta'}$ on a double-logarithmic scale in Fig. 4.4b. We find the best data collapse onto a single universal curve for $\beta' = 0.869(6)$. The scaling function can be well modeled by

$$f(x) = x_c^\beta (x^{\nu\beta} + x_c^{\nu\beta})^{-1/\nu}, \tag{4.6}$$

where x_c and ν parameterize the position and sharpness between inactive and active phase, respectively. The power-law scaling ansatz for the final density n_f for $x \gg x_c$ is given by $n_f \propto \Omega^{-2\beta} n_0^{1-\beta/\beta'}$. Fitting the rescaled data in double-logarithmic scale yields the dashed blue line, with $\beta = 0.910(4)$, $\nu = 10.6(8)$ and $x_c = 641(3)\,\mathrm{kHz}^2\mu\mathrm{m}^{-3/\beta'}$, where the parenthesis indicate the standard deviation of the fitted parameters from bootstrap resampling. The evenly symmetric scatter of the normalized fit residuals in the inset of Fig. 4.4b confirm the usefulness of this function in describing the data from the absorbing across to the active phase.

The solid lines are mean-field solutions from the Langevin equation (see Eq. 2.20), which show qualitatively the same features, but differs in the expected driving threshold as well as the power-law exponent [72].

4.3 Critical response in terms of power-law distributed excitation avalanches

For the first two signatures of SOC, we considered the remaining atom density in the trap as observable. With the new Rydberg atom detection capabilities (see. Sec. 3.5), we can finally turn to investigate the active density directly.

As before, the experiments start with the atom cloud in the optical dipole trap onto which the UV excitation laser is applied for a time t. For detection purposes, we now address the Rydberg state $|r\rangle = |66p_{3/2}\rangle$, but the other experimental conditions and parameters remain similar as in previous experiments. At the end of the UV pulse, the existing Rydberg atoms are ionized by quickly switching on a large electric field. The created ions are guided towards a MCP detector. Subsequently, an absorption image is taken to again extract the remaining atom density. This means that we get access to both the ground state atom density as well as a direct measure of the active (Rydberg) density.

The remaining trapped atom density after a Rydberg excitation of length t in Fig. 4.5a exhibits qualitatively the same behavior as previously. The observed slower time scale can be attributed to the longer lifetime and larger C_6 coefficient of the newly selected Rydberg state. Each of the 200 data points corresponds to an individual experimental run, where besides the density we also display the Rydberg atom number, cf. Fig. 4.5b. We observe a fast initial increase of the excitation number within $t \lesssim 2\,\mathrm{ms}$, where the detector is saturated from $2-5\,\mathrm{ms}$. Simultaneously, the atom density is strongly reduced due to the large active density fraction. After $10\,\mathrm{ms}$, the density has evolved close to its stationary state on the observed timescale of $40\,\mathrm{ms}$[6]. At the same time, we observe strong fluctuations of up to 800 Rydberg excitations from $10\,\mathrm{ms}$ on, which we attribute to the critical response of the system close the critical point with a small dynamical gap due to the presence of seed excitations in the form of avalanches with a broad distribution in time and size. The dashed lines again show the mean-field solution to the Langevin equation, describing the atom number well but lacking completely the critical response in the form of avalanches.

---

[6] There are additional slower loss processes present, which will become apparent for longer observation times, like off-resonant Rydberg excitation, heating in the optical trap or collisions with background atoms, but are not important on our experimental timescales.

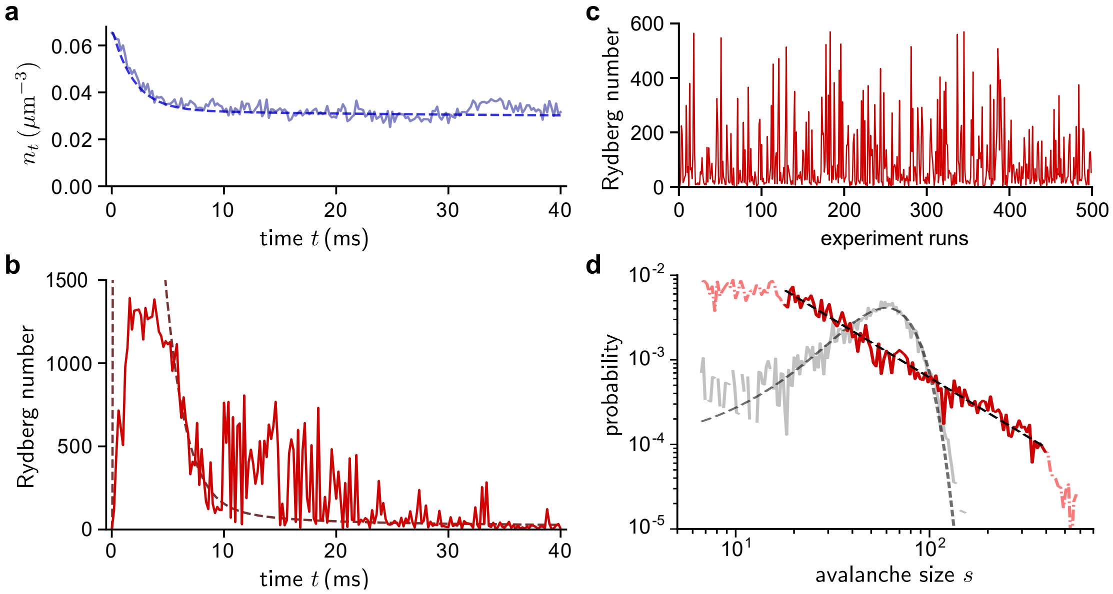

Fig. 4.5: Power-law distributed avalanche size in the SOC dynamics. **a** Evolution of the remaining atom density in the dipole trap after a Rydberg excitation time t. **b** Simultaneously measured number of Rydberg atoms in the atom cloud. Large fluctuations are visible in this measurement of the active component for $\geq 10\,\mathrm{ms}$. The shown data corresponds to 200 individual experimental realizations. The dashed lines in subfigures a, b are mean-field predictions, where the effective volume of the atom cloud was adjusted for optimal agreement. **c** Exemplary 500 out of the, in total, 3630 individual experimental measurements of the Rydberg atom number at $t = 25\,\mathrm{ms}$. Note the strong fluctuations in the excitation number. **d** Corresponding probability distribution of the avalanche size s. The instantaneous Rydberg excitation number at $t = 25\,\mathrm{ms}$ is repeatedly measured for 3630 experimental runs. After logarithmic binning, the data (red line) is truncated to a linear part in log-log space (highlighed by the solid red line). A maximum-likelihood estimation yields a power-law exponent of $\alpha = 1.37(2)$, depicted as the black dashed line. The gray data corresponds to a control measurement, where we excite on resonance with a short laser pulse, but otherwise leave the experimental sequence unchanged. This measurement does not exhibit a power-law distribution, but rather a stretched Poissonian distribution (fit shown as gray dashed line). Adapted from [72].

We conduct 3630 individual measurements of the Rydberg excitation number at $t = 25\,\mathrm{ms}$, where we see large fluctuations of the excitation number (For better visibility, only 500 exemplary subsequent runs are shown in Fig. 4.5c). To investigate the corresponding probability distribution more closely we replot the data as a probability distribution function (red line) with logarithmic bins in Fig. 4.5d. In the window from $20 \leq s \leq 400$, corresponding to 2450 measurements, we visually observe good agreement with linear behavior in this log-log scale, corresponding to power-law behavior over 1.5 orders of magnitude. The upper cut-off around $s \gtrsim 500$ is given by the finite system size and/or the detector saturation, whereas the lower plateau $s \lesssim 20$ is caused by the detection noise floor. A maximum likelihood estimator yields a power-law exponent of $\alpha = -1.37(2)$ (black dashed line), with the standard deviation in parenthesis estimated by bootstrap resampling (see Sec.4.5). This exponent agrees with exponents for other system which have been conjectured to show SOC [117, 141, 142], but experimental imperfections could affect the apparent critical properties [129] and more in-detailed studies are necessary to confirm that exact scaling exponent. The gray line corresponds to a control measurement using $1\,\mu\mathrm{s}$ long, on resonance UV pulses, showing the expected stretched Poissonian distribution (dashed line) instead of a power-law distribution, as evidence that the power-law behavior is not due to the detector or other parasitic effects in our experimental setup.

In summary, we observed power-law distributed excitation avalanches (signature (iii)) in the SOC dynamics of our driven-dissipative Rydberg system. Therefore, we demonstrated all three criteria for SOC, giving strong evidence that our system can be used as a testbed for SOC dynamics. However it is an interesting open question, how close one can experimentally reach the self-organized critical state. Theoretically one needs infinite separation of time scales in the absence of fluctuations and noise to reach the true critical state. It will be elaborated more on this question in the remaining sections of this chapter.

4.4 Motional stabilization around the self-organized critical state

The observation of the three signatures of self-organized criticality (SOC) in the previous two sections raises interesting questions on the effect of experimental imperfections, such as finite separation of timescales, experimental noise or inhomogeneous atom density. Already a finite experimental time should hinder reaching the true critical point due to diverging length and timescales [129]. This has led to so called self-organized quasi criticality, where the system stays close to the critical point, with excursions into the subcritical and supercritical regions [129, 143].

Here, the effect of the inhomogeneous Gaussian density distribution induced by the trapping potential will be investigated by looking at absorption images at different times through the dynamics towards the SOC state. This leads us to unravel an interesting mechanism stabilizing the SOC state in our experiment.

While we will focus here on the experimental part of this study, more details on the corresponding theory results can be found in the manuscript in Ref. [109]. Here, a hydrodynamic Langevin equation was developed to include the thermal atom motion during the SOC dynamics. The resulting numerical simulations show very good agreement with the experimental observations and support the claim of stabilization of the SOC state in our system by motional atom rearrangement in the trap potential.

Ideal SOC dynamics
First of all, we consider the ideal case with a perfectly large separation of timescales between facilitation rate κ (drive), density n, Rydberg decay rate Γ, feedback mechanism (loss) $b\Gamma$ which brings the system towards the SOC state, and the spontaneous (off-resonant) excitation rate τ: $\kappa n \approx \Gamma \gg b\Gamma \gg \tau$.

The dashed blue line in Fig. 4.6b illustrates the expected temporal trajectory of the atom density $n_{\vec{x},t}$ and the active density in the excited state $\rho_{\vec{x},t}$. Starting in the active phase, excitation clusters will quickly grow around seed excitations, leading to a fast increase in excitation number (i). As the feedback mechanism has a lower rate, the density decreases towards the critical density n_c on a slower timescale (ii), and the system very slowly approaches the critical point (iii, orange cross), where $n_{\vec{x},t} = n_\mathrm{c}$ and $\rho_{\vec{x},t} = 0$. Theoretically, it requires an infinite time to reach the critical point due to diverging length and timescales and it should be impossible to experimentally observe ideal SOC [129].

Dynamics towards the SOC state in an inhomogeneous density distribution
If we turn to our experimental system, we notice some of imperfections regarding the ideal SOC conditions. The separation of timescales between feedback and off-resonant seed excitation has a finite value. Furthermore, we deal with an inhomogeneous atom density distribution, which is well-described by a Gaussian distribution for a thermal atom cloud, shown as the black line in Fig. 4.6a. This means usually part of the cloud starts in the supercritical phase whereas some parts, mainly the wings, are subcritical. The growth of Rydberg excitations (i) in the supercritical phase leads to a loss of atoms out of the trap (ii-a) and hence a reduction in atom density (Fig. 4.6a,b). Due to the finite separation of timescales, the system is expected to overshoot below the critical density n_c (dotted orange) and the dynamics will stop in the subcritical regions, i.e. below the critical density. At the same time, the atom motion in the trapping potential provides a

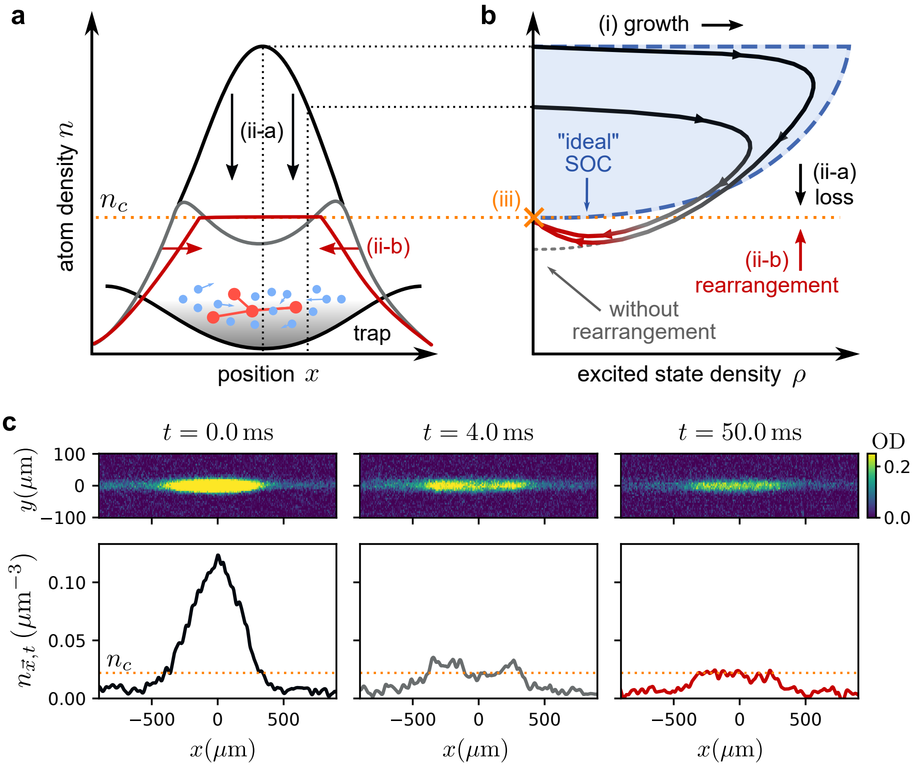

Fig. 4.6: Stabilization of the self-organized critical state induced by the trapping potential. **a** Evolution of the ground state density n and **b** excited state density ρ in the optical dipole trap during off-resonant excitation of ground state atoms (blue disks) to a Rydberg state (red disks). Initially, the Rydberg excitation number grows quickly due to avalanches triggered from single seed excitations (i). The corresponding atom loss (ii-a) causes the Gaussian density profile (black line) to drop. In the ideal SOC case (dashed blue line), the dynamics would stop right at the critical point (orange cross) with critical density n_c and $\rho = 0$. In the case of finite time and experimental imperfections, the loss is expected to overshoot below n_c (gray density profile, the overshoot below n_c is exaggerated for clearer illustrative purposes). The rearrangement mechanism provided by the trap potential effectively refills the trap center from the flanks. This counteracts the loss in the central region and drives the system back towards the critical density, resulting in a flat-top extended critical region (red density profile). The arrows indicate the flow direction over time. **c** Absorption images (*top*) and three-dimensional atom density cross-sections through the center of the cloud (*bottom*) after three exemplary Rydberg excitation times t. The experimentally observed behavior is quite similar to the model described above. Initially at $t = 0\,\mathrm{ms}$, the atom distribution follows a Gaussian profile as expected for a thermal cloud in a near-harmonic trap potential. Fast atom loss leads to a dip in the cloud center where the density was initially highest ($t = 4\,\mathrm{ms}$). For longer times $t = 50\,\mathrm{ms}$, we observe a flat-top profile at a density that we attribute to the critical density n_c. The three-dimensional ground state density profiles were obtained via an inverse Abel transformation of the absorption images. Adapted from [109].

rearrangement mechanism of the atoms towards the center (ii-b). This counteracts the loss in the center by increasing the density once more and keeping the system around the critical point (iii) for an extended time and over an extended region over the trap center (flat-top). We will see that this refilling rate is slow compared to the loss rate, but fast compared to off-resonant seeding rate τ (see measurement of the redistribution timescale below).

Experimental approach

The experimental sequence is similar to Sec. 4.2 and 4.3. The experiments start with an ultracold gas of $N \approx 10^5$ potassium-39 atoms in an cigar-shaped optical trap. After evaporating down the trap power by approximately a factor of ten, the final temperature is $\sim 10\,\mu\mathrm{K}$ with trapping frequencies of $\omega_x/2\pi = 60\,\mathrm{Hz}$ and $\omega_{y,z} = 900\,\mathrm{Hz}$ in the weak and tight axes, respectively. The corresponding widths of the Gaussian atom distribution ($e^{-1/2}$) are $\sigma_x = 200\,\mu\mathrm{m}$ and $\sigma_{y,z} = 10\,\mu\mathrm{m}$ again for the weak and tight axes.

At time $t = 0\,\mathrm{ms}$, we couple the ground state $|g\rangle = |4s_{1/2}, F = 1\rangle$ to the Rydberg state $|r\rangle = |66p_{3/2}\rangle$ with a detuning of $\Delta/2\pi = 30\,\mathrm{MHz}$. To strongly suppress single-particle excitations, we operate in the regime $\Omega \ll \Delta$ [46, 68, 69, 131–140]. The facilitation radius is at a distance of $R_{\mathrm{fac}} = 4.5\,\mu\mathrm{m}$ (cf. Sec. 2.3). Rydberg excitations decay with a calculated rate of $\Gamma/2\pi = 0.84\,\mathrm{kHz}$, which either brings them back to the ground state $|g\rangle$ or into inactive states $|0\rangle$. After a UV Rydberg excitation phase of time t, we measure both the number of Rydberg excitations via field ionization detection (Sec. 3.5) and the ground state atom distribution via absorption imaging from the side (Sec. 3.1).

Exemplary absorption images after different UV laser exposure times t of $0\,\mathrm{ms}$, $4\,\mathrm{ms}$, and $50\,\mathrm{ms}$ are presented in the top row of Fig. 4.6c. There we can already see the qualitatively different regimes described above: the initially Gaussian cloud, a dip in the center of the atom cloud due to fast atom loss and a finally flat-top profile stabilized by the atom reloading from the wings driven by the trap potential. A problem arises in quantitatively comparing the measurements to the model predictions as the dimension along the propagation of the imaging light (x-axis) is integrated out in these two dimensional absorption images. To reconstruct the three-dimensional atom distribution through the center of the cloud, we apply inverse Abel transformations on the absorption images [144–146]. The results are presented in the bottom row in Fig. 4.6c. We observe a high similarity of these density profiles to the ones discussed above (e.g. Fig. 4.6a). Initially at $t = 0\,\mathrm{ms}$, the gas has the approximate Gaussian shape expected for an optically trapped thermal gas, well visible in the central cross-section along the elongated axis. At $t = 4\,\mathrm{ms}$, a dip in the center with initially highest density has developed. For even longer times $t = 50\,\mathrm{ms}$, this dip is filled in and the cloud shows a flat top, which we take as a measure for the critical density n_c.

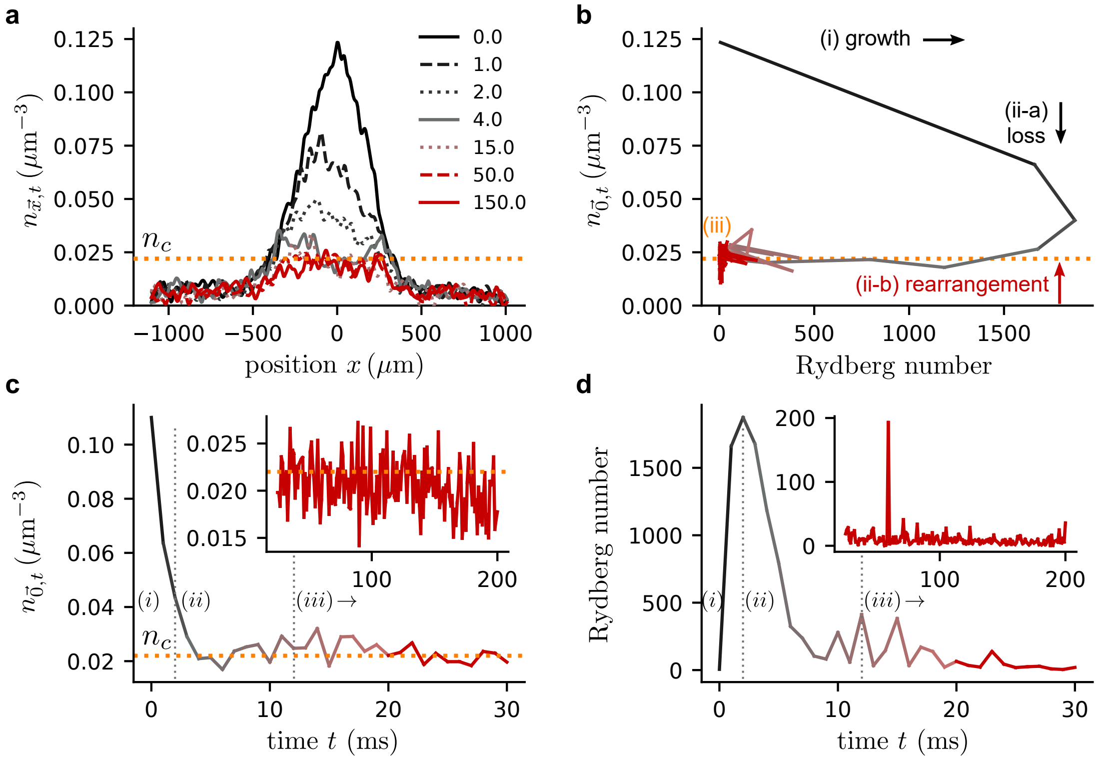

Fig. 4.7: Evolution of the spatial density profile during SOC dynamics in the dipole trap. **a** Atom density $n_{\vec{x},t}$ cross section though the center of the cloud after Rydberg laser exposure times of $0, 1, 2, 4, 15, 50$ and $150\,\mathrm{ms}$ (see labels). Initially at $t = 0\,\mathrm{ms}$ (black line), we observe an approximately Gaussian density profile as expected for the thermal cloud in the dipole trap. Fast loss in the center of the cloud results in a dip after $t = 4\,\mathrm{ms}$ (gray line). For later times, the density profile shows a flat top at the critical density n_c (orange dotted line) while at the same time the width of the cloud reduces. The three-dimensional density was reconstructed using an inverse Abel transformation on absorption images (see text for more details). **b** Atom density in the center of the cloud against the corresponding cloud-integrated Rydberg excitation number during the SOC dynamics up to $200\,\mathrm{ms}$. Initially, we start with a density $n_{\vec{0},t} \approx 0.125\,\mu\mathrm{m}^{-3}$ and zero Rydberg excitations. Subsequently, we observe a growth of the Rydberg number (i) which comes with a reduction in the atom density (ii-a). Around the critical density n_c, we observe overshoots below as well as above due to the rearrangement of atoms in the trapping potential (ii-b). This mechanisms sustains the system close to the critical point (iii) for extended periods. **c** Central atom density as a function of the laser excitation time t. After a fast initial loss, within the first $5\,\mathrm{ms}$, down towards the critical density, we observe an increase in the density due to refilling in the range $10 - 20\,\mathrm{ms}$, before it drops back down again after around $30\,\mathrm{ms}$. At later times, the atom density stays quite constant around n_c from 25 up to $200\,\mathrm{ms}$ (see *inset* with same axes dimensions). **d** Corresponding number of Rydberg excitations in the atom cloud as a function of the laser excitation time t. The excitation number quickly rises within the first $2\,\mathrm{ms}$ before it drops due to the simultaneous reduction in the atom density. This is followed by a range of larger activity fluctuations ($10 - 20\,\mathrm{ms}$) which we attribute to fast refilling of atoms. At later times from $25 - 200\,\mathrm{ms}$, the activity is small, but generally non-zero with fluctuations to higher numbers (see *inset* with same axes dimensions). Note that each time point corresponds to an individual run of the experiment.

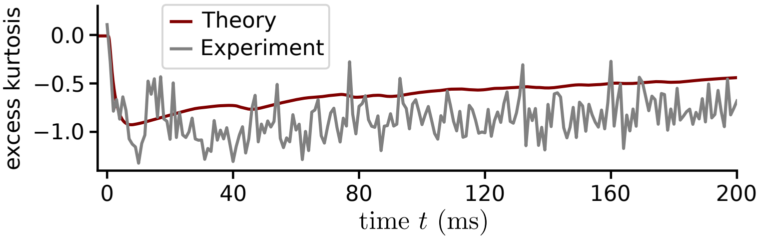

Fig. 4.8: Observation of melting of the flat-top profile via the excess kurtosis. Excess kurtosis of the density profile through the trap center as a function of the exposure time of the excitation laser t. The gray line is obtained from the reconstructed density from the experimental measurements whereas the red line is obtained from the simulated data.

To investigate this more quantitatively, we repeat the experiment for every millisecond from 0 up to $200\,\mathrm{ms}$ UV excitation exposure time t. Fig. 4.7a presents exemplary slices of the atom density distribution though the center of the cloud at $t = 0, 1, 2, 4, 15, 50, 150\,\mathrm{ms}$. Here we can observe in finer detail how the Gaussian distribution develops a dip in the center with ongoing excitation time t and how atom rearrangement leads to a flat-top profile and shrinking width at late times. We take the height of this plateau as a measure for the critical density n_c. As we measure both density distribution and the Rydberg excitation number, we can plot the atom density in the center of the trap against the corresponding Rydberg number in the cloud to get the relation between the active and ground state density during the SOC dynamics (see Fig. 4.7b[7]). At $t = 0\,\mathrm{ms}$ laser exposure time, the atom density in the center of the trap is about $n_{\vec{0},0} = 0.125\,\mu\mathrm{m}^{-3}$ with zero Rydberg excitations. As our laser parameters are tuned such that we are in the active phase, facilitated excitation outweighs the decay of Rydberg atoms we observe growing excitation number (i) within the first $2\,\mathrm{ms}$. This is visible in Fig. 4.7d, where the Rydberg number is plotted against time t. On a similar timescale we observe fast loss of atoms out of the trap (ii-a) within the first $5\,\mathrm{ms}$, as visible in Fig. 4.7c, showing the central atom density as a function of time t. In the range of $10 - 20\,\mathrm{ms}$, the density increases again which is a sign of refilling towards the trap center. This coincides with increased excitation values and fluctuations thereof. At around $30\,\mathrm{ms}$, the atom density in the center of the trap stays constant around a value of 0.022, which we take as a measure of the critical density n_c. For even later times, the density still stays quite constant around n_c (see Fig. 4.7c inset), but the activity has not died out. Instead, a largely fluctuating, non-zero excitation number consistent with excitation avalanches is seen, indicating that the system has not entered the inactive phase yet, but stays around the critical point (see Fig. 4.7d inset). Although atoms are lost due to the avalanches, these are relatively small (~ 10) compared to the amount of ground state atoms in the cloud ($\gtrsim 1000$) and so no loss is visible in the atom density.

---

[7] Note that this analysis is not directly comparable to Fig. 4.6b, as the experimental access is limited to the integrated Rydberg number throughout the cloud.

Observing the melting of the flat-top profile

To quantify the time evolution of the density, and how it differs from the underlying Gaussian distribution, we use the excess kurtosis EK. The excess kurtosis is related to the kurtosis Kurt via

$$\mathrm{EK}(t) = \mathrm{Kurt}(t) - 3 = \int \left(\frac{x-\mu}{\sigma_x} \right)^4 n(\vec{x}, t)\, dx = \frac{\mu_4}{\sigma_x^4} - 3 \tag{4.7}$$

with the standard deviation σ_x, the mean μ and the forth central moment μ_4. An univariate normal distribution has an excess kurtosis of $\mathrm{EK} = 0$. Hence a non-zero excess kurtosis indicates a deviation from the thermal Gaussian distribution in the harmonic trap. Negative values mean that there are less outliers, like in a flat-top distribution, whereas positive values indicate a distribution that asymptotically approaches zero more slowly compared to a normal distribution.

In Fig. 4.8, we display the excess kurtosis as a function of the UV exposure time t. The gray line was obtained by calculating the excess kurtosis from the reconstructed experimental density profiles through the cloud center along x, i.e. the same data as was used in Fig. 4.7, whereas the red line was obtained from theory[8]. Initially the density profile is approximately Gaussian with an excess kurtosis close to 0. After a quick drop down to a value around -1, the excess kurtosis increases, but is still well below zero after $t = 200\,\mathrm{ms}$, and hence the thermalization time of the system for regaining a Gaussian density profile is well beyond $200\,\mathrm{ms}$. This in turn means that the SOC state is maintained for at least ten times longer compared to the self-organization timescale of about $10\,\mathrm{ms}$.

Measurement of the atom density redistribution in the dipole trap

If we add a hold time t_{hold} between the excitation laser pulse and the imaging light pulse, we observe a change of the flat-top density profile back towards a Gaussian profile. To characterize the associated atom reloading timescale more qualitatively, we start with a non-Gaussian profile created by $5\,\mathrm{ms}$ of detuned Rydberg excitation. Subsequently we turn off the Rydberg laser and keep the atoms in the dipole trap for a hold time t_{hold} of $1, 3, 5, 10, 15$ and $20\,\mathrm{ms}$. Then, we take an absorption image to reconstruct the atom density distribution through the cloud center (see Fig. 4.9a for the corresponding cross sections). As we are interested in the atom density change due to the trap potential, we take the difference between longer hold times with respect to the first measurement (Fig. 4.9b). We clearly observe that the initial profile with a dip in the center refills towards a near-Gaussian profile after $10\,\mathrm{ms}$ hold time in the trap without Rydberg excitation. Along with the density increase in the center we observe fewer atoms in the wings of the distribution about $\pm 250\,\mu\mathrm{m}$ from the center. At $15\,\mathrm{ms}$ and $20\,\mathrm{ms}$, the density slightly drops again in the center and increases in the wings. Overall, we confirm atomic

---

[8] See manuscript of Ref. [109] for more details on the theory.

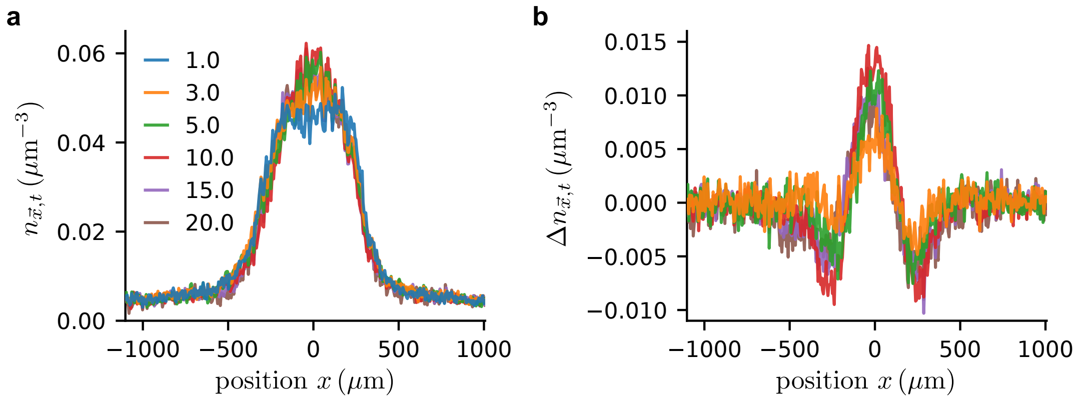

Fig. 4.9: **Observation of density refilling in the trapping potential.** **a** Reconstructed atom density slice through the center of the cloud for six different hold times t_{hold} of $1, 3, 5, 10, 15$ and $20\,\mathrm{ms}$ (see color coding). The hold time defines the time where the atom cloud is held in the trap without the Rydberg excitation laser. Starting with a non-Gaussian density profile, created by $5\,\mathrm{ms}$ of detuned Rydberg excitation, during the first $\approx 10\,\mathrm{ms}$ hold time a transport of atoms from the wings towards the center is seen. This refilling of the center visible as an increase of density in the center in combination with a reduction at the wings. At later times, e.g. $20\,\mathrm{ms}$, there seems to be a small oscillation back to the wings, reducing the density in the center. **b** Difference of the late hold times with respect to the first measurement at $1\,\mathrm{ms}$ for better visibility of the density change. Up to $10\,\mathrm{ms}$ (red), positive values in the center and negative ones at the wings at around $\pm 250\,\mu\mathrm{m}$ are visible. The color coding of the time traces is consistent with subfigure a.

rearrangement in the trap, leading to atom reloading in the center on a timescale of $\sim 10\,\mathrm{ms}$, which is slower compared to the loss and matches well the expected timescale from previous observations.

After having discovered this intrinsic refilling mechanism, in the next section we will introduce a controlled mechanism of how to implement reloading into our experimental system.

4.5 A controlled reloading mechanism for sustaining the SOC state

Here, we will experimentally introduce a controlled reloading mechanism to counteract particle loss over time, as additionally shown in the phase diagram of the underlying absorbing state phase transition [147] in Fig. 4.10a. The idea is that the facilitated excitation rate depends on both the ground state density n and the excitation laser Rabi frequency Ω. Whereas in the previous section the trap potential provided an atom replenishment mechanism, here the effective facilitation rate is controlled by the laser intensity Ω [148].

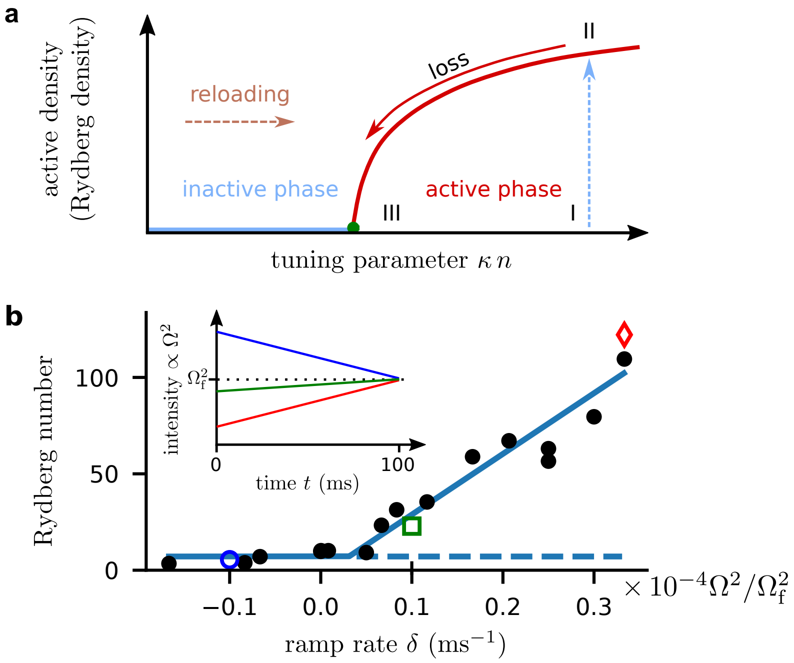

Fig. 4.10: Effective reloading mechanism for sustaining the self-organized critical point. **a** Underlying absorbing state phase diagram with the inactive (zero active density, blue) and active phase (non-zero active density, red), separated by the critical point (green). If we start the experiment in the active phase, we see a fast initial increase in the excitation number (I)→(II), which is then accompanied by atom loss (II)→(III) driving the system towards the critical point (SOC). Here we add a tunable effective reloading mechanism (brown) which counteracts this loss, experimentally realized via ramping the Rydberg laser intensity and with it the effective facilitation rate during the Rydberg excitation time t (see also inset of subfigure b). **b** Measurement of the mean Rydberg number as a function of the laser intensity ramp rate δ. Similar behavior to subfigure a is observed, where a small positive ramp value δ_c is separating the inactive and active phase. The blue line is a fit with a piece-wise constant and linear function, yielding a $\delta_c = 0.03 \times 10^{-4}\mathrm{ms}^{-1}\Omega^2/\Omega_f^2$. The black points are the mean over typically 50 experimental runs. The colored points depict larger statistics measurement in the inactive phase (blue, negative ramp), close to the critical point (green, small positive ramp) and in the active phase (red, positive ramp), where the corresponding ramps of the laser power are illustrated in the inset.

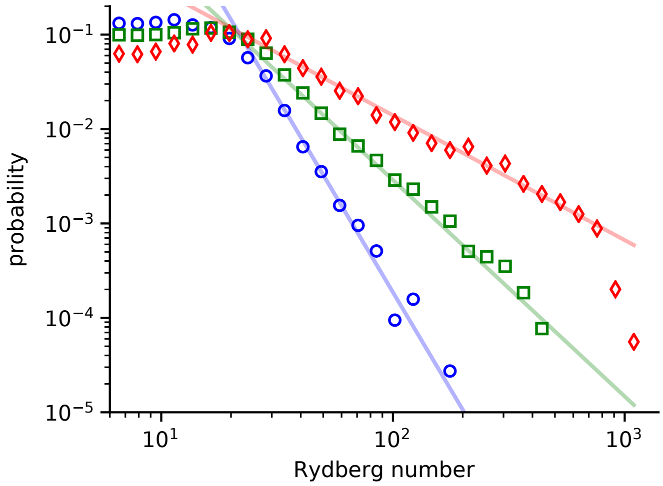

Fig. 4.11: Power-law exponent of the avalanche size distribution around the critical point. Empirical probability distribution of the Rydberg number for datasets in the inactive phase (blue), close to the critical point (green) and in the supercritical phase (red). The data is binned on logarithmically spaced intervals. The solid lines on this double logarithmic scale are obtained from a maximum likelihood estimator for a decaying power-law function with lower and upper bound.

Experimental system

The experimental system is identical to the previous sections, except for the new feature of linearly ramping the Rydberg laser intensity during the exposure time with rate δ. Small positive ramp rates counteract the loss of atoms and maintains the avalanches, while small negative ramp rates drive the system into the absorbing state. Fig. 4.10b presents the mean Rydberg number over typically 50 experimental runs for different intensity ramp values over a total exposure of $100\,\mathrm{ms}$. We observe two distinct regimes: for negative and small positive ramps the Rydberg excitation number is constantly close to zero, which we attribute to the inactive, absorbing phase. For larger positive ramp values, an approximately linear increase of the excitation number is seen with δ, which is indicative of the active phase, where the avalanche activity survives due to the effective reloading mechanism. The blue solid line refers to a fit of a piece-wise constant and linear function, yielding $\delta_\mathrm{c} = 0.03 \times 10^{-4}\mathrm{ms}^{-1}\Omega/\Omega_\mathrm{f}$, where the ramp rate is set in relation to the final Rabi frequency value Ω_f at the end of the $100\,\mathrm{ms}$ ramp. The colored symbols depict three measurements where more statistics were taken. The negative ramp (blue circle) brings one deeper into the inactive phase, whereas a slight positive ramp of $\delta = 0.1 \times 10^{-4}\mathrm{ms}^{-1}\Omega/\Omega_\mathrm{f}$ (green square) is close to the critical point and a higher ramp value (red rhombi) keeps the system in the active phase.

Avalanche size statistics

To quantify the excitation dynamics behavior in different points in the phase diagram, we analyze the large statistics data[9] for three δ values of -0.1, 0.1 and $0.33 \times 10^{-4}\Omega^2/\Omega_f^2$, plotted in Fig. 4.10b as blue circle, green square and red rhombi. In Fig. 4.11, we first bin the data into logarithmically spaced intervals and the plot the corresponding normalized probability distributions on double logarithmic scale. All three datasets show an initially roughly constant plateau up to a Rydberg number of 11, which could be created by several kinds of measurement noise. For higher Rydberg numbers, the probability drops linearly on the double logarithmic scale, which indicates a power-law decay.

The probability density function (PDF) for a power-law with lower bound x_{min} and upper bound x_{max} is given by

$$p(x) = \frac{1-\alpha}{x_{\text{max}}^{1-\alpha} - x_{\text{min}}^{1-\alpha}}\, x^{-\alpha}\, \theta(x - x_{\text{min}})\, \theta(x_{\text{max}} - x), \tag{4.8}$$

where the bounds are introduced by the Heaviside step function $\theta(x)$ and assuming a negative exponent, i.e. $\alpha > 0$. The corresponding likelihood function for N values in X is

$$\mathcal{L}(\alpha|X) = \prod_{i=1}^{N} \frac{1-\alpha}{x_{\text{max}}^{1-\alpha} - x_{\text{min}}^{1-\alpha}}\, x_i^{-\alpha}. \tag{4.9}$$

The corresponding log likelihood function is

$$\begin{aligned}\ell(\theta|X) = \log \mathcal{L}(\alpha|X) &= \log \prod_{i=1}^{N} \frac{1-\alpha}{x_{\text{max}}^{1-\alpha} - x_{\text{min}}^{1-\alpha}}\, x_i^{-\alpha} = \sum_{i=1}^{N} \log\left(\frac{1-\alpha}{x_{\text{max}}^{1-\alpha} - x_{\text{min}}^{1-\alpha}}\, x_i^{-\alpha}\right) \\ &= -\alpha \sum_{i=1}^{N} \log x_i + N \frac{1-\alpha}{x_{\text{max}}^{1-\alpha} - x_{\text{min}}^{1-\alpha}}. \end{aligned} \tag{4.10}$$

The highest likelihood, i.e. the maximum likelihood estimator

$$\hat{\alpha} = \arg\max_{\alpha} \left[-\alpha \sum_{i=1}^{N} \log x_i + N \frac{1-\alpha}{x_{\text{max}}^{1-\alpha} - x_{\text{min}}^{1-\alpha}}\right] \tag{4.11}$$

can be found by numerical maximization of ℓ or by analytically setting the derivative w.r.t. α to zero, which is a necessary condition for a maximum: $\frac{\partial \ell(\alpha)}{\partial \alpha} = 0$.

The straight colored lines in Fig. 4.11 are obtained from the maximum likelihood estimator $\hat{\alpha}$ (Eq. 4.11) applied to 1000 bootstrap resamplings of the data. This yields mean and standard deviation values for the power-law exponent of $\alpha = 4.1 \pm 0.3$ in the subcritical region (blue), $\alpha = 2.3 \pm 0.2$ close to the critical point (green), and $\alpha = 1.3 \pm 0.1$ in the supercritical region (red). The drop in the last two points in the supercritical region (red) are in the range of our expected system size and hence might be due to finite size effects.

---

[9] About 4000 experimental repetitions for the inactive (blue) and active (red) phase as well as about 2400 individual experimental runs close to the critical point (green).

The observation of these power-law distributions with nonuniversal power-law exponents is quite surprising. First, the blue data was conjectured to lie in the absorbing phase, where zero activity is expected. This could be explained by local fluctuations and noise in the experiment, locally crossing into the supercritical region. The second noteworthy point is that assuming an absorbing state phase transition, universality is only expected to occur exactly at the critical point. However, we observe power-law distributions even in the close by subcritical and supercritical regions. It would be interesting to further investigate the origin of this behavior. An extended Griffiths phase due to disorder could provide an explanation for the observed power-law distributions with changing exponents (see Sec. 5.3).

Conclusion

The three signatures presented in this chapter, notably including the excitation avalanche statistics, establish self-organization to a critical state in our driven-dissipative Rydberg system, which is a landmark concept of how complexity emerges in nature [21, 149]. Remembering back to the introduction on complex systems (cf. Sec. 1.1), this dynamics towards the SOC state with a constant density might at first seem not very complex. However, this neglects the fact that this is a critical state with in principle vanishing dynamical gap and diverging length scales, leading to the observed large possible fluctuations in the excitation number distributed according to a power law. This raises the interesting question about the feasibility of observing SOC in an experimental, imperfect system. A stabilization mechanism was discovered, which keeps the system close to the critical state for an extended period of time, provided by the restoring atomic motion in the trap potential. This mechanism is evidenced by an extended critical region in the trap center with a characteristic flat-top density profile. Instead of relying on this implicit refilling process, a tunable effective reloading mechanism was implemented via ramping of the excitation laser power and was used to probe the avalanche statistics around the critical point.

In general, these results establish driven-dissipative Rydberg atoms as a well-controlled platform for studying specifically self-organized criticality and in general non-equilibrium physics. For future experiments, it would be interesting to study self-organization in a structured atomic gas (cf. Sec. 3.3.3) with more control on the spatial disorder and to investigate the origin of the changing power-law exponent in the avalanche size distribution. Furthermore, there are still many open questions on how quantum effects would alter SOC. One expectation is that the underlying second order absorbing state phase transition might change to a first order phase transition [150, 151].

In the next chapter, we will study the initial growth regime of the Rydberg atom number under facilitated excitation in a similar experimental setting, where the dimple trap has been replaced with a two-dimensional pancake trap.

5

Epidemic growth and Griffiths effects on an emergent Rydberg network

This chapter is based on the following manuscript:
[152] **Epidemic growth and Griffiths effects on an emergent network of excited atoms**, T. M. Wintermantel, M. Buchhold, S. Shevate, M. Morgado, Y. Wang, G. Lochead, S. Diehl, and S. Whitlock, arXiv:2007.07697 (2020), accepted in Nature Communications

Whether it be telecommunication, transportation, social or biological processes, the complex dynamics of an exceptionally broad and diverse range of real-world systems emerges on complex networks. Despite this diversity, surprisingly similar dynamical behavior is often observed in many seemingly different systems, which can be traced back to comparable features of their underlying network structure. A case in point is the prediction for epidemic growth: A disease outbreak is very sensitive to the type of disease, the behavior of individuals and the contact network structure, yet epidemics generically feature a sharp threshold between quiescent and active regimes and a characteristic time dependence [38]. These features are often described by dynamical models on complex networks [37, 39, 153–155] that have also found applications in viral marketing [156], finance [157], and traffic flow [158]. A common challenge in these fields is to find general principles governing complex system dynamics and to pinpoint how apparent universal characteristics emerge from the underlying network structure.

In this chapter, we develop a link between the collective excitation dynamics of our ultracold atom gas during facilitated Rydberg excitation and the spreading of epidemics. Subexponential growth, which is an empirically observed feature of real-life epidemics is also a general feature our experimental system dynamics. To investigate the underlying processes, a complex network model is devised describing the data very well with one free parameter characterizing the network heterogeneity. The importance of disorder leading to rare-region effects points towards an extended Griffiths phase. This might also provide important physical insight into other non-equilibrium critical states in driven-dissipative systems and a mechanism to explain power-law observations in complex systems dynamics.

5.1 Microscopic ingredients for an epidemic

Microscopic processes

First of all, we extract the microscopic processes that govern the excitation dynamics in our potassium cloud exposed to detuned Rydberg excitation, depicted in Fig. 5.1a,b. Since we address and single out a specific transition out of the full energy level structure with the Rydberg excitation laser, a two-level description consisting of an atomic ground state $|g\rangle$ (blue disks, healthy) and an excited Rydberg state $|r\rangle$ (red disks, infected) is used[1]. Here, sufficiently large separation to other energy levels and similar couplings for all involved sublevels is assumed. The main two processes are (i) Rydberg atoms decay with a rate Γ (recovery) and (ii) facilitated excitation of neighboring ground-state atoms, that satisfy certain constraints with respect to their position and velocity, with rate κ (transmission) (cf. Sec. 2.3). This nonlinear excitation scheme can lead to rapid spreading of the excitations throughout the system, illustrated by growing excitation clusters in Fig. 5.1a [68, 133, 136, 159, 160]. The competition between κ and Γ leads to a second-order non-equilibrium phase transition [124, 161] between an active (finite excitation number) and inactive (zero excitations) phase (cf. Sec. 4.1). Once the inactive, absorbing phase with zero excitation number has been entered, the system can not escape this phase anymore.

In the following we will investigate the intriguing growth dynamics resulting from the competition between these two processes as well as the connection to epidemic models with recovery and transmission processes.

Experimental sequence

To study the short-time growth of Rydberg excitations we start from an ultracold thermal gas of 3×10^4 potassium-39 atoms in their ground state $|g\rangle = |4s_{1/2}\rangle$ (see Fig. 5.1a). The atom cloud is confined in the so-called pancake trap (see Sec. 3.3.2), which is effectively two-dimensional with respect to the Rydberg facilitation dynamics. The atom density distribution has a peak density of $n_{2D}(x\!=\!y\!=\!0) = 0.76\,\mu\mathrm{m}^{-2}$ and $e^{-1/2}$ Gaussian widths of $\sigma_x = 125\,\mu\mathrm{m}$ and $\sigma_y = 50\,\mu\mathrm{m}$. The experimental sequence consists of three steps, as illustrated in Fig. 5.1c:

1. To start the dynamics at a well-defined time $t = 0\,\mathrm{ms}$, a short resonant laser pulse on the $|g\rangle = |4s_{1/2}, F = 1\rangle \rightarrow |r\rangle = |66p_{1/2}\rangle$ transition prepares around 8 Rydberg seed excitations placed randomly throughout the cloud. Due to our experimental setup, it is challenging to change the UV laser frequency on such a short timescale without changing the beam pointing vector. Instead, we exploit the DC Stark effect to tune in and out of resonance. We keep the laser frequency fixed at $\Delta = -30\,\mathrm{MHz}$

---

[1] Due to the short experimental timescales that will be used here, we neglect atom loss out of the system to removed states.

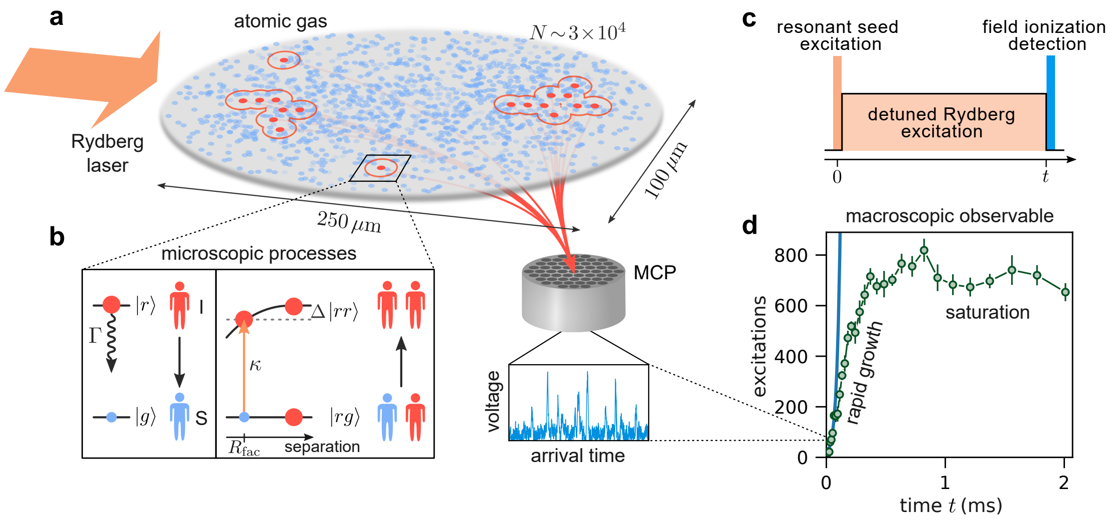

Fig. 5.1: Experimental system for studying Rydberg excitation growth. a Illustration of the experimental setup for the study of excitation growth. The cloud of potassium atoms is held in a two-dimensional trap with narrow vertical extent. An ultra-violet (UV) laser field, which illuminates the whole cloud, off-resonantly couples the ground state (blue disks) to the Rydberg state (larger red disks). A microchannel plate detector (MCP) in the vacuum chamber is used to detect the number of Rydberg excitations. Rydberg atoms are first ionized by a large electric field and then accelerated onto the MCP by additional guiding electrodes (depicted by red flight trajectories), where the impinging ions are multiplied and create voltage spikes (see exemplary blue voltage time trace). **b** Each atom can be reduced to a two-level system with a ground state $|g\rangle$ and excited Rydberg state $|r\rangle$. Rydberg atoms either decay back to the ground state with rate Γ or facilitate additional excitations with rate κ at a characteristic distance R_{fac} (illustrated by red circles). These two processes are analogous to the recovery from infected (I) to susceptible (S) and the transmission of an infection where an infected individual infects a susceptible neighbor. **c** The experimental sequence consists of three distinct phases. First, a small number of seed excitations is prepared among the cloud by a short resonant laser pulse. During the subsequent off-resonant Rydberg excitation, the system evolves according to the microscopic processes depicted in subfigure b, that can give rise to growing excitation clusters spreading throughout the system. After different exposure times t, the Rydberg atoms are field ionized and detected on the MCP detector. **d** Exemplary data trace showing two different stages of the dynamics: after a rapid growth, the excitation number saturates at around 700 Rydberg excitations. For comparison, the blue line represents exponential growth. Error bars display the standard error of the mean over 16 experiment repetitions. Adapted from [152].

below the zero field resonance and make use of an electric field of $0.28\,\mathrm{Vcm}^{-1}$ to tune the atoms into resonance (cf. Sec. 3.5). After turning on the laser for a short $4\,\mu\mathrm{s}$ resonant pulse, the electric field as well as the intensity of the laser are turned off for $6\,\mu\mathrm{s}$ to account for finite switching times of the electric field.

2. Subsequently, we apply the off-resonant laser field with $\Delta = -30\,\mathrm{MHz}$ (i.e. the with electric field turned off) and experimentally varied intensity. Secondary excitations can now be facilitated at a distance $R_{\mathrm{fac}} = 3.5\,\mu\mathrm{m}$ (depicted by red circles in Fig. 5.1a), where the laser detuning is compensated by the calculated Rydberg pair-state energy such that the excitation becomes resonant (cf. Sec. 2.3). This two-body facilitation rate κ is hence proportional to the UV laser intensity, which in turn can be experimentally varied over a wide range using an acousto-optic modulator. The following experimental studies cover the κ values in the range from $3.3\,\mathrm{kHz}$ to $10\,\mathrm{kHz}$. The value of the facilitation rate κ is obtained from the initial growth rate $r = 27(8)\,\mathrm{kHz}$ at high intensity and very short times $t \ll \tau$ (Fig. 5.1d). In this regime, we can neglect many-body effects and assume that the growth is dominated by the bare facilitated excitation between a Rydberg and a ground-state atom. The initial growth rate is then divided by an estimate of the mean number of atoms that fulfill the facilitation condition ($\bar{\mu} = 2.7$, see spatial SIS model presented in Sec. 5.3) assuming isolated seed excitations. The calculated spontaneous decay rate of Rydberg excitations is $\Gamma = 0.84\,\mathrm{kHz}$, which includes black-body decay. Off-resonant Rydberg excitation of single ground-state atoms is very unlikely, with an estimated rate $\lesssim 1\,\mathrm{kHz}$ for the whole cloud.

3. After a variable exposure time t from $0\,\mathrm{ms}$ up to $2\,\mathrm{ms}$, the total number of excitations in the cloud is inferred via field ionization detection (see Sec. 3.5). A large electric field ionizes the Rydberg atoms and additional electrodes guide the resulting ions onto a microchannel plate (MCP) detector, where the ion charge is multiplied, creating a voltage spike. We record the voltage-time trace on a fast oscilloscope (see exemplary time trace in Fig. 5.1a) and use a conversion factor including finite detection fidelity to obtain the original Rydberg number. This conversion factor from the integrated MCP voltage to the number of Rydberg excitations was calibrated from an independent Rydberg excitation experiment, where we tracked the number of atoms remaining in the optical trap via absorption imaging. From this we infer the number of atoms removed from the gas after a long exposure assuming each Rydberg atom is lost from the trap with rate Γ and gauge it against the corresponding ion signal.

Excitation growth dynamics

The competition between the seemingly simple processes of nonlinear (facilitated) excitation and decay already gives rise to complex dynamical phases and evolution [72, 161–165]. However, in the full many-body system it is even more challening to link microscopic prosses to macroscopic observables like the exciation number: 3×10^4 multilevel atoms with random positions and velocities, interacting with each other and the light field [165–167]. This is why we first turn to experimentally investigate the resulting dynamics. In Figure 5.1d, we present a measurement of the excitation number as a function of laser exposure time t for a facilitated excitation rate of $\kappa = 10\,\mathrm{kHz}$, where we can observe two different regimes:

1. During the first approx. $0.5\,\mathrm{ms}$ after the initial seed creation, the number of Rydberg excitations grows very fast. Within the first $0.19\,\mathrm{ms}$, corresponding to the Rydberg lifetime, the excitation number grows from its initial value around 8 to more than 400, which corresponds to more than 5 doubling steps of the excitation number. Despite this fast growth, it follows a slower growth characteristic compared to exponential growth $\propto 2^{t/t_0}$, plotted as the blue line. We will investigate this in more detail in the next section 5.2.
2. After $t \approx 0.5\,\mathrm{ms}$, the excitations saturate at a high constant number. This value however, is still significantly lower than the estimated maximum excitations number in the system of $\gtrsim 2000$, obtain from area considerations for inter-Rydberg spacings of $\sim R_{\mathrm{fac}}$, and also below the detector saturation. We will shed light on this when developing a theoretical model in Sec. 5.3. On even longer timescales than those studied here ($\gtrsim 10\,\mathrm{ms}$), the system should relax to an absorbing or self-organised critical (SOC) state due to atom loss out of the system [72, 110], as reported in chapter 4.

5.2 Observation of epidemic growth

As the microscopic processes in our Rydberg gas (see Fig. 5.1) map closely to the spreading and recovery processes in epidemics, we will borrow methods from observational epidemics to study the excitation growth in our driven-dissipative Rydberg gas.

Many real-life epidemics follow a characteristic power-law dependent growth, which is parametrized by the phenomenological generalized growth model (GGM) [38]

$$C'(t) = rC^p(t). \tag{5.1}$$

Here, C' is the incidence rate, $C = \int_0^t C'(t')dt'$ is the cumulative number of infections, r controls the growth rate at early times and p is called the deceleration of growth parameter, which is an important parameter in classifying epidemics [38]. $p = 1$ corresponds to exponential growth in time, while $p < 1$ corresponds to subexponential,

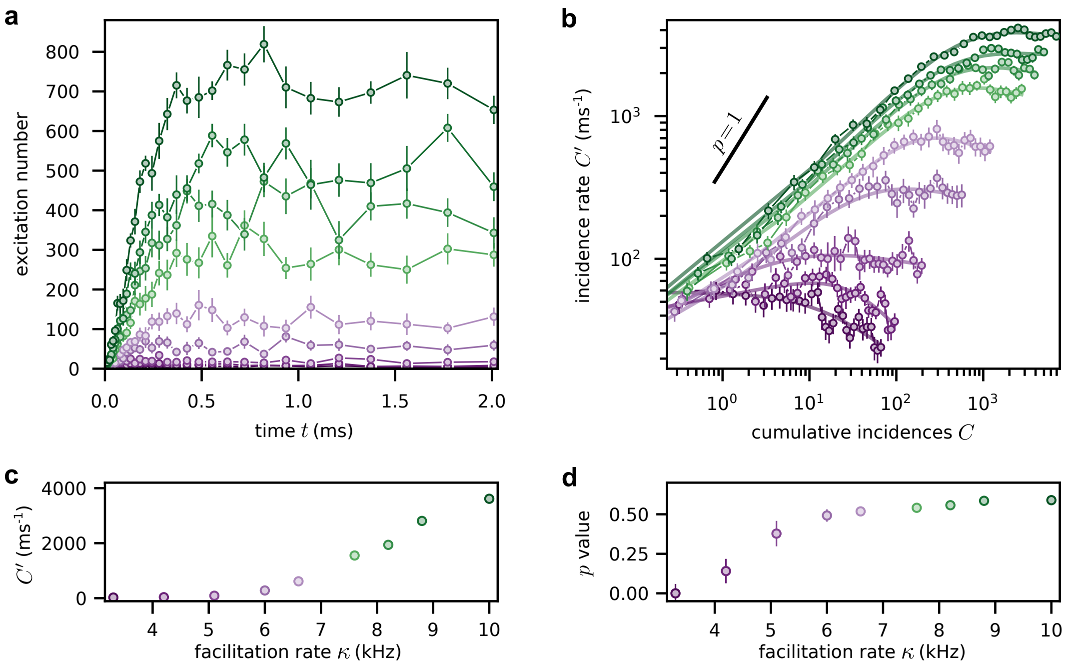

Fig. 5.2: **Subexponential, power-law growth in the Rydberg excitation curves for different facilitation rates. a** Number of instantaneous excitations as a function of excitation time t for facilitation rates of $\kappa = \{3.3, 4.2, 5.1, 6.0, 6.6, 7.6, 8.2, 8.8, 10.0\}$ kHz, color-coded from purple to green with increasing value. Error bars display the standard error of the mean over typically 16 repetitions of the experiment. **b** Incidence rate C' versus cumulative incidences C for the same facilitation rates as in subfigure a. The solid lines correspond to fits of the extended generalized growth model (see text for more details), yielding the corresponding deceleration of growth parameters p. Error bars show the standard error of the mean over typically 16 repetitions of the experiment. **c** Transition from a subcritical state ($C' \approx 0$) to an active state ($C' > 0$) at late times $t = 2\,\mathrm{ms}$ as a function of the facilitation rate κ. **d** Deceleration of growth parameter p versus facilitation rate κ. The p values are obtained from the fits of the data to the generalized growth model, as presented in subfigure b. Uncertainties computed from the standard deviation over 100 bootstrap resamplings are shown as error bars except where they are smaller than the data points.

power-law growth $\propto t^{\eta}$ with $\eta = p/(1-p)$. To incorporate the plateau after the initial fast growth phase visible in our data, we extend the GGM model (Eq. 5.1) to

$$C'(t) = rC^{p}(t)\left[1 + \left(\frac{C(t)}{K}\right)^{\frac{p-\alpha}{\beta}}\right]^{-\beta}. \qquad (5.2)$$

Here, p is again the deceleration of growth parameter whereas α is the exponent of the late-time relaxation phase. K and β together determine the location and sharpness of the crossover between growth and plateau/relaxation. At the crossover $C = K$, the incidence rate is $C' = rK^{p}/2^{\beta}$. In the case of $\alpha < 0$, the number of excitations decreases to zero at late times, corresponding to a recovery in epidemics. For $\alpha = 0$, the excitation number stays non-zero at a constant excitation number $C' = rK^p$, describing an endemic state where infection and recovery rates are balanced.

Figure 5.2a shows the complete experimental data-set[2] up to $2\,\mathrm{ms}$ off-resonant laser excitation and for facilitation rate values of $\kappa = \{3.3, 4.2, 5.1, 6.0, 6.6, 7.6, 8.2, 8.8, 10.0\}\,\mathrm{kHz}$, color-coded from purple to green. In Figure 5.2b, we present the same raw data in terms of C', given by the instantaneous number of excitations divided by their lifetime $\tau = (2\pi\Gamma)^{-1}$, against its time integral C. The straight lines up to the plateau on a double logarithmic scale, that are especially visible for the higher κ values, provide evidence that the incidence rate C' follows the GGM over several decades. At the same time, the growth is clearly subexponential by comparing the slopes to the exponential case where $p = 1$ (solid black line with a steeper slope). To get quantitative information, we fit the extended GGM (Eq. 5.2, solid lines in Fig. 5.2b) to the data. For the highest κ value we obtain a deceleration of growth parameter of $p = 0.59(1)$ that is comparable to empirical observations of real epidemics [38]. Fig. 5.2d presents the p values from the fits to the different facilitated excitation rates κ. In conclusion, power-law growth with varying exponents from $p = 0$ up to $p \lesssim 0.6$ is a typical feature of the system dynamics.

Another important feature is that the C' saturation value depends on the different κ curves, where the three curves with lowest κ rates shows evidence of slow relaxation back towards zero incidences (Fig. 5.2b). Looking at the last data point at $t = 2\,\mathrm{ms}$ as shown in Fig. 5.2c already indicates a transition from a subcritical $(C' \approx 0)$ to an active $(C' > 0)$ phase as a function of the facilitation rate κ, where Γ is fixed.

In the domain of epidemics, power-law growth with $p < 1$ is linked to underlying features like spatial constraints and heterogeneity in the underlying network structure [38]. In the next section, we will take this insight into account when devising a spatial network model to bridge between the microscopic details of the system and its macroscopic observables.

5.3 Role of heterogeneity and Griffiths effects in a SIS network model

In order to model our experimental observations and in turn to gain deeper insights into the underlying key features of our system, we developed a physically motivated susceptible-infected-susceptible (SIS) network model (cf. Sec.2.4). The basic idea is to subdivide the two-dimensional atom cloud into cells, which in turn reduce into nodes in a network (Fig. 5.3). Analogous to epidemics, each cell holds N_i atoms/individuals

---

[2] The dark green data is identical to the data trace shown in Fig. 5.1d.

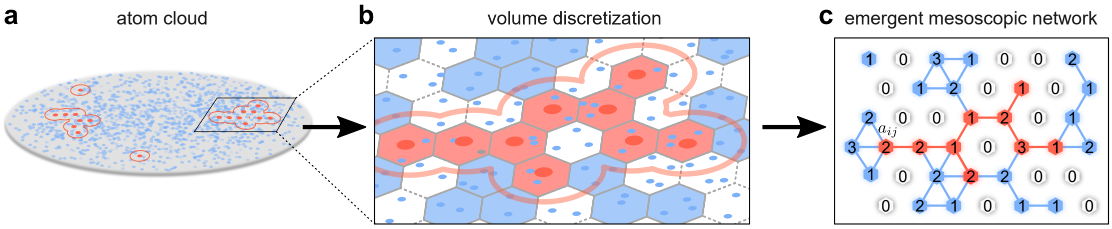

Fig. 5.3: Emergent heterogeneous Rydberg network. **a** To describe the excitation dynamics in the atom cloud a susceptible-infected-susceptible (SIS) model is developed on a heterogeneous network that emerges from the atom cloud. **b** Coarse graining of the system into hexagonal cells, which allows for the densest possible tiling in two dimensions. Each cell i contains either zero ($I_i = 0$, healthy, blue or white shading) or one ($I_i = 1$, infected, red shading) Rydberg excitations (red disks). Additionally, cells with at least one ground state atom (blue disks) that fulfills the facilitation conditions $N_i \geq 1$ can potentially be excited over time (susceptible, blue shading). Empty cells with $N_i = 0$ have zero excitation probability (white shading). **c** The coarse-grained cells are translated into network nodes, where the hexagonal cell structure with six nearest neighbors translates into a corresponding triangular network structure defined by the adjacency matrix a_{ij}. The infection probability of each node is weighted by the number of atoms in that cell that can undergo facilitated excitation N_i (shown in each node). Accordingly, vacant cells ($N_i = 0$) translate into disconnected nodes that do not participate in the excitation dynamics. This results in a weighted, heterogeneous emergent network structure (see text for more details).

that fullfill the facilitation condition, i.e. that are susceptible. Cells/nodes that contain at least one susceptible atom ($N_i > 0$) can be in either of two states: susceptible ($N_i > 0$ and zero Rydberg excitation $I_i = 0$, shaded in blue) or already infected (one Rydberg excitation, $I_i = 1$, red shading). Vacant cells with $N_i = 0$ are not susceptible and translate to missing nodes in the network (white shading). We describe the probability of infection for node i by the following stochastic master equation [37]

$$\frac{dE[I_i(t)]}{dt} = E\left[-\Gamma I_i(t) + \kappa N_i \Big(1 - I_i(t)\Big) \sum_j a_{ij} I_j(t)\right], \tag{5.3}$$

where $E[\cdot]$ denotes the expectation value. The probability of transmission of the infection from node j to i is mainly governed by the node weights N_i and the adjacency matrix a_{ij}. In the special case of constant node weights $N_i = \mathrm{const.}$ together with all to all connectivity $a_{ij} = 1$, this model reduces to the well studied homogeneous compartmental SIS model [37] which exhibits exponential growth of the infection number. On the other hand, adjacency matrices with spatial structure can result in more complex spatio-temporal evolution [168].

Now we turn to practically build such a model for our Rydberg gas (see Fig. 5.3a). We decide to use hexagonal cells (see Fig. 5.3b), because this provides the densest tiling of strongly interacting Rydberg excitations in two-dimensional space [169]. These hexagonal cells with area $\sim R_{\mathrm{fac}}^2$ translate to a triangular network, where the adjacency matrix a_{ij} has values of $a_{ij} = 1$ for each of the six nearest neighbors i of each node j, and zero otherwise (see Fig. 5.3c). To introduce heterogeneity, as suggested by the observation of power-law growth, we sample the number of susceptible particles per cell N_i, i.e. the number of atoms within cell i that fulfill the facilitation condition, from a Poissonian distribution with a spatially dependent mean $\mu_i = \epsilon(\kappa) n_{2\mathrm{d}}(x_i, y_i) R_{\mathrm{fac}}^2$. Here, $n_{2\mathrm{d}}(x_i, y_i)$ accounts for the two-dimensional Gaussian atom density distribution in the trap and the free parameter $\epsilon(\kappa) < 1$ sets the accessible phase space fraction for facilitated excitation. Thus, this heterogeneous network model (Eq. 5.3) has a spatially fluctuating weighted degree of $s_i = \sum_j a_{ij} N_j$ per node i, with a mean and variance approximately equal to $6\mu_i$.

We take a numerical Monte-Carlo approach [170] to solve this model (Eq. 5.3), where in each time step we compute the transition rate R_i for each node i according to

$$R_i = \kappa N_i (1 - I_i) \sum_j a_{ij} I_j + \Gamma I_i. \tag{5.4}$$

Then randomly one node m is picked from the weighted distribution proportional to the rate values R_i and flip its state $I_m \rightarrow 1 - I_m$. The timestep is normalized by the sum over all weights and randomness is added by the natural logarithm of a random variable X sampled from a uniform distribution in $[0, 1)$

$$dt = -\ln(X) / (2\pi \sum_i R_i). \tag{5.5}$$

The simulations start with a fixed number of $\sum_i I_i(t = 0) = 8$ seed excitations randomly distributed among the nodes according to their weights N_i.

Fig. 5.4a presents again the incidence rate C' as a function of the cumulative incidences C on a double logarithmic scale, where the data points correspond to the data in Fig. 5.2b with the same color coding from purple to green for the κ values of $\{3.3, 4.2, 5.1, 6.0, 6.6, 7.6, 8.2, 8.8, 10.0\}\,\mathrm{kHz}$. Here the solid lines, resulting from numerical simulations of the SIS model on a heterogeneous network from 0 up to $160\,\mathrm{ms}$, show very good agreement with the experimental observations. Fig. 5.4b presents the last data point at $t = 2\,\mathrm{ms}$ as well as the corresponding simulation result. We observe the same structure with an inactive phase of close to zero activity ($C' \approx 0$) and an active phase ($C' > 0$) for higher κ values. The upper part of Fig. 5.4c compares the deceleration of growth parameter p obtained from fitting both the experimental data (disks) and the SIS network simulation (solid black line with standard deviation as shaded area) with the extended generalized growth model (Eq. 5.2). Uncertainties are calculated from 100 bootstrap resamplings. The bottom part shows the late-time power-law relaxation exponent α as obtained from fits of the extended generalized growth model to the nu-

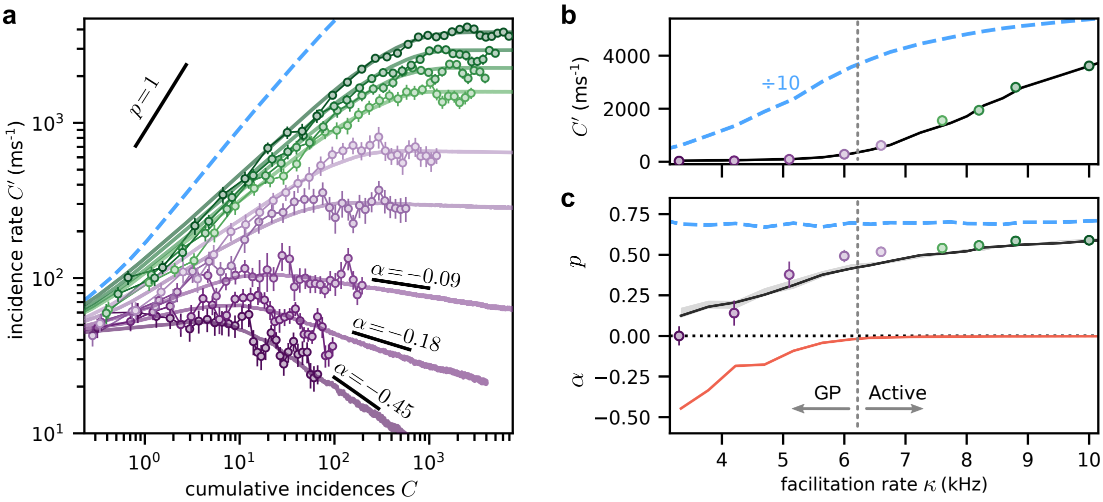

Fig. 5.4: Epidemic network simulations reproducing power-law growth and Griffiths effects. **a** Incidence rate C' versus cumulative incidences C for facilitation rates of $\kappa = \{3.3, 4.2, 5.1, 6.0, 6.6, 7.6, 10.0\}\,\mathrm{kHz}$, which are represented via the color shading from purple to green. The error bars are obtained from the standard error of the mean of typically 16 experiment repetitions. The solid lines are the results of simulations using a susceptible-infected-susceptible (SIS) model on a heterogeneous network (see text for more details). The blue dashed line corresponds to a simulation on a locally homogeneous network without vacant nodes, with $\kappa = 10\,\mathrm{kHz}$ and a comparable system size. **b** Transition from a subcritical state ($C' \approx 0$) to an active state ($C' > 0$) at late times $t = 2\,\mathrm{ms}$ as a function of κ. The solid black curve and the blue dashed curve show SIS model simulations on the heterogeneous and homogeneous network, respectively. They clearly exhibit different thresholds and incidence rates. **c** The top part presents the deceleration of growth parameter p as a function of the facilitated excitation rate κ. The p values are obtained from the fits of the generalized growth model to the experimental data points (disks), to the numerical SIS simulations on heterogeneous networks (black line) and to numerical SIS simulations on locally homogeneous networks (blue dashed line). The shown error bars/ shaded error regions are computed from the standard deviation over 100 bootstrap resamplings. The bottom part presents the relaxation exponent α versus κ from the SIS simulations on a heterogeneous network (orange line). The vertical gray dashed line indicates roughly the cross-over point between the Griffiths phase (GP) and the active phase. Adapted from [152].

merical data from the heterogeneous SIS network model (orange line). We observe that the low κ curves decay at late times consistent with power-law relaxation with varying exponents α. For higher κ values, where $\alpha = 0$, the system stays in the endemic state with finite C' at late times. Interestingly, the transition regions of all three parameters C', p and α coincide well, where the cross-over point is roughly indicated by the vertical dashed line in Fig. 5.4b,c. In summing up the observations in this figure, the SIS network model fully reproduces the three key features in the various κ curves: the initial fast power-law growth with $p < 0.6$, the various plateau heights and the late-time relaxation for the lowest κ curves.

As mentioned, $\epsilon(\kappa)$ is the only free parameter in the model with best data-simulation agreement for $\epsilon(\kappa) = \{0.023, 0.027, 0.037, 0.056, 0.067, 0.078, 0.083, 0.088, 0.094\}$. This parameter sets the accessible phase space fraction for facilitated excitation and directly controls the network structure by shifting the weighted node degree distributions. Now we investigate the effect of this heterogeneity by comparing it to a locally homogeneous network, i.e. constant node values without vacant nodes such that each node has six neighbors as given by the underlying triangular network structure, but keeping the same average node degree $N_i = \mu_i$. We obtain the blue dashed lines in Fig. 5.4, which drastically differ from the experimental and simulated heterogeneous network data. They show faster initial growth, higher plateaus saturating close to the system size limit, a critical point shifted to lower κ values and higher as well as constant p values of about 0.7.

This shows that heterogeneity, introduced via sampling of the node weight from a Poissonian distribution with a mean proportional to $\epsilon(\kappa)$, is an important parameter in reproducing the emergent macroscopic dynamics. In the next section, we will take a closer look at the effect of $\epsilon(\kappa)$ on the networks that we used in our simulations.

Characterization of the emergent network structure

Now, we present an analysis of the emergent network structures for each of the $\epsilon(\kappa)$ values that were found to yield the best data agreement in the heterogeneous network simulations.

In the case of $\kappa = 10\,\mathrm{kHz}$, the network features about 2300 non-vacant nodes with $N_i > 0$ and the local s_i follow approximately Poissonian distributions with $\langle s_i \rangle = \mathrm{var}(s_i) \leq 5.3$, which is maximal at the trap center. These values change for the lowest curve with $\kappa = 3.3\,\mathrm{kHz}$ to approximately 660 non-vacant nodes and $\langle s_i \rangle = \mathrm{var}(s_i) \leq 1.3$.

Besides the bare number of nodes, the connection structure between the nodes is important, which we will characterize in terms of the weighted degree distribution and the cluster size distribution. In Fig. 5.5a,b we present the weighted degree distributions in the inactive phase ($\kappa = 3.3\,\mathrm{kHz}, \epsilon(3.3\,\mathrm{kHz}) = 0.023$) and in the active phase($\kappa =$

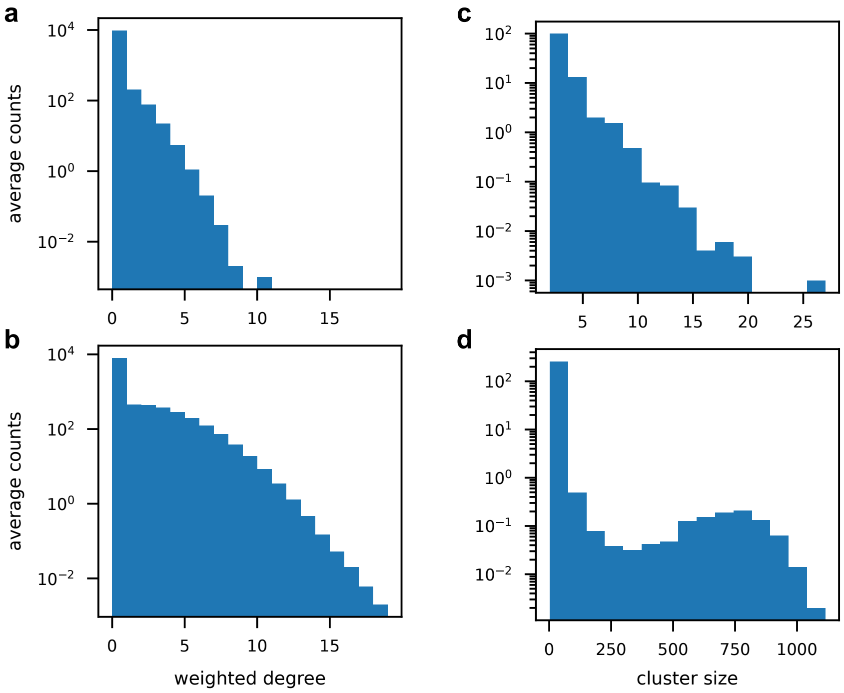

Fig. 5.5: **Characterization of the network structure in the epidemic network simulations.** The network that is used to obtain the good agreement between data and susceptible-infected-susceptible simulations is characterized in terms of the weighted degree distribution for **a** the lowest value of the facilitated excitation rate $\kappa = 3.3\,\mathrm{kHz}$ (inactive phase) and for **b** the highest value $\kappa = 10\,\mathrm{kHz}$ (active phase). Furthermore, the cluster size distribution is presented for the same two values of **c** $\kappa = 3.3\,\mathrm{kHz}$ and **d** $\kappa = 10\,\mathrm{kHz}$. Each distribution was obtained by averaging over 1000 individual preparations of the corresponding network structure. Adapted from [152].

$10\,\mathrm{kHz}, \epsilon(10\,\mathrm{kHz}) = 0.094$), with the system size limited to a maximum of 10000 nodes. Each distribution was obtained by averaging over 1000 individual preparations of the corresponding network structure. The weighted degree distributions are qualitatively similar, following an approximately Gaussian dependence as evidenced by the parabolic shape on a semilog scale. Still, one observes a shift of the weighted degree distribution towards larger values for the higher κ value.

Another important feature determining how large excitations can grow on the network is the connected component or cluster size. A cluster is defined as a set of nodes where each node can reach any other node via edges, and the cluster size is the corresponding number of nodes in this set. This means that the cluster size determines the maximum size a single excitation can grow to in the corresponding cluster. Fig. 5.5c presents the cluster size distribution for the inactive phase with $\kappa = 3.3\,\mathrm{kHz}$. It has an approximate exponentially decaying shape, meaning that large connected clusters are exponentially rare. In the active phase with $\kappa = 10\,\mathrm{kHz}$, the network features much larger connected clusters with a peak in the distribution around 750 (Fig. 5.5d). Another interesting quantity to look at in future investigations would be the spectral dimension, which can be defined as the return probability of a random walk on the network [171].

Landau-Zener probability for facilitated excitation

Having seen that the heterogeneous spatial SIS network model is an efficient coarse grained model of the observed system dynamics via the stochastic master equation in Eq. (5.3). The finding that heterogeneity in the network is important is surprising. Knowing that on average the atoms travel more than the facilitation radius during a Rydberg state lifetime at the measured temperature of the gas, one could expect atomic motion to quickly wash out any effects of spatial disorder. However, in the following we reason that the facilitation rate is not only constraint by the relative spatial positions of the atoms, but also by the relative velocity.

From the simulations we infer that the fraction of atoms that fulfill the facilitation constraint and hence participate in the excitation dynamics is small, which can be understood by an additional velocity condition for Rydberg facilitation (cf. Sec.2.4 and corresponding Fig. 2.4). If we assume a large relative velocity between the Rydberg atom and the ground state atom, then the ground state atom spends a small amount of time in the spatial facilitation shell. We model this velocity dependence with the Landau-Zener transition probability, which restricts facilitation to atoms with small relative velocities $v \lesssim v_{\mathrm{LZ}} \ll v_{\mathrm{th}}$. The Landau-Zener velocity can be written as

$$v_{\mathrm{LZ}} = \pi^2\Omega^2/\dot{V}, \tag{5.6}$$

where Ω is the Rabi frequency and $\dot{V}$ is the slope of the Rydberg-Rydberg interaction potential at the facilitation radius R_{fac} [165]. The number of atoms that fulfill the facilitation condition in a neighboring cell within the Rydberg state lifetime τ is given by

$$\epsilon = \Phi\tau f_v/n_{2d}R_{fac}^2 \approx \sqrt{\pi}\tau v_{\mathrm{LZ}}/(3R_{\mathrm{fac}}). \tag{5.7}$$

Here, the flux of atoms passing through a 1/6 segment of the facilitation shell (due to the hexagonal coarse grained cell structure that we assume) is $\Phi = \pi R_{fac} n_{2d} v_{th}/3$. $f_v \approx v_{\mathrm{LZ}}/\sqrt{\pi} v_{\mathrm{th}}$ is the fraction of atoms that fulfill the Landau-Zener condition with relative velocity $|v| < v_{\mathrm{LZ}}$. And $n_{2d}R_{fac}^2$ is the mean number of atoms in each cell.

Realistic experimental values of $R_{\mathrm{fac}} = 3.5\,\mu\mathrm{m}$, $\dot{V} = 1 \times 10^5\,\mathrm{kHz}\,\mu\mathrm{m}^{-1}$ [50] and $\Omega \sim 100\,\mathrm{kHz}$ yield a Landau-Zener velocity of $v_{\mathrm{LZ}} = 1\,\mu\mathrm{m/ms}$, which is small compared to the thermal atom velocity of $v_{\mathrm{th}} = 65\,\mu\mathrm{m/ms}$ at a temperature of $20\,\mu\mathrm{K}$. Putting these numbers into the equation for the phase space fraction (Eq. 5.7) yields $\epsilon = 0.03\left(\frac{\Omega}{100\,\mathrm{kHz}}\right)^2$. This simple model that we developed here seems to provide a reasonable estimate, as this value of ϵ is compatible to the values obtained from the simulation-experiment comparison. Despite the fact that we neglected microscopic details like the possible occurrence of several excitation resonances due to Zeeman sublevels or potential forces between the (Rydberg) atoms.

Hence, the Landau-Zener transition probability for the Rydberg facilitation gives an explanation why only atom pairs with small relative velocities $v_{\mathrm{LZ}} \lesssim 1\,\mu\mathrm{m/ms}$ contribute to the spreading of facilitated excitations [165] and provides a qualitative explanation for the inferred low $\epsilon(\kappa) \ll 1$ values and its approximate κ dependence, as v_{LZ} depends on the intensity via Ω. Furthermore, this sets the timescale for diffusion in phase space longer than the duration of our observations $\gtrsim 2\,\mathrm{ms}$. Hence, we interpret the spatial constraints and effectively static heterogeneity as features of an emergent network structure that is dynamically created during the excitation laser coupling [172].

Spatial disorder

In condensed matter systems, spatial disorder has been observed to be a key ingredient for exotic many-body phases, localization effects and glassy behavior [173]. While there is still much to explore regarding analogous effects of disorder and heterogeneity on the here studied non-equilibrium processes on networks, the appearance of an exotic phase, the so-called Griffiths phase, has been an exciting theoretical prediction [174–176]. This Griffiths phase has been proposed to create an extended critical region around the critical point between the inactive/ subcritical and the active phase with modified non-equilibrium critical properties like power-law dynamical behavior with changing exponents and slow relaxation.

Interestingly, the importance of disorder with associated Griffiths effects could explain open questions regarding our experimental observations.

1. It is challenging to combine the very fast initial growth together with plateau heights well below the system size in a locally homogeneous network (without missing nodes). Fast initial growth requires high κ values compared to Γ, lying in the supercritical region for a locally homogeneous network where the excitation number can grow close to the system size limit. Spatial disorder with a heterogeneous network allows the combination of both features in the simulation such that they match the data (cf. Fig. 5.4a), where rare connected regions allow a fast initial spreading of the excitations, but at the same time limit the final size as they only span over a fraction of the system size.

2. Another important feature are the two phases with a low, close to zero incidence rate $C' \approx 0$ (inactive) and an active phase $C' > 0$ for higher κ values (see Fig. 5.4b). Again, for similar reasons as above, it is very challenging to get agreement for a homogeneous model, where the transition point of the disorder-free absorbing state phase transition is expected at lower $\kappa \lesssim \Gamma$ values [176].

3. We observe power-law behavior with changing exponents in the initial growth (deceleration of growth parameter p) and in the late-time relaxation (relaxation exponents α), varying with facilitated excitation rate κ and associated heterogeneity parameter $\epsilon(\kappa)$ (see Fig. 5.4a,c). Such changing exponents is one defining characteristic of the Griffiths phase [176]. While the experiments were limited to $< 2\,\mathrm{ms}$ to minimize the impact of atom loss, the SIS network simulations were run for much longer times, showing power-law relaxation over two orders of magnitude for the curves with three lowest κ values (Fig. 5.4a).

Consequently, we associate the transition point in the incidence rate at late times C', the deceleration of growth parameter p as well as the late-time power-law relaxation exponent α around $\kappa \approx 6\,\mathrm{kHz}$ (Fig. 5.4b,c) with a transition from an extended Griffiths phase (GP) towards an active phase. The Griffiths phase shows a small late-time activity $C'(2\,\mathrm{ms}) \approx 0$, a changing deceleration of growth parameter $p(\kappa) \lesssim 0.6$ and a power-law relaxation at late times $\alpha < 0$. On the other hand, the active phase has a finite activity $C'(2\,\mathrm{ms}) > 0$, a basically constant deceleration of growth parameter $p \approx 0.6$ and constant plateau height on the observed simulation timescale of up to $160\,\mathrm{ms}$ ($\alpha \approx 0$).

Conclusion

These results establish the applicability of our controllable driven-dissipative Rydberg platform for experimental network science to investigate the connections between simplified numerical models and real-world complex systems dynamics. The introduction and tunability of the Rydberg facilitation process has made possible the discovery of subexponential, power-law growth of the excitation number on an emergent Rydberg network with associated Griffiths effects. In the future it would be interesting to introduce more control on the network structure and the associated heterogeneity via the new optical tweezer setup (cf. Sec. 3.3.3), for example to study the facilitation condition and excitation growth as a function of the distance between microtraps in regular lattices as well as special layouts (e.g. quasi-crystalline Penrose pattern or ring structures as presented in Fig. 3.5), to deliberately introduce disorder and study its effect on the power-law behavior in the Griffiths region, or to access the full spatio-temporal system evolution [169]. The discovery of the importance of spatial disorder in the emergent heterogeneous networks despite the particle motion implies that similar effects could well be present in various non-equilibrium systems, e.g. in noisy room temperature environments [110, 133], and that the complex network approach might be suitable there, too. For example, it would be interesting to check if a susceptible-infected-removed (SIR) network model would be a suitable approach to reproduce the self-organized criticality dynamics observed in the previous chapter 4 and if Griffiths effects could explain the nonuniversal power-law distributions. This might help in better understanding non-equilibrium criticality without fine tuning [72, 110, 177] or for devising effective containment strategies on complex networks [178].

6

Proposal for unitary and non-unitary quantum cellular automata

Sections 6.1-6.6 of this chapter are based on the following publication:
[100] **Unitary and Nonunitary Quantum Cellular Automata with Rydberg Arrays**, T. M. Wintermantel, Y. Wang, G. Lochead, S. Shevate, G. K. Brennen, and S. Whitlock, Physical Review Letters 124, 070503 (2020)

Classical cellular automata (CA) are based on a simple and rather small set of rules, yet they can develop complex dynamics and structures thoughout their evolution, for example emergence in the form of self-organization or complex dynamical structures [13, 179–182]. That is why CA have been proposed and applied to a plethora of domains, ranging from games (e.g. the famous Conway's Game of Life [183, 184]), modelling dynamical physical systems [185] as an alternative to differential equations (for example the Navier-Stokes equation [186]), the formation of complex patterns in nature [187], cryptography [188], up to universal computation (for example it has been shown that the rule 110 cellular automaton is Turing complete [189]). Hence it would be interesting to investigate the corresponding complex effects in its quantum analogue, the quantum cellular automata (QCA) [190–192]. Furtermore, QCA has also been shown to allow for universal quantum computation [193–196]. Hence, this approach might allow for alternative protocols to gate-based [49, 197–199] and adiabatic [200–202] quantum information processing.

In this chapter, we propose a physical system for the implementation of the QCA paradigm based on ultracold Rydberg atoms confined in an array of microtraps [100], motivated by the newly implemented optical tweezer capabilities (Sec. 3.3.3). This approach benefitts from the beneficial properties of Rydberg atoms, like fast multiqubit interactions [61, 107, 197, 203–206] and the possibility of non-trivial dissipative interaction [164, 197, 207–212]. This Rydberg QCA framework is inherently parallelizable, does not require single-site addressing [193–196, 213–216] and takes advantage of unitary and non-unitary interactions.

We first introduce a multifrequency Rydberg excitation scheme which generalizes the two-body Rydberg blockade and facilitation conditions to, in principle, n-body neighborhoods. Applying this multifrequency field to atomic arrays allows for the implementation of QCA rules conditional on the state of the neighbors (Sec. 6.1). The derivation of an effective two-level model (Sec. 6.2) allows for more extensive computational studies of the Rydberg QCA dynamics (Sec. 6.3). One powerful application of the QCA framework is the creation of entangled states: either by a block-partitioned protocol starting from a specific state (Sec. 6.4); or by global addressing in combination with a quantum-classical variational optimization loop (Sec. 6.5), which steers the dissipative QCA dynamics towards highly entangled steady states (Sec. 6.6). The approach to implementing Rydberg QCA presented thus far restricts us to totalistic rules, i.e. rules that only depend on the absolute number of excited neighbors, but not on which side they are. We present a method to expand the Rydberg QCA framework to include non-totalistic rules (Sec. 6.7). Lastly, we compare the Rydberg QCA rules in terms of coupling parameters to the rules used for classical elementary cellular automata (Sec. 6.8).

6.1 Multifrequency Rydberg excitation in atom arrays

The physical platform for implementing cellular automata consists of two main parts: the spatial arrangement of the atoms into well-defined structures and the coupling scheme conditional on the neighborhood. For simplicity, we constrain ourselves to a one-dimensional arrangement and nearest-neighbor interactions, as depicted in Fig. 6.1a, resulting in three-body interaction rules.[1] The ground state atoms (empty symbols) are held in individual optical microtraps, equally spaced by the distance a and laser-coupled to Rydberg states (solid symbols). Let us focus on the three-site neighborhood $j-1$, j and $j+1$. Fig. 6.1b shows the corresponding energy level structure for the atom on site j, where the ground state $|g\rangle$ is coupled to the Rydberg state $|r\rangle$ with Rabi frequency θ^k. The Rydberg state is also coupled via amplitude ϕ^k to a third, short-lived state $|e\rangle$, which then decays to $|g\rangle$ with rate Γ. If we assume that all three atoms in the local neighborhood $j-1$,j,$j+1$ are initially in the ground state $|g\rangle$ (i.e. $k=0$ neighboring Rydberg atoms), the resonance frequencies to couple to the Rydberg state on site j are

$$\begin{aligned}\omega_\theta^{k=0} &= E_r\\ \omega_\phi^{k=0} &= E_r - E_e,\end{aligned}$$

where we have set the reduced Planck constant to $\hbar \equiv 1$. If one of the neighbors is already excited to the Rydberg state with fully isotropic Rydberg interactions, the excitation of site j requires the additional Rydberg-Rydberg interaction energy V. This means, the light fields with frequencies $\omega_\theta^{k=0}$ and $\omega_\phi^{k=0}$, become off-resonant for $k=1$ (Rydberg

---

[1] By including beyond nearest-neighbor interactions or going to spatial geometries in two or three dimensions, one can equally well implement n-body conditional interactions.

blockade effect). On the other hand, a light field which is detuned by V, becomes resonant again (Rydberg facilitation) for one neighboring Rydberg excitation ($k\!=\!1$)

$$\begin{aligned}\omega_\theta^{k=1} &= E_r + V\\ \omega_\phi^{k=1} &= E_r - E_e + V.\end{aligned}$$

The remaining possible configuration is that both neighboring sites are Rydberg atoms ($k = 2$) with fully isotropic and purely additional Rydberg interactions, resulting in twice the interaction energy shift V such that the laser field must be shifted by $2V$ to be resonant

$$\begin{aligned}\omega_\theta^{k=2} &= E_r + 2V\\ \omega_\phi^{k=2} &= E_r - E_e + 2V.\end{aligned}$$

Hence, by compensating the light fields for the interaction shifts kV, we can realize coherent coupling amplitudes θ^k and ϕ^k conditional on the number k of neighbors in $|r\rangle$. Mathematically, we describe the two multifrequency coupling fields as

$$\begin{aligned}\mathcal{E}_j^\theta(t) &= \frac{1}{2}\sum_k \theta_j^k \mathrm{e}^{i(E_r+kV)t} + c.c.\\ \mathcal{E}_j^\phi(t) &= \frac{1}{2}\sum_k \phi_j^k \mathrm{e}^{i(E_r-E_e+kV)t} + c.c.\,.\end{aligned} \tag{6.1}$$

These enter the interaction part of the time-dependent Hamiltonian

$$\hat{H}(t) = \hat{H}_{\text{int}} + \hat{H}_{\text{atom}} = \sum_j (\hat{\sigma}_j^{gr}\mathcal{E}_j^\theta(t) + \hat{\sigma}_j^{er}\mathcal{E}_j^\phi(t) + h.c.) + V\hat{\sigma}_j^{rr}\hat{\sigma}_{j+1}^{rr} + \hat{H}_{\text{atom}} \tag{6.2}$$

with $\hat{\sigma}^{ab} = |a\rangle\langle b|$, $\hat{H}_{\text{atom}} = E_r\hat{\sigma}_j^{rr} + E_e\hat{\sigma}_j^{ee}$ and we restrict to nearest-neighbor interactions V between sites.

We transform to a rotating frame via the unitary transformation $\hat{H}' = \hat{U}^\dagger\hat{H}_{\text{int}}\hat{U}$ where $\hat{U} = \exp(-i\hat{H}_{\text{atom}}t)$ and average out the rapidly varying phases that depend upon E_r and E_e.

Now we can describe the system by a time-dependent quantum master equation in Lindblad form acting on the density matrix ρ

$$\partial_t\rho = \mathcal{L}[\rho] = -i[\hat{H},\rho] + \mathcal{D}[\rho], \tag{6.3}$$

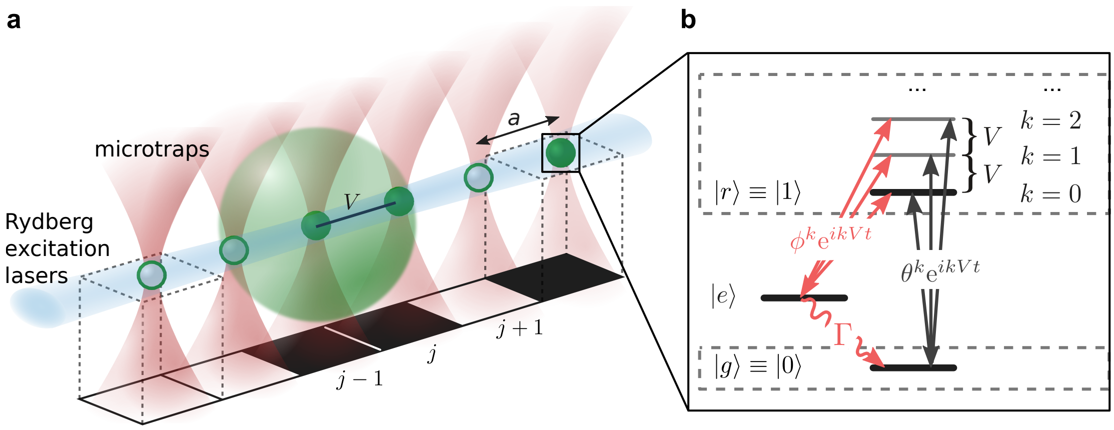

Fig. 6.1: **Quantum cellular automata implementation using atomic arrays together with multifrequency Rydberg excitation.** **a** Optical microtraps allow the controlled spatial atomic arrangement, for example in the shown linear chain. The period a sets the nearest-neighbor Rydberg-Rydberg interaction V (indicated by the green shaded sphere), and open and solid symbols depict the ground state $|g\rangle$ and Rydberg state $|r\rangle$. **b** Multifrequency Rydberg excitation in a three-level system with k neighboring Rydberg atoms allows for couplings conditional on the neighborhood. The ground state $|g\rangle$ is coherently coupled to the Rydberg state $|r\rangle$ with Rabi frequency θ^k. For k neighboring Rydberg atoms, the shift of the $|r\rangle$ resonance by k times the interaction energy V is compensated for by detuning θ^k by the same amount. Dissipation can be induced in a controlled way by the coherent coupling of $|r\rangle$ with Rabi frequency ϕ^k to a short-lived intermediate state $|e\rangle$, which has a fast decay rate Γ back to the ground state. Adapted from [100].

with the Hamiltonian in the rotating wave approximation

$$\hat{H}=\sum_{j,k}\Big(\frac{\theta_j^k}{2}e^{ikVt}\hat{\sigma}_j^{gr}+\frac{\phi_j^k}{2}e^{ikVt}\hat{\sigma}_j^{er}+h.c.\Big)+V\hat{\sigma}_j^{rr}\hat{\sigma}_{j+1}^{rr}, \tag{6.4}$$

where the index j runs over all sites and $k=0,1,2$ over the number of nearest-neighbor Rydberg atoms. Dissipation is included via

$$\mathcal{D}[\rho]=\sum_j \hat{L}_j\rho\hat{L}_j^\dagger-(\hat{L}_j^\dagger\hat{L}_j\rho+\rho\hat{L}_j^\dagger\hat{L}_j)/2, \tag{6.5}$$

where the jump operators $\hat{L}_j=\sqrt{\Gamma}\hat{\sigma}_j^{ge}$ describe the spontaneous decay out of the $|e\rangle$ state. The Rydberg decay $\sqrt{\gamma}\hat{\sigma}_j^{gr}$ is assumed to be much slower than the rest of the dynamics and is neglected for now.

To estimate physical parameters, we consider potassium-39 atoms with a ground state $|g\rangle=|4s_{1/2}\rangle$, an excited state $|e\rangle=|4p_{3/2}\rangle$ and the Rydberg state $|r\rangle=|80s_{1/2}\rangle$. The coherent couplings θ^k from $|g\rangle$ to $|r\rangle$ can be achieved using a two-photon resonance with a large detuning from the intermediate state $|e\rangle$, while ϕ^k can be implemented by a single-photon field. The multiple tones of each light field can be generated from an

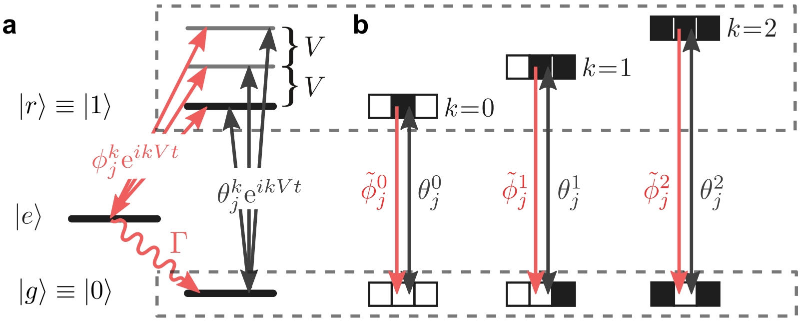

Fig. 6.2: Effective model for quantum cellular automata in Rydberg arrays. **a** Full three-level coupling scheme to Rydberg levels shifted by $k = 0, 1, 2$ neighboring Rydberg atoms. **b** Effective two-level model after elimination of the intermediate state $|e\rangle$ (see text for more details), realizing coherent and dissipative couplings between $|0\rangle$ and $|1\rangle$ on site j conditional on the number k of neighboring sites in $|1\rangle$. Adapted from [100].

electro-optical modulator. An array distance of $a = 6\,\mu\text{m}$ between the atoms translates to an Rydberg-Rydberg interaction energy of $V/2\pi = 50\,\text{MHz}$, which is well resolved compared to the spectroscopic linewidth, so that spurious excitation are very rare. Atom arrays with this resolution can be realized using a digital micromirror device (DMD), as demonstrated in section 3.3.3.

In the following section, we will use these parameters in the numerical investigation of this system for quantum cellular automata.

6.2 Effective two-level description of Rydberg quantum cellular automata

After we developed the conceptual idea in the previous section, we now turn to study the model numerically. The full three-level description allows for preliminary numerical studies, but more extensive ones are limited by the computation time. An effective two-level description derived in this section will speed up the computations and allow for more in-depth numerical studies.

We start from the full Hamiltonian in rotating wave approximation, describing the three-level system in equation (6.4), shown in Fig. 6.2a. The idea is to assume that the nearest-neighbor interaction V and the decay rate Γ are the dominant scales $V \gg \Gamma > \theta_j^k, \phi_j^k$, which allows to neglect non-resonant couplings of the driving field and adiabatically eliminate the intermediate state $|e\rangle$. At first, we transform the Hamiltonian in equation (6.4) to the interaction picture with respect to the nearest-neighbor interaction. The corresponding unitary transformation is $U = \exp\left(-iVt\sum_j \hat{\sigma}_j^{rr}\hat{\sigma}_{j+1}^{rr}\right)$

where $U^\dagger\hat{\sigma}^{\lambda r}U = [\mathrm{P}^0_{j-1} + \mathrm{P}^1_{j-1}e^{-iVt}]\hat{\sigma}^{\lambda r}_j[\mathrm{P}^0_{j+1} + \mathrm{P}^1_{j+1}e^{-iVt}]$ [217], with $\lambda = g, e$, and the projection operators $\mathrm{P}^0_j = 1 - \hat{\sigma}^{rr}_j$ and $\mathrm{P}^1_j = \hat{\sigma}^{rr}_j$. The resulting Hamiltonian is

$$\begin{aligned}
\hat{H}(t) = \sum_j\sum_k & \underbrace{\left(\frac{\theta^k_j}{2}\mathrm{P}^0_{j-1}\hat{\sigma}^{gr}_j\mathrm{P}^0_{j+1} + \frac{\phi^k_j}{2}\mathrm{P}^0_{j-1}\hat{\sigma}^{er}_j\mathrm{P}^0_{j+1}\right)}_{\hat{H}_{k,0}(j)}\mathrm{e}^{ikVt} \\
& + \underbrace{\left(\frac{\theta^k_j}{2}\mathrm{P}^0_{j-1}\hat{\sigma}^{gr}_j\mathrm{P}^1_{j+1} + \frac{\phi^k_j}{2}\mathrm{P}^0_{j-1}\hat{\sigma}^{er}_j\mathrm{P}^1_{j+1} + \frac{\theta^k_j}{2}\mathrm{P}^1_{j-1}\hat{\sigma}^{gr}_j\mathrm{P}^0_{j+1} + \frac{\phi^k_j}{2}\mathrm{P}^1_{j-1}\hat{\sigma}^{er}_j\mathrm{P}^0_{j+1}\right)}_{\hat{H}_{k,1}(j)}\mathrm{e}^{i(k-1)Vt} \\
& + \underbrace{\left(\frac{\theta^k_j}{2}\mathrm{P}^1_{j-1}\hat{\sigma}^{gr}_j\mathrm{P}^1_{j+1} + \frac{\phi^k_j}{2}\mathrm{P}^1_{j-1}\hat{\sigma}^{er}_j\mathrm{P}^1_{j+1}\right)}_{\hat{H}_{k,2}(j)}\mathrm{e}^{i(k-2)Vt} + h.c. \\
= \sum_j\sum_{k,k'} & \hat{H}_{k,k'}(j)\mathrm{e}^{i(k-k')Vt} + h.c. \qquad (6.6)
\end{aligned}$$

In the next step, we perform a second-order adiabatic elimination in the Floquet picture, described in Ref. [218] Eq.(35)

$$\hat{H}' = \sum_k(\hat{H}_{k,k} + \hat{H}^\dagger_{k,k}) + \frac{1}{V}\sum_{k'\neq k}\frac{1}{k'-k}[\hat{H}^\dagger_{k,k'}, \hat{H}_{k,k'}]. \qquad (6.7)$$

The first sum describes resonant coupling whereas the second sum accounts for off-resonant cross-talks (effective light shifts and couplings within manifolds of same k). If we restrict ourselves to the resonant terms only, the time-independent effective Hamiltonian is

$$\hat{H}' = \frac{1}{2}\sum_j\sum_{\alpha,\beta}\mathrm{P}^\alpha_{j-1}\left[\theta^k_j\hat{\sigma}^{gr}_j + \phi^k_j\hat{\sigma}^{er}_j + h.c.\right]\mathrm{P}^\beta_{j+1}, \qquad (6.8)$$

with the projection indices $\alpha, \beta = \{0, 1\}, k = \alpha + \beta$.

As a last step, we have to include the spontaneous decay described by the jump operator $\hat{L}_j = \sqrt{\Gamma}\hat{\sigma}^{ge}_j$ into our effective description. Again, we adiabatically eliminate the short-lived $|e\rangle$ states and derive effective jump operators L^{eff}_j acting on the g, r subspace using the effective operator formalism accoridng to Ref. [219]. With the slow and fast subspaces $\mathbb{P}\sigma^{e\alpha}_j = 0$ and $\mathbb{Q}\sigma^{e\alpha}_j = \sigma^{e\alpha}_j$ ($\alpha = g, r$) the non-Hermitian Hamiltonian is

$$\hat{H}_{nh} = \mathbb{Q}\hat{H}'\mathbb{Q} - \frac{i}{2}\sum_j\hat{L}^\dagger_j\hat{L}_j. \qquad (6.9)$$

We assume $\Gamma \gg |\phi_k|$, meaning that we can neglect states with more than one $|e\rangle$ state. In this case the first term is zero and we are left with

$$\hat{H}_{nh} = -\frac{i\Gamma}{2}\sum_j \hat{\sigma}_j^{ee}, \tag{6.10}$$

which enters into the effective Hamiltonian

$$\hat{H}^{\text{eff}} = \mathbb{P}\hat{H}'\mathbb{P} - \underbrace{\frac{1}{2}\mathbb{V}^-[\hat{H}_{nh}^{-1} + (\hat{H}_{nh}^{-1})^\dagger]\mathbb{V}^+}_{=0} = \frac{1}{2}\sum_j\sum_{\alpha,\beta} \mathrm{P}_{j-1}^{\alpha}\left[\theta_j^k\hat{\sigma}_j^{gr} + (\theta_j^k)^*\hat{\sigma}_j^{rg}\right]\mathrm{P}_{j+1}^{\beta}, \tag{6.11}$$

with $\mathbb{V}^- = \mathbb{P}\hat{H}'\mathbb{Q}$ and $\mathbb{V}^+ = \mathbb{Q}\hat{H}'\mathbb{P}$. In the first step, we use that the inverse of $\hat{H}_{nh}$ is a purely imaginary diagonal matrix such that the two terms in the bracket fully subtract each other. Now, the effective jump operators are

$$\begin{aligned}\hat{L}_j^{\text{eff}} &= \hat{L}_j\hat{H}_{nh}^{-1}\mathbb{V}^+ = \frac{i}{\sqrt{\Gamma}}\hat{\sigma}_j^{ge}(\sum_i \hat{\sigma}_i^{ee})^{-1} \times \mathbb{Q}\sum_{i'}\left(\sum_{\alpha,\beta}\mathrm{P}_{i'-1}^{\alpha}[\theta_j^k\hat{\sigma}_{i'}^{gr} + \phi_j^k\hat{\sigma}_{i'}^{er} + h.c]\mathrm{P}_{i'+1}^{\beta}\right)\mathbb{P} \\ &= \frac{i}{\sqrt{\Gamma}}\sum_{\alpha,\beta}\mathrm{P}_{j-1}^{\alpha}\phi_j^k\hat{\sigma}_j^{ge}(\hat{\sigma}_j^{ee})^{-1}\hat{\sigma}_j^{er}\mathrm{P}_{j+1}^{\beta} = \frac{i}{\sqrt{\Gamma}}\sum_{\alpha,\beta}\phi_j^k\mathrm{P}_{j-1}^{\alpha}\hat{\sigma}_j^{gr}\mathrm{P}_{j+1}^{\beta}.\end{aligned} \tag{6.12}$$

We use $(\sum\hat{\sigma}^{ee})^{-1}\mathbb{Q} = (\sum\hat{\sigma}^{ee})^{-1}$ and that the action of $\mathbb{P}$ from the right hand side changes $\mathrm{P}_{j\pm1}^0 \to |g\rangle\langle g|_{j\pm1}$ and restricts $\hat{\sigma}_{i'}^{er}$ to states that initially have no $|e\rangle$ excitations, i.e. exactly one $|e\rangle$ at site i' after application of the operator, which allows us to remove the sums over i, i'.

In summing up, we arrive at the effective master equation for the dynamics

$$\partial_t\rho = \mathcal{L}^{\text{eff}}[\rho] = -i[\hat{H}^{\text{eff}}, \rho] + \mathcal{D}_{\hat{L}^{\text{eff}}}[\rho] \tag{6.13}$$

with the effective Hamiltonian and Lindbladian terms

$$\hat{H}^{\text{eff}} = \frac{1}{2}\sum_j\sum_{\alpha,\beta}\theta_j^k\mathrm{P}_{j-1}^{\alpha}\hat{X}_j\mathrm{P}_{j+1}^{\beta}, \tag{6.14}$$

$$\hat{L}^{\text{eff}} = \frac{1}{2}\sum_j\sum_{\alpha,\beta}\sqrt{\tilde{\phi}_j^k}\mathrm{P}_{j-1}^{\alpha}(\hat{X}_j - i\hat{Y}_j)\mathrm{P}_{j+1}^{\beta}, \tag{6.15}$$

where $\sqrt{\tilde{\phi}_j^k} \approx \phi_j^k/\sqrt{\Gamma}$, $\theta_j^k \in \mathbb{R}$ and $\hat{X}_j, \hat{Y}_j, \hat{Z}_j$ are Pauli matrices. As a reminder, $\alpha, \beta = \{0, 1\}, k = \alpha + \beta$ and the projector $\mathrm{P}^\alpha = |\alpha\rangle\langle\alpha|$. We depict this effective model in Fig. 6.2b alongside the full three-level system (Fig. 6.2a). This model realizes coherent θ_j^k and dissipative ϕ_j^k couplings between $|g\rangle \equiv |0\rangle$ (open symbols) and $|r\rangle \equiv |1\rangle$ (solid symbols) conditional on the number of Rydberg excitations k on sites $j-1$ and $j+1$. This

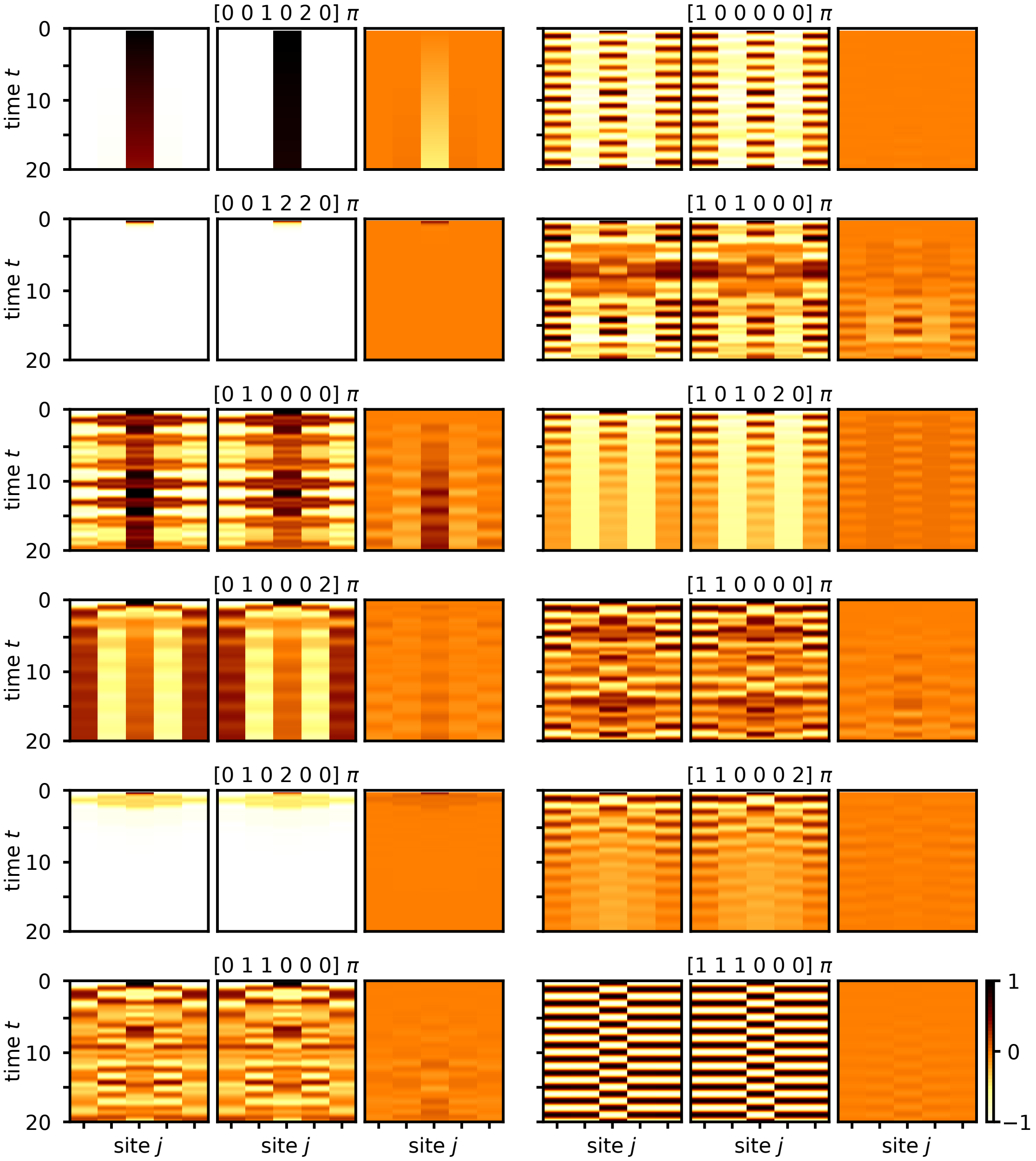

Fig. 6.3: Comparing the time dynamics resulting from the full three-level description and its effective two-level counterpart for 12 representative QCA rules. The label of each subfigure indicates the chosen parameter set in the notation $[\theta^0, \theta^1, \theta^2, \tilde{\phi}^0, \tilde{\phi}^1, \tilde{\phi}^2]$. The continuous time evolution of the magnetization $\langle Z_j \rangle$ on site j, represented via the shown colormap, is calculated for 20 time units for a linear chain of five sites with open boundary conditions, starting from the initial state $|00100\rangle$. A magnetization of 1 (black) indicates a pure Rydberg excitation $|1\rangle$ whereas value of -1 (white) indicates the full ground state $|0\rangle$. Each subfigure in turn consists of three panels: *left:* three-level master equation simulation including time-dependent couplings, *center:* effective two-level master equation simulation and *right:* difference of the magnetization $\langle Z_j \rangle$ between the three-level and two-level results.

effective PXP model [211, 220–224] will allow us to realize different totalistic QCA rules.

Now we numerically compare the full three-level model equations (6.3), (6.4), (6.5) and the corresponding effective two-level model equations (6.14), (6.15), which are solved using a linear multistep method and the QuTiP package [225]. We define a QCA rule by the driving strengths $[\theta^0, \theta^1, \theta^2, \tilde{\phi}^0, \tilde{\phi}^1, \tilde{\phi}^2]$ of the coherent (first three parameters) and dissipative (last three parameters) couplings in MHz. For now, we consider global coupling fields, which act simultaneously on the whole array and hence we drop the spatial index j. Fig. 6.3 shows the time evolution of the magnetization $\langle Z_j \rangle$ for 12 representative QCA rules (out of the $2^6 = 64$ possible binary combinations of the six coupling parameters θ^k, $\tilde{\phi}^k$) by solving the full three-level master equation (left panel), the effective two-level description (central panel) and the difference between both for better comparison (right panel). The coupling parameters are indicated in the label of each subfigure, with $\phi^k = \sqrt{\Gamma \tilde{\phi}^k}$. The other parameters are the nearest-neighbor Rydberg interaction energy $V = 50\pi$ (in units where $t = 1$), the intermediate decay rate $\Gamma = 6\pi$ and the Rydberg decay rate $\gamma = 8\pi \cdot 10^{-4}$. The initial state, where only the central one of the five sites is in $|1\rangle$ and all others are $|0\rangle$, is evolved for 20 time units. The boundary condition between the first and fifth site is open.

Generally, we observe good agreement between the results of the full and the effective model, visible by a homogeneously orange right panel. For a few rules we see a small discrepancy, which is not surprising as the above parameters are close to the limit of validity of the hierarchy scale $V \gg \Gamma \gg (\theta^k, \phi^k) \gg \gamma$, used in approximations in deriving the effective model. In rule $[0, 0, 1, 0, 2, 0]\,\pi$ (*top-left*), we only have resonant couplings between $|0\rangle \leftrightarrow |1\rangle$ for two neighboring $|1\rangle$ states ϕ^2 and for one neighboring state $|0\rangle$ and $|1\rangle$ each ϕ^1. The initial state $|00100\rangle$ is dark with respect to these two couplings, hence we see no temporal change for the effective two-level case. However, the excited state population decays with a time constant of about 50 time units in the three-level case. We can attribute the decay to slow off-resonant depumping caused by the $\phi^{k=1}$ coupling acting on the $k = 0$ subspace, which is neglected in the effective model. Hence, increasing V/Γ would reduce this off-resonant effect and improve the agreement.

In the following section, we use this effective two-level description to have a closer look at the dynamics resulting from the different QCA rules.

6.3 Complex dynamics with totalistic rules

In this section we will deploy the effective two-level Hamiltonian to numerically investigate the interesting, complex dynamics that can emerge in this QCA implementation with totalistic rules, i.e. rules that only depend on the number of excited neighbors. Furthermore, we compare the continuous time evolution with its discrete, block-partitioned counterpart.

The formal solution of the effective Lindblad equation (6.13) can be written as

$$\rho(t) = (\hat{M})^t \rho(0), \tag{6.16}$$

where $\hat{M} = \exp(\mathcal{L}^{\text{eff}})$ and $\rho(0)$ is the density matrix of the initial state. Now we present two distinct cases of how to time-evolve the QCA system:
(i) Continuous-time, global evolution: We take time t as a continuous variable and assume global addressing, meaning that the coupling lasers are applied to the whole array simultaneously, hence the operator $\hat{M}$ acts on all sites and we can drop the spatial index. Fig. 6.4a illustrates the continuous QCA rule $[\theta^0, \theta^1, \theta^2, \tilde{\phi}^0, \tilde{\phi}^1, \tilde{\phi}^2] = [0, 1, 0, 0, 0, 2]\pi$ for $N = 9$ sites, starting from the initial state $|000010000\rangle$ and for open boundary conditions. The two active couplings θ^1 and $\tilde{\phi}^2$ act continuously on the whole chain. θ^1 coherently couples the two states on site j, if j has one excited neighbor in $|1\rangle$, whereas the dissipative down-pumping $\tilde{\phi}^2$ is conditional on two neighboring excitations. As sketched in Fig. 6.4c, continuous time evolution together with open boundary conditions could be experimentally achieved by a linear atom array with a single Rydberg excitation beam (shaded blue). This is analogue to the approach we have already presented in the previous section 6.1.
(ii) Discrete-time, block-partitioned evolution: Here we restrict the time steps to full π-pulses between the two states $|0\rangle$ and $|1\rangle$, such that the resulting states are restricted to the binary subspace of $|0\rangle$ and $|1\rangle$, similar to classical cellular automata. To achieve this, we have to apply the operations in a block-partitioned scheme by separating the array into two subarrays A and B of odd and even sites [216]. This way, the two neighboring sites (inactive sublattice) stay unaltered during the operations acting on the central site j (active sublattice). Otherwise, the full population transfer would be hindered by the state changing neighbors controlling the couplings on site j. The operator $\hat{M}_A$ ($\hat{M}_B$) acts only on the A (B) sites. For simplicity, we take the same values of the coupling parameters for both lattices. One time step corresponds to consecutively updating both sublattices by applying the operator $\hat{M} = \exp(\mathcal{L}_B)\exp(\mathcal{L}_A)$. The strength of the coherent rules θ is restricted to 0 and π, where a value of π realizes a full transfer in between the two levels ($|0\rangle$ and $|1\rangle$) for each of the two sublattices. For the dissipative rules, it corresponds to jump probabilities of 0 and $1 - \exp(-2\pi)$, respectively.
Fig. 6.4b illustrates the discrete, block-partitioned time evolution of rule $[0, 1, 0, 0, 0, 2]\,\pi$. The two active couplings θ^1 and $\tilde{\phi}^2$ act in alternation on one of the two sublattices, as illustrated to the left of the vertical time axis. The initial state is dark with respect to the couplings θ^1_A and $\tilde{\phi}^2_A$, so it stays unchanged in $|000010000\rangle$. Next, θ^1_B rotates the neighboring B sites $j = 4$ and $j = 6$ up to the state $|000111000\rangle$. Now a full AB update

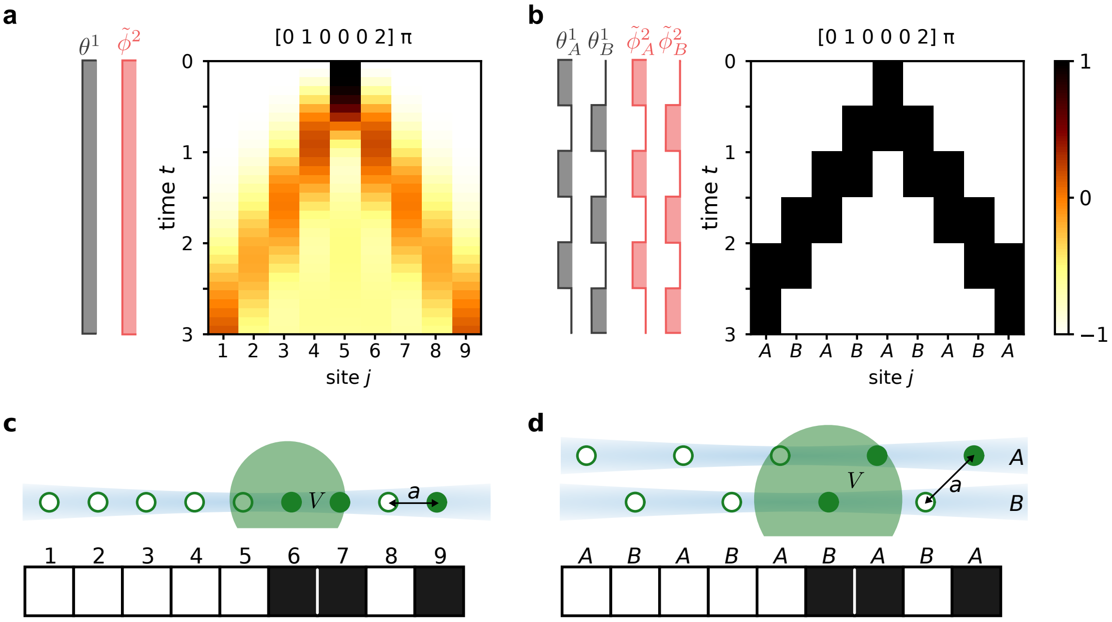

Fig. 6.4: **Continuous-time and discrete-time quantum cellular automata rules.** **a** Continuous time evolution of the magnetization $\langle Z_j \rangle$ (color coding) for the rule $[\theta^0, \theta^1, \theta^2, \tilde{\phi}^0, \tilde{\phi}^1, \tilde{\phi}^2] = [0, 1, 0, 0, 0, 2]\,\pi$. A magnetization of 1 (black) indicates a Rydberg excitation $|1\rangle$ whereas value of -1 (white) indicates the ground state $|0\rangle$. The $N = 9$ sites are initialized in $|000010000\rangle$. The two active couplings θ^1 and $\tilde{\phi}^2$ are continuously applied to the whole array. The coherent coupling θ^1_j (dissipative down-pumping $\tilde{\phi}^2$) is conditional on having one (two) excited neighbor(s). **b** Corresponding discrete-time, block-partitioned evolution of the same rule. Here, the two active couplings θ^1 and $\tilde{\phi}^2$ act alternately on sublattice A or B, as depicted by the pulse sequence left to the vertical time axis. The initial state is dark with respect to the couplings θ^1_A and $\tilde{\phi}^2_A$, so the state stays unchanged in $|000010000\rangle$. Next, the B sites are updated, where θ^1_B rotates the sites $j = 4$ and $j = 6$ up to the state $|000111000\rangle$. Now a full AB update cycle is finished and it starts from the beginning with the A sites, where $\tilde{\phi}^2_A$ pumps the central site down and ϕ^1_A rotates $j = 3$ and $j = 7$ up etc. **c** Sketch of an experimental setup for continuous Rydberg QCA, where atoms are held in a linear array of microtraps and are coupled to Rydberg states (solid symbols) by an excitation laser (blue shading). The corresponding QCA state string is portrayed at the bottom. **d** Possible implementation of discrete time evolution with $ABABA..$ block partitioning, where we can individually address the odd A and even B sites with two distinct excitation beams.

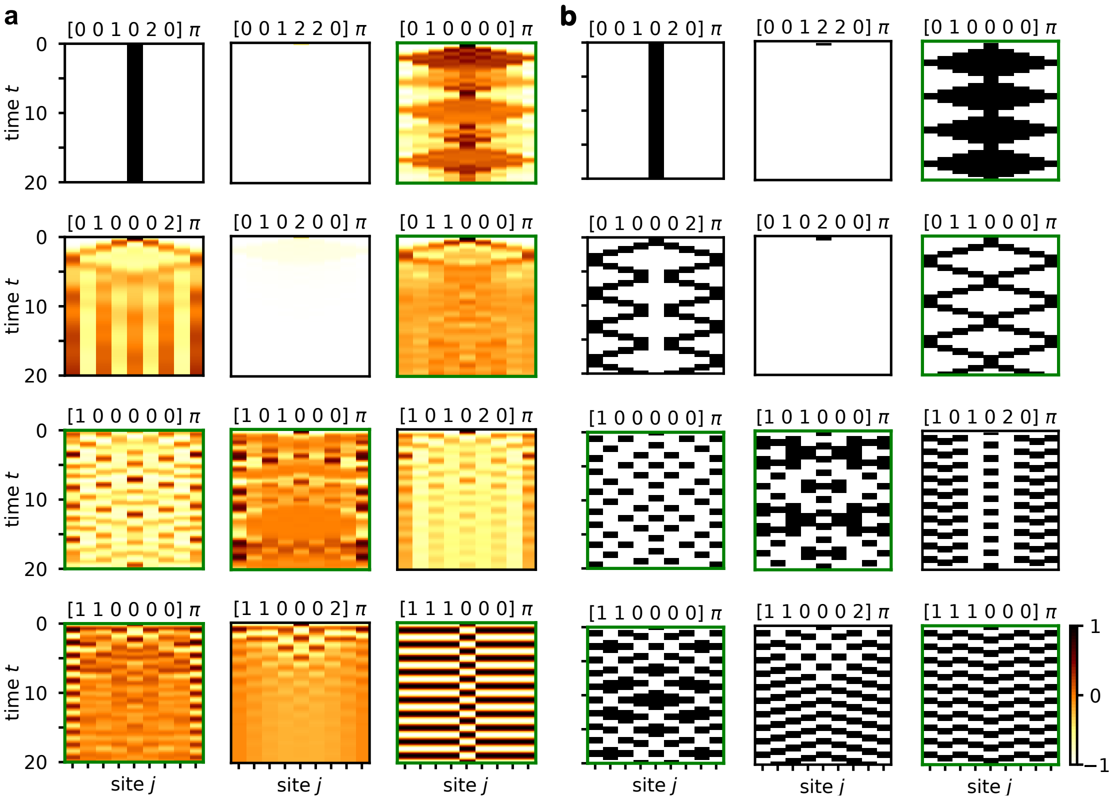

Fig. 6.5: Numerical simulation of the dynamics for 12 representative Rydberg QCA rules. **a** Continuous time evolution of the magnetization $\langle Z_j \rangle$ (encoded by the colormap) without block partitioning. A magnetization of 1 (black) indicates a Rydberg excitation $|1\rangle$ whereas value of -1 (white) indicates the ground state $|0\rangle$. The $N = 9$ sites are initialized in $|000010000\rangle$ and then time-evolved for 20 time units using the effective two-level model with open boundary conditions, neglecting additional Rydberg decay. The label of each subfigure depicts the coupling strengths in the notation $[\theta^0, \theta^1, \theta^2, \tilde{\phi}^0, \tilde{\phi}^1, \tilde{\phi}^2]$. The green borders highlight fully coherent rules, where only θ^k couplings are present. **b** Corresponding discrete time evolution via block partitioning $ABABABABA$, where the discrete timings realize full π pulses of the coherent couplings between both states (see text for more details). Adapted from [100].

step is finished, corresponding to a time $t = 1$. Next, the update process starts again from the beginning with the A sites. Then $\tilde{\phi}_A^2$ pumps the central site down while ϕ_A^1 rotates $j = 3$ and $j = 7$ up to the state $|001101100\rangle$. Subsequently, θ_B^1 acts on $j = 2$ and $j = 8$ as well as $j = 4$ and $j = 6$, yielding $|011000110\rangle$. Fig. 6.4d presents a possible physical implementation, where we use a zigzag chain to allow for separate addressing of the sites in the two sublattices A and B by two separate Rydberg beams (blue shading). Alternatively, it also works in a linear chain, if the even and odd sites can be addressed separately by the Rydberg excitation light, e.g. in a setup similar to Ref. [9].

Fig. 6.5 shows the same 12 representative Rydberg QCA rules for (i) continuous (subfigure a) and (ii) discrete, block-partitioned (subfigure b) time evolution according to the coupling parameters shown in the label of each subfigure. The colormap encodes temporal evolution of the magnetization $\langle Z_j \rangle$ on site j for 20 time units, where white (black) colors indicate the state $|0\rangle$ ($|1\rangle$). The evolution of the effective two-level model starts from the initial state, where only the central of the 9 sites is in the $|1\rangle$ state, while all the other sites are initialized to $|0\rangle$. We assume open boundary conditions between the first and last site. The green borders indicate rules where only coherent θ^k couplings are present. For this exploratory simulations here, we will restrict ourselves to binary coupling values of 0 or 1. First of all, the dynamics resemble the classical cellular automata, for example a fixed point (e.g. $[0,0,1,2,2,0]\,\pi$, $[0,0,1,2,0,0]\,\pi$), periodic (e.g. $[0,1,0,0,0,0]\,\pi$, $[1,1,1,0,0,0]\,\pi$) and complex/fractal-like (e.g. $[1,0,0,0,0,0]\,\pi$, $[1,1,0,0,0,0]\,\pi$) behavior [226]. For a few special rules, the behavior for discrete and continuous time is identical (e.g. $[0,0,1,0,2,0]\,\pi$) or quite similar (e.g. $[0,0,1,2,2,0]\,\pi$). But in general, the initial similarity becomes washed out as the continuous time evolution loses contrast. Now let us look at a few rules in more detail:

- $[0,0,1,0,2,0]\,\pi$: The initial state $|000010000\rangle$ is dark with respect to both the active couplings, as θ^2 acts only for two neighboring $|1\rangle$ while $\tilde{\phi}^1$ is conditional on one neighbor in $|0\rangle$ and the other in $|1\rangle$. This rule looks identical for (i) continuous and (ii) discrete, block-partitioned time evolution.

- $[0,0,1,2,2,0]\,\pi$: The coupling $\tilde{\phi}^0$ acts on the central site $j=5$, which has both neighbors in $|0\rangle$. (i) In the discrete case, this site is pumped down into the $|0\rangle$ with jump probability of $1-e^{-2\pi}$ per time unit. (ii) In the continuous time plot, we observe the corresponding gradual decay of the magnetization.

- $[0,1,0,0,0,0]\,\pi$: (i) In the continuous-time case with global addressing, the coherent coupling θ^1 initially still acts on the sites $j=4,6$ next to the central site and starts to rotate their state vector up. However, as these sites develop into a superposition $\alpha\,|0\rangle+\beta\,|1\rangle$, the central site has $|0\rangle$ and $|1\rangle$ components as neighbors and θ^1 rotates the central site simultaneously down. We see this rotation down on site $j=5$ while $j=4,6$ rotate up during the first time unit. In general, this application of the couplings to all sites at the same time leads a visible loss of contrast. Still, θ^1 leads to an overall spreading of the initial central excitation up to the system borders. (ii) Now we check see how block partitioning with discrete time steps changes the systems response. The central site is part of the A sublattice. In the first update step, the coupling θ^1_A has no effect as there is no odd site with a $|0\rangle$ and $|1\rangle$ neighbor. Subsequently, on the even B sites, $j=4$ and $j=6$ fulfill this condition and are flipped up to $|1\rangle$. In the second time step, the A sites $j=3,7$ and subsequently B sites $j=2,8$ are flipped to $|1\rangle$ (each of these flips/steps are visible in the plot). Due to the block partitioning, the inner sites are protected against rotations back down. This continues up until the border $j=1,9$ are flipped up. As the open boundary conditions are equivalent to two additional fictitious sites at the two ends, which are fixed to $|0\rangle$, the border sites are rotated down again in the next A update. This effectively leads to a reflection, and the inverse process flips down the sites again while propagating the $|0\rangle - |1\rangle$ border to the center, where the processes start from the beginning, resulting in the periodic structure. We already see, that boundary effects have an important influence on the resulting dynamics in finite systems sizes. Despite different contrasts, we see a qualitatively similar behavior between the continuous and discrete time case. There are differences though, such as a stretched period of the darker rhombi and additional weaker structures in between for the continuous update scheme.

- $[0,1,1,0,0,0]\,\pi$: Compared to the previous rule, there is an additional coherent coupling θ^2 for two $|1\rangle$ neighbors. (i) The loss of contrast is strong after a time of $t \approx 5$. Since this is one of the fully coherent rules, this loss of contrast is not due to dissipation/decoherence, but could be explained by the build up of entanglement during QCA evolution. (ii) θ^2 rotates the central site back down to $|0\rangle$ during the second time unit, which lifts the protection of the inner sites against θ^1, hence the inside of the rhombi are $|0\rangle$ states. Furthermore, the period time is longer compared to before.

- $[0,1,0,0,0,2]\,\pi$: Instead of the coherent coupling, this rule has a dissipative coupling $\tilde{\phi}^2$ for two $|1\rangle$ neighbors. (i) The continuous time evolution without block partitioning shows a very different structure after about $t = 5$. After an initial rhobus structure, an antiferromagnetic periodicity in space develops, where the central site is $|1\rangle$ now. In fact the dynamics seem to develop towards a non-trivial steady state $|101010101\rangle$. This can be under stood in term of dark state engineering, as the state $|101010101\rangle$ is dark with respect to the applied couplings θ^1 and $\tilde{\phi}^2$. (ii) As the dissipative coupling is one-directional downwards, the central site is not rotated back up after one periodicity and stays in $|0\rangle$. Otherwise the dynamics is similar to the previous rule, except for a slightly smaller time period.

- $[1,1,1,0,0,0]\,\pi$: Both, discrete and continuous time evolution show very similar results. Especially, when considering that the small spatial zigzag pattern for case (ii) is an artifact that stems from the subsequent discrete updating of the two sublattices.

- $[1,1,0,0,0,0]\,\pi$: The two panels show different behavior, especially due to the drastic loss of contrast in case (i). Since this is another of the solely coherent rules, this loss of contrast is again not due to dissipation/decoherence, but could be explained by the build up of entanglement.

Despite the results presented here we just a first exploration of a small subset of all possible QCA dynamics, we saw that the different totalistic Rydberg QCA rules allow for

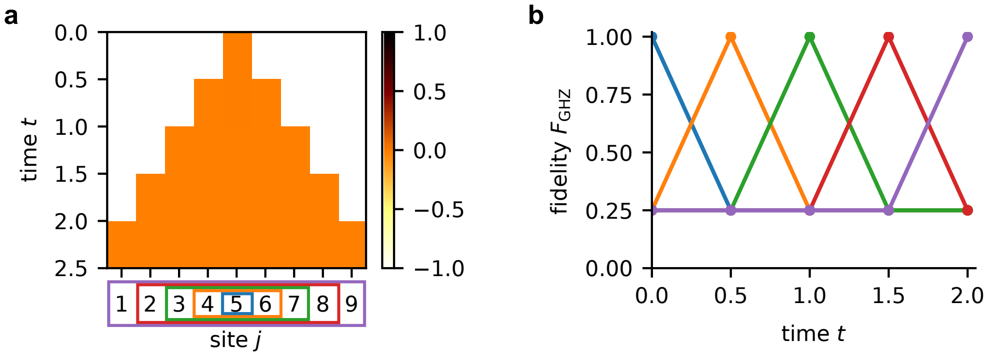

Fig. 6.6: **Creation of entanglement in discrete, block-partitioned QCA. a** State of the sites during the entanglement generation protocol, characterized by the magnetization $\langle Z_j \rangle$, encoded via the colormap. In the initial state at $t=0$, all sites are in $|0\rangle$, except for the central site, which is in an equal superposition of $|0\rangle$ and $|1\rangle$ with magnetization zero. **b** Fidelity between the resulting state after each update step with the GHZ^N state of the central N sites. As also highlighted on the x labels in subfigure a, the blue, orange, green, red and purple lines correspond to $N=1,3,5,7$ and 9. At the end of the protocol, we end up with the GHZ state of 9 entangled sites.

a broad variety of interesting dynamics, for example a spatially antiferromagnetically ordered steady state. Note that the presented rules are only a tiny subset of all possible rules and corresponding dynamics that could be expanded upon, for example, by allowing arbitrary amplitudes in the coupling parameters or temporal sequences of different rules. In the following two sections, we will investigate, how we can use QCA to prepare desired states in a more deterministic way.

6.4 Creation of entangled states using block partitions

In the previous section we saw that even fully coherent QCA dynamics seemed to lead to a loss of coherence which we attributed to entanglement. In this section we will explore this further by purposefully generating the maximally entangled Greenberger–Horne–Zeilinger (GHZ) state [227, 228] using the quantum cellular automata formalism [216] in a linear chain with 9 sites, block-partitioned into $ABABABABA$:

1. We start in the initial state $|0000\rangle \otimes \frac{1}{\sqrt{2}}(|0\rangle + |1\rangle) \otimes |0000\rangle$, where the central site is in an equal superposition of $|0\rangle$ and $|1\rangle$ and all other sites are in $|0\rangle$.
2. Apply the rule $[0,1,0,0,0,0]\,\pi$ to even sites B. Remember, that this coupling strength corresponds to a full population transfer between $|0\rangle$ and $|1\rangle$. This creates the state $|000\rangle \otimes \frac{1}{\sqrt{2}}(|000\rangle + |111\rangle) \otimes |000\rangle$.
3. Apply the rule $[0,1,0,0,0,0]\,\pi$ to even sites A, yielding the state $|00\rangle \otimes \frac{1}{\sqrt{2}}(|00000\rangle + |11111\rangle) \otimes |00\rangle$.

4. Continue this procedure until the entanglement has propagated up to the border, i.e. for an odd number of sites N, this requires $(N-1)/2$-times application of rule $[0,1,0,0,0,0]\,\pi$ alternately on both sublattices.

Now that we have understood the idea behind the method, we can turn to the corresponding simulation using the effective two-level Rydberg QCA model. In Fig. 6.6a, we see the magnetization along z encoded in the color map. For the initial state ($t=0$), the magnetization $\langle Z_j \rangle$ is -1, corresponding to the $|0\rangle$ state, except for the central site, which is in the superposition $1/\sqrt{2}(|0\rangle + |1\rangle$ with $\langle Z_0 \rangle = 0$. At time $t=0.5$, we applied the rule the first time on the odd site, such that the region with zero magnetization along z increases by the two neighboring sites. At $t=1$, a full update cycle of both the two sublattices is finished, resulting in the central 5 sites being in the GHZ state. After another full update cycle at $t=2$, the entanglement has propagated up to the borders. Fig. 6.6b presents this propagation of the entanglement more quantitatively as the fidelity between the density matrix ρ of the N central sites and the $\mathrm{GHZ}^N = |0\rangle^{\otimes N} + (-1)^{\frac{N+3}{2}} |1\rangle^{\otimes N}$ state with $N=1,3,5,7,9$

$$F_{\mathrm{GHZ}} = \mathrm{Tr}\left[\sqrt{\sqrt{\rho}\,|\mathrm{GHZ}^N\rangle\langle \mathrm{GHZ}^N|\,\sqrt{\rho}}\right]^2 . \tag{6.17}$$

The blue, orange, green, red and purple line corresponds to $N=1,3,5,7,9$, as also highlighted on the x labels of subfigure a. As all the GHZ^N states have $|0\rangle^{\otimes N}$ in common, the baseline fidelity is at 0.25. Inspecting the fidelities at different times, we can confirm that the GHZ^3, GHZ^5, GHZ^7 and GHZ^9 state is created after after $1, 2, 3$ and 4 update steps. Once having created the GHZ^N state, we can also easily access the antiferromagnetic GHZ^N state $1/\sqrt{2}(|010101010\rangle + |101010101\rangle)$ by applying the rule $[1,0,1,0,0,0]\,\pi$ to the B sites for example.

This is an efficient procedure to produce the GHZ state, slightly faster than the recent demonstration of using an adiabatic sweep in Ref. [229]. However, this protocol requires a precise initial state and addressing of the two sublattices with precise timings for the π pulses. For experimental ease, we will investigate an alternative protocol in the next section, which lift these requirements, i.e. which work with global addressing in continuous time and which are independent of the initial state.

6.5 Hybrid quantum-classical variational optimization

The Rydberg QCA architecture based upon tunable, conditional, coherent and dissipative interactions offers a large variety of possible dynamics. At the same time, it is challenging to find the parameter set giving the desired dynamics or output state. In this section, we will introduce a hybrid quantum-classical optimization loop, which is based on the variational principle [230] and has been successfully demonstrated for finding ground states of unitary quantum systems [231–234]. We will investigate which optimization algorithm is most suited to steer the non-unitary QCA dynamics in continuous, global time evolution (without block partitioning) towards useful quantum states.

Fig. 6.7a depicts the physical system that we consider: six sites which are arranged in a ring structure with spacing a to implement closed boundary conditions. This could be achieved using our DMD microtrap setup (Sec. 3.3.3) or a setup similar to Ref. [235]. The Rydberg coupling beam (shaded blue) addresses all sites simultaneously for continuous-time Rydberg QCA evolution.

The goal of this section is to devise a method to steer the quantum evolution in this system towards useful states. This means we need an objective function $\langle C\rangle$[2] for which we seek the best parameter set $\vec{\theta}, \vec{\phi}$. However, the quantum-mechanical calculation of the expectation values can be computationally very demanding. That is where the hybrid quantum-classical optimization comes into play (see Fig. 6.7b): We start with an initial guess for the parameters $\vec{\theta}, \vec{\phi}$. The quantum system evolves according to the given rule towards the corresponding trial state $\rho(\vec{\theta}, \vec{\phi})$. Subsequently, we measure certain observables, in our case the magnetization along z via the Pauli matrices $\langle Z_j\rangle$ and $\langle Z_j Z_{j+1}\rangle$. These values are used to calculate the corresponding value of the objective function $\langle C\rangle$. The classical optimization algorithm compares this value with the target value and chooses new trial parameters, trying to approach the target value. Now, one iteration of the optimization loop has finished and a new loop starts over again with these new trial parameters.

In the following proof of principle demonstration, the classical optimization uses methods provided by the Pygmo package [236, 237], which offers various optimization algorithms. We restrict the search space for each parameter in the QCA rule $[\theta^0, \theta^1, \theta^2, \tilde{\phi}^0, \tilde{\phi}^1, \tilde{\phi}^2]$ to the range $[0, \pi]$. The QCA system consists of six sites in a linear array with periodic boundary condition. We start from the initial state $|000000\rangle$ (but we observe similar results for different initial states) and solve for the steady state of the Rydberg QCA dynamics again using the QuTiP package [225]. In Fig. 6.7c, we compare the convergence for minimizing the cost function $\langle C\rangle$ (see Sec. 6.6 for more details) as a function of the loop iterations for five algorithms: differential evolution (DE, blue) [238], self-adaptive differential evolution (DE 1220, orange) [237], artificial bee colony algorithm (green) [239, 240], particle swarm optimization (PSO, red) [241, 242] and generational particle swarm optimization (GPSO, purple) [237]. The solid line and the shaded area depict the mean and the standard deviation over 10 optimization runs with in total 100 individual population trajectories. We see that the two particle swarm optimization

---

[2] See next section 6.6 for the definition of the objective function.

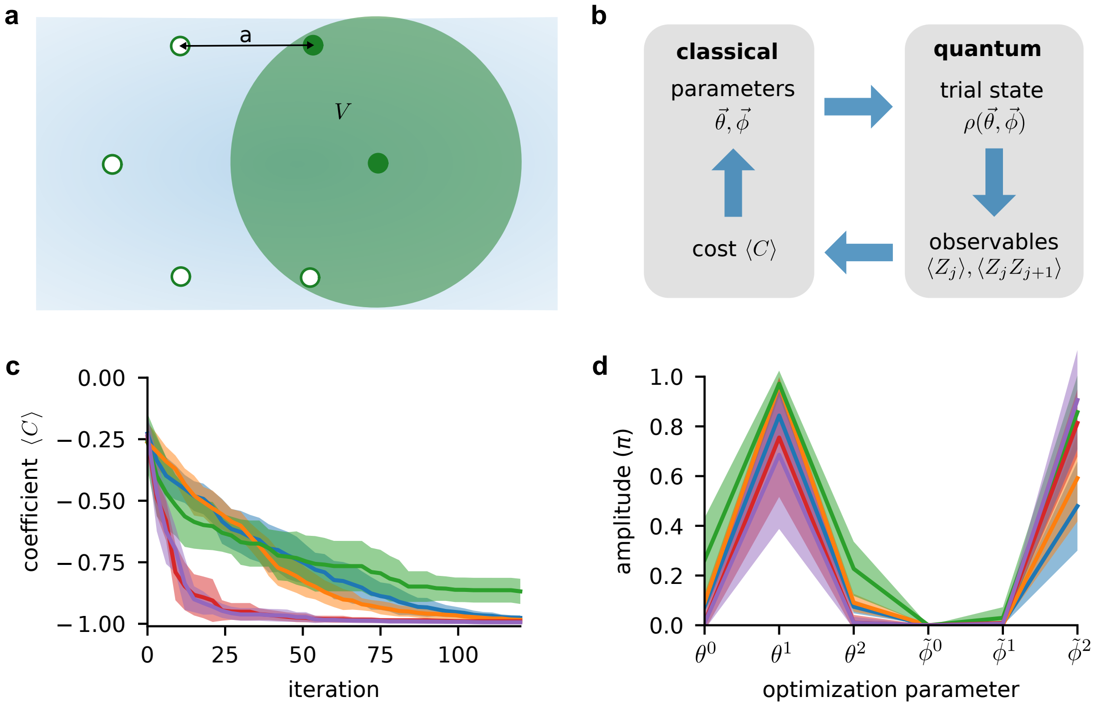

Fig. 6.7: **Variational optimization on the Rydberg QCA dynamics. a** Experimental system for Rydberg quantum cellular automata, which will be steered by the optimization loop. We assume $N = 6$ sites, spaced by distance a with nearest-neighbor Rydberg-Rydberg interaction V (indicated by the green shaded circle), which are globally addressed by the Rydberg coupling laser beam (shaded blue) for continuous-time evolution. Closed boundary conditions are realized by the ring shape. **b** Hybrid quantum-classical variational optimization loop. The loop starts with a parameter set $\vec{\theta}, \vec{\phi}$ governing the QCA evolution towards a trial state with density matrix $\rho(\vec{\theta}, \vec{\phi})$. Subsequently, the expectation values of the magnetization along the quantization axis z, $\langle Z_j \rangle$ and $\langle Z_j, Z_{j+1} \rangle$, are measured in the quantum system. The results are fed back to compute a classical cost function $\langle C \rangle$. For this, a classical optimization algorithm generates a new trial set of parameters, trying to optimize the cost. This starts the described loop again from the beginning. **c** Comparing different genetic optimization algorithms for variational optimization applied to Rydberg QCA. The cost $\langle C \rangle$ (see Sec. 6.6 for more details) is shown as a function of optimization iterations for five algorithms: differential evolution (blue), differential evolution 1220 (orange), bee colony (green), particle swarm optimization (red) and particle swarm optimization gen (purple). The particle swarm optimization algorithms show fastest convergence towards the optimal value of $\langle C \rangle = -1$. The shaded area depicts the standard deviation over 10 optimization runs with in total 100 trajectories. **d** Final optimal parameter set found in subfigure c after 120 iterations for the same five algorithms. Note that the abscissa is discrete and that the points were only joined for better visual connection of the corresponding values.

methods converge the fastest towards the optimal value of $\langle C\rangle = -1$. The two algorithms based on differential evolution also converge close to $\langle C\rangle = -1$, but at a slower speed, requiring approximately double the number of iterations compared to the PSO algorithms. In the shown range up to 120 optimization loop iterations, the bee colony algorithm initially reduces the cost, however it does not converge towards $\langle C\rangle = -1$, but does not surpass a value lower than approximately -0.9.

At the same time, we can compare the final parameters found by the hybrid quantum-classical optimization loop, displayed in Fig. 6.7d. Again, the solid lines depict the mean parameter values and the shaded area the standard deviation over 10 optimization runs with in total 100 trajectories of individual populations. All algorithms, seem to converge to roughly similar, yet distinguishable Rydberg QCA rules. In summing up, the particle swarm optimization algorithm appears to be a good choice and will be chosen in the next section as the applied optimization algorithm.

In the next section, we will go into more detail concerning the chosen objective function $\langle C\rangle$ and in interpreting the coupling strengths in the optimized final rule parameters.

6.6 Steering the many-body quantum dynamics to entangled quantum states

In quantum state engineering via open system dynamics, the corresponding Liouvillian $\mathcal{L}$ produces desirable states as the stationary state of the quantum dynamics [164, 197, 207–212]. However, finding $\mathcal{L}$ is typically difficult. We show here that using the hybrid quantum-classical optimization loop presented in the previous section 6.5, we can find Rydberg QCA rules that produce entangled states, e.g. for quantum information processing or quantum sensing, as the steady state of the quantum dynamics.

In a first step, we have to choose an objective function, on which the hybrid loop optimizes. Our goal is to generate entangled states, which can be used as a resource in e.g. meteorology [243] or measurement-based quantum computing [244]. One convenient observable for us to focus on is the separability of states. For this, we take the elements of the covariance matrix of the magnetization along z between sites i and j

$$C_{i,j} = \mathrm{Tr}[\rho(\hat{Z}_i - \langle\hat{Z}_i\rangle)(\hat{Z}_j - \langle\hat{Z}_j\rangle)] \tag{6.18}$$

and average the system over all neighboring sites

$$\langle C\rangle = 1/N \sum_j C_{j,j+1}. \tag{6.19}$$

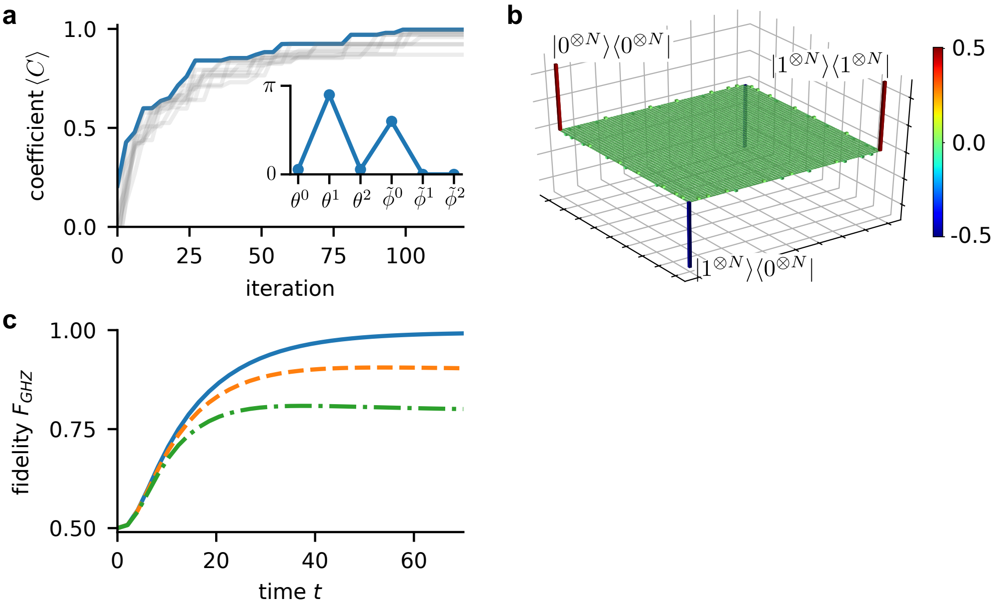

Fig. 6.8: Steering the steady state of the Rydberg QCA dynamics in a chain of $N = 6$ sites towards the GHZ^N state. a Convergence of the variational optimization towards the optimal value $\langle C\rangle = 1$ with the number of loop iterations. Each of the 10 populations of the particle swarm optimization is shown as gray line, where the blue line highlights the best individual at each update step. *Inset:* Optimal variational parameters governing the QCA evolution obtained after 120 loop iterations. **b** Graphical representation of the steady-state density matrix (imaginary parts are $< 7 \cdot 10^{-4}$) resulting from the optimal parameter set shown in the inset of subfigure a. The color bar encodes the real-valued entries. **c** Time-evolution of the fidelity between the state obtained by the optimal parameter set and the GHZ^N state. The system converges towards the highly-entangled state within ~ 70 time units (blue line). The dashed orange (dashed-dotted green) line show the same evolution including an additional Rydberg state decay with a rate $\gamma/\pi = 0.8\,\mathrm{kHz}$ $(2.4\,\mathrm{kHz})$ (see text for other parameters). Adapted from [100].

For a pairwise inseparable state, this measure tends towards the two extremal values $\langle C\rangle = \pm 1$, whereas a value of zero $\langle C\rangle = 0$ corresponds to a separable state. In the following, we will explore the two options of first maximizing and second minimizing $\langle C\rangle$.

Steering the steady state of the Rydberg QCA dynamics towards the GHZ state. At first, we will consider the case, where the hybrid quantum classical loop maximizes the cost towards $\langle C\rangle = 1$. As in the previous section 6.5, we simulate six sites in a linear array with closed boundary condition for the steady-state of the continuous time evolution with global addressing (i.e. no block partitioning) in the effective two-level description, starting from the initial state $|000000\rangle$. Fig. 6.8a displays the convergence of the optimization loop for 120 update steps of the particle swarm optimization algorithm with 10 populations. The evolution of each of the 10 populations is shown as solid line, where the individual with the best cost value is emphasized in blue. We observe robust convergence towards the maximal value $\langle C\rangle = 1$ within 100 optimization loops. The inset shows the parameter set corresponding to the optimal individual after 120 iterations: $[0.058, 0.938, 0.058, 0.626, 0, 0]\,\pi$. The dominant entries are the coherent coupling θ^1 for one excited neighbor and the dissipative coupling ϕ^0 for zero excited neighbors. Next, we inspect the density matrix corresponding to the state obtained with these coupling strengths (see Fig. 6.8b). We see that the first and last entry of the diagonal populations, $|0\rangle^{\otimes N}\langle 0|^{\otimes N}$ and $|1\rangle^{\otimes N}\langle 1|^{\otimes N}$, are close to $+0.5$, and the coherence elements between these two states are close to the value -0.5. All other entries are close to 0 and the imaginary parts in the density matrix entries are negligible ($< 7 \cdot 10^{-4}$). This density matrix very closely resembles the density matrix of the N-particle Greenberger–Horne–Zeilinger (GHZ) state $|\mathrm{GHZ}^N\rangle = 1/\sqrt{2}(|0\rangle^{\otimes N} - |1\rangle^{\otimes N})$, where we chose $N = 6$ for this demonstration. This means, that the optimization loop succeeded in finding a parameter set that steers the quantum evolution towards a highly entangled quantum state, which is steady state of the Rydberg QCA dynamics. To get an intuition of how this works, we will inspect the found optimal rule more closely. The dominant entry is the coherent coupling θ^1 for one excited neighbor, for which the $|\mathrm{GHZ}^N\rangle$ state is dark. The dissipative coupling for no excited neighbor ϕ^0 likewise does not change the $|\mathrm{GHZ}^N\rangle$ state. But the other two coherent entries θ^0 and θ^2, which are small and equal, do act on the GHZ state. The θ^0 coupling is necessary to leave the otherwise dark initial state $|000000\rangle$. To keep a fixed phase relation between $|000000\rangle$ and $|111111\rangle$ requires θ^2 to be of the same magnitude. For different initial states, the optimization loop will find slightly different values, but overall we observe similar behavior.

To further quantify the resulting state, we introduce the fidelity F_{GHZ} as a measure for the similarity between the density matrix $\rho(t)$ of the state produced by Rydberg QCA and the density matrix $|\mathrm{GHZ}^N\rangle\langle \mathrm{GHZ}^N|$ of the above defined GHZ state

$$F_{\mathrm{GHZ}}(t) = \mathrm{Tr}\left[\sqrt{\sqrt{\rho(t)}\,|\mathrm{GHZ}^N\rangle\langle \mathrm{GHZ}^N|\,\sqrt{\rho(t)}}\right]^2 , \qquad (6.20)$$

with the matrix trace operator $\mathrm{Tr}[\,\cdot\,]$ (c.f. Eq. 6.17). Fig. 6.8c shows the fidelity F_{GHZ} as a function of the QCA evolution time t using the optimal parameters of Fig. 6.8a, inset. Without Rydberg state decay (solid blue), as assumed in the optimization loop, the system reaches a highly-entangled state with an fidelity of ≥ 0.99 within the shown 70 time units. Experimentally, however, the Rydberg state has a finite radiative lifetime, for example $200\,\mu\mathrm{s}$ for the $|r\rangle = |80s_{1/2}\rangle$ Rydberg state, which we add as a Rydberg state decay of $\gamma/\pi = 0.8\,\mathrm{kHz}$ (dashed orange). Still, the obtainable fidelity is $F_{\mathrm{GHZ}} \gtrsim 0.9$. Experimentally, it has been observed that this lifetime can be reduced by off-resonant scattering effects to other short-lived states in the intermediate state manifold of the two-photon Rydberg excitation scheme [9]. Although these effects strongly depend on the chosen detuning and Rabi frequencies, we conservatively include these effects by

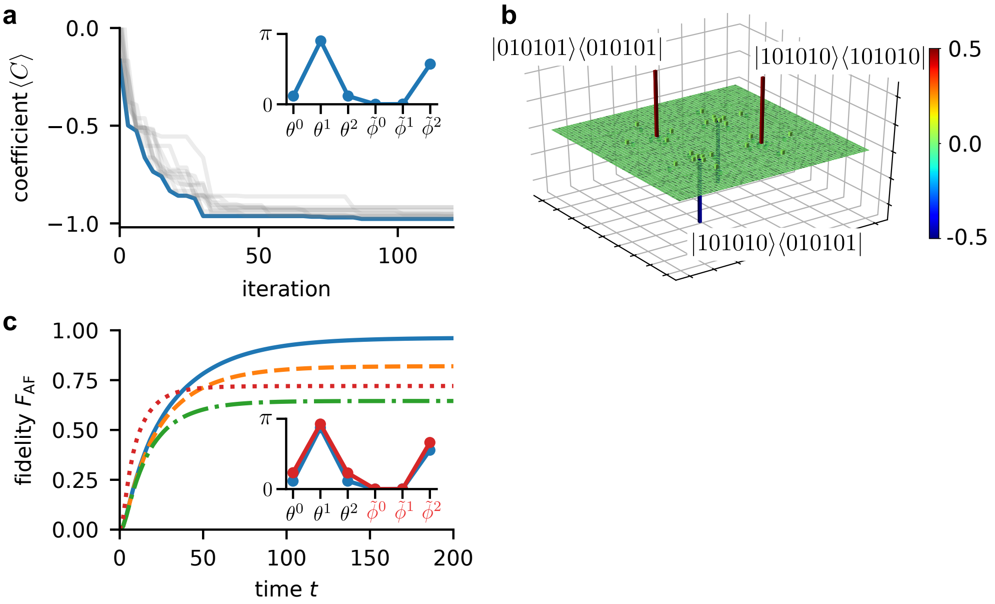

Fig. 6.9: Steering the steady state of the Rydberg QCA dynamics in a chain of $N = 6$ sites towards the antiferromagnetic GHZ^N state. **a** Convergence of the variational optimization towards the optimal value $\langle C \rangle = -1$ with the number of loop iterations. Each of the 10 populations of the particle swarm optimization is shown as gray line, where the blue lines highlights the best individual at each update step. *Inset:* Optimal variational parameters governing the QCA evolution obtained after 120 loop iterations. **b** Graphical representation of the steady-state density matrix (imaginary parts are $< 6 \cdot 10^{-4}$) resulting from the optimal parameter set shown in the inset of subfigure a. The color bar encodes the real-valued entries. **c** Time-evolution of the fidelity between the QCA state obtained from the optimal parameter set and the antiferromagnetic GHZ^N state. The system surpasses the entanglement threshold of $\langle C \rangle = 0.5$ after 20 time units (blue line). The dashed orange (dashed-dotted green) line show the same evolution including an additional Rydberg state decay with a rate $\gamma/\pi = 0.8\,\mathrm{kHz}$ $(2.4\,\mathrm{kHz})$. Rerunning the variational optimization loop including $\gamma/\pi = 2.4\,\mathrm{kHz}$ Rydberg state decay leads to new optimal variational parameters, shown in red in the inset. The previous parameter set of subfigure a inset is shown in blue for comparison. This reoptimized parameters yield an increased final fidelity (dotted red line) as well as a faster initial convergence. Adapted from [100].

increasing the effective decay rate three-fold to $2.4\,\mathrm{kHz}$ (dashed-dotted green). Still, the attainable fidelity of the steady state surpasses $F_{\mathrm{GHZ}} \gtrsim 0.8$.

Steering the steady-state of the Rydberg QCA dynamics towards the antiferromagnetic GHZ state.

In the following, we turn to minimizing the coefficient $\langle C \rangle$ in the hybrid optimization loop, where the optimal value is coefficient $\langle C \rangle = -1$. Apart from this, we use the same parameters and methods as above, where we were maximizing the coefficient $\langle C \rangle$ instead. The result is presented in Fig. 6.9a, where the 10 populations (gray lines) of the particle swarm optimization algorithm converge towards the minimum $\langle C \rangle = -1$ within the displayed 120 update steps of the optimization loop. The blue line emphasizes the best individual at each iteration, which closely approaches the minimum in $\lesssim 100$ loop steps. The optimal parameter strengths corresponding to the best individual after 120 iterations are $[0.122, 0.941, 0.122, 0, 0.003, 0.597]\,\pi$ (see inset). As before, the coherent coupling for one excited neighbor θ^1 is dominant. The other important term is now ϕ^2, i.e. the dissipation if both neighbors are excited. To better qualify the resulting state, we look at its density matrix representation (Fig. 6.9b). There are two entries on the diagonal, $|010101\rangle\langle 010101|$ and $|101010\rangle\langle 101010|$, withe the values close to $+0.5$. The two off-diagonal coherences between these two entries are approximately -0.5. All other entries are close to 0, while all the imaginary parts are $< 6 \cdot 10^{-4}$ and hence negligible. This density matrix resembles closely the antiferromagnetic GHZ^N state for six particles $|\mathrm{AF}\rangle = 1/\sqrt{2}(|010101\rangle - |101010\rangle)$. Looking at the applied rule, the antiferromagnetic GHZ^N state is again a dark state with respect to the two dominant rule entries θ^1 and ϕ^2, which explain why it is an attractive steady-state of the dynamics. The two coherent couplings θ^0 and θ^2 are required to couple out of the initial state. Again, different initial states yield comparable results.

To quantitatively compare the two density matrices resulting from the Rydberg QCA evolution $\rho(t)$ and of the antiferromagnetic GHZ state $|\mathrm{AF}\rangle\langle \mathrm{AF}|$, we define the fidelity between both states as

$$F_{\mathrm{AF}}(t) = \mathrm{Tr}\left[\sqrt{\sqrt{\rho(t)}\,|\mathrm{AF}\rangle\langle \mathrm{AF}|\,\sqrt{\rho(t)}}\right]^2 . \qquad (6.21)$$

The blue line in Fig. 6.9c displays F_{AF} as a function of time, neglecting uncontrolled dissipation from the Rydberg state. After reaching the classical threshold of 0.5 within $t = 20$, the fidelity reaches a value close to 1 after $t \approx 150$. Now we again add the Rydberg state decay by additional jump operators with a rate of $\gamma/\pi = 0.8\,\mathrm{kHz}$, which reduces the fidelity $F \gtrsim 0.82$ (orange dashed line). The dotted-dashed green line shows the fidelity for a reduced Rydberg lifetime, which can be caused by off-resonant scattering effects to other short-lived states in the intermediate state manifold of the two-photon Rydberg excitation scheme [9]. With this increased decay rate of $2.4\,\mathrm{kHz}$, the fidelity still reaches 0.65.

So far, this additional Rydberg decay has been added by hand into the Rydberg QCA model while still using the optimal parameters found by optimization of the system without this decay. However, the hybrid quantum-classical optimization loop might adapt to this extra decay and find a new optimal parameter set. Reoptimization including the additional Rydberg state decay with $\gamma/\pi = 2.4\,\mathrm{kHz}$ indeed yields a slightly different parameter set $[0.251, 0.998, 0.248, 0, 0, 0.715]\,\pi$. The inset of Fig. 6.9c presents these in red together with the previous values of subfigure a in blue for better comparison. The dotted red line in the main figure shows the fidelity $F_{\mathrm{AF}}(t)$ corresponding to the new ruleset. Apparently, reoptimization under the new conditions ($\gamma/2\pi = 2.4\,\mathrm{kHz}$) leads to a faster initial increase as well as a higher final value of $F \gtrsim 0.72$ compared to the case without reoptimization (dotted-dashed green). Hence, the feedback of the optimization loop helps to adapt to and correct for error sources and experimental imperfections. Additionally, this new rule leads to a faster crossing of the classical threshold of 0.5 after 13 time units and higher fidelity up to $t \approx 38$ even compared to the case without any Rydberg decay (blue line). This suggests, that by optimizing for short times instead of the steady state, one could find parameter sets with faster initial rising of the fidelity.

In conclusion, this hybrid quantum-classical optimization approach provides a viable alternative to prepare the GHZ state compared to the previously presented procedure in section 6.4. It comes with the advantage that it does not require a specific initial state, block partitioning or exact timing and powers of the individual pulses.

6.7 Implementing non-totalistic rules

So far, we have been restricted to totalistic QCA rules, meaning that it does not matter if the excitation is on the left or right of the site. This is a direct consequence of the equidistant spacing of the sites and the symmetric interaction. In this section we will explore the possibility of breaking this symmetry to introduce non-totalistic rules into Rydberg QCA, which depend on which side the excitation sits.

Three-level model for non-totalistic Rydberg QCA
Let us consider the setup of Fig. 6.10a with the block-partitioned sublattices A (odd sites) and B (even sites). In a first step, we break the symmetry of the interaction V_{AB} and V_{BA}, where the index labels the order of the two interacting sites reading from left to right. We achieve this by introducing two different lattice periods a, b alternating between neighboring sites. An alternative way would be to exploit spatially non-symmetric interactions.

Consequently, the Rydberg manifold splits up into four levels with energy shifts 0, V_{AB}, V_{BA} and $V_{AB}+V_{BA}$ (Fig. 6.10b). We can now write down the three-level model of the ground state $|g\rangle$, the excited state $|e\rangle$ and the state in the Rydberg manifold $|r\rangle$, where we add in the new constraints closely following the derivation of sections 6.1 and 6.2. We consider a multifrequency coupling field of the form $\mathcal{E}_j = \mathcal{E}_j^\theta + \mathcal{E}_j^\phi$, where

$$\begin{aligned}
\mathcal{E}_j^\theta(t) &= \frac{1}{2}\sum_{\alpha,\beta=0}^{1} \theta_j^{\alpha\beta} \mathrm{e}^{iE_r t + iV_j^{\alpha\beta} t} + c.c. \\
\mathcal{E}_j^\phi(t) &= \frac{1}{2}\sum_{\alpha,\beta=0}^{1} \phi_j^{\alpha\beta} \mathrm{e}^{i(E_r - E_e)t + iV_j^{\alpha\beta} t} + c.c.,
\end{aligned} \tag{6.22}$$

with

$$\begin{aligned}
V_j^{00} &= 0 \\
V_j^{10} &= \begin{cases} V_{BA} & \text{for } j \in A \\ V_{AB} & \text{for } j \in B \end{cases} \\
V_j^{01} &= \begin{cases} V_{AB} & \text{for } j \in A \\ V_{BA} & \text{for } j \in B \end{cases} \\
V_j^{11} &= V_{AB} + V_{BA},
\end{aligned} \tag{6.23}$$

restricting ourselves to nearest-neighbor interactions V_{AB}, V_{BA} between sites j. These enter the interaction part of the time-dependent Hamiltonian

$$\hat{H}(t) = \hat{H}_{\text{int}} + \hat{H}_{\text{atom}} = \sum_j (\hat{\sigma}_j^{gr} \mathcal{E}_j^\theta(t) + \hat{\sigma}_j^{er} \mathcal{E}_j^\phi(t) + h.c.) + \frac{V_j^{10}}{2} \hat{\sigma}_{j-1}^{rr} \hat{\sigma}_j^{rr} + \frac{V_j^{01}}{2} \hat{\sigma}_j^{rr} \hat{\sigma}_{j+1}^{rr} + \hat{H}_{\text{atom}} \tag{6.24}$$

with, $\hat{\sigma}^{ab} = |a\rangle\langle b|$ and $\hat{H}_{\text{atom}} = E_r \hat{\sigma}_j^{rr} + E_e \hat{\sigma}_j^{ee}$.

In the rotating wave approximation, the Hamiltonian reads

$$\hat{H} = \sum_j \sum_{\alpha,\beta} \Big(\frac{\theta_j^{\alpha\beta}}{2} e^{iV_j^{\alpha\beta} t} \hat{\sigma}_j^{gr} + \frac{\phi_j^{\alpha\beta}}{2} e^{iV_j^{\alpha\beta} t} \hat{\sigma}_j^{er} + h.c. \Big) + \frac{V_j^{10}}{2} \hat{\sigma}_{j-1}^{rr} \hat{\sigma}_j^{rr} + \frac{V_j^{01}}{2} \hat{\sigma}_j^{rr} \hat{\sigma}_{j+1}^{rr}, \tag{6.25}$$

where the index j runs over all sites and $\alpha, \beta \in \{0, 1\}$ depict the state of the two neighboring sites.

Derivation of an effective two-level model

Analogous to the derivation in section 6.2, we transform the Hamiltonian in equa-

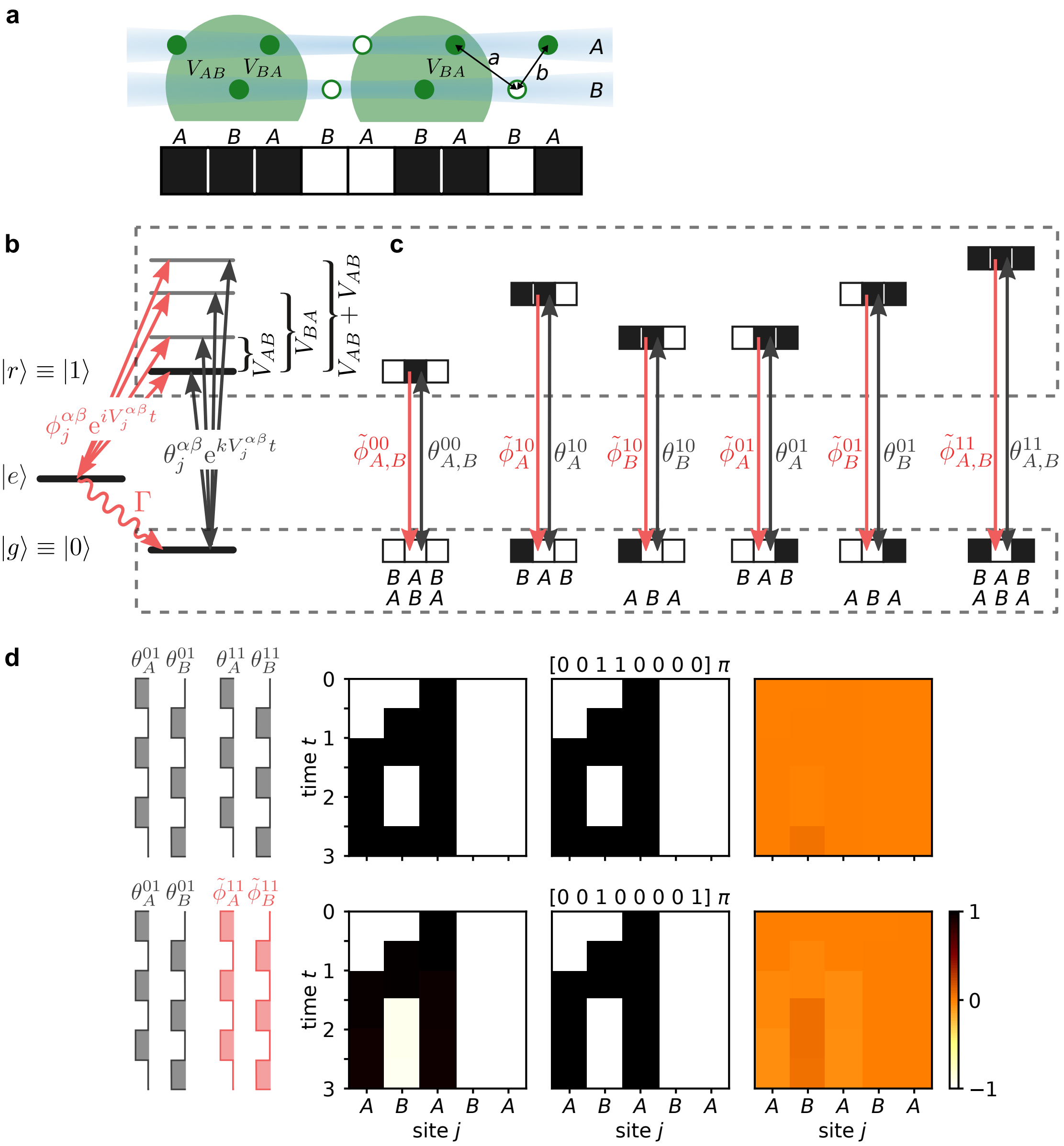

Fig. 6.10: **Implementing non-totalistic Rydberg QCA rules.** **a** Arrangement of ground state ($|0\rangle$, open symbols) and Rydberg excited ($|1\rangle$, filled symbols) atoms in microtraps. Non-totalistic rules require breaking the symmetry between a neighboring excitation being on the left or the right. For this, we introduce two alternating lattice constants a, b, which in turn lead to two Rydberg-Rydberg interaction energies between neighboring sites V_{AB} and V_{BA}. Additionally, the block-partitioned sites A and B can be addressed individually by the Rydberg coupling lasers (blue shading). **b** Full three-level structure for non-totalistic Rydberg QCA. As an interaction on the left and the right causes two different interaction energies (V_{AB}, V_{BA}), the Rydberg manifold is split into four levels. **c** Effective two-level model for non-totalistic Rydberg QCA. Each of the four levels can be addressed individually, mapping unambiguously to the four cases of zero excitation $\theta^{00}, \tilde{\phi}^{00}$, one excitation to the left $\theta^{10}, \tilde{\phi}^{10}$, one excitation to the right $\theta^{01}, \tilde{\phi}^{01}$ and two neighboring excitations $\theta^{11}, \tilde{\phi}^{11}$. Note, that depending on the sublattice, the frequencies of $\theta^{10}, \tilde{\phi}^{10}$ and $\theta^{01}, \tilde{\phi}^{01}$ may have to be swapped. **d** Comparison of the full three-level model and the effective two-level description. The panels show the dynamics of the magnetization $\langle Z_j \rangle$ for two exemplary rules, labeled as $[\theta^{00}, \theta^{10}, \theta^{01}, \theta^{11}, \tilde{\phi}^{00}, \tilde{\phi}^{10}, \tilde{\phi}^{01}, \tilde{\phi}^{11}]$ (see text for more details). To the left of the vertical time axis, the time sequence of the active couplings is shown. For each rule, there are three panels: *left:* three-level master equation simulation including time-dependent couplings, *center:* effective two-level master equation simulation and *right:* residual between the latter two.

tion (6.25) to the interaction picture with respect to the nearest-neighbor interaction. The corresponding unitary transformation is

$$U = \exp\left(\sum_j \left(-\frac{iV_j^{10}t}{2}\hat{\sigma}_{j-1}^{rr}\hat{\sigma}_j^{rr} - \frac{iV_j^{01}t}{2}\hat{\sigma}_j^{rr}\hat{\sigma}_{j+1}^{rr}\right)\right), \tag{6.26}$$

where $U^\dagger \hat{\sigma}^{\lambda r} U = [\mathrm{P}_{j-1}^0 + \mathrm{P}_{j-1}^1 e^{-iV_j^{10}t}]\hat{\sigma}_j^{\lambda r}[\mathrm{P}_{j+1}^0 + \mathrm{P}_{j+1}^1 e^{-iV_j^{01}t}]$ [217], with $\lambda = g, e$, the projection operators $\mathrm{P}_j^0 = 1 - \hat{\sigma}_j^{rr}$ and $\mathrm{P}_j^1 = \hat{\sigma}_j^{rr}$. The resulting Hamiltonian reads

$$\begin{aligned}
\hat{H}(t) = \sum_j \sum_{\alpha,\beta} & \underbrace{\left(\frac{\theta_j^{\alpha\beta}}{2}\mathrm{P}_{j-1}^0\hat{\sigma}_j^{gr}\mathrm{P}_{j+1}^0 + \frac{\phi_j^{\alpha\beta}}{2}\mathrm{P}_{j-1}^0\hat{\sigma}_j^{er}\mathrm{P}_{j+1}^0\right)}_{\hat{H}_{\alpha,\beta,0,0}(j)} \mathrm{e}^{iV_j^{\alpha\beta}t} \\
& + \underbrace{\left(\frac{\theta_j^{\alpha\beta}}{2}\mathrm{P}_{j-1}^0\hat{\sigma}_j^{gr}\mathrm{P}_{j+1}^1 + \frac{\phi_j^{\alpha\beta}}{2}\mathrm{P}_{j-1}^0\hat{\sigma}_j^{er}\mathrm{P}_{j+1}^1\right)}_{\hat{H}_{\alpha,\beta,0,1}(j)} \mathrm{e}^{i(V_j^{\alpha\beta}-V_j^{01})t} \\
& + \underbrace{\left(\frac{\theta_j^{\alpha\beta}}{2}\mathrm{P}_{j-1}^1\hat{\sigma}_j^{gr}\mathrm{P}_{j+1}^0 + \frac{\phi_j^{\alpha\beta}}{2}\mathrm{P}_{j-1}^1\hat{\sigma}_j^{er}\mathrm{P}_{j+1}^0\right)}_{\hat{H}_{\alpha,\beta,1,0}(j)} \mathrm{e}^{i(V_j^{\alpha\beta}-V_j^{10})t} \\
& + \underbrace{\left(\frac{\theta_j^{\alpha\beta}}{2}\mathrm{P}_{j-1}^1\hat{\sigma}_j^{gr}\mathrm{P}_{j+1}^1 + \frac{\phi_j^{\alpha\beta}}{2}\mathrm{P}_{j-1}^1\hat{\sigma}_j^{er}\mathrm{P}_{j+1}^1\right)}_{\hat{H}_{\alpha,\beta,1,1}(j)} \mathrm{e}^{i(V_j^{\alpha\beta}-V_j^{11})t} + h.c. \\
= \sum_j \sum_{\alpha,\beta,\alpha',\beta'} & \hat{H}_{\alpha,\beta,\alpha',\beta'}(j)\mathrm{e}^{i(V_j^{\alpha\beta}-V_j^{\alpha'\beta'})t} + h.c.
\end{aligned} \tag{6.27}$$

In the next step, we do a second-order adiabatic elimination in the Floquet picture and restrict ourselves to the resonant terms only. The time-independent effective Hamiltonian is

$$\hat{H}' = \frac{1}{2}\sum_j \sum_{\alpha,\beta} \mathrm{P}_{j-1}^{\alpha}\left[\theta_j^{\alpha\beta}\hat{\sigma}_j^{gr} + \phi_j^{\alpha\beta}\hat{\sigma}_j^{er} + h.c.\right]\mathrm{P}_{j+1}^{\beta}, \tag{6.28}$$

with the projection indices $\alpha, \beta = \{0, 1\}$.

As a last step, we have to include the spontaneous decay described by the jump operator $\hat{L}_j = \sqrt{\Gamma}\hat{\sigma}_j^{ge}$ in our effective description. Again, we adiabatically eliminate the short-lived $|e\rangle$ states and derive effective jump operators L_j^{eff} acting on the g, r subspace using the effective operator formalism accoridng to Ref. [219]. With the slow and fast subspaces $\mathbb{P}\sigma_j^{e\lambda} = 0$ and $\mathbb{Q}\sigma_j^{e\lambda} = \sigma_j^{e\lambda}$ $(\lambda = g, r)$ the non-Hermitian Hamiltonian is

$$\hat{H}_{nh} = \mathbb{Q}\hat{H}'\mathbb{Q} - \frac{i}{2}\sum_j \hat{L}_j^\dagger \hat{L}_j. \tag{6.29}$$

We assume $\Gamma \gg |\phi_k|$, meaning that we can neglect states with more than one $|e\rangle$ state. In this case the first term is zero and we are left with

$$\hat{H}_{nh} = -\frac{i\Gamma}{2}\sum_j \hat{\sigma}_j^{ee}, \tag{6.30}$$

which enters the effective Hamiltonian

$$\hat{H}^{\text{eff}} = \mathbb{P}\hat{H}'\mathbb{P} - \underbrace{\frac{1}{2}\mathbb{V}^-[\hat{H}_{nh}^{-1} + (\hat{H}_{nh}^{-1})^\dagger]\mathbb{V}^+}_{=0} = \frac{1}{2}\sum_j\sum_{\alpha,\beta} \mathrm{P}_{j-1}^\alpha \left[\theta_j^{\alpha\beta}\hat{\sigma}_j^{gr} + (\theta_j^{\alpha\beta})^*\hat{\sigma}_j^{rg}\right] \mathrm{P}_{j+1}^\beta, \tag{6.31}$$

with $\mathbb{V}^- = \mathbb{P}\hat{H}'\mathbb{Q}$ and $\mathbb{V}^+ = \mathbb{Q}\hat{H}'\mathbb{P}$. In the first step, we use that the inverse of $\hat{H}_{nh}$ is a purely imaginary diagonal matrix such that the two terms in the bracket fully subtract each other. Now, for the effective jump operators it follows

$$\begin{aligned} \hat{L}_j^{\text{eff}} &= \hat{L}_j\hat{H}_{nh}^{-1}\mathbb{V}^+ = \frac{i}{\sqrt{\Gamma}}\hat{\sigma}_j^{ge}(\sum_i \hat{\sigma}_i^{ee})^{-1} \times \mathbb{Q}\sum_{i'}\left(\sum_{\alpha,\beta}\mathrm{P}_{i'-1}^\alpha[\theta_j^{\alpha\beta}\hat{\sigma}_{i'}^{gr} + \phi_j^{\alpha\beta}\hat{\sigma}_{i'}^{er} + h.c]\mathrm{P}_{i'+1}^\beta\right)\mathbb{P} \\ &= \frac{i}{\sqrt{\Gamma}}\sum_{\alpha,\beta}\mathrm{P}_{j-1}^\alpha\phi_j^{\alpha\beta}\hat{\sigma}_j^{ge}(\hat{\sigma}_j^{ee})^{-1}\hat{\sigma}_j^{er}\mathrm{P}_{j+1}^\beta = \frac{i}{\sqrt{\Gamma}}\sum_{\alpha,\beta}\phi_j^{\alpha\beta}\mathrm{P}_{j-1}^\alpha\hat{\sigma}_j^{gr}\mathrm{P}_{j+1}^\beta. \end{aligned} \tag{6.32}$$

where we use $(\sum\hat{\sigma}^{ee})^{-1}\mathbb{Q} = (\sum\hat{\sigma}^{ee})^{-1}$ and the action of $\mathbb{P}$ from the right hand side changes $\mathrm{P}_{j\pm1}^0 \to |g\rangle\langle g|_{j\pm1}$ and restricts $\hat{\sigma}_{i'}^{er}$ to states that initially have no $|e\rangle$ excitations, i.e. exactly one $|e\rangle$ at site i' after application of the operator, which allows us to remove the sums over i, i'.

In summing up, we arrive at the effective master equation for the dynamics

$$\partial_t\rho = \mathcal{L}^{\text{eff}}[\rho] = -i[\hat{H}^{\text{eff}}, \rho] + \mathcal{D}_{\hat{L}^{\text{eff}}}[\rho], \tag{6.33}$$

with the effective Hamiltonian and Lindblad terms

$$\hat{H}^{\text{eff}} = \frac{1}{2}\sum_j\sum_{\alpha,\beta}\theta_j^{\alpha\beta}\mathrm{P}_{j-1}^\alpha\hat{X}_j\mathrm{P}_{j+1}^\beta, \tag{6.34}$$

$$\hat{L}^{\text{eff}} = \frac{1}{2}\sum_j\sum_{\alpha,\beta}\sqrt{\tilde{\phi}_j^{\alpha\beta}}\mathrm{P}_{j-1}^\alpha(\hat{X}_j - i\hat{Y}_j)\mathrm{P}_{j+1}^\beta, \tag{6.35}$$

where $\sqrt{\tilde{\phi}_j^{\alpha\beta}} \approx \phi_j^{\alpha\beta}/\sqrt{\Gamma}$, $\theta_j^k \in \mathbb{R}$ and $\hat{X}_j, \hat{Y}_j$, $\hat{Z}_j$ are Pauli matrices. As a reminder, $\alpha, \beta = \{0, 1\}$ and the projector $\mathrm{P}^\alpha = |\alpha\rangle\langle\alpha|$.

Fig. 6.10c shows the resulting effective model couplings. As an A site interacts with V_{BA} with a left-neighboring excitation, but a B site interacts with V_{AB} with a left-neighboring excitation, the frequency of the couplings $\theta_j^{10}, \tilde{\phi}_j^{10}$ and $\theta_j^{01}, \tilde{\phi}_j^{01}$ depend if $j \in A$ or $j \in B$. Hence, the frequency of these must be swapped at each block-partitioned update step.

Totalistic vs. non-totalistic Rydberg QCA dynamics

Now let us turn to the examples in Fig. 6.10d, where we can understand this model step by step and, furthermore, compare the full three-level and effective two-level models. The three panels for each rule show the z magnetization $\langle Z_j \rangle$ (see color bar) as a function of evolution time t for the three-level model on the left, the effective two-level model in the center and the residual between the two on the right. The rules describing the coupling strengths are labeled in the notation $[\theta^{00}, \theta^{10}, \theta^{01}, \theta^{11}, \tilde{\phi}^{00}, \tilde{\phi}^{10}, \tilde{\phi}^{01}, \tilde{\phi}^{11}]$. To the left of the vertical time axis t, time traces of the corresponding active couplings are sketched for the two sublattices.

For the rule $[0, 0, 1, 1, 0, 0, 0, 0]\,\pi$, only the coherent couplings for an excitation on the right θ_j^{01} and for two excitations θ_j^{11} are non-zero. In the block-partitioned scheme, we alternately apply the rule to sublattice A and B, starting with sublattice A, i.e. the odd sites. The initial state $|00100\rangle$ however is dark to the rule, so the state stays unchanged. On the even sites, the coupling θ_B^{01} becomes active with amplitude π, which was chosen to correspond to a full transfer from $|0\rangle$ to $|1\rangle$. Hence, we get $|01100\rangle$ in the second update step. These two steps correspond to a full update cycle of both sublattices with time of $t = 1$. Now the updating starts from the beginning on A sites, where θ_A^{01} rotates the first site up to leave $|11100\rangle$. For the B site on $j = 2$, θ_B^{11} now rotates this site down to get $|10100\rangle$. The update step on A leaves the state unchanged, and subsequently θ_B^{11} rotates the second site back up.

The difference to the second rule $[0, 0, 1, 0, 0, 0, 0, 1]\,\pi$ is that the active coupling acting for two excited neighbors is dissipative ϕ_j^{11}. That explains why the second site stays in $|0\rangle$ in the last step instead of being transferred back up.

We conclude good agreement between the three and effective two-level models. In general, the agreement is comparable to before (section 6.2), where for some combinations of coupling we observe effects due to off-resonant scattering. Here we use the same parameters with $V_{AB} = 50\,\pi$ and $V_{BA} = 2V_{AB}$ to keep the interaction energy splittings similar.

Fig. 6.11 shows the dynamics of the magnetization $\langle Z_j \rangle$ for 30 rules $[\theta^{00}, \theta^{10}, \theta^{01}, \theta^{11}, \tilde{\phi}^{00}, \tilde{\phi}^{10}, \tilde{\phi}^{01}, \tilde{\phi}^{11}]$, calculated with the effective two-level model. The central site is in $|1\rangle$ at $t = 0$, while all other sites are initialized to $|0\rangle$. The boundary conditions are open and

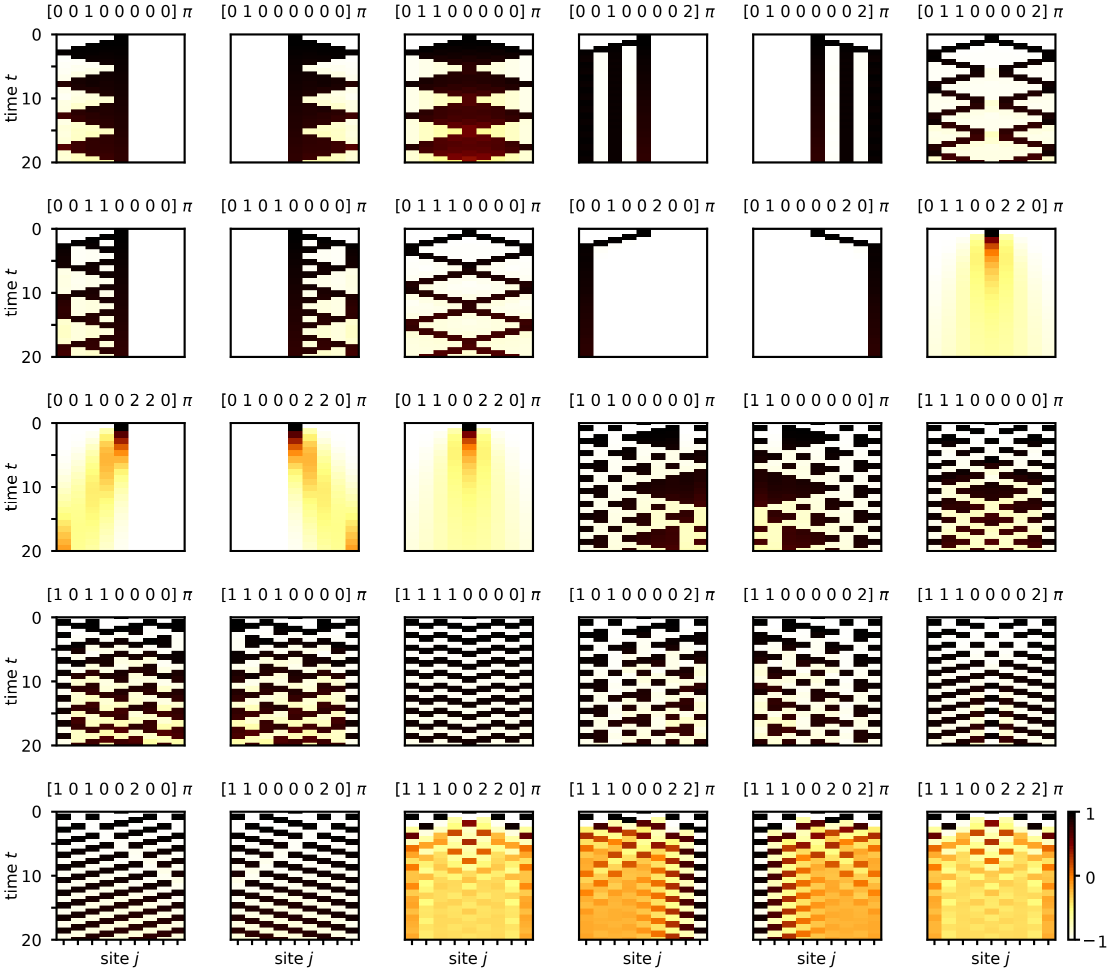

Fig. 6.11: **Rydberg QCA dynamics with non-totalistic rules.** Time-evolution of the magnetization $\langle Z_j \rangle$ for 30 representative rules. The label of each subfigure indicates the corresponding coupling strengths in the notation $[\theta^{00}, \theta^{10}, \theta^{01}, \theta^{11}, \tilde{\phi}^{00}, \tilde{\phi}^{10}, \tilde{\phi}^{01}, \tilde{\phi}^{11}]$. In each row, there are two groups of three panels, where for each group the first two panels are non-totalistic rule pairs and the third one is the corresponding totalistic rule. Each simulation starts in the initial state $|000010000\rangle$, which is time evolved for 20 time steps using the effective two-level model with open boundary conditions and with a Rydberg decay of rate $\gamma/\pi = 0.8\,\mathrm{kHz}$. For most rules, the totalistic rule resembles its non-totalistic pairs, but for some we observe qualitatively different behavior.

we include a Rydberg decay with a rate of $\gamma/\pi = 0.8\,\mathrm{kHz}$. These 30 rules are a subset of the total 256 possible binary combinations of the 8 coupling parameters, representing the most interesting, non-trivial dynamics. The rules are arranged into groups of three, where the first two are non-totalistic rules and the third panel is their totalistic counterpart. Inspecting the rules more closely yields the following observations:

- The first group of three in the first row is an example of where the totalistic rule is directly composed of the two non-totalistic ones.

- For the second group in the first row, we see that this is not always the case. The rule $[0, 1, 1, 0, 0, 0, 0, 2]\,\pi$ is periodic whereas $[0, 0, 1, 0, 0, 0, 0, 2]\,\pi$ and $[0, 1, 0, 0, 0, 0, 0, 2]\,\pi$ are not, instead showing a constant staggered pattern on one half.

- The first group in the second row shows similar but still distinct behavior for non-totalistic vs. totalistic rules. Both show a periodicity, but with a different period and the non-totalistic rules show extra small features.

- The second group in the second row is quite interesting. $[0, 0, 1, 0, 0, 2, 0, 0]\,\pi$ and $[0, 1, 0, 0, 0, 0, 2, 0]\,\pi$ transport the initially central excitation in one direction towards the border with no loss of contrast. Whereas combining both rules to $[0, 1, 1, 0, 0, 2, 2, 0]\,\pi$ results in diffusion and total loss of contrast.

- In the first group in row three, the totalistic rule $[0, 1, 1, 0, 0, 2, 2, 0]\,\pi$ is the same as above. For the non-totalistic ones $[0, 0, 1, 0, 0, 2, 2, 0]\,\pi$ and $[0, 1, 0, 0, 0, 2, 2, 0]\,\pi$, we now keep both the dissipative couplings on. The excitation is still transported towards one side, but spreads and loses contrast quickly. However, the contrast starts to increase again when reaching the borders, where it accumulates.

- All three rules $[1, 0, 1, 0, 0, 0, 0, 0]\,\pi$, $[1, 1, 0, 0, 0, 0, 0, 0]\,\pi$ and $[1, 1, 1, 0, 0, 0, 0, 0]\,\pi$ show fractal structures as in triangles or rhombi appearing in different sizes.

- For the rules in the fourth row, the non-totalistic rules display complex dynamics, whereas the totalistic rules develop periodic structures.

- In the first group of the last row, the two non-totalistic rules develop periodic wave fronts, which have a full contrast and are tilted to the left or right. The rule $[1, 1, 1, 0, 0, 2, 2, 0]\,\pi$ however displays symmetric periodicity with a clear loss of contrast.

- In the last group, only the dissipative couplings change for the three cases, the coherent coupling stay unchanged. This results in a directional loss of contrast towards left or right in the first two panels.

■■■	■■□	■□■	■□□	□■■	□■□	□□■	□□□
□	□	■	■	■	■	□	□

Tab. 6.1: **Elementary CA rule 60.** Depending on the configuration of the local three-site neighborhood in the first row, the state of the central site is updated to the value in the second row in each update step. As white (black) encode the state 0 (1), the second row can be written as 00111100, which represents the decimal number 60 in the binary numeral system.

Often, the non-totalistic rules show similar dynamics as their totalistic combination, for example a comparable periodicity. This is not always the case, though.

In summary, non-totalistic rules allow for even richer, spatially non-symmetric dynamics. Interesting application include shuffling of excitation in quantum simulation and quantum information settings. An interesting idea to explore in the future would be to implement the continuous-time non-totalistic rules in a Floquet picture by applying the discrete, block-partitioned scheme described above via Trotterization, i.e. where many short discrete pulses on the sublattices emulate the continuous evolution with global addressing.

6.8 Mapping to classical cellular automata

In the introduction of this chapter, we mentioned classical cellular automata (CA) having interesting properties and applications. Here we would like to investigate the connection between classical CA and the Rydberg quantum cellular automata (QCA) framework we have developed so far.

As for the classical part, we focus on the elementary CA framework [187]. In each update step, a new row is added to the existing row according to the given rule. The rule describes the new value of the central site depending on the configuration of its local three-site neighborhood. Tab. 6.1 illustrates using the example of rule 60. All the possible configurations of the three sites are displayed in the first row, with the corresponding new value of the central site in the row below. These updated values determine the name of the rule by converting this binary string into a decimal number. The color code maps the state 0 to white and the state 1 to black, hence the second row can be represented as 00111100 or 60 in the decimal numeral system.

To find a mapping in between Rydberg QCA and elementary CA rules, we inspect the effect of the couplings $\vec{\theta}, \vec{\phi}$ on the three-site neighborhoods (Tab. 6.2). For discrete-time evolution, $\theta = \pi$ corresponds to a full transfer between the two states $|0\rangle$ and $|1\rangle$ (up-down or down-up flip), and $\phi = 2\pi$ implements a one-directional down-flip to

	■■■	■■□	■□■	■□□	□■■	□■□	□□■	□□□
$\phi_j^{00} = 2\pi$						□		□
$\phi_j^{10} = 2\pi$		□		□				
$\phi_j^{01} = 2\pi$					□		□	
$\phi_j^{11} = 2\pi$	□		□					
$\theta_j^{00} = \pi$						□		■
$\theta_j^{10} = \pi$		□		■				
$\theta_j^{01} = \pi$					□		■	
$\theta_j^{11} = \pi$	□		■					

Tab. 6.2: Relation between classical elementary CA and Rydberg QCA rules. The first row shows all possible three-site neighborhood configurations of elementary CA. The set of Rydberg QCA couplings is given in the first column with corresponding amplitudes. The first four couplings ϕ realize a uni-directional down-flip of the central site, whereas the last four coupling θ result in a bi-directional up-down or down-up flip. The white squares (state 0) and black squares (state 1) indicate the new state of the central site for the given neighborhood configuration and if the corresponding coupling is turned on. If a coupling is off, it does not alter the neighborhood. Up-flips are not directly implemented with the given Rydberg QCA couplings, but they can be emulated by combining first a down-flip with a subsequent down-up flip.

$|0\rangle$ with probability $1 - \exp(-2\pi)$. The white and black squares in the table are the new value of the central site of the corresponding neighborhood and coupling. If a coupling is zero on the other hand, it does not change the state of the central site. From this table we can, for example, infer that the Rydberg QCA couplings $[\theta^{00}, \theta^{10}, \theta^{01}, \theta^{11}, \tilde{\phi}^{00}, \tilde{\phi}^{10}, \tilde{\phi}^{01}, \tilde{\phi}^{11}] = [0, 1, 0, 1, 0, 0, 0, 0]\,\pi$ correspond to CA rule 60.

Some CA rules require one-directional up-flips, which are not directly implemented with our Rydberg QCA couplings. However, we can emulate this by first applying the dissipative down pumping followed by the corresponding coherent up-rotation. For example to implement a rule including $\underset{\blacksquare}{\blacksquare\blacksquare\blacksquare}$ $\underset{\blacksquare}{\blacksquare\square\blacksquare}$, we can first apply ϕ^{11}, such that the central sites are in the 0 state and subsequently apply θ^{11}, which will flip the central spin up to 1 in both cases.

There is still one caveat, however. While for classical CA, we can create a copy of the current configuration and apply the update rules on this copy, the no-cloning theorem [245] forbids us to make a copy of our single array Rydberg QCA system. We have already seen that if we apply the rules globally, the neighbors, determining the applied couplings, can change their state at the same time as the central spin does. To disentangle this, we implemented block partitioning $ABABA..$, so with our current QCA implementation we can only provide a mapping to block-partitioned classical CA.

Conclusion

We have seen that the multifrequency Rydberg excitation scheme opens up new possibilities by the increased addressing capability in the Rydberg manifold, exemplified here by the quantum cellular automata framework with Rydberg atoms in optical tweezer arrays. Both totalistic and non-totalistic Rydberg QCA rules give rise to interesting, complex dynamics in both the continuous, global and the discrete-time, block-partitioned evolution. Interestingly, this framework is well-suited for hybrid quantum-classical optimization, which helps to overcome the difficulty in predicting microscopic rules that yield a certain macroscopic system evolution. This is successfully demonstrated by finding optimized rules that steer the quantum dynamics towards entangled steady states.

Although the presented results are very interesting, we have only investigated a restricted subset of the possible dynamics so far and there are several future opportunities. For example, we could allow more flexibility in the rules. Instead of applying the same rule throughout the full evolution, changing the rule after a certain time interval, after an update step or having different rules for the different sublattices would allow a more versatile behavior. In the discrete time, block-partitioned case, we have been restricting ourselves to full rotations between the states $|0\rangle$ and $|1\rangle$, while continuous parameters in the rules would also allow superpositions thereof. Taking this further, it might be possible to emulate global addressing by Trotterization of the update step on the A and B sublattice via fast alternation of short coupling pulses. In the variational optimization for state preparation, there might exist even better results when optimizing on the short-time solution instead of the long-time steady state, where experimental errors and imperfections have had more time to accumulate. Another interesting opportunity would be to extend the dimension of the array. A two-dimensional square lattice, which is feasible with state-of-the-art techniques [6–9, 246], would result in four nearest neighbors with more distinct level splittings in the Rydberg manifold and in turn a larger space of possible rules.

Experimentally, the next step would be to implement this proposal using the optical tweezer setup of Sec. 3.3.3, where two crucial tasks concern the atomic sample preparation and the coherent Rydberg coupling. As for the atomic sample preparation, one could either choose preparation schemes for a single atom per trap, or explore the possibility to work with Rydberg-blockaded ensembles is each microtrap. The Rydberg coupling requires on the one hand to implement the multifrequency laser manipulation scheme and on the other hand the identification of the limiting decoherence processes with possible subsequent improvements to increase coherence.

Conclusion and outlook

7

To summarize, the main results in this thesis fall conceptually into two parts: First, the introduction of a mapping between an ultracold gas of Rydberg excited potassium atoms and open complex systems, together with the resulting development of a controllable platform to study the complex non-equilibrium dynamics that can emerge in driven-dissipative systems. Secondly, the successful demonstration of this framework via three main scientific findings: (i) The discovery of self-organization to a critical state with Rydberg excitation avalanches; (ii) The connection of power-law behavior in the Rydberg excitation number to epidemic spreading and Griffiths effects on an emergent heterogeneous network; (iii) A novel implementation of quantum cellular automata using Rydberg arrays. These findings incorporate key phenomena and concepts of open complex systems, including nonlinear behavior, self-organization, scale invariance, criticality, avalanches, power-law distributions, power-law growth and relaxation, complex networks and cellular automata. These results can help to explore and answer long standing questions concerning emergent properties, phase structure and universality in non-equilibrium systems.

The prevalence of emergent complex behavior in nature, science and society, where apparently very different systems can show quite similar behavior, is demonstrated by several examples in section 1.2. One prime example is self-organized criticality [21, 22], which has been conjectured as a way to explain the emergence of complex structures and scale invariant behavior in various systems in nature [113, 117, 118, 141, 142]. However, experimental systems which allow to investigate these phenomena in a controlled and tunable setting have remained scarce. Motivated by this, a mapping is established between open complex systems and the ultracold Rydberg system, initiating an experimental platform for studying non-equilibrium phenomena (see Sec. 1.1). This physical system consists of individual potassium atoms in a certain trapping volume surrounded by vacuum and under laser driving to Rydberg states. The exaggerated properties of Rydberg atoms (cf. Sec. 2.1) in combination with the Rydberg interactions can be used to introduce dissipation and correlated excitation processes, for example via the nonlinear Rydberg facilitation effect (cf. Sec. 2.3). Tunability in the system is provided by the selection of different Rydberg states (principal quantum number and orbital angular momentum), the laser driving as well as the spatial atom distribution via the trapping potential. When the Rydberg facilitation (laser driving) and the dissipation are tuned to be of comparable scale, the competition between these two antagonistic processes can lead to a transition from an absorbing state into an active phase. The underlying experimental setup (see chapter 3) is based on the apparatus developed in Heidelberg and was rebuilt in Strasbourg due to the move of the laboratory. Here, I want to highlight new upgrades mainly concerning the optical trapping capabilities and the Rydberg detection.

In the following three main scientific findings, we view dissipation not as a detrimental effect, but we embrace it as an integral part in the complex systems dynamics. The first major result is the discovery of the aforementioned phenomenon of self-organized criticality (SOC) in the dynamics of the driven-dissipative many-body system under facilitated Rydberg excitation (cf. chapter 4). This already establishes a powerful framework to explore self-organization and non-equilibrium critical phenomena in a controlled and tunable environment and can help answer the question of why complex structures and scale invariant behavior is so prevalent in nature. We identify the competition between facilitation and decay, resulting in an absorbing state phase transition, together with a feedback mechanism towards the critical state (nonlinear atom loss) as key elements for the self-organization dynamics towards the critical state. Experimentally, SOC is confirmed via three signatures: First, self-organization of the atomic density to a stationary state n_f, which is independent on the initial density as long as it starts above or equal to n_f. In the case where the initial density is already below n_f, the density stays unchanged over the experimental timescale. Second, scale invariance of the stationary, self-organized density via a rescaling ansatz of the laser driving. And third, critical excitation avalanches at the self-organized state showing large fluctuations in size, described by a power-law distribution with an exponent of $\alpha = -1.37(2)$. This raises the question of how well SOC can be observed experimentally, as a real system is expected to overshoot the critical point due to noise and imperfections as well as due to the theoretically diverging time and length scales. Interestingly, we find an inherent stabilization mechanism towards the critical state in the system, provided by the thermal atom motion in the trapping potential of the optical dipole trap. In essence, atom reloading from the wings sustains an extended critical region in the trap center with a characteristic flat-top profile for an extended period of time. An effective reloading mechanism can also be introduced in a controlled manner via ramping of the excitation laser intensity, which affects the facilitation probability and can compensate for the lower densities by atom loss. This technique allows to measure the avalanche size distribution close to the critical point, as well as close by in the subcritical and supercritical phase, showing power-law behavior with a changing exponent. The origin of this is an interesting open questions for further studies and raises questions on the (non)universality of SOC as well as the relation of the SOC to other non-equilibrium universality classes, for example to the directed percolation universality class of the underlying absorbing state phase transition [124, 161].

Chapter 5 establishes a connection between the collective excitation dynamics of ultracold atoms in a two-dimensional trapping potential and epidemic spreading, where in both cases complex network models turn out as a beneficial layer in bridging between the behavior of the individuals and the resulting global dynamics. This establishes the experimental Rydberg system as a platform for studying non-equilibrium dynamics on complex emergent networks. The observation of Griffiths effects associated with a heterogeneous network structure (quenched disorder) provides a way to explain the emergence of power laws with non-universal exponents. Experimentally, the power-law growth of the excitation number can be well described by the generalized growth model, which a heuristic model commonly used to describe epidemic spreading. In real-life observations of disease spreading, subexponential growth is commonly related to spatial constraints and heterogeneity in the underlying network structure. Building on this connection, we develop a susceptible-infected-susceptible model on a heterogeneous networks which turns out to be an efficient approach to reproduce the experimental observations of power-law growth followed by a plateau or by power-law relaxation. The introduction of heterogeneity was a key element, where the origin of the quenched disorder despite atom motion can be understood by a phase-space facilitation condition. This spatial disorder is expected to result in new behavior, one of them being the emergence of an exotic phase, the so-called Griffiths phase, which replaces the critical point by an extended region. The observed power-law behavior with changing exponents as a function of the facilitation rate are indicative such Griffiths effects in the physical system.

Motivated by the new optical tweezer capabilities (cf. Sec. 3.3.3), chapter 6 proposes a novel quantum cellular automata implementation in a linear atom chain with multifrequency Rydberg addressing, where the non-unitary, dissipative rules play an important part in the emergence of complex dynamics and the entanglement generation. As in the case of classical cellular automata, this is an ideal framework to stringently study how macroscopic complex dynamics can emerge from relatively simple local interactions between individuals on the microscopic level. In the proposal, unitary and nonunitary rules, which are defined on a local three-site neighborhood, are introduce via a coherent multifrequency Rydberg excitation scheme with controlled dissipation to the ground state. An effective two-level model is derived to simulate the quantum dynamics corresponding to different rules. The interesting global dynamics resulting from certain microscopic rules motivates a possible application for quantum state preparation. As the mapping between the microscopic and the macroscopic scale is complex, a hybrid quantum-classical optimization loop is used to steer the resulting dynamics to useful quantum states. Specifically, we demonstrate the generation of the entangled N-particle Greenberger–Horne–Zeilinger state in an atomic chain with global multifrequency Rydberg addressing, which is a promising resource for quantum metrology [243] and quantum information processing [244]. A block partitioned scheme, where the odd and even sites can be addressed by two individual laser beams allows for a higher state control and non-totalistic rules. Hence, quantum cellular automata represents a well-suited approach to explore the complex quantum dynamics by relating macroscopic effects to microscopic rules while the generation of entanglement might be a useful resource for quantum metrology or alternative approaches to quantum information processing.

In short, these results represent successful applications of this framework to explore complex systems dynamics including the observation of key phenomena of complex systems as well as the application of central concepts thereof. These findings form the basis to soon answer open questions concerning non-equilibrium behavior, phase structures and universality classes and at the same time open exciting new research avenues. Promising future research directions result from the new optical tweezer setup, the introduction of more coherence towards studying quantum phenomena as well as new experimental detection capabilities.

Now that the spatial structuring of atoms via the optical tweezer setup has been successfully demonstrated (cf. Sec. 3.3.3), this opens several new interesting research opportunities, for example to study the effect of different spatial atom distributions on the SOC dynamics. The effect of atom motion on reloading and disorder would become apparent by comparing a continuous trap, where the atoms can freely move throughout the whole trap volume, to a spatially structured cloud which is quasi-continuous with respect to the facilitation condition but restricts atom motion to much smaller trap volumes. Similarly, one could experimentally map out the facilitation shell by tuning the lattice period. With irregular structures with respect to the facilitation shell one could explore the effect of disorder in the facilitation dynamics in a controlled way to investigate potential Griffiths or localization effects. Furthermore, different atom reservoirs could be deterministically created in the trapping potentials to control the atom reloading current or size of these reservoirs. Very similar ideas can be applied to experiments on the initial Rydberg excitation growth dynamics. As the dependence on the initial seed is high in this regime, it would be interesting to deterministically create the seed excitation at certain spatial positions, e.g. by making use of differential light shifts at certain selected traps.

For the studies of these dynamics under the Rydberg facilitation condition it might be useful to work with atomic ensembles in the optical tweezer traps, as they provide an atom reservoir for prolonged dynamics. For the envisaged application for quantum cellular automata, it is still an open question if Rydberg blockaded ensembles in the superatom picture or single atom occupancy per tweezer would be beneficial as both come with advantages and challenges. Blockaded ensembles allow for easier array filling without defects (empty traps) and the $\sqrt{N}$ enhancement of the collective Rabi frequency [66], where N is the number of atoms per blockade volume. Additional Rydberg effects in the dense mictrotraps, like Trilobite molecules, as well as number fluctuations of the atom number between traps might pose challenges. While single-atom tweezers offer experienced techniques for preparation and Rydberg excitation [6–9, 246], unitary filling of the array still requires some technical effort.

Additionally, the coherent manipulation of the atoms in the optical tweezers to Rydberg states is necessary for quantum cellular automata, but would also be interesting for other experimental studies. This coherence should first be characterized to identify and improve the limiting decoherence mechanisms, like laser linewidths, differential light shifts or Doppler shifts. At the same time, the multifrequency Rydberg excitation scheme for quantum cellular automata requires an experimental upgrade. It is envisioned to add multiple radio frequencies to address the different levels in the Rydberg manifold. Here, one will have to watch out for suppression of unwanted carriers, sidebands and possible cross-talk effects between the different frequencies. Introducing more coherence into the system is also expected to change the phase transition underlying our observation of SOC, the absorbing state phase transition, from a second order to a first order phase transition in the quantum contact process [150, 151, 247, 248]. Hence it is an interesting open question how quantum effects would change the resulting SOC dynamics. As quenched disorder has generally a much stronger effect on quantum phase transitions compared to classical phase transitions, entering the coherent regime is conjectured to strongly impact the extended Griffiths phase, replacing it with a quantum Griffiths phase [249].

Concerning the detection capabilities, it would be useful to spatial detect the Rydberg excitations, as it is available with the high-resolution imaging setup for ground-state atoms. This could be achieved via down pumping schemes with subsequent ground state detection or possibly via spatial ion detection [235, 246, 250–253].

In summary, I have established an ultracold gas under laser excitation to Rydberg states as a powerful framework for exploring complex systems dynamics, evidenced by the three main scientific findings: (i) Self-organized criticality; (ii) Power-law behavior and Griffiths effects on an emergent Rydberg network; (iii) A proposal for Rydberg quantum cellular automata. And there are certainly many more fascinating phenomena waiting to be discovered.

Bibliography

[1] K. E. Boulding, “General Systems Theory - The Skeleton of Science”, Management Science **2** (1956).

[2] W. Buckley, *Sociology and modern systems theory* (Prentice-Hall, 1967).

[3] Y. Bar-Yam, A. F. Siegenfeld, et al., “An introduction to complex systems science and its applications”, Complexity **2020**, 1 (2020).

[4] Y. Bar-Yam, *Dynamics of complex systems* (CRC Press, 2019).

[5] H. J. Metcalf and P. van der Straten, “Laser cooling and trapping”, in (Springer-Verlag New York, 1999).

[6] R. Dumke, M. Volk, T. Müther, et al., “Micro-optical realization of arrays of selectively addressable dipole traps: a scalable configuration for quantum computation with atomic qubits”, Phys. Rev. Lett. **89**, 097903 (2002).

[7] F. Nogrette, H. Labuhn, S. Ravets, et al., “Single-atom trapping in holographic 2d arrays of microtraps with arbitrary geometries”, Phys. Rev. X **4**, 021034 (2014).

[8] D. Barredo, S. de Léséleuc, V. Lienhard, T. Lahaye, and A. Browaeys, “An atom-by-atom assembler of defect-free arbitrary two-dimensional atomic arrays”, Science **354**, 1021 (2016).

[9] H. Bernien, S. Schwartz, A. Keesling, et al., “Probing many-body dynamics on a 51-atom quantum simulator”, Nature **551**, 579 (2017).

[10] Y. Wang, S. Shevate, T. M. Wintermantel, et al., “Preparation of hundreds of microscopic atomic ensembles in optical tweezer arrays”, npj Quantum Inf. **6**, 54 (2020).

[11] Y. Bar-Yam, “Complexity rising: from human beings to human civilization, a complexity profile, encyclopedia of life support systems”, United Nations, Oxford, UK (2002).

[12] M. Batty, *Cities and complexity: understanding cities with cellular automata, agent-based models, and fractals* (The MIT Press, 2007).

[13] J. Neumann, A. W. Burks, et al., *Theory of self-reproducing automata*, Vol. 1102024 (University of Illinois press Urbana, 1966).

[14] V. Colizza and A. Vespignani, “Epidemic modeling in metapopulation systems with heterogeneous coupling pattern: theory and simulations”, Journal of Theoretical Biology **251**, 450 (2008).

[15] W. O. Kermack, A. G. McKendrick, and G. T. Walker, “A contribution to the mathematical theory of epidemics”, Proceedings of the Royal Society of London. Series A, Containing Papers of a Mathematical and Physical Character **115**, 700 (1927).

[16] R. M. Anderson, B Anderson, and R. M. May, *Infectious diseases of humans: dynamics and control* (Oxford university press, 1992).

[17] E. A. Guggenheim, “The principle of corresponding states”, The Journal of Chemical Physics **13**, 253 (1945).

[18] M. M. Boer, R. J. Sadler, R. A. Bradstock, A. M. Gill, and P. F. Grierson, “Spatial scale invariance of southern australian forest fires mirrors the scaling behaviour of fire-driving weather events”, Landscape Ecology **23**, 899 (2008).

[19] G. Boffetta, V. Carbone, P. Giuliani, P. Veltri, and A. Vulpiani, “Power laws in solar flares: self-organized criticality or turbulence?”, Phys. Rev. Lett. **83**, 4662 (1999).

[20] E. O.-O. Max Roser Hannah Ritchie and J. Hasell, “Coronavirus Pandemic (COVID-19)”, Our World in Data, https://ourworldindata.org/coronavirus (2020).

[21] P. Bak, C. Tang, and K. Wiesenfeld, “Self-organized criticality: an explanation of the 1/f noise”, Phys. Rev. Lett. **59**, 381 (1987).

[22] P. Bak, C. Tang, and K. Wiesenfeld, “Self-organized criticality”, Phys. Rev. A **38**, 364 (1988).

[23] E. T. Lu and R. J. Hamilton, “Avalanches and the distribution of solar flares”, The astrophysical journal **380**, L89 (1991).

[24] B. Gutenberg and C. F. Richter, “Frequency of earthquakes in california”, Bulletin of the Seismological Society of America **34**, 185 (1944).

[25] C. A. Cross, “The Size Distribution of Lunar Craters”, Monthly Notices of the Royal Astronomical Society **134**, 245 (1966).

[26] F. Scholkmann, “Power-law scaling of the impact crater size-frequency distribution on pluto: a preliminary analysis based on first images from new horizons flyby”, Progress in Physics **12**, 26 (2016).

[27] G. K. Zipf, “Human behaviour and the principle of least-effort. Cambridge, MA”, Addison-Wesley (1949).

[28] H. M. Gupta, J. A. R. Campanha, and R. A. G. Pesce, “Power-law distributions for the citation index of scientific publications and scientists”, en, Brazilian Journal of Physics **35**, 981 (2005).

[29] P. Vilfredo, “Cours d’économie politique”, Œuvres complètes, tI-II, Genève, Droz (1896).

[30] M. Levy and S. Solomon, “New evidence for the power-law distribution of wealth”, Physica A: Statistical Mechanics and its Applications **242**, 90 (1997).

[31] R. L. Axtell, “Zipf distribution of u.s. firm sizes”, Science **293**, 1818 (2001).

[32] A.-L. Barabási and R. Albert, “Emergence of scaling in random networks”, Science **286**, 509 (1999).

[33] M. Newman, “Power laws, pareto distributions and zipf’s law”, Contemporary Physics **46**, 323 (2005).

[34] A. Clauset, C. R. Shalizi, and M. E. Newman, “Power-law distributions in empirical data”, SIAM review **51**, 661 (2009).

[35] Y. Khaluf, E. Ferrante, P. Simoens, and C. Huepe, “Scale invariance in natural and artificial collective systems: a review”, Journal of the royal society interface **14**, 20170662 (2017).

[36] Á. Corral and Á. González, “Power law size distributions in geoscience revisited”, Earth and Space Science **6**, 673 (2019).

[37] R. Pastor-Satorras, C. Castellano, P. Van Mieghem, and A. Vespignani, “Epidemic processes in complex networks”, Rev. Mod. Phys. **87**, 925 (2015).

[38] C. Viboud, L. Simonsen, and G. Chowell, “A generalized-growth model to characterize the early ascending phase of infectious disease outbreaks”, Epidemics **15**, 27 (2016).

[39] G. Chowell, L. Sattenspiel, S. Bansal, and C. Viboud, “Mathematical models to characterize early epidemic growth: a review”, Phys. Life Rev. **18**, 66 (2016).

[40] B. F. Maier and D. Brockmann, “Effective containment explains subexponential growth in recent confirmed COVID-19 cases in China”, Science **368**, 742 (2020).

[41] K. Roosa, Y. Lee, R. Luo, et al., “Real-time forecasts of the COVID-19 epidemic in China from February 5th to February 24th, 2020”, Infectious Disease Modelling **5**, 256 (2020).

[42] E. Shim, A. Tariq, W. Choi, Y. Lee, and G. Chowell, “Transmission potential and severity of COVID-19 in South Korea”, International Journal of Infectious Diseases **93**, 339 (2020).

[43] G. L. Vasconcelos, A. M. Macêdo, G. C. Duarte-Filho, et al., “Complexity signatures in the COVID-19 epidemic: power law behaviour in the saturation regime of fatality curves”, medRxiv (2020).

[44] A. Tariq, Y. Lee, K. Roosa, et al., “Real-time monitoring the transmission potential of COVID-19 in Singapore, March 2020”, BMC Medicine **18**, 1 (2020).

[45] T. F. Gallagher, *Rydberg atoms*, Cambridge Monographs on Atomic, Molecular and Chemical Physics (Cambridge University Press, 1994).

[46] R. Löw, H. Weimer, J. Nipper, et al., “An experimental and theoretical guide to strongly interacting Rydberg gases”, J. Phys. B **45**, 113001 (2012).

[47] A. Browaeys, D. Barredo, and T. Lahaye, “Experimental investigations of dipole–dipole interactions between a few Rydberg atoms”, J. Phys. B **49**, 152001 (2016).

[48] J.-H. Choi, B. Knuffman, T. C. Liebisch, A. Reinhard, and G. Raithel, in , Vol. 54, edited by P. Berman, C. Lin, and E. Arimondo, Advances In Atomic, Molecular, and Optical Physics (Academic Press, 2007), pp. 131 –202.

[49] M. Saffman, T. G. Walker, and K. Mølmer, “Quantum information with Rydberg atoms”, Rev. Mod. Phys **82**, 2313 (2010).

[50] N. Šibalić, J. Pritchard, C. Adams, and K. Weatherill, “ARC: An open-source library for calculating properties of alkali Rydberg atoms”, Comput. Phys. Commun **220**, 319 (2017).

[51] L. A. M. Johnson, H. O. Majeed, B Sanguinetti, T. Becker, and B. T. H. Varcoe, “Absolute frequency measurements of 85rb nf7/2 Rydberg states using purely optical detection”, New Journal of Physics **12**, 063028 (2010).

[52] C.-J. Lorenzen and K Niemax, “Quantum defects of then2p1/2,3/2levels in39k i and85rb i”, Physica Scripta **27**, 300 (1983).

[53] N. Šibalić, E. J. Robertson, J. D. Pritchard, et al., *ARC-Alkali-Rydberg-Calculator*, version v2.1.1.

[54] K. Singer, J. Stanojevic, M. Weidemüller, and R. Côté, “Long-range interactions between alkali Rydberg atom pairs correlated to the ns-ns, np-np and nd-nd asymptotes”, Journal of Physics B: Atomic, Molecular and Optical Physics **38**, S295 (2005).

[55] A. Reinhard, T. C. Liebisch, B. Knuffman, and G. Raithel, “Level shifts of rubidium Rydberg states due to binary interactions”, Phys. Rev. A **75**, 032712 (2007).

[56] S. Whitlock, “Many-body physics with Rydberg atoms”, HGFSP Graduate Days Lecture (2014).

[57] T. Förster, “Zwischenmolekulare Energiewanderung und Fluoreszenz”, Annalen der Physik **437**, 55 (1948).

[58] I. Mourachko, D. Comparat, F. de Tomasi, et al., “Many-body effects in a frozen Rydberg gas”, Phys. Rev. Lett. **80**, 253 (1998).

[59] W. R. Anderson, J. R. Veale, and T. F. Gallagher, “Resonant dipole-dipole energy transfer in a nearly frozen Rydberg gas”, Phys. Rev. Lett. **80**, 249 (1998).

[60] D. Jaksch, J. I. Cirac, P. Zoller, et al., “Fast quantum gates for neutral atoms”, Phys. Rev. Lett. **85**, 2208 (2000).

[61] M. D. Lukin, M. Fleischhauer, R. Cote, et al., “Dipole blockade and quantum information processing in mesoscopic atomic ensembles”, Phys. Rev. Lett **87**, 037901 (2001).

[62] K. Singer, M. Reetz-Lamour, T. Amthor, L. G. Marcassa, and M. Weidemüller, “Suppression of excitation and spectral broadening induced by interactions in a cold gas of Rydberg atoms”, Phys. Rev. Lett. **93**, 163001 (2004).

[63] D. Tong, S. M. Farooqi, J. Stanojevic, et al., “Local blockade of Rydberg excitation in an ultracold gas”, Phys. Rev. Lett. **93**, 063001 (2004).

[64] T. F. Gallagher and P. Pillet, in *Advances in atomic, molecular, and optical physics*, Vol. 56, Advances In Atomic, Molecular, and Optical Physics (Academic Press, 2008), pp. 161 –218.

[65] E Urban, T. A. Johnson, T Henage, et al., “Observation of Rydberg blockade between two atoms”, Nature Physics **5**, 110 (2009).

[66] A. Gaëtan, Y. Miroshnychenko, T. Wilk, et al., “Observation of collective excitation of two individual atoms in the Rydberg blockade regime”, Nature Physics **5**, 115 (2009).

[67] D. Comparat and P. Pillet, “Dipole blockade in a cold Rydberg atomic sample”, J. Opt. Soc. Am. B **27**, A208 (2010).

[68] C. Ates, T. Pohl, T. Pattard, and J. M. Rost, “Antiblockade in Rydberg excitation of an ultracold lattice gas”, Phys. Rev. Lett. **98**, 023002 (2007).

[69] T. Amthor, C. Giese, C. S. Hofmann, and M. Weidemüller, “Evidence of antiblockade in an ultracold Rydberg gas”, Phys. Rev. Lett. **104**, 013001 (2010).

[70] C. Ates, T. Pohl, T. Pattard, and J. M. Rost, “Many-body theory of excitation dynamics in an ultracold Rydberg gas”, Phys. Rev. A **76**, 013413 (2007).

[71] M Marcuzzi, J Schick, B Olmos, and I Lesanovsky, “Effective dynamics of strongly dissipative Rydberg gases”, Journal of Physics A: Mathematical and Theoretical **47**, 482001 (2014).

[72] S. Helmrich, A. Arias, G. Lochead, et al., “Signatures of self-organized criticality in an ultracold atomic gas”, Nature **577**, 481 (2020).

[73] S. Meszinska, “Sub-Doppler spectroscopy of Rydberg states of potassium”, Master thesis, University of Heidelberg (2014).

[74] A. Sayer, “Fiber-based beam-distribution-system for potassium magneto-optical traps”, Bachelor thesis, University of Heidelberg (2014).

[75] C. Schweiger, “Laser excitation of ultracold potassium Rydberg atoms”, Bachelor thesis, University of Heidelberg (2015).

[76] N. Pehoviak, “Strongly Interacting Ultracold Potassium Atoms via Rydberg Dressing”, Master thesis, University of Heidelberg (2015).

[77] R. Sayer, “Magnetic field switching with a H-bridge circuit to control ultracold atoms”, Bachelor thesis, University of Heidelberg (2016).

[78] E. Pavlov, “Setup and characterization of stable optical traps for ultracold potassium”, Master thesis, University of Heidelberg (2016).

[79] T. M. Wintermantel, “In-situ fluorescence imaging of ultracold potassium in an optical tap”, Master thesis, University of Heidelberg (2016).

[80] H. Hirzler, “Analysis and reduction of spectral broadening in high resolution Rydberg excitation”, Master thesis, University of Heidelberg (2017).

[81] S. Helmrich, “Phase structure and dynamics of driven-dissipative Rydberg spin systems”, PhD thesis, University of Heidelberg (2018).

[82] A. Arias, “Probing the non-equilibrium dynamics and coherence properties of Rydberg-enhanced gases”, PhD thesis, University of Heidelberg (2019).

[83] M. A. Morgado Vargas, “Rydberg excitation in small atomic ensembles”, Master thesis, University of Strasbourg (2019).

[84] Blender Online Community, “Blender - a 3D modelling and rendering package, v. 2.81”, Stichting Blender Foundation, Amsterdam (2019).

[85] B. Höltkemeier, “2D MOT as a source of a cold atom target”, Diploma thesis, University of Heidelberg (2011).

[86] T. G. Tiecke, “Properties of Potassium, v1.03”, (2019).

[87] J. Dalibard and C. Cohen-Tannoudji, “Laser cooling below the Doppler limit by polarization gradients: simple theoretical models”, J. Opt. Soc. Am. B **6**, 2023 (1989).

[88] H. J. Metcalf and P. van der Straten, “Laser cooling and trapping of atoms”, J. Opt. Soc. Am. B **20**, 887 (2003).

[89] M Weidemüller, T Esslinger, M. A Ol'shanii, A Hemmerich, and T. W Hänsch, “A novel scheme for efficient cooling below the photon recoil limit”, EPL **27**, 109 (1994).

[90] D. R. Fernandes, F. Sievers, N. Kretzschmar, et al., “Sub-Doppler laser cooling of fermionic 40K atoms in three-dimensional gray optical molasses”, EPL **100**, 63001 (2012).

[91] G. Salomon, L. Fouché, P. Wang, et al., "Gray-molasses cooling of 39k to a high phase-space density", EPL **104**, 63002 (2013).

[92] A. T. Grier, I. Ferrier-Barbut, B. S. Rem, et al., "Lambda-enhanced sub-Doppler cooling of lithium atoms in d1 gray molasses", Phys. Rev. A **87**, 063411 (2013).

[93] G. Salomon, L. Fouché, S. Lepoutre, A. Aspect, and T. Bourdel, "All-optical cooling of 39K to bose-einstein condensation", Phys. Rev. A **90**, 033405 (2014).

[94] S. Falke, E. Tiemann, C. Lisdat, H. Schnatz, and G. Grosche, "Transition frequencies of the d lines of 39k, 40k, and 41k measured with a femtosecond laser frequency comb", Phys. Rev. A **74**, 032503 (2006).

[95] G. Faraoni, "Nonlinear light propagation through a strongly interacting Rydberg gas", Universit'a di Pisa (2014).

[96] R. Grimm, M. Weidemüller, and Y. B. Ovchinnikov, "Optical dipole traps for neutral atoms", Adv. Atom. Mol. Opt. Phy. **42**, 95 (2000).

[97] C. Chin, R. Grimm, P. Julienne, and E. Tiesinga, "Feshbach resonances in ultracold gases", Rev. Mod. Phys. **82**, 1225 (2010).

[98] C. D'Errico, M. Zaccanti, M. Fattori, et al., "Feshbach resonances in ultracold 39K", New J. Phys. **9**, 223 (2007).

[99] R. Jáuregui, "Nonperturbative and perturbative treatments of parametric heating in atom traps", Phys. Rev. A **64**, 053408 (2001).

[100] T. M. Wintermantel, Y. Wang, G. Lochead, et al., "Unitary and nonunitary quantum cellular automata with Rydberg arrays", Phys. Rev. Lett. **124**, 070503 (2020).

[101] A. Arias, S. Helmrich, C. Schweiger, et al., "Versatile, high-power 460 nm laser system for Rydberg excitation of ultracold potassium", Opt. Express **25**, 14829 (2017).

[102] A Kramida, Y. Ralchenko, J Reader, and N. A. Team, "NIST Atomic Spectra Database", Gaithersburg, MD: NIST. (2019).

[103] R. W. P. Drever, J. L. Hall, F. V. Kowalski, et al., "Laser phase and frequency stabilization using an optical resonator", Appl. Phys. B **31**, 97 (1983).

[104] E. D. Black, "An introduction to pound–drever–hall laser frequency stabilization", Am. J. Phys. **69**, 79 (2001).

[105] C. S. Hofmann, G. Günter, H. Schempp, et al., "An experimental approach for investigating many-body phenomena in Rydberg-interacting quantum systems", Front. Phys. **9**, 571 (2014).

[106] P. Schauß, M. Cheneau, M. Endres, et al., "Observation of spatially ordered structures in a two-dimensional Rydberg gas", Nature **491**, 87 (2012).

[107] J. Zeiher, P. Schauß, S. Hild, et al., "Microscopic characterization of scalable coherent Rydberg superatoms", Phys. Rev. X **5**, 031015 (2015).

[108] C. S. Hofmann, "Emergence of correlations in strongly interacting ultracold Rydberg gases", PhD thesis, University of Heidelberg (2013).

[109] K. Klocke, T. W. Wintermantel, G. Lochead, S. Whitlock, and M. Buchhold, “Hydrodynamic stabilization of self-organized criticality in a driven Rydberg gas”, arXiv:2009.11908 (2020).

[110] D.-S. Ding, H. Busche, B.-S. Shi, G.-C. Guo, and C. S. Adams, “Phase diagram and self-organizing dynamics in a thermal ensemble of strongly interacting Rydberg atoms”, Phys. Rev. X **10**, 021023 (2020).

[111] R Wang, M Aghigh, K. Marroquín, et al., “Radio frequency field-induced electron mobility in an ultracold plasma state of arrested relaxation”, arXiv:2006.16412 (2020).

[112] J. Hesse and T. Gross, “Self-organized criticality as a fundamental property of neural systems”, Frontiers in Systems Neuroscience **8**, 166 (2014).

[113] W. L. Shew, W. P. Clawson, J. Pobst, et al., “Adaptation to sensory input tunes visual cortex to criticality”, Nature Physics **11**, 659 (2015).

[114] K. W. Birkeland and C. C. Landry, “Power-laws and snow avalanches”, Geophysical Research Letters **29**, 49 (2002).

[115] A. Sornette and D. Sornette, “Self-organized criticality and earthquakes”, EPL **9**, 197 (1989).

[116] B. Drossel and F. Schwabl, “Self-organized critical forest-fire model”, Phys. Rev. Lett. **69**, 1629 (1992).

[117] B. D. Malamud, G. Morein, and D. L. Turcotte, “Forest fires: an example of self-organized critical behavior”, Science **281**, 1840 (1998).

[118] C. J. Rhodes and R. M. Anderson, “Power laws governing epidemics in isolated populations”, Nature **381**, 600 (1996).

[119] J. P. Gleeson, J. A. Ward, K. P. O’Sullivan, and W. T. Lee, “Competition-induced criticality in a model of meme popularity”, Phys. Rev. Lett. **112**, 048701 (2014).

[120] R. Dickman, “Numerical study of a field theory for directed percolation”, Phys. Rev. E **50**, 4404 (1994).

[121] M. A. Munoz, G. Grinstein, R. Dickman, and R. Livi, “Critical behavior of systems with many absorbing states”, Phys. Rev. Lett. **76**, 451 (1996).

[122] A. Vespignani and S. Zapperi, “Order parameter and scaling fields in self-organized criticality”, Phys. Rev. Lett. **78**, 4793 (1997).

[123] I. Dornic, H. Chaté, and M. A. Muñoz, “Integration of Langevin equations with multiplicative noise and the viability of field theories for absorbing phase transitions”, Phys. Rev. Lett. **94**, 100601 (2005).

[124] M. Henkel, H. Hinrichsen, and S. Lübeck, *Non-equilibrium phase transitions: absorbing phase transitions*, Vol. 1 (Springer, 2008).

[125] S. Field, J. Witt, F. Nori, and X. Ling, “Superconducting vortex avalanches”, Phys. Rev. Lett. **74**, 1206 (1995).

[126] V. Frette et al., “Avalanche dynamics in a pile of rice”, Nature **379**, 49 (1996).

[127] R. Dickman, M. A. Muñoz, A. Vespignani, and S. Zapperi, "Paths to self-organized criticality", Brazilian Journal of Physics **30**, 27 (2000).

[128] E. Altshuler and T. H. Johansen, "Colloquium: experiments in vortex avalanches", Rev. Mod. Phys. **76**, 471 (2004).

[129] J. A. Bonachela and M. A. Muñoz, "Self-organization without conservation: true or just apparent scale-invariance?", Journal of Statistical Mechanics: Theory and Experiment **2009**, P09009 (2009).

[130] N. W. Watkins, G. Pruessner, S. C. Chapman, N. B. Crosby, and H. J. Jensen, "25 years of self-organized criticality: concepts and controversies", Space Science Reviews **198**, 3 (2016).

[131] T. E. Lee, H. Häffner, and M. C. Cross, "Collective quantum jumps of Rydberg atoms", Phys. Rev. Lett. **108**, 023602 (2012).

[132] R. Heidemann, U. Raitzsch, V. Bendkowsky, et al., "Evidence for coherent collective Rydberg excitation in the strong blockade regime", Physical Review Letters **99**, 163601 (2007).

[133] A. Urvoy, F. Ripka, I. Lesanovsky, et al., "Strongly correlated growth of Rydberg aggregates in a vapor cell", Phys. Rev. Lett. **114**, 203002 (2015).

[134] H. Weimer, R. Löw, T. Pfau, and H. P. Büchler, "Quantum Critical Behavior in Strongly Interacting Rydberg Gases", Phys. Rev. Lett. **101**, 250601 (2008).

[135] M. Gärttner, K. P. Heeg, T. Gasenzer, and J. Evers, "Dynamic formation of Rydberg aggregates at off-resonant excitation", Phys. Rev. A **88**, 043410 (2013).

[136] C. Simonelli, M. M. Valado, G. Masella, et al., "Seeded excitation avalanches in off-resonantly driven Rydberg gases", J. Phys. B: At. Mol. Opt. Phys. **49**, 154002 (2016).

[137] R. Faoro, C. Simonelli, M. Archimi, et al., "Van der waals explosion of cold Rydberg clusters", Phys. Rev. A **93**, 030701 (2016).

[138] I. Lesanovsky and J. P. Garrahan, "Out-of-equilibrium structures in strongly interacting Rydberg gases with dissipation", Phys. Rev. A **90**, 011603 (2014).

[139] M. M. Valado, C. Simonelli, M. D. Hoogerland, et al., "Experimental observation of controllable kinetic constraints in a cold atomic gas", Phys. Rev. A **93**, 040701 (2016).

[140] G. Pupillo, A. Micheli, M. Boninsegni, I. Lesanovsky, and P. Zoller, "Strongly Correlated Gases of Rydberg-Dressed Atoms: Quantum and Classical Dynamics", Phys. Rev. Lett. **104**, 223002 (2010).

[141] A. Klaus, S. Yu, and D. Plenz, "Statistical analyses support power law distributions found in neuronal avalanches", PLOS ONE **6**, 1 (2011).

[142] L. de Arcangelis, C. Godano, E. Lippiello, and M. Nicodemi, "Universality in solar flare and earthquake occurrence", Phys. Rev. Lett. **96**, 051102 (2006).

[143] J. A. Bonachela, S. de Franciscis, J. J. Torres, and M. A. Muñoz, "Self-organization without conservation: are neuronal avalanches generically critical?", Journal of Statistical Mechanics: Theory and Experiment **2010**, P02015 (2010).

[144] N. H. Abel, “Auflösung einer mechanischen Aufgabe.”, Journal für die reine und angewandte Mathematik **1826**, 153 (1826).

[145] D. D. Hickstein, S. T. Gibson, R. Yurchak, D. D. Das, and M. Ryazanov, “A direct comparison of high-speed methods for the numerical abel transform”, Review of Scientific Instruments **90**, 065115 (2019).

[146] S. Gibson, D. D. Hickstein, R. Yurchak, et al., *Pyabel/pyabel*, version v0.8.2, 2019.

[147] M Marcuzzi, E Levi, W Li, et al., “Non-equilibrium universality in the dynamics of dissipative cold atomic gases”, New Journal of Physics **17**, 072003 (2015).

[148] K. Klocke and M. Buchhold, “Controlling excitation avalanches in driven Rydberg gases”, Phys. Rev. A **99**, 053616 (2019).

[149] P Bak and M Paczuski, “Complexity, contingency, and criticality”, Proceedings of the National Academy of Sciences **92**, 6689 (1995).

[150] M. Marcuzzi, M. Buchhold, S. Diehl, and I. Lesanovsky, “Absorbing state phase transition with competing quantum and classical fluctuations”, Phys. Rev. Lett. **116**, 245701 (2016).

[151] M. Buchhold, B. Everest, M. Marcuzzi, I. Lesanovsky, and S. Diehl, “Nonequilibrium effective field theory for absorbing state phase transitions in driven open quantum spin systems”, Phys. Rev. B **95**, 014308 (2017).

[152] T. M. Wintermantel, M. Buchhold, S. Shevate, et al., “Epidemic growth and Griffiths effects on an emergent network of excited atoms”, arXiv:2007.07697 (2020).

[153] A. Barrat, M. Barthelemy, and A. Vespignani, *Dynamical processes on complex networks* (Cambridge University Press, 2008).

[154] P. Van Mieghem, *Performance analysis of complex networks and systems* (Cambridge University Press, 2014).

[155] G. Chowell, C. Viboud, L. Simonsen, and S. M. Moghadas, “Characterizing the reproduction number of epidemics with early subexponential growth dynamics”, J. R. Soc. Interface **13**, 20160659 (2016).

[156] M. Bampo, M. T. Ewing, D. R. Mather, D. Stewart, and M. Wallace, “The effects of the social structure of digital networks on viral marketing performance”, Inf. Syst. Res. **19**, 273 (2008).

[157] R. Peckham, “Contagion: epidemiological models and financial crises”, J. Public Health (Oxf.) **36**, 13 (2014).

[158] M. Saberi, H. Hamedmoghadam, M. Ashfaq, et al., “A simple contagion process describes spreading of traffic jams in urban networks”, Nat. Commun. **11**, 1 (2020).

[159] H. Schempp, G. Günter, M. Robert-de Saint-Vincent, et al., “Full counting statistics of laser excited Rydberg aggregates in a one-dimensional geometry”, Phys. Rev. Lett. **112**, 013002 (2014).

[160] N. Malossi, M. M. Valado, S. Scotto, et al., “Full counting statistics and phase diagram of a dissipative Rydberg gas”, Phys. Rev. Lett. **113**, 023006 (2014).

[161] R. Gutiérrez, C. Simonelli, M. Archimi, et al., “Experimental signatures of an absorbing-state phase transition in an open driven many-body quantum system”, Phys. Rev. A **96**, 041602 (2017).

[162] T. E. Lee, H. Häffner, and M. C. Cross, “Antiferromagnetic phase transition in a nonequilibrium lattice of Rydberg atoms”, Phys. Rev. A **84**, 031402 (2011).

[163] I. Lesanovsky and J. P. Garrahan, “Kinetic constraints, hierarchical relaxation, and onset of glassiness in strongly interacting and dissipative Rydberg gases”, Phys. Rev. Lett. **111**, 215305 (2013).

[164] C. Carr, R. Ritter, C. G. Wade, C. S. Adams, and K. J. Weatherill, “Nonequilibrium phase transition in a dilute Rydberg ensemble”, Phys. Rev. Lett. **111**, 113901 (2013).

[165] S. Helmrich, A. Arias, and S. Whitlock, “Uncovering the nonequilibrium phase structure of an open quantum spin system”, Phys. Rev. A **98**, 022109 (2018).

[166] E. A. Goldschmidt, T. Boulier, R. C. Brown, et al., “Anomalous broadening in driven dissipative Rydberg systems”, Phys. Rev. Lett. **116**, 113001 (2016).

[167] M. Marcuzzi, J. Minar ár, D. Barredo, et al., “Facilitation dynamics and localization phenomena in Rydberg lattice gases with position disorder”, Phys. Rev. Lett. **118**, 063606 (2017).

[168] D. J. Watts and S. H. Strogatz, “Collective dynamics of ’small-world’ networks”, Nature **393**, 440 (1998).

[169] P. Schauß, J. Zeiher, T. Fukuhara, et al., “Crystallization in Ising quantum magnets”, Science **347**, 1455 (2015).

[170] A. Chotia, M. Viteau, T. Vogt, D. Comparat, and P. Pillet, “Kinetic Monte Carlo modeling of dipole blockade in Rydberg excitation experiment”, New J. Phys **10**, 045031 (2008).

[171] A. P. Millán, G. Gori, F. Battiston, T. Enss, and N. Defenu, “Complex networks with tuneable dimensions as a universality playground”, arXiv:2006.10421 (2020).

[172] S. Bettelli, D. Maxwell, T. Fernholz, et al., “Exciton dynamics in emergent Rydberg lattices”, Phys. Rev. A **88**, 043436 (2013).

[173] T. Vojta, “Disorder in quantum many-body systems”, Annu. Rev. Condens. Matter Phys **10**, 233 (2019).

[174] A. G. Moreira and R. Dickman, “Critical dynamics of the contact process with quenched disorder”, Phys. Rev. E **54**, R3090 (1996).

[175] T. Vojta and M. Dickison, “Critical behavior and Griffiths effects in the disordered contact process”, Phys. Rev. E **72**, 036126 (2005).

[176] M. A. Muñoz, R. Juhász, C. Castellano, and G. Ódor, “Griffiths phases on complex networks”, Phys. Rev. Lett. **105**, 128701 (2010).

[177] P. Moretti and M. Muñoz, “Griffiths phases and the stretching of criticality in brain networks”, Nat. Commun. **4**, 2521 (2013).

[178] C. Buono, F. Vazquez, P. A. Macri, and L. A. Braunstein, “Slow epidemic extinction in populations with heterogeneous infection rates”, Phys. Rev. E **88**, 022813 (2013).

[179] S. A. Kauffman, “Emergent properties in random complex automata”, Physica D: Nonlinear Phenomena **10**, 145 (1984).

[180] H.-H. Chou and J. A. Reggia, “Emergence of self-replicating structures in a cellular automata space”, Physica D: Nonlinear Phenomena **110**, 252 (1997).

[181] N. Israeli and N. Goldenfeld, “Coarse-graining of cellular automata, emergence, and the predictability of complex systems”, Phys. Rev. E **73**, 026203 (2006).

[182] J. E. Hanson, “Cellular automata, emergent phenomena in”, in *Encyclopedia of complexity and systems science*, edited by R. A. Meyers (Springer New York, New York, NY, 2009), pp. 768–778.

[183] M. Gardner, “The fantastic combinations of john conway’s new solitaire game “life””, Sci. Am. **223**, 120 (1970).

[184] M. Gardner, “On cellular automata, self-reproduction, the garden of eden and the game “life””, Sci. Am. **224**, 112 (1971).

[185] B. Chopard and M. Droz, *Cellular automata modeling of physical systems* (1998).

[186] U. Frisch, B. Hasslacher, and Y. Pomeau, “Lattice-gas automata for the Navier-Stokes equation”, Phys. Rev. Lett. **56**, 1505 (1986).

[187] S. Wolfram, *A new kind of science* (Wolfram Media, 2002).

[188] S. Wolfram, “Cryptography with cellular automata”, in Conference on the theory and application of cryptographic techniques (Springer, 1985), pp. 429–432.

[189] M. Cook, “Universality in elementary cellular automata”, Complex Syst. **15**, 1 (2004).

[190] K. Wiesner, “Quantum cellular automata”, in *Encyclopedia of complexity and systems science*, edited by R. A. Meyers (Springer New York, New York, NY, 2009), pp. 7154–7164.

[191] T. Farrelly, “A review of quantum cellular automata”, arXiv:1904.13318 (2019).

[192] P. Arrighi, “An overview of quantum cellular automata”, Natural Computing **18**, 885 (2019).

[193] S. Lloyd, “A potentially realizable quantum computer”, Science **261**, 1569 (1993).

[194] R. Raussendorf, “Quantum cellular automaton for universal quantum computation”, Phys. Rev. A **72**, 022301 (2005).

[195] K. G. H. Vollbrecht and J. I. Cirac, “Reversible universal quantum computation within translation-invariant systems”, Phys. Rev. A **73**, 012324 (2006).

[196] J. Watrous, “On one-dimensional quantum cellular automata”, in Proceedings of IEEE 36th Annual Foundations of Computer Science (1995), pp. 528–537.

[197] H. Weimer, M. Müller, I. Lesanovsky, P. Zoller, and H. P. Büchler, “A Rydberg quantum simulator”, Nat. Phys **6**, 382 (2010).

[198] D. Petrosyan, M. Saffman, and K. Mølmer, “Grover search algorithm with Rydberg-blockaded atoms: quantum Monte Carlo simulations”, J. Phys. B: At. Mol. Opt. Phys. **49**, 094004 (2016).

[199] M. Ostmann, J. Minar, M. Marcuzzi, E. Levi, and I. Lesanovsky, “Non-adiabatic quantum state preparation and quantum state transport in chains of Rydberg atoms”, New J. Phys **19**, 123015 (2017).

[200] T. Keating, K. Goyal, Y. Y. Jau, et al., “Adiabatic quantum computation with Rydberg-dressed atoms”, Phys. Rev. A **87**, 052314 (2013).

[201] W. Lechner, P. Hauke, and P. Zoller, “A quantum annealing architecture with all-to-all connectivity from local interactions”, Sci. Adv. **1**, e1500838 (2015).

[202] A. W. Glaetzle, R. M. W. van Bijnen, P. Zoller, and W. Lechner, “A coherent quantum annealer with Rydberg atoms”, Nat. Commun. **8**, 15813 (2017).

[203] R. G. Unanyan and M. Fleischhauer, “Efficient and robust entanglement generation in a many-particle system with resonant dipole-dipole interactions”, Phys. Rev. A **66**, 032109 (2002).

[204] L. Isenhower, M. Saffman, and K. Mølmer, “Multibit CkNOT quantum gates via Rydberg blockade”, Quantum Inf Process **10**, 755 (2011).

[205] M. Ebert, M. Kwon, T. G. Walker, and M. Saffman, “Coherence and Rydberg blockade of atomic ensemble qubits”, Phys. Rev. Lett **115**, 093601 (2015).

[206] F. M. Gambetta, W. Li, F. Schmidt-Kaler, and I. Lesanovsky, “Engineering nonbinary Rydberg interactions via phonons in an optical lattice”, Phys. Rev. Lett. **124**, 043402 (2020).

[207] F. Verstraete, M. M. Wolf, and J. I. Cirac, “Quantum computation and quantum-state engineering driven by dissipation”, Nat. Phys **5**, 633 (2009).

[208] D. Rao and K. Mølmer, “Dark entangled steady states of interacting Rydberg atoms”, Phys. Rev. Lett **111**, 033606 (2013).

[209] D. D. B. Rao and K. Mølmer, “Deterministic entanglement of Rydberg ensembles by engineered dissipation”, Phys. Rev. A **90**, 062319 (2014).

[210] X. Q. Shao, J. B. You, T. Y. Zheng, C. H. Oh, and S. Zhang, “Stationary three-dimensional entanglement via dissipative Rydberg pumping”, Phys. Rev. A **89**, 052313 (2014).

[211] M. Roghani and H. Weimer, “Dissipative preparation of entangled many-body states with Rydberg atoms”, Quantum Sci. Technol. **3**, 035002 (2018).

[212] Z. X. Ding, C. S. Hu, L. T. Shen, et al., “Dissipative entanglement preparation via Rydberg antiblockade and Lyapunov control”, Laser Phys. Lett. **16**, 045203 (2019).

[213] S. C. Benjamin, “Schemes for parallel quantum computation without local control of qubits”, Phys. Rev. A **61**, 020301 (2000).

[214] S. C. Benjamin, “Quantum computing without local control of qubit-qubit interactions”, Phys. Rev. Lett. **88**, 017904 (2001).

[215] J. Twamley, “Quantum-cellular-automata quantum computing with endohedral fullerenes”, Phys. Rev. A **67**, 052318 (2003).

[216] G. K. Brennen and J. E. Williams, “Entanglement dynamics in one-dimensional quantum cellular automata”, Phys. Rev. A **68**, 042311 (2003).

[217] I. Lesanovsky, “Many-body spin interactions and the ground state of a dense Rydberg lattice gas”, Phys. Rev. Lett **106**, 025301 (2011).

[218] M. Sanz, E. Solano, and Í. L. Egusquiza, “Beyond adiabatic elimination: effective hamiltonians and singular perturbation”, in Applications + practical conceptualization + mathematics = fruitful innovation, edited by R. S. Anderssen, P. Broadbridge, Y. Fukumoto, et al. (2016), pp. 127–142.

[219] F. Reiter and A. S. Sørensen, “Effective operator formalism for open quantum systems”, Phys. Rev. A **85**, 032111 (2012).

[220] I. Lesanovsky, “Many-body spin interactions and the ground state of a dense Rydberg lattice gas”, Phys. Rev. Lett **106**, 025301 (2011).

[221] B. Olmos, I. Lesanovsky, and J. P. Garrahan, “Facilitated spin models of dissipative quantum glasses”, Phys. Rev. Lett. **109**, 020403 (2012).

[222] C. J. Turner, A. A. Michailidis, D. A. Abanin, M. Serbyn, and Z. Papić, “Quantum scarred eigenstates in a Rydberg atom chain: entanglement, breakdown of thermalization, and stability to perturbations”, Phys. Rev. B **98**, 155134 (2018).

[223] I. Lesanovsky, K. Macieszczak, and J. P. Garrahan, “Non-equilibrium absorbing state phase transitions in discrete-time quantum cellular automaton dynamics on spin lattices”, Quantum Sci. Technol. **4**, 02LT02 (2019).

[224] M. Ostmann, M. Marcuzzi, J. P. Garrahan, and I. Lesanovsky, “Localization in spin chains with facilitation constraints and disordered interactions”, Phys. Rev. A **99**, 060101 (2019).

[225] J. Johansson, P. Nation, and F. Nori, “Qutip 2: a Python framework for the dynamics of open quantum systems”, Comput. Phys. Commun **184**, 1234 (2013).

[226] L. E. Hillberry, “Entanglement and complexity in quantum elementary cellular automata”, PhD thesis, Colorado School of Mines. Arthur Lakes Library (2016).

[227] D. M. Greenberger, M. A. Horne, and A. Zeilinger, “Going beyond bell’s theorem”, in *Bell’s theorem, quantum theory and conceptions of the universe*, edited by M. Kafatos (Springer Netherlands, Dordrecht, 1989), pp. 69–72.

[228] D. M. Greenberger, M. A. Horne, A. Shimony, and A. Zeilinger, “Bell’s theorem without inequalities”, American Journal of Physics **58**, 1131 (1990).

[229] A. Omran, H. Levine, A. Keesling, et al., “Generation and manipulation of Schrödinger cat states in Rydberg atom arrays”, Science **365**, 570 (2019).

[230] T. Helgaker, P. Jorgensen, and J. Olsen, *Molecular electronic-structure theory* (John Wiley & Sons, 2014).

[231] A. Peruzzo, J. McClean, P. Shadbolt, et al., “A variational eigenvalue solver on a photonic quantum processor”, Nat. Commun **5**, 4213 (2014).

[232] P. J. J. O’Malley, R. Babbush, I. D. Kivlichan, et al., “Scalable quantum simulation of molecular energies”, Phys. Rev. X **6**, 031007 (2016).

[233] A. Kandala, A. Mezzacapo, K. Temme, et al., “Hardware-efficient variational quantum eigensolver for small molecules and quantum magnets”, Nature **549**, 242 (2017).

[234] C. Kokail, C. Maier, R. van Bijnen, et al., “Self-verifying variational quantum simulation of lattice models”, Nature **569**, 355 (2019).

[235] H. Labuhn, D. Barredo, S. Ravets, et al., “Tunable two-dimensional arrays of single Rydberg atoms for realizing quantum Ising models”, Nature **534**, 667 (2016).

[236] F. Biscani and D. Izzo, “A parallel global multiobjective framework for optimization: pagmo”, Journal of Open Source Software **5**, 2338 (2020).

[237] F. Biscani, D. Izzo, W. Jakob, et al., “Esa/pagmo2: pagmo 2.12.0 (version v2.12.0)”, Zenodo.org (2019).

[238] R. Storn and K. Price, “Differential evolution–a simple and efficient heuristic for global optimization over continuous spaces”, Journal of global optimization **11**, 341 (1997).

[239] D. Karaboga and B. Basturk, “A powerful and efficient algorithm for numerical function optimization: artificial bee colony (abc) algorithm”, Journal of global optimization **39**, 459 (2007).

[240] M. Mernik, S.-H. Liu, D. Karaboga, and M. Črepinšek, “On clarifying misconceptions when comparing variants of the artificial bee colony algorithm by offering a new implementation”, Information Sciences **291**, 115 (2015).

[241] J. Kennedy and R. Eberhart, “Particle swarm optimization”, in Proceedings of icnn’95-international conference on neural networks, Vol. 4 (IEEE, 1995), pp. 1942–1948.

[242] R. Poli, J. Kennedy, and T. Blackwell, “Particle swarm optimization”, Swarm intelligence **1**, 33 (2007).

[243] W. Dür, M. Skotiniotis, F. Froewis, and B. Kraus, “Improved quantum metrology using quantum error correction”, Phys. Rev. Lett **112**, 080801 (2014).

[244] N. H. Nickerson, Y. Li, and S. C. Benjamin, “Topological quantum computing with a very noisy network and local error rates approaching one percent”, Nat. Commun **4**, 1756 (2013).

[245] W. K. Wootters and W. H. Zurek, “A single quantum cannot be cloned”, Nature **299**, 802 (1982).

[246] I. S. Madjarov, J. P. Covey, A. L. Shaw, et al., “High-fidelity entanglement and detection of alkaline-earth Rydberg atoms”, Nature Physics, 1 (2020).

[247] C. Pérez-Espigares, M. Marcuzzi, R. Gutiérrez, and I. Lesanovsky, “Epidemic dynamics in open quantum spin systems”, Phys. Rev. Lett. **119**, 140401 (2017).

[248] F. Carollo, E. Gillman, H. Weimer, and I. Lesanovsky, “Critical behavior of the quantum contact process in one dimension”, Phys. Rev. Lett. **123**, 100604 (2019).

[249] T. Vojta, “Quantum griffiths effects and smeared phase transitions in metals: theory and experiment”, Journal of Low Temperature Physics **161**, 299 (2010).

[250] A. Schwarzkopf, R. E. Sapiro, and G. Raithel, “Imaging spatial correlations of Rydberg excitations in cold atom clouds”, Phys. Rev. Lett. **107**, 103001 (2011).

[251] P. Schauß, M. Cheneau, M. Endres, et al., “Observation of spatially ordered structures in a two-dimensional Rydberg gas”, Nature **491**, 87 (2012).

[252] G. Günter, M. Robert-de Saint-Vincent, H. Schempp, et al., “Interaction enhanced imaging of individual Rydberg atoms in dense gases”, Phys. Rev. Lett. **108**, 013002 (2012).

[253] T Manthey, T. M. Weber, T Niederprüm, et al., “Scanning electron microscopy of Rydberg-excited Bose-Einstein condensates”, New Journal of Physics **16**, 083034 (2014).

List of Figures

List of Tables

Acknowledgements

I would like to take this opportunity to express my gratitude to all the people who have supported me throughout this thesis.

- First, I would like to kindly thank my supervisors Prof. Matthias Weidemüller and Prof. Shannon Whitlock for their support and guidance, and especially for debarking with me on the cotutelle adventure.
- I would like to thank Prof. Selim Jochim for readily agreeing to be a referee of my thesis.
- Likewise, I would like to convey my thanks to my committee members Prof. Tilman Enss and Prof. Ulrich Schwarz.
- Thanks to Prof. Pierre Collet for the QMAT mentoring and his enthusiasm for the quantum world.
- Thanks to the whole exotic quantum matter team for the group spirit and a great and productive time: Alda Arias, Bleuenn Begoc, Henrik Hirzler, Stephan Helmrich, Graham Lochead, Manuel Morgado, Sayali Shevate and Yibo Wang.
- I want to thank the whole QD group for a great atmosphere and thrilling kicker matches.
- Thanks to Claudia Krämer and Corinne Ledger for their help with all organizational issues.
- I also want to thank the workshops for the construction of parts which were essential for this thesis. I am particularly grateful to Herr Ziegler and his team for their indispensable support in moving the experiment from Heidelberg to Strasbourg.
- Thanks to all the people who made the cotutelle agreement finally happen, especially to Virginie Herbasch and Elisabeth Miller. Thanks to the Franco-German University (DFH) for their support via the cotutelle de thèse stipend: Diese Arbeit wurde von der Deutsch-Französischen Hochschule (DFH) finanziell gefördert.
- Special thanks to Ina, my parents, my brother, my whole family and friends for their love and support throughout my whole life.